TU Delft

Delft University of Technology

Sensor-based quality inspection of secondary resources

Laser-induced breakdown spectroscopy

Xia, H.

DOI
10.4233/uuid:d6fa8b1f-0f9b-4ed3-aedc-b4e93c83b2fc

Publication date
2021

Document Version
Final published version

Citation (APA)
Xia, H. (2021). *Sensor-based quality inspection of secondary resources: Laser-induced breakdown spectroscopy*. [Dissertation (TU Delft), Delft University of Technology].
https://doi.org/10.4233/uuid:d6fa8b1f-0f9b-4ed3-aedc-b4e93c83b2fc

Important note
To cite this publication, please use the final published version (if applicable).
Please check the document version above.

Copyright
Other than for strictly personal use, it is not permitted to download, forward or distribute the text or part of it, without the consent of the author(s) and/or copyright holder(s), unless the work is under an open content license such as Creative Commons.

Takedown policy
Please contact us and provide details if you believe this document breaches copyrights.
We will remove access to the work immediately and investigate your claim.

This work is downloaded from Delft University of Technology.
For technical reasons the number of authors shown on this cover page is limited to a maximum of 10.

SENSOR BASED QUALITY INSPECTION OF SECONDARY RESOURCES

LASER-INDUCED BREAKDOWN SPECTROSCOPY

Han XIA

SENSOR BASED QUALITY INSPECTION OF SECONDARY RESOURCES

LASER-INDUCED BREAKDOWN SPECTROSCOPY

SENSOR BASED QUALITY INSPECTION OF SECONDARY RESOURCES

LASER-INDUCED BREAKDOWN SPECTROSCOPY

Proefschrift

ter verkrijging van de graad van doctor
aan de Technische Universiteit Delft,
op gezag van de Rector Magnificus prof.dr.ir. T.H.J.J. van der Hagen,
voorzitter van het College voor Promoties,
in het openbaar te verdedigen op woensdag 8 september 2021 om 10:00 uur

door

Han XIA

Master of Science in Physical Technologies, Technische Universiteit Clausthal, Duitsland
geboren te Suichang, Zhejiang, China.

Dit proefschrift is goedgekeurd door de

Promotor: Prof.dr. P.C. Rem
Copromotor: Dr.ir. M.C.M. Bakker

Samenstelling promotiecommissie:

Rector Magnificus	voorzitter
Prof.dr. P.C. Rem	Technische Universiteit Delft, promotor
Dr.ir. M.C.M. Bakker	Technische Universiteit Delft, copromotor
Onafhankelijke leden:	
Prof.dr.ir A.H.M. Smets	Technische Universiteit Delft
Prof.dr. A.V. Metrikine	Technische Universiteit Delft
Prof.dr.ing. M.H. Tierean	Transilvania University of Brasov
Dr. Y. Yang	Technische Universiteit Delft
Dr.ir. M. Sandtke	Spectral Industries
Prof.dr.ir. R. Benedictus	Technische Universiteit Delft, reservelid

Keywords: LIBS, Quality Inspection, Recycling, Demolition Concrete, Classification

Printed by: ProefschriftMaken, Eindhoven, the Netherlands

Copyright © 2021 by Han Xia

ISBN: 978-94-6366-437-0

An electronic version of this dissertation is available at
http://repository.tudelft.nl/.

Dedicated to my beloved family.

Han Xia

CONTENTS

Summary **xi**

Samenvatting **xiii**

1 Introduction **1**
1.1 Motivation . . . 1
1.2 Objectives and methodology . . . 3
1.3 Non-contact sensor techniques applicable for recycling: an overview . . . 4
1.4 Technologies and procedures in LIBS: A literature review . . . 9
1.5 LIBS in the recycling industry . . . 14
1.6 Dutch economic perspective . . . 17
1.7 A closed concrete lifecycle . . . 19
1.8 Outline . . . 22
1.9 Acknowledgements . . . 24
References . . . 24

2 Physics of nanosecond LIBS **35**
2.1 Transient processes and model assumptions . . . 35
2.1.1 Account of the main processes behind LIBS . . . 35
2.1.2 Implications for application of LIBS . . . 41
2.1.3 Assumptions and parameters in the model . . . 42
2.2 Modelling the laser experiment . . . 43
2.2.1 Heating and melting . . . 43
2.2.2 Vapour plume formation . . . 46
2.2.3 Transmission of incident laser light . . . 48
2.2.4 Shock wave and elastic energy . . . 52
2.2.5 Vapour expansion . . . 53
2.2.6 Optical emission spectra . . . 54
References . . . 55

3 Experimental study in laser deployment and data quality **61**
3.1 Adaptive optics and light collection from the plasma plume . . . 62
3.1.1 Angled light collection . . . 64
3.1.2 Ray tracing for parabolic mirrors . . . 66
3.1.3 Testing light collection from a parabolic mirror . . . 71
3.1.4 Spectrometer calibration . . . 72
3.2 Synchronization of laser pulse and acquisition window . . . 73
3.3 Characterization of the laser beam . . . 76
3.3.1 Laser beam profile . . . 76
3.3.2 1064 nm Laser light dissipation . . . 79
3.4 Open air shot stability and data quality . . . 80
3.5 LIBS observation depth and laser angle . . . 83
3.6 Relation between laser fluence and ablated mass . . . 89
References . . . 94

4 Properties of LIBS spectra **96**
4.1 Study of variations in LIBS spectra . . . 97
4.1.1 Variation caused by optical throughput . . . 100
4.1.2 Variation caused by laser fluence . . . 102

4.2 Case study using normalized LIBS data . . . 104
4.2.1 Classification of coins using single shot data . . . 104
4.2.2 Classification of binary mixtures . . . 107
4.2.3 Matrix effect: Tracking lithium in different matrices . . . 114
4.2.4 Sensitive detection of a thin calcium layer on sand grains . . . 116
4.2.5 Relation between LIBS spectra of sand and concrete strength . . . 119
References . . . 120

5 Model-based single-shot LIBS 121
5.1 Signal processing for model-based LIBS: Plasma electron density & temperature . . . 123
5.2 Derivation of model-based LIBS . . . 125
5.3 Modelling LIBS spectral lines . . . 130
5.4 Model based LIBS applied to cementitious materials . . . 136
5.4.1 XRF as a reference technique. . . . 136
5.4.2 XRF and LIBS samples and calibration . . . 138
5.4.3 Selection of LIBS emission lines for calibration . . . 141
5.4.4 Calibration based LIBS in a comparison with XRF . . . 144
5.4.5 Model based LIBS, performance and sensitivity . . . 145
5.4.6 MLIBS study of processed concrete . . . 148
References . . . 152

6 Statistical classification of EOL building materials 154
6.1 Basics of classification . . . 155
6.2 Detailing of potential statistical techniques . . . 157
6.2.1 Principal Component Analysis (PCA) . . . 158
6.2.2 Partial least squares (PLS) . . . 159
6.2.3 Adaptive boosting (Adaboost) . . . 162
6.3 Case study: classification of cement, concrete, and waste pollutants . . . 164
6.3.1 PCA-Adaboost . . . 166
6.3.2 PLS-DA . . . 168
6.4 Case study: classification of moving waste materials . . . 169
6.4.1 Samples and setup . . . 169
6.4.2 LIBS spectra of eight waste materials. . . . 172
6.4.3 PLS-DA results on eight waste materials . . . 175
6.4.4 PCA-Adaboost on eight waste materials . . . 178
6.4.5 Effect of ensemble average . . . 182
6.5 Correlation between LIBS data and concrete quality . . . 184
6.6 Quantitative element analysis using PLS . . . 189
6.7 Demonstration of inline LIBS in an industrial setting . . . 192
6.7.1 Inline LIBS classification results on RCA . . . 192
6.7.2 LIBS unit, setting, and materials . . . 193
6.7.3 Results for inline LIBS qualification of RCA . . . 194
References . . . 196

7 Conclusions 197
7.1 Principles and processes . . . 197
7.2 Techniques and inline adaptation. . . . 199
7.3 Questions for future research . . . 202

Appendices 203
.1 Appendix A: Most abundant LIBS emission lines of cementitious materials . . . 204
References . . . 210
.2 Appendix B: laser ablation parameters on six materials using white light interferometry image analysis-method 1 with varying working distance . . . 214
.3 Appendix C: laser ablation parameters on four materials using white light interferometry image analysis-method 2 with varying laser fluence . . . 217

Acknowledgements **218**

Curriculum Vitæ **221**

List of Publications **222**

SUMMARY

The quality control of materials from waste is an important step for acceptance in new high-quality products. Given the large volumes and complexity of waste streams, this requires advanced sensor technology such as the Laser Induced Breakdown Spectroscopy (LIBS) investigated in this thesis. Recyclers often rely solely on manual sorting and visual inspection, which is far less reliable and accurate than sensor technology that enables automated inspection. The main source of waste in this thesis is demolition concrete. It is characterized by large amounts of moisty granular material, varying amounts and types of impurities, and a dusty environment. This presents a major challenge to introduce an optical inspection technique such as LIBS.

The research starts with a literature study into the state of the art of LIBS as a material identification technique. This is followed by a more physically oriented literature review of the transient processes and parameters involved in ablation and plasma formation by a high power pulsed Nd:YAG 1064 nm laser. From this follows the development of models to account for the different processes and phases of the matter. To this end, the different transient processes are separated and analysed by making use of local equilibrium conditions. Subsequently, the influence of the optics and associated hardware that is necessary to obtain good optical data is investigated. This knowledge is supplemented by a study of light collection and data processing techniques to further improve the quality and reproducibility of the optical data, given the challenging conditions in a recycling factory. Subsequently, to better understand the potential and limitations of experimental LIBS data, the useful information about the chemical composition and technical properties of the material sample is tested under different conditions.

The aforementioned separate physical models have been compiled into a complete plasma model (MLIBS for short). This can explain the properties and emissions of a laser induced plasma. This model can also be used in reverse to determine the composition of sampled elements in a laser induced plasma. The focus is on the ability not to average data to eliminate noise, but to use the data from each laser shot usefully for identification. This is called single-shot data and it is the most efficient way to implement LIBS in practice, because the price of LIBS hardware increases rapidly with the number of shots a laser has to deliver per second. The last part of research is on statistical techniques that can use all relevant information in LIBS data to make the best decision when it comes to identifying different complex materials. By accumulating statistics, the material composition of contaminated concrete waste flows can be determined more reliably. Based on the entire research in this thesis, a prototype LIBS platform has been developed and integrated with a conveyor belt for the inspection of demolition concrete in a recycling plant. The platform withstood harsh outdoor conditions and successfully demonstrated the capabilities of automated inspection with LIBS. Development of the prototype included the design and integration of a laser system, optics, electronic control equipment, real-time data acquisition system, spectral data processing software, and a weatherproof protective frame.

- Chapter 1 describes the motivation, objectives, methodology and background of the research from a recycling perspective. It explains why LIBS is a promising sensor technology for automated quality control. It concludes with the technical literature review.
- Chapter 2 discusses the possible physical processes and parameters in an ablation experiment with a high power pulsed YAG 1064nm laser, based on the physical literature. The processes are modelled separately as if they were individual events in time rather than transient and overlapping. This approximation is accurate when there is local thermal equilibrium. To allow for different thermodynamic pathways (processes) for laser ablation, the final plasma state is modelled as the result of a sequence of classical phase changing processes and ionization. The model parameters can be specified for minerals or for metals that also occur as contaminants in concrete waste.

- Chapter 3 investigates methods for adaptive optics with good data quality so that no autofocus hardware is needed to keep the granular concrete on the conveyor continuously in the focus of the laser and the light collection. Physical causes of sampling bias are highlighted and linked to the average composition of the materials. Relationships between LIBS spectra and ablation parameters are explained using white light interferometry measurements. Single-shot normalization schemes are proposed to suppress possible noise such as variations in mean energy in the data sets.
- Chapter 4 investigates the properties and sensitivity of LIBS spectra. In particular the variations that come from the sampled material surface. Factors to be investigated are, for example, the ablated mass, laser-plasma interactions and the matrix effect. Reliable multi-element quantitative calibration curves have been shown to compensate for the identified spectral variations.
- Chapter 5 builds the plasma model for laser induced plasma emissions. It has been developed to provide a quantitative estimate of the elemental composition of the plasma, without the need for calibration or supervised training sets. The model has been tested for its suitability to identify different materials.
- Chapter 6 implements promising and robust statistical algorithms for the classification of complex materials. The algorithms are tested and compared for their suitability for practical application.
- Chapter 7 presents the conclusions and recommendations for further research.

SAMENVATTING

De kwaliteitscontrole van materialen uit afval is een belangrijke stap voor acceptatie in nieuwe hoogwaardige producten. Gezien de grote volumes en complexiteit van afvalstromen vereist dit geavanceerde sensortechnologie, zoals de Laser Induced Breakdown Spectroscopy (LIBS) dat in dit proefschrift wordt onderzocht. Recyclers vertrouwen vaak nog alleen op handmatige sortering en visuele inspectie, wat veel minder betrouwbaar en nauwkeurig is dan sensortechnologie die geautomatiseerde inspectie mogelijk maakt. De belangrijkste bron van afval in dit proefschrift is betonpuin uit sloop. Het wordt gekenmerkt door grote hoeveelheden vochtig en korrelig materiaal, verschillende hoeveelheden en soorten verontreinigingen, en een stoffige omgeving. Dit betekent een grote uitdaging om een optische inspectietechniek zoals LIBS te introduceren.

Het onderzoek start met een literatuurstudie naar de huidige kennis van LIBS als materiaal identificatie techniek. Dit wordt gevolgd door een meer fysisch georiënteerde literatuurstudie naar de transiente processen en parameters die een rol spelen in de ablatie en plasmavorming door een hoogvermogen gepulsde Nd:YAG 1064 nm laser. Hieruit volgt de ontwikkeling van modellen voor de verantwoording van de afzonderlijke processen en fases van de materie. Daartoe worden de onderscheiden transiente processen afgezonderd en geanalyseerd door gebruik te maken van lokale evenwichtscondities. Vervolgens wordt de invloed van de optica en bijbehorende hardware onderzocht die nodig is om goede optische data te verkrijgen. Deze kennis wordt aangevuld met een studie naar lichtcollectie en data bewerkingstechnieken om de kwaliteit en reproduceerbaarheid van de optische data verder te verbeteren, gezien de uitdagende omstandigheden in een recycling fabriek. Vervolgens, om het potentieel en de beperkingen van experimentele LIBS data beter te begrijpen, wordt de bruikbare informatie over de chemische samenstelling en technische eigenschappen van het materiaal sample onder verschillende omstandigheden getest.

De eerder genoemde afzonderlijke fysische modellen zijn samengesteld tot een volledig plasma model (afgekort MLIBS). Deze kan de eigenschappen en emissies van een laser geïnduceerd plasma verklaren. Dit model kan ook omgekeerd worden gebruikt om de samenstelling van gesampelde elementen in een laser geïnduceerd plasma te bepalen. De focus ligt op de mogelijkheid om data niet te hoeven middelen om ruis te elimineren, maar om de data van elk laser shot nuttig te gebruiken voor identificatie. Dit noemt men single-shot data, en het is de meest efficiënte manier om LIBS toe te passen in de praktijk omdat de prijs van LIBS hardware snel stijgt met het aantal shots dat een laser per seconde moet leveren. Het laatste onderzoek is naar statistische technieken die gebruik kunnen maken van alle relevante informatie in LIBS data om zo de beste beslissing te kunnen maken als het gaat om identificatie van verschillende complexe materialen. Door statistieken te accumuleren kan de materiele samenstelling van vervuilde betonpuin stromen betrouwbaarder worden bepaald. Op basis van het gehele onderzoek in dit proefschrift is een prototype LIBS platform ontwikkeld en geïntegreerd met een transportband voor de inspectie van betonpuin in een recyclingfabriek. Het platform doorstond de zware omstandigheden in de buitenlucht en demonstreerde met succes de mogelijkheden van geautomatiseerde inspectie met LIBS. De ontwikkeling van het prototype omvatte het ontwerp en integratie van een laser systeem, optica, elektronische controle apparatuur, real-time data acquisitiesysteem, software voor spectrale data verwerking, en een weer bestendig beschermend frame.

- Hoofdstuk 1 beschrijft de motivatie, doelstellingen, methodologie en achtergrond van het onderzoek vanuit een recycling perspectief. Het verklaart waarom LIBS een veelbelovende sensortechnologie is voor geautomatiseerde kwaliteitscontrole. Het besluit met het technisch literatuuronderzoek.

- Hoofdstuk 2 bespreekt de mogelijke fysische processen en parameters in een ablatie experiment met een hoogvermogen gepulsde Nd:YAG 1064 nm laser, gebaseerd op de fysische literatuur. De processen worden afzonderlijk gemodelleerd alsof het individuele gebeurtenissen in de tijd zijn in plaats van transient en overlappend. Deze benadering is nauwkeurig als er sprake is van lokaal thermisch evenwicht.

Om verschillende thermodynamische paden (processen) voor laserablatie toe te laten wordt de uiteindelijke plasmatoestand gemodelleerd als het resultaat van een opeenvolging van klassieke faseveranderingsprocessen en ionisatie. De modelparameters kunnen worden gespecificeerd voor mineralen of voor metalen die ook als vervuiling in betonpuin voorkomen.

- Hoofdstuk 3 onderzoekt methodes voor adaptieve optica met goede data kwaliteit zodat er geen autofocus hardware nodig is om het korrelige betonpuin op de lopende band continue in de focus te houden van de laser en de lichtcollectie. Fysieke oorzaken van sampling bias worden uitgelicht en gekoppeld aan de gemiddelde samenstelling van de materialen. Relaties tussen LIBS spectra en ablatie parameters worden verklaard met behulp van wit licht interferometriemetingen. Single-shot normalisatieschema's worden voorgesteld om mogelijke ruis zoals variaties in gemiddelde energie in de data sets te onderdrukken.

- Hoofdstuk 4 onderzoekt de eigenschappen en gevoeligheid van LIBS spectra. In het bijzonder de variaties die afkomstig zijn van het gesampelde materiaaloppervlak. Factoren die worden onderzocht zijn bijvoorbeeld de geablateerde massa, laser-plasma interacties en het matrixeffect. Aangetoond is dat betrouwbare kwantitatieve kalibratiecurves op basis van meerdere elementen kunnen compenseren voor de geïdentificeerde spectrale variaties.

- Hoofdstuk 5 bouwt het plasma model voor laser geïnduceerde plasma emissies. Het is ontwikkeld om een kwantitatieve schatting te kunnen geven van de elementaire samenstelling van het plasma, zonder dat kalibratie of supervised training sets nodig zijn. Het model is getest op zijn geschiktheid om verschillende materialen te kunnen identificeren.

- Hoofdstuk 6 implementeert veelbelovende en robuuste statistische algoritmen voor de classificatie van complexe materialen. De algoritmes worden getest en vergeleken op hun geschiktheid voor praktische toepassing.

- Hoofdstuk 7 presenteert de conclusies en aanbevelingen voor vervolgonderzoek.

1

INTRODUCTION

1.1. MOTIVATION

Recycling of building waste is taking on an increasingly important role in Europe as it is stimulated by social and legislative pressure and driven by environmental, economic, social and technical trends, such as:

- Exhaustion of natural resources as the easy accessible sources get depleted due to increasing market demand.
- The CO_2 emissions, generated by cement and concrete production.
- Road capacity needed for transportation of building materials and demolition waste.
- Increasing volumes of recyclables brings economy of scale in the recycling markets.
- Changing attitude towards the negative environmental impacts of our linear consumption economy, such as the mindless consumption and discarding of valuable materials, water, air and soil pollution, and adverse effects on biodiversity and human health.
- Advances in more efficient and cost-effective recycling techniques.
- More consideration in product design for sustainable materials, recycling and reuse.

Processes used in mechanical recycling, such as sieving and sorting, do not modify the chemical makeup of materials. This means that the cleaned materials can get a new lease of life in new production to help satisfy the increasing world demand for raw materials.

In addition, by processing End-of-Life (EOL) materials into separate output fractions with excellent quality, the materials are less likely to serve as a low-grade material replacement (down-cycling). Meanwhile, processing EOL products with a variety of well documented quality grades should lead to a broad acceptance of recycled materials and new applications. This, in turn, should lead to new markets opening up, adding value to the recycled materials. A key step in this economic chain of events is that the quality of recycled material needs to be documented and guaranteed, i.e. compared to accepted standards, in the same way as is common practice for primary raw materials. On-site processing, such as advocated in Urban Mining, reduces transport and associated energy consumption. Moreover, localised processing allows for supervision and tracking of the intrinsically valuable material streams, which prevents them from disappearing and ending up somewhere in a low-grade application, waste incineration plant or landfill. Onsite recycling of building materials stands or falls with the availability of mobile technologies. In that regard a trend is emerging towards smaller and compact technologies, which also helps to economically process smaller volumes of materials. This trend can help unlock for recycling the many smaller building waste streams which at present are not deemed economically viable for recycling.

The present day notion of quality for recycled materials is commonly based on contracts, i.e. an agreement on a minimum quality standard that is acceptable for a particular customer. The replacement of primary raw materials on a true market scale, as is mandatory for the circular economy where secondary supply chains must be closed, is possible only if the recycled materials can be shown to comply with broadly accepted standards. A bottleneck in present day recycling is that waste materials go through several stages of processing which may be carried out by as many different companies. This complicates matters for the product manufacturers, because this shattered array of recycling companies do not offer a unified and reliable supply chain. This fragmentation in waste management also translates in lack of transparency and traceability of the waste materials. Due to the mixing of different materials in waste streams, the large waste volumes, and the shredding of waste prior to sorting, all measures that could improve traceability of the product are bound to fail. For example, the material type indicators on plastic products

cannot serve as useful indicators for sorting in the recycling plant. In that sense, the product material indicators can serve only to accommodate separate collection of wastes at home to produce more homogenous streams for recycling in the first place. This leads us to conclude that inline identification of materials and products by intelligent and versatile sensors is vital for improving and assessing quality. Moreover, the data and information provided by the sensors are also important for improving the processing steps upstream in the recycling plant and to build historical databases on waste source composition and recyclability.

1.2. OBJECTIVES AND METHODOLOGY

This research is driven by a vision to develop laser-induced breakdown spectroscopy (LIBS) into a potential tool for inspection of end of life building materials, particularly concrete demolition waste. The main objectives are:

1. Identify the dominant physical processes in a LIBS experiment and investigate how they depend on material properties (minerals and metals) and laser settings.
2. Investigate the efficient optical setup with application to (moving) waste materials.
3. Investigate the potential information content of LIBS data.
4. Investigate data processing and characterization algorithms needed for a reliable identification or classification of waste materials inspected under industrial conditions.
5. Implement a LIBS platform and test the potential for (inline) inspection of building wastes.

For the first objective we identify the processes in a pulsed laser experiment using a literature study. Because the physics behind a LIBS experiment is complex and processes are highly transient, we investigate the dominant processes quantitatively by modelling them as separate events. To that end local thermal equilibrium (LTE) is assumed to allow for a more accurate (stationary) model. Specifically, we use a uniform approach to model the different possible ablation mechanisms, which is as a sequence of classical phase changing processes and ionization to explain the final state of the laser induced plasma. Objectives 2

1

to 4 are pursued by dedicated experiments and implementing models and data processing algorithms in specialized software such as Matlab. This should lead to improved physical insights and potential of LIBS, and hopefully reveal new and more efficient ways to apply it. An important example is inline inspection and quality assessment technology, for example directly installed above a conveyor belt in an industrial setting. To test this capability according to objective 5, a functional LIBS-conveyor platform is designed and built. It is then put to the test for a variety of demolition waste materials and eventually tested at an industrial concrete production site in Hoorn, the Netherlands.

1.3. NON-CONTACT SENSOR TECHNIQUES APPLICABLE FOR RECYCLING: AN OVERVIEW

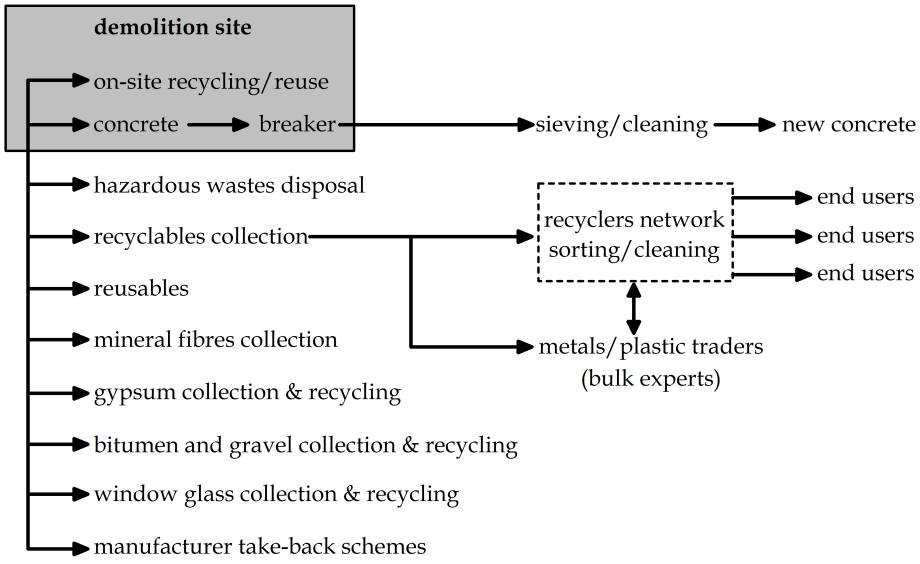


Figure 1.1: Organization of material flows from a demolition site in the Netherlands.

Fig. 1.1 shows an overview of typical materials streams from a building demolition site in the Netherlands. Stony materials such as mixed granulate (brick, concrete) can be reused on-site in roadbeds or for landscaping. Concrete waste is first broken down to size on the demolition site by mobile breakers before it is transported to a concrete recycling facility where it is sieved and cleaned before it can be used in new concrete production. For example, typical pollutants in concrete waste that should be removed first are soil, wood, plastics, rubbers, gypsum, glass, foams, clay and metals. In addition, concrete waste

from older demolished structures in the Netherlands from before 1982 may contain some asbestos. At present, it is mainly the coarse concrete waste fraction > 4 mm that is reused in new concrete. The sandy fraction < 4 mm is reused in for example road beds or landscaping. Nevertheless, efforts are underway to extract also the cementitious fraction from the sandy fraction and reuse that as an additive (e.g. filler) or even as a cement replacement in new concrete production. Hazardous wastes such as asbestos and old diesel tanks are removed by specialist companies. Recyclables such as metals, plastics, and wood are taken to a network of recyclers. There the materials are cleaned and sorted. Recyclers sell the purified products to end users such as manufacturers of building materials, either in the Netherlands or elsewhere in Europe. Raw waste materials such as metals and plastics may have enough intrinsic value to be exported to recycling markets abroad or even other parts of the world by bulk traders. Reusable end of life products such as wooden panels, doors and electrical equipment are stripped and mostly taken away by second hand dealers to be sold off elsewhere. In according with Dutch regulations (Bouwbesluit), materials that can degrade the quality and value of other recyclables are collected separately and, if possible, recycled. For example gypsum, bitumen and insulation mineral fibres (e.g. rock wool). Window glass is collected separately because it sensitive to pollutants, but also as a service by glass recyclers to stimulate recycling of building glass that otherwise could end up diluted in the much more voluminous stony waste. Finally, more and more manufacturers offer a take back scheme for their end of life products, for example artificial grass lawns and carpets. Typical sorting technologies are sieves, shredders, magnets, eddy current separators, density separators (for example air knives, sink-float, magnetic liquid separation), and sensor technologies for sorting and quality inspection which we discuss in more detail further on.

Fig. 1.2 shows a compacted overview of sensor technologies that operate in different physical domains, such as frequency [Hz], wavelength [nm], energy [eV] and colour temperature [K]. An integrated sensor system makes use of an external excitation source that interacts with the target material and brings it into a state or condition that activates or promotes the stimulus to which the sensor is sensitive. In LIBS the excitation source is a pulsed laser, the state is plasma, and the stimuli are the spectral emissions that are collected by optic

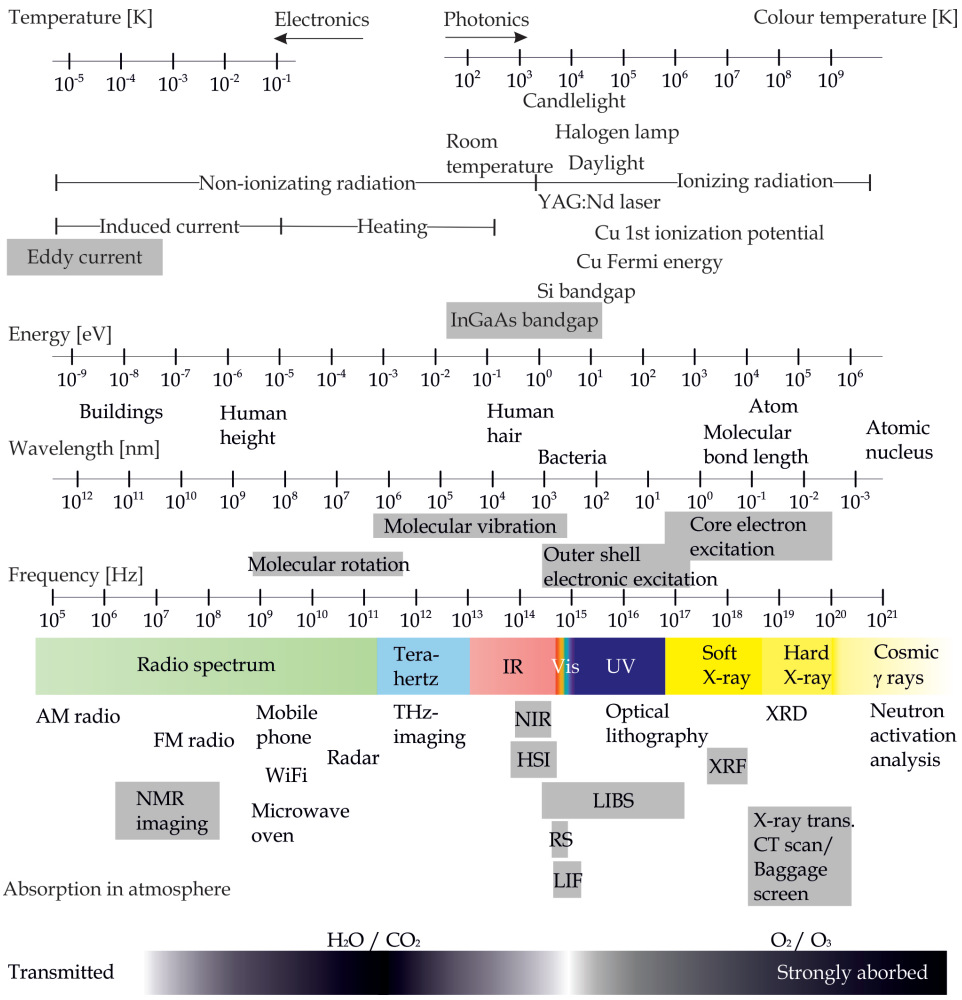


Figure 1.2: Potential sensor technologies for inline quality inspection in recycling work in different domains [1–4]. A grey bar indicates range; and otherwise it corresponds to the first letter.

fibres, dispersed by the spectrograph, and finally detected by CCD sensor elements. Soft X-ray (cf. opacity in Fig. 1.2) is an ionizing source that has limited application due to their rapid absorption in air. High energy radiation sources such as hard X-rays and gamma rays penetrate nearly all materials (except for heavy elements), but are hazardous and therefore not popular in recycling. High energy particle techniques (e.g. α, β particles, neutrons) are associated with radionuclide sources. The reason these are not popular is not so much that they require adequate shielding, but more because its application requires expensive access safety precautions, special permits and trained personnel to operate and maintain it. Ultrasound refers to mechanical vibrations or waves beyond the audible spectrum of the human ear. A higher frequency produces a smaller wavelength, which translates into a proportionally higher sensitivity for reflections at small features. The waves can carry information over distance about material related parameters (e.g. stiffness, mass density,

absorption), material imperfections (e.g. cracks, indentations, inclusions), or through wave scattering on size and shape of small objects (size distribution) or surfaces (roughness, corrugation, gaps). A disadvantage for stand-off applications above a conveyor belt in recycling is that ultrasonic waves attenuate rapidly with frequency, while using a low frequency has the disadvantage of a low resolution. Light (ultra violet to near infrared) or radar-like electromagnetic waves (from Terahertz down to radio frequencies) with good transmission characteristics are excellent candidates for recycling applications in ambient air.

Optical spectroscopy in the range from UV to IR offers quite distinguishing material fingerprints for quality inspection. The spectra correspond to atomic and molecular scales that can be correlated to chemical and physical properties on larger scales. Some of the better known spectroscopic techniques include nuclear magnetic resonance imaging (NMR), Terahertz imaging (THz), NIR/IR, Hyper Spectral Imaging (HSI), Raman scattering (RS), laser-induced fluorescence (LIF) spectroscopy and LIBS. NIR/IR and HSI detect the molecular vibrational and rotational absorption in the range $900-2300\ nm$ [5]. For these techniques the intensity of the light source may be relatively low (e.g. halogen or xenon lamps with $10^{-2}\ W \cdot cm^{-2}$, which demands a detector with high sensitivity and/or longer integration times. The NIR/IR is an accepted technology in industry. However, its identification of black materials (e.g. plastics and rubbers filled with carbon black pigment) is notoriously challenging due to their wide absorption bandwidth of the light source.

RS relies on molecular vibrations whose transitions are shifted, typically $\pm$ 200 nm, w.r.t. the laser wavelength, e.g. 785 nm [6]. Using a laser power density of 10 W/cm^2, RS has a typical absorption cross section of $10^{-28}\ cm^2$ per molecule [5], which demands a very sensitive detector, such as a photomultiplier. With an incident laser power density $10^3\ W/cm^2$, LIF is based on resonance transitions in the visible range, i.e. electronic transitions $200-800\ nm$ [6] and is more selective. But LIF is also a more sensitive technique by virtue of the relatively large absorption cross section corresponding to electronic transitions in the visible range [7].

1

In LIBS, the pulsed laser with intensity exceeding 10^8 W/cm^2 breaks down the material and typically produces a plasma spectrum that covers a very wide range of mostly non-resonance electronic transitions, running from soft X-rays to the IR. These emissions originate from species that partition the absorbed laser energy in many possible ways which makes that the spectrum carries an abundance of material related information. Compared to LIF this abundance comes at the small cost of a smaller absorption cross section and associated decreased sensitivity and selectivity for targeted species.

Some sensor measurements require a second actuator to further improve the sensitivity or selectivity for the targeted stimulus. For example in NMR first an external magnetic field is applied to induce split energy levels based upon nuclear angular magnetic momentum (Larmor precession). Secondly, a short electromagnetic pulse with a frequency (energy) corresponding to a difference in nuclear magnetic spin energy levels is activated to induce resonance transitions. This excited state of the nucleus is shortly lived after the excitation and the energy is re-emitted as an electromagnetic wave that can be detected using a suitable antenna. The major drawbacks are that NMR cannot detect metal contaminants, is probably too slow for recycling applications, and unreliable under harsh conditions in industry. Another example is inductively coupled plasma mass spectrometry (ICP-MS), where a tiny amount of the sample material is first dissolved into a suitable solvent to break down its material matrix into atoms/ions/molecules. Next, inductive-coupled plasma is employed to ionize the dissolved particles, after which electric and magnetic fields are applied to interact with the ions according to the Lorentz-force and Newtonian second law. The elements can then be discriminated according to their ionic mass-to-charge ratios. The main drawbacks for recycling of ICP-MS are that the result strongly depends on the skills of the sample preparing operator, which classify it as a laboratory technique. In contrast, a technique like THz imaging, which is sensitive mainly to the frequency dependent dielectric properties of a material, requires virtually no material preparations and proves to be successful in some specific applications [8]. Building a powerful device (transmitter and detector) for the THz frequencies is problematic, which is known as THz gap [9]. There is no naturally existing semiconductor material with a band-gap corresponding to the THz photon energy. The frequency is also too high for direct processing by commercial

electronic circuitry, limited by the parasitic capacitance, seeing that modern radar runs up to 10^2 GHz [10, 11]. In fact, the most expensive state of the art semiconductor technology, e.g. inter-subband engineering for quantum well [12], is required for filling the THz gap. It excludes this potential technique for near-future recycling applications.

Returning to LIBS, its spectra are commonly detected using semiconducting materials, for which there is ample choice. The lower and upper limits for a semiconductor detector can be estimated from the energy gap and ionization potential, respectively. For instance, Si is applicable for $200-1000$ nm (UV-Vis-NIR) and $InGaAs$ for $1000-2000$ nm (NIR-MIR). By changing the stoichiometry of the compound $In_aGa_bAs_c$ the range may be shifted to $1200-2400$ nm [1]. The observed signal-to-noise ratio depends on factors such as light intensity, detector noise level, sample surface condition, number of emitting species, and air humidity. Nevertheless, due to the strong light emissions from a laser induced plasma plume the detector does not have to be extremely sensitive and can build a noise free signal within a few hundred microseconds integration time. This way, LIBS facilitates a cost-effective, versatile, fast, stand-off measurement technology for recycling purposes.

1.4. TECHNOLOGIES AND PROCEDURES IN LIBS: A LITERATURE REVIEW

LIBS emerged first as an analytical method after the invention of laser in the 1960s [13]. It provides spectral fingerprints of all the elements in solid, liquid and gas phases in either benign or hazardous environments [14]. During a LIBS measurement a high power pulsed laser beam is focused onto a sample surface to ablate tiny amounts of material. The hot material vapours become excited to plasma. The plasma plume is composed of individual atoms, electrons and ions, as well as molecules, radicals and clusters which may be newly formed or remnants of the original material. Element-specific information can be extracted from the abundant emission lines in the acquired LIBS spectrum, which amplitudes may be linked to element contents in the ablated material. This transient process allows for rapid measurements that facilitate real-time assessment of materials. The method is contact-free and may be applied with minimal, or even without, sample preparations. With the development of modern and cheaper photonic instrumentation

(laser, spectrometer and optical components decrease ca. 8% in price per year) and efficient data analysis and chemometrics algorithms, the state-of-art LIBS setup can be compact and mobile for in-situ applications. Despite these advances the LIBS technique has only recently been accepted as an inline sensor in various industrial applications. Different choices for LIBS instrumentation are made for different applications.

A diode pumped Q-switched Nd:YAG solid state - 1064 nm laser is the "working horse" laser for LIBS. The major advantages are higher energy conversion efficiency-to-cost ratio [$J/€$], robustness and maintenance demand, and larger penetration depth into the target material surface [15], [16] (p. 57). By tuning the laser wavelength to a strong emission line of an element in the sample the background noise can be suppressed and the signal sensitivity improved, which is called the resonance effect [14] (p. 12). Traditional LIBS is a non-resonance technique as the laser is usually not tuned. A laser source can also be used as a means for triggering and synchronization. Then, the incident laser beam is split and connected to a delayed pulse generator that in turn triggers a spectrometer or a gate shutter installed in front of the spectrometer or CCD detector [17],[18],[14] (p. 322). A focusing lens concentrates the laser beam to increase the power density above the breakdown threshold of the sample material. The shape and cross section of the focus can be tailored by different lenses. A line-shaped plasma may be produced using a cylindrical lens [19] that has a better lateral homogeneity [16]. Focal length and f-factor are the main parameters characterizing a lens. The incidence angle of the incident laser beam w.r.t. the normal of the sample surface is usually set between 0, in which case part of the YAG laser energy will be absorbed by the plasma plume corona and decrease ablation efficiency, and 45 degrees which is the most used setting [16] (p. 48), [20] (p. 85). Using a lens with a long focal length, strings of mini-plasma can be initiated by the dust particles in the path of the laser beam [21]. Therefore an off-axis light collector is preferred as it avoids the detection of air breakdown emissions. According to [20] (p. 47), mirrors can eliminate aberration which makes that pierced spherical mirrors are preferable, like in a Newton telescope. A longer Rayleigh length (focus depth) for the laser beam is needed to make sample positioning less critical in case of surface roughness [22] and to better cope with sample vibrations influencing the measurements [23].

In any optical application it is important to protect the optic components from dust, ablation debris and vibrations [24]. In general, three dust protection configurations are possible: a mechanical shutter, gas flooding or a sealing plate. In a test of several hours of LIBS operation the ablation debris (soil particles from the sample) was visible on a quartz plate installed to protect the focusing lens [25], demonstrating its necessity.

It is reported that the Echelle spectrograph holds advantages over the traditional Czerny-Turner spectrographs in terms of higher spectral resolution over a wider wavelength range [19], [26]. However, a Czerny-Turner spectrograph may be more sensitive as it uses fewer dispersing components [27]. The laser-induced plasma is relatively short lived, so the detector must be sensitive and requires a trigger. The colour response, i.e. the wavelength sensitivity, of the light detection system needs to be calibrated. Different types of standard calibration lamp sources are available to perform a calibration in different wavelength ranges, such as a tungsten lamp [28], mercury lamp [29], [30] for wavelength range calibration, deuterium lamp [31] (p. 92) or halogen lamp [32] for intensity profile calibration. Band pass filters may be used to selectively detect spectral lines.

The main task of quantitative LIBS analysis is to relate detected spectral intensities to corresponding concentrations of elements. As a first step, standard or reference samples with a range of known chemical compositions have to be prepared, where different sample matrices may lead to different calibration curves. By applying different sample preparation methods and laser sources, the matrix dependency may to some extent be overcome [33] at the cost of increased complexity of the measurement and analysis procedure. Typically, cements and supplementary materials (e.g. fly ash, slag) contain the major elements Ca, Si, Al, Fe and O and the minor elements Na, K and Mg. Each sample is milled and grinded to a powder by using a ball mill or grinder. Binder (e.g. KBr [34] or Silver powder [33]) is added to bond the powder. Subsequently, a pellet or hydraulic press is used to turn the mixed powder into a dense sample. More details on sample preparation, testing methods and data sheets of cement and concrete types can be found in industrial norms, e.g. DIN EN 196[1]. Traditionally a sample is split into two parts, one half is used for LIBS and the other

[1] Deutsches Institut fuer Normung e.V. (DIN). German version EN

1

for a nominal measurement method such as wet chemistry analysis [35], potentiometric titration [36], ICP [15], [37] or XRF [38].

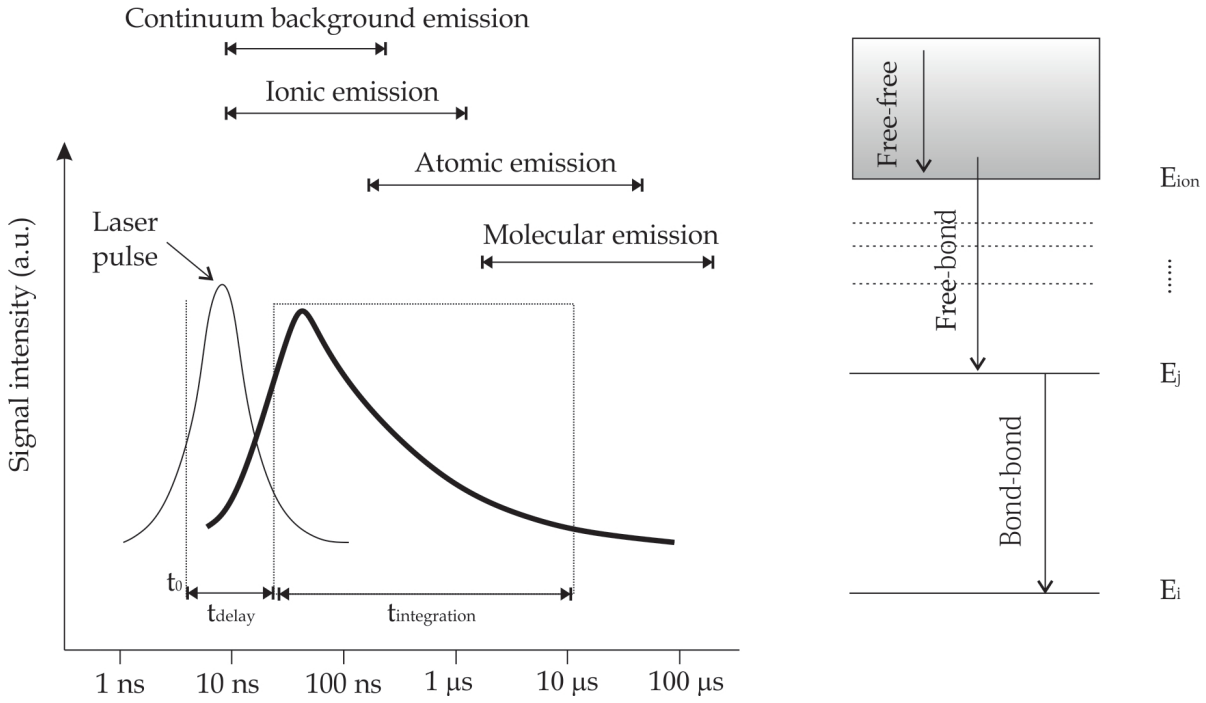


Figure 1.3: Left: Time evolution of plasma after firing of incidence laser, reproduced from [14] (p. 7). Right: typical transitions in an atom or ion reproduced from [31] (p. 25). E_i, E_j, E_{ion} are lower, higher and ionization energy levels, respectively.

Several methods have been reported that aim at reheating or re-exciting of the already laser-induced plasma to boost plume temperature and ionization levels. For example by accelerating a minority of ion species to high velocities using radio waves with a frequency equal to the cyclotron frequency of the ions [39],[40] (p. 230). Other examples are excitation by optical resonance [31] or spatial confinement effects [41], [42]. Figure 1.3 shows a time evolution of plasma emissions after firing a laser pulse at t_0 of which three important types can be discerned: bremsstrahlung (free-free), radiative recombination (free-bound), and decay of excited atoms, ions, or molecules (bound-bound) [30]. Different species of a certain element are produced with different delay time and vanish after different residence time, which has certain consequences for LIBS application. Firstly, emissions from different species of the same element may overlap. Secondly, emissions from different species belonging to different elements complicate the overlapping spectrum further. For multi-element analysis an adaptable time delay (t_{delay}) and integration time ($t_{integration}$) are needed in a compromise between figure of merits, for example signal-to-background

ratio (SBR), signal-to-variance ratio (SVR), and limit of detection (LOD).

LIBS offers limited capability for distinguishing fine structures in energy states due to the large diversity in excited species. For example, electron-ion recombination does not yield any information on the original valences. It is therefore difficult to distinguish different states of valences of a certain element like a compound or an oxidation state. Instead, efforts could be made to collect the distinct emissions from neutral atoms. Doucet et al. [43] succeeded in determining isotope ratios in air using poorly resolved emission lines. On another research line, laser plasma emits light in all directions and may therefore provide spatial-resolved information.

The LIBS spectra are interpreted by assigning the spectral lines to specific elements while the amplitude (number of photons) gives information about its contents in the sampled material. Currently acknowledged libraries and databases for emission lines, wavelengths, relative intensities and transition probabilities for each element may be found, e.g, in the NIST Atomic Spectra Database. The common approach for carrying out a quantitative analysis of an unknown sample is by first establishing a calibration curve, i.e. the emission intensity as a function of the probable range of concentration based on a set of reference samples [16]. Only if the unknown sample has similar chemical composition, matrix, and constant experimental parameters as the references can a calibration curve be determined. The calibration approach is not favoured in industry due to the large effort and cost. Therefore LIBS research focuses on multivariate regression methods such as Principal Components Analysis (PCA) [44, 45], Partial Least Squares Regression (PLS) [46–49], Artificial Neural Network (ANN) [17, 50, 51], and model based calibration-free LIBS (CF-LIBS) [52–54].

Though ambient gas breakdown is commonly a complicating factor in LIBS, for a precisely known content of a gas, it can be applied as a standard emission. Wilsch et al. [55] used C (I) 833.5 nm and Gehlen et al. [56] used O (I) 844.54 nm as the internal standard. The challenge is how to ignite the gas in the sample plasma in a consistent manner. To eliminate the background noise (e.g. daylight) a subtraction of the baseline without laser

[57] may be performed. The normalized intensity of a simultaneous measured standard spectral line allows reducing the fluctuations of the measured signal, which are significant for heterogeneous samples. Owing to the lower quantum efficiency of optical detectors in the near infrared range, the same intensity of continuum radiation may apprear several orders of magnitude higher than in the UV or visible range [27].

1.5. LIBS IN THE RECYCLING INDUSTRY

The first LIBS sensor for inline evaluation of bulk minerals on a conveyor belt was reported in 2004 [58]. The sorting of cast and wrought aluminum alloy particles on a moving conveyor belt ($2-4\ m/s$) was realized using LIBS as detection system with a laser pulse frequency of 100 Hz [59]. A LIBS-based inline inspection machine was used to identify steel pipe fittings (300/hour) in a production line and, moreover, also investigated was the long-time stability of a LIBS system in a production plant over a five year period [60]. Quantitative analysis of phosphate and coal transported on a conveyor belt has been conducted using inline LIBS [61]. Shredded scrap samples on a conveyor belt (2 m/s) were inspected by a LIBS system in [62]. The 3D object detection combined with a 3D scanning inline LIBS system for single file sorting of Al cast and wrought alloys ($3\ m/s, 4\ tonnes/hour$) has been demonstrated in [63].

The main challenges for inline LIBS inspection are listed in Tab. 1.1 together with possible counter options. The industrial acceptance of LIBS technology for inline operation is boosted by the rapid development in performance to price ratio of commercial lasers. Factors such as laser power and lens-to-sample surface distance may vary from laser pulse to pulse, leading to corresponding fluctuations of the plasma emissions. This negative influence is greatly reduced by ensemble averaging spectra [81] at the cost of a reduction in effective sampling rate. When detecting low concentrations ($< 0.1\ wt\%$) the resonance lines are typically strongest and are preferred for quantitative analysis. For relative high concentrations (say $> 1\ wt\%$) the non-resonance or weak resonance lines are the better choice as they are less susceptible to self-absorption effects [14] (p. 151). To ensure proper sampling a micro-lens array has been developed in [82] to collect more plasma emissions from different parts of the plume, and representative bulk analysis has been improved by

Table 1.1: Main technical challenges, key factors, and options for inline LIBS applications.

Challenge	Factor	Counter options
Environment	Dust	Enclosure; cleaned gas flow; efficient focusing
	Moisture	Enclosure; dry gas flow
	Temperature	Control; shielding
	Vibration	Damping; larger observation depth; minimal optical setup
Sampling	Laser positioning	From above/below/angled
	Working distance	Autofocusing; larger observation depth
	Sampling rate	Needed for representative sampling
	Dropout spectra	Detect & eliminate based on reference spectra or on average trends in the dataset
	Thick particle layer	Enforce homogeneous feeding; characterize and compensate for inhomogeneity; go to monolayer feeding; go to single file particle feeding
	Laser energy variations	Increase laser power & repetition rate & number of average spectra
Multi-element analysis	Sensitivity / reliability	Optimize laser and optical collection; use resonance emission lines ; use non-resonance or weak emission lines
	Selectivity	Select wavelength range
	Fractionation	Sample preparation; increase laser power
	Matrix effect	Calibrate with matrix-matched sample sets; use internal standards; use standardless method

spatial-averaging of the inhomogeneous samples that had a thin coating of different materials. The departure of the analytical sample from the stoichiometric state due to ablation, transport, and/or particles atomization is called fractionation [83]. One possible way to minimize fractionation is to further increase the laser power density [54, 84]. Building material such as concrete may contain different amounts of water, stored free in its pores, bonded in a gel state, or fixed as crystalline water. The pore and gel water can be removed either by annealing to 180 $^{\circ}C$ [70] using first IR pulsed heat irradiation or by sample preparation such as milling, drying and pressing samples into pellets [85]. It is also reported that the ablation efficiency of concrete is higher when first applying a water film to the sample, which is explained by stronger electron collisions that take place under dense water confinement [86]. The so-called matrix effect refers to cases where the emissions of a minority element are affected by the physical properties and composition of the whole sample [14] (p. 26). For concrete, the matrix is heterogeneous and made from natural materials from different origins. If a matrix is non-uniform, independent of the minor element concen-

Table 1.2: Chronological development of LIBS applied to building materials.

Year	Reference	Major achievement
1995	[64]	1st application of LIBS to concrete
1996	[65]	Quantitative analysis of [Pb] in concrete
2000	[66]	Detection of [Ca], [Al], [Si] in concrete
2004	[67]	Part I: Determine cement types based on [Ca], [Si], [Al], [Mg]
	[68]	Part II: Detection of [S] & quantitative analysis of [Cl] in concrete
2004	[69]	Detection of [C] in carbonated concrete
2005	[70]	Quantitative analysis of [S] in cement, mortar & concrete
2005	[55]	Quantitative analysis of [Cl] in concrete
2006	[22]	Quantitative analysis of [Cl] in cement paste, mortar & concrete distinguishes aggregate & cement
2006	[71]	Correlate concrete strength with LIBS signal
2007	[33]	Quantitative analysis of [Nb], [Ti], [Ta], [Co] in cemented tungsten carbides
2007	[72]	Detection of S corrosion in concrete
2009	[56]	Quantitative analysis of [Cl] ($< 0.1\ wt\%$) in cement paste with He
2009	[37]	Multi-element analysis of [Cl], [Ca], [Si], [Al], [Fe], [Ba], [Cr], [Mg], [Mn], [P], [S], [Na] in different types of cement
2009	[35]	Depth profiles of [S] in concrete
2009	[73]	Mobile LIBS demonstrator for on-site concrete quality control
2009	[74]	Portable LIBS in concrete repair
2010	[36]	Double-pulse LIBS for quantitative analysis of [Cl] in concrete ($< 0.008\ wt\%$)
2011	[75]	Quantitative analysis of [Ca], [Si], [K], [Mg], [Al], [Na], [Ti], [Mn], [Sr] in cement
2011	[76]	Sensitivity enhancement of [Cl] in reinforced concrete
2011	[77]	Detection of [Cl] in reinforced concrete
2011	[78]	2D mapping of [Cl], [Li], [Na] in concrete
2012	[79]	Remote detection of brick, cement paste, rebar, sand, wood, PVC
2013	[80]	Determination of [F] in glass ionomer cement

tration, the LIBS signal can vary significantly along the sample surface. This issue could be solved for known matrices by developing a quantitative model that accounts for the matrix and, in effect, would pave the way to a calibration free LIBS method.

Tab. 1.2 shows a chronological overview of LIBS in applications with building materials. The first application of LIBS in the building and construction field was in the mid-90s for the purpose of diagnosis and repair. There the focus was on detection of concrete-damaging substances containing Cl or S. Fig. 1.4 shows an example of how LIBS may be applied in the recycling industry. Other fields of engineering using LIBS are in excavators in mining and quarrying [63, 87, 88].

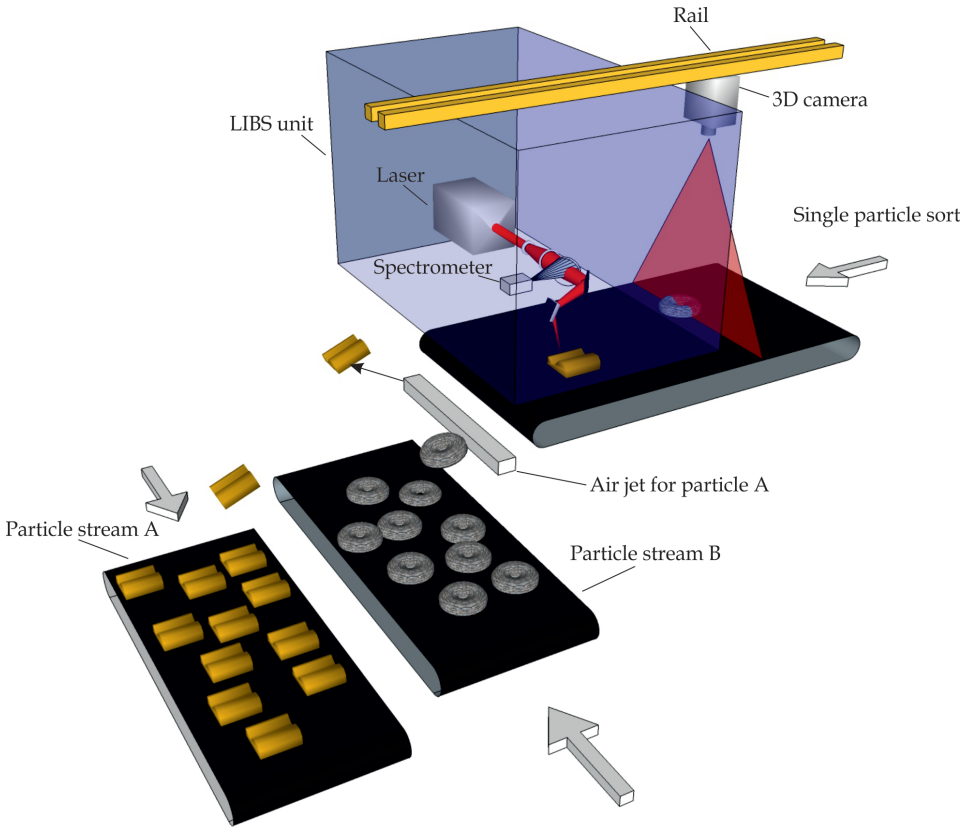


Figure 1.4: Inline laser-LIBS sorting reproduced from [63, 87]. Right-top: mixed particles A and B are fed on a belt moving 3 m/s. The position and geometry of a particle is measured with a 3D camera to time the LIBS measurement and determine its chemical composition. Depending on a threshold, the particle is then discharged using compressed air into one of two output streams.

1.6. DUTCH ECONOMIC PERSPECTIVE

Industrial acceptance of a new recycling technology is linked to the question how much value it adds to the recycled product or, similarly, whether it can open up a new market for the recycled material. The present day Dutch market for coarse ($> 4\ mm$) recycled concrete aggregates and natural gravel for the purpose of producing new concrete is fluctuating with processing and transport costs. The current market price (2020) for both natural gravel and recycle aggregates typically varies between 10 and 25 euro per ton. In future the demand for concrete is expected to keep growing, as will the prices for the raw materials. On the other hand, more and more concrete waste is becoming available and is bound to outgrow the demand for road bed fill in near future. Therefore, recycling concrete waste into new concrete is the logical new decree as laid down in so-called green deals between the Dutch government and industry. Moreover, legislation can provide economic incentives to give preference to recycled materials over natural resources. A major advantage of recycled concrete aggregates is its local availability and associated savings in transport costs. For

1

example, it costs roughly 10 cent/km/ton to transport natural gravel by truck. This puts the recycled aggregates in an economically favourable position.

The added value of an inspection technology like LIBS is more difficult to determine because it is not a part of the primary production system. This fact is also a hindrance in its industrial acceptance, because the value for the company cannot be calculated in a straight-forward way. It is the bare necessity for a company to prove to their clients that the material conforms to standards that creates the added value of LIBS, so one could say that quality inspection is a market enabling technology. But this requires documented and broadly accepted quality standards to be in place, which is not yet the case for the still developing market of recycled concrete aggregates. Nevertheless, the need of recycle concrete to comply with strength and safety regulations is nowadays related to certain Dutch norms. Those norms specify maximum levels of different contaminant types, depending on the structural loading or aesthetic demands to which the new concrete will be exposed. Thanks to these requirements, the inline LIBS system can already prove its value by detecting if the recycled materials comply with acceptable contaminant contents for the intended application. The present day recycling of aggregates in new concrete makes up ~ 5% of the total Dutch concrete aggregate market. At this level, the recycled concrete producers can still afford to select the cleanest concrete waste sources, thereby avoiding the need for sensor inspection. Nevertheless, in view of the green deal and the expected surplus in concrete waste and the expected growth in use of recycled aggregates, the cleanest sources of concrete waste will be used up quickly and the need for LIBS inspection is bound to grow. It may be instructive to provide an estimate of the running costs for a LIBS system for recycled aggregates for a company producing 100 tonnes per hour of concrete aggregates during 2000 hour/year. The total costs (incl. the fixed yearly cost and operation yearly cost) during 5 year of depreciation of the LIBS equipment investments are ca. 0.6 $€/ton$ (2016) for the launching costumer. When laser equipment becomes mainstream, and including 8% general decrease in prices per year, these costs are expected to drop quickly. For example, at present (2020) the LIBS cost is expected to lie around 0.4 $€/ton$, as laser diode lifespan has increased by a factor of 10. More details on the LIBS cost breakdown are show in Tab. 1.3.

Table 1.3: Costs in 2016 of a LIBS inline quality inspection system for EOL concrete recycling business case: Investment cost INV[€] consisting of all LIBS components amounts to 81000 € in total. Assuming 5 year depreciation against 5% interest, the fixed yearly cost (FYC[€/yr]) = ($INT + 5\% \cdot (INV + 80\% \cdot INV + 60\% \cdot INV + 40\% \cdot INV + 20\% \cdot INV)$)/5[$yrs$] = 18630[€/$yr$]. Assuming 20% of fixed investment per year for energy consumption and basic maintenance, personnel cost of 25€/hr for 1 manhour/day (e.g. start/stop LIBS), and the replacement of diode package per 10^8 pulses w/ 2000 operational hrs/yr), the operation yearly costs OYC[€/yr] = $20\% \cdot INV + 365[days] \cdot 25 + 100[Hz] \cdot 3600[sec/hr] \cdot 2000[hrs/yr]/10^8[pulses/diode] \cdot 10000€/diode$ = 97325[€/yr]. Total costs per year (TYC) during depreciation $TYC = FYC + OYC$ = 115955€/yr. Total costs per ton (TCT) for 100 ton/hour processing during 2000 hrs/yr $TCY = TYC/100[tons/hr]/2000[hrs/yr]$ = 0.58€/ton.

Type of cost	Item	Cost [Euros]
Investment cost (INV)	YAG:Nd diode pumped pulsed laser 20 mJ /100 Hz	40000
	water cooling chiller	5000
	optics	1000
	spectrometer	5000
	mobile laser chamber	10000
	real-time processing hard/softwar	20000
Fixed yearly cost (FYC)	5 year depreciation against 5% interest	18630
Operation yearly cost (OYC)	20% of fixed investment/year (energy + basic maintenance)	16200
	1 manhour/day (e.g. start/stop LIBS)	9125
	replacement diode package per 10^8 pulses (assuming 2000 operational hours/year)	72000

1.7. A CLOSED CONCRETE LIFECYCLE

The current levels of virgin lime and cement production are exhausting natural resources and account for nearly 9% of the global CO_2 emissions [89] (p. 134). In the business-as-usual case (cf. Fig. 1.5) the majority of the demolition concrete is currently applied in the Netherlands in road foundations, but a surplus will soon surpass the demand. This has triggered a lot of research, like the EU-C2CA project [90], into the reuse of the EOL concrete in new concrete. The recycling of EOL concrete aims at technologies that can recover up to 60 ~ 70 $wt\%$ of the concrete in demolition waste streams. To this end, the demolition concrete is converted into clean aggregates (i.e. low cement paste contents) and a fine calcium-rich fraction (high cement paste contents) as a low-CO_2 feedstock replacement for limestone in the production of new cement. If the transformation from demolition concrete to recycle aggregates and new concrete can be done in-situ or at least localized, the recycling of the EOL building and the building of a new one may be efficiently integrated into a single project.

Separation of EOL concrete into calcium-rich cement paste and silica-rich aggregates is facilitated by the innovative Advanced Dry Recovery (ADR) technology. As an important first processing step it classifies moist broken concrete $0-16\ mm$ in an otherwise dry process into a fine fraction and coarse fraction with the cut typically between 2 and 4 mm [92]. It

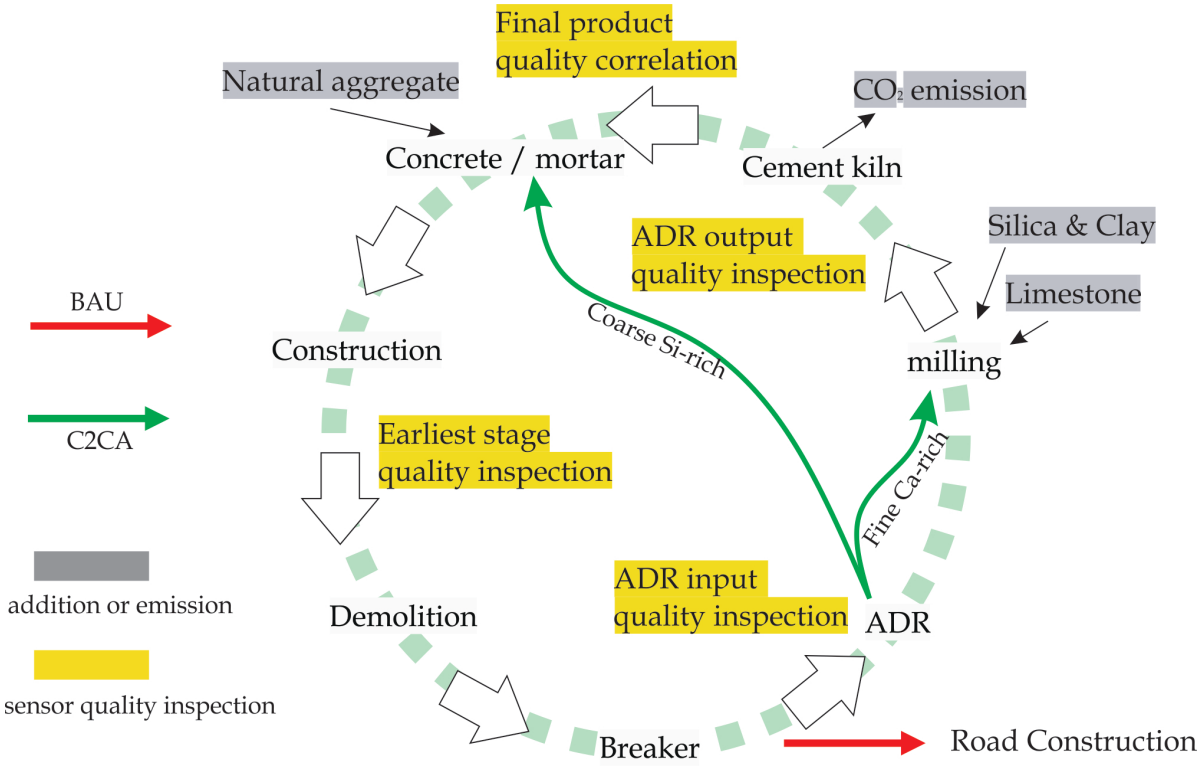


Figure 1.5: The business-as-usual approach and new (EU-C2CA project) closed cycle for demolition concrete, reproduced from [91].

should therefore be appreciated that moisture in demolition waste is practically a fact of life in the Netherlands, and moist granular materials cannot be sieved with a dry conventional deck sieve below 10 mm. The potential economic value of both fractions depends also on the level of cross-contamination. Too much porous brick in the aggregates product influences the new mortar through the crucial water-cement ratio and workability. On the other hand, too many pieces of wood affect the strength of the new concrete and its visual aesthetic appearance. To enhance the liberation of cement stone in the fines product, thermal treatment and/or milling may be required [93, 94].

A key step in closing the cycle for concrete is proposed in the EU-C2CA project and concerns the quality assurance of the recycle materials. After all, closing a loop means that a concrete producer must ensure that the materials will meet his quality criteria (cf. Tab. 1.4) and that the agreed supply is guaranteed. If not, they will quickly revert back to primary material suppliers. The quality of coarse recycled aggregates is mainly determined by the concentration of pollutant materials from the demolition, such as brick, gypsum, glass, rebar, plastics, wood and foam, and must comply with norms/standars (cf. Tab. 1.4). The

Table 1.4: Categories for constituents of coarse recycled aggregates w/ specified contamination levels [95, 96].

Constituent	Content [wt%]	Category
Rc	⩾90	Rc_{90}
	⩾80	Rc_{80}
	⩾ 70	Rc_{70}
	⩾50	Rc_{50}
	< 50	$Rc_{Declared}$
	No requirement	Rc_{NR}
Rc + Ru	⩾ 95	Rcu_{95}
	⩾90	Rcu_{90}
	⩾70	Rcu_{70}
	⩾50	Rcu_{50}
	< 50	$Rcu_{Declared}$
	No requirement	Rcu_{NR}
Rb	⩽ 10	Rb_{10-}
	⩽ 30	Rb_{30-}
	⩽ 50	Rb_{50-}
	>50	$Rb_{Declared}$
	No requirement	Rb_{NR}
Ra	⩽ 1	Ra_{1-}
	⩽ 5	Ra_{5-}
	⩽ 10	Ra_{10-}
X + Rg	⩽ 0,5	$XRg_{0.5-}$
	⩽ 1	XRg_{1-}
	⩽ 2	XRg_{2-}
	Content $[cm^3/Kg]$	
FL	⩽0.2*	$FL_{0.2-}$
	⩽2	FL_{2-}
	⩽5	FL_{5-}

Rc: Concrete, concrete products, mortar concrete masonry units
Ru: Unbound aggregate, natural stone, hydraulically bound aggregate
Rb: Clay masonry units (i.e. bricks and tiles), calcium silicate masonry units, aerated non-floating concrete
Ra: Bituminous materials
FL: Floating material in volume
X: Others, incl. cohesive (i.e. clay and soil), miscellaneous: metals (ferrous and non-ferrous),non-floating wood, plastic and rubber, gypsum plaster
Rg: Glass
*The ⩽ 0,2 category is intended only for special applications requiring high quality surface finish.

quality of the very fine cement paste product is mainly determined by the elemental contents.

The state-of-the-art in quality control of coarse aggregates and cement is regular visual inspection and/or intermittent in-situ sampling-and-laboratory analyses. Both are time consuming and expensive and give insufficient information if the waste composition changes continuously. The issue is that demolition waste is quite variable material and the more so if it originates from different buildings and locations. Continuous inline quality control can be an option for continuous sampling and an objective compositional assessment. It can also build statistics for technical and marketing purposes. As a technical driver this may

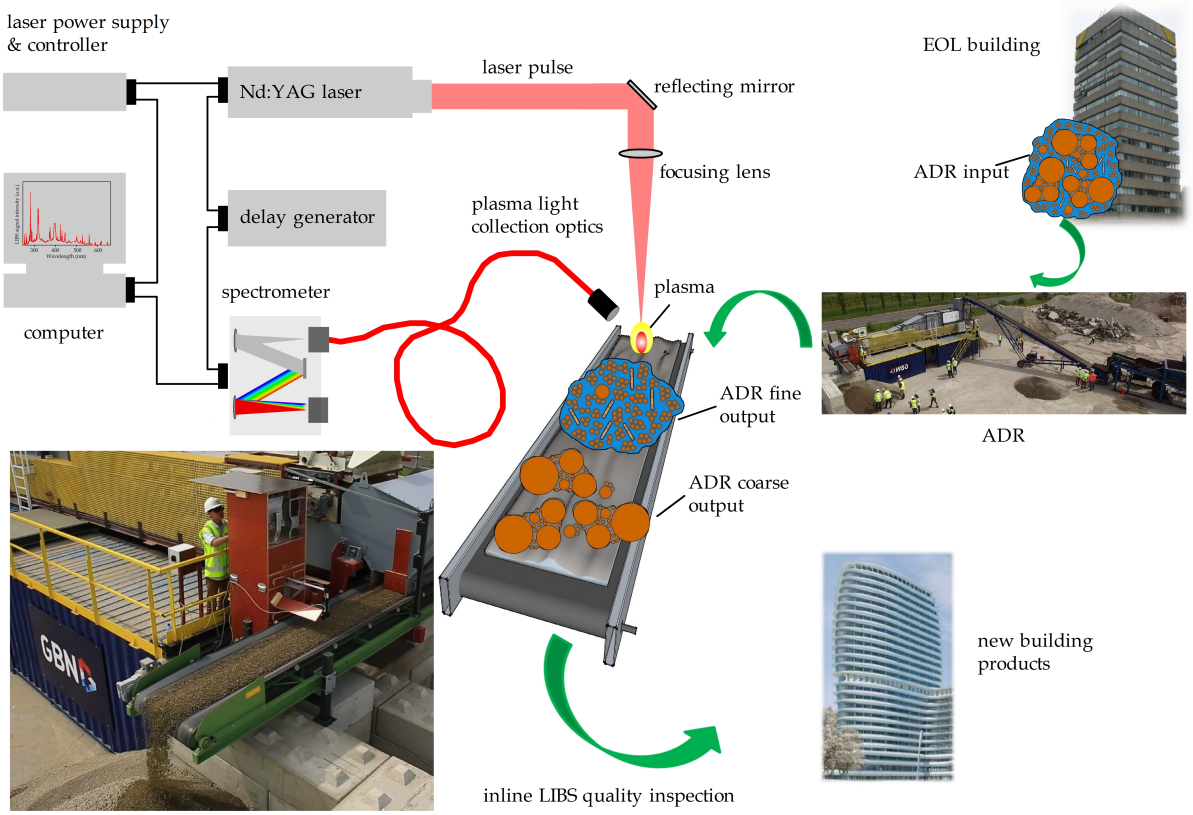


Figure 1.6: The LIBS principle of inline operation as developed in this work. Photo in the left bottom corner: Inline LIBS for quality inspection on ADR coarse 4-12 mm output at 30 tons/hour demonstrated in Hoorn, the Netherlands on 10th June 2016.

be a basis for the definition of standards and certification of procedures, technology and products related to demolition concrete waste. In this way, the recycled products can replace primary materials in a wide range of concrete applications in a future closed lifecycle of concrete, driven by a market of supply and demand. Fig. 1.6 shows the principle of the inline LIBS quality inspection sensor system developed in this work, and its application on the ADR coarse fraction ($4-12\ mm$).

1.8. OUTLINE

- Chapter 1 states the research motivation, objectives, methodology and background from the recycling perspective and explains why LIBS is proposed as a promising sensor technology for inline quality control applied in recycling. It is followed by a literature review of LIBS inline applications in various fields.

- Chapter 2 first discusses the possible physical processes in a $ns-IR$ pulsed laser experiment, based on literature study. On this basis the dominant processes are modelled as individual events, which is more accurate in case local thermal equilibrium

is obtained. To allow for different thermodynamic ablation mechanisms, dependent on specific material properties and laser settings, we choose to model the resulting plasma state as resulting from a sequence of classical phase changing processes and an ionization stage. The parameters introduced in the models may be specified for organic material, minerals or metals, because these types of material may be found in concrete waste and need to be identified by LIBS in case of quality inspection.

- Chapter 3 describes the methodology to set up a LIBS system including laser, spectrometer synchronization and how to design and configure adaptive optics to minimize the number of anomalous shots (miss shots or shots with insufficient signal-to-noise ratio), hence to increase sampling rate without using auto-focusing. Surface sampling biases are explained by physics origins that can be used to correct the material composition in material bulk. The relations between LIBS spectra and ablation parameters measured by white light interferometry are investigated, and single-shot spectral normalization schemes are proposed.

- Chapter 4 discusses the properties of LIBS spectra and presents reliable multi-element quantitative calibration curves that compensate for laser-induced plasma uncertainties originating from target material dependent laser ablation, laser-plasma interaction and matrix effect. We discuss the properties of LIBS spectra and present reliable multi-element quantitative calibration curves that compensate for laser-induced plasma uncertainties.

- Chapter 5 builds the model for laser-induced plasma emission for reliable determination of major element contents quantitatively, without using calibration or supervised training sample sets. This method is applied to predicting & monitoring input and output products from a demolition recycling production line.

- Chapter 6 implements robust statistical algorithms to increase inline classification rates of materials, which are applied to various demolition concrete components.

- Chapter 7 presents conclusions and gives recommendations for further studies.

1

1.9. ACKNOWLEDGEMENTS

This research was funded by the European Commission in the framework of the FP7 Collaborative project "Advanced Technologies for the Production of Cement and Clean Aggregates from Construction and Demolition Waste (C2CA)", Grant Agreement No. 265189. Moreover, this research was financially supported by the European Commission in the framework of he Horizon 2020 research and innovation program "HISER project", Grant Agreement No. 642085.

REFERENCES

[1] R. Kessler, *Prozessanalytik: Strategien und Fallbeispiele aus der industriellen Praxis* (Wiley, 2012).

[2] J. Bushberg and J. Boone, *The Essential Physics of Medical Imaging* (Wolters Kluwer Health, 2011).

[3] D. Lide, *CRC Handbook of Chemistry and Physics, 90th Edition* (Taylor & Francis, 2009).

[4] E. Boeker and R. van Grondelle, *Environmental Physics* (Wiley, 2000).

[5] B. Schrader, *Infrared and Raman Spectroscopy: Methods and Applications* (Wiley, 2008).

[6] R. W. Kessler, *Perspectives in process analysis,* Journal of Chemometrics **27**, 369 (2013).

[7] H. Stroke, *Advances in Atomic, Molecular, and Optical Physics*, Advances In Atomic, Molecular, and Optical Physics No. v. 51 (Elsevier Science, 2005).

[8] Y.-S. Jin, G.-J. Kim, and S.-G. Jeon, *Terahertz dielectric properties of polymers,* (2006).

[9] D. L. Woolard, E. R. Brown, M. Pepper, and M. Kemp, *Terahertz frequency sensing and imaging: A time of reckoning future applications?* Proceedings of the IEEE **93**, 1722 (2005).

[10] K. B. Cooper, R. J. Dengler, G. Chattopadhyay, E. Schlecht, J. Gill, A. Skalare, I. Mehdi, and P. H. Siegel, *A high-resolution imaging radar at 580 GHz,* IEEE Microwave and Wireless Components Letters **18**, 64 (2008).

[11] L. Hao, H. M. Rein, T. Suttorp, and J. Bock, *Fully integrated sige vcos with powerful output buffer for 77-ghz automotive radar systems and applications around 100 GHz,* IEEE Journal of Solid-State Circuits **39**, 1650 (2004).

[12] B. S. Williams, H. Callebaut, S. Kumar, Q. Hu, and J. L. Reno, *3.4-THz quantum cascade laser based on longitudinal-optical-phonon scattering for depopulation,* Applied Physics Letters **82**, 1015 (2003).

[13] I. Schechter, *Laser induced plasma spectroscopy: A review of recent advances,* Reviews in Analytical Chemistry **16**, 173 (1997).

[14] *Laser-Induced Breakdown Spectroscopy (LIBS) : Fundamentals and Applications*, 1st ed. (Cambridge University Press, Cambridge, 2006).

[15] J. L. Gottfried, F. C. De Lucia Jr, C. A. Munson, and A. W. Miziolek, *Laser-induced breakdown spectroscopy for detection of explosives residues: A review of recent advances, challenges, and future prospects,* Analytical and Bioanalytical Chemistry **395**, 283 (2009).

[16] Y.-I. Lee, K. Song, and J. Sneddon, *Laser-Induced Breakdown Spectrometry* (Nova Science, 2000).

[17] V. Motto-Ros, A. S. Koujelev, G. R. Osinski, and A. E. Dudelzak, *Quantitative multi-elemental laser-induced breakdown spectroscopy using artificial neural networks,* Journal of the European Optical Society-Rapid Publications **3** (2008).

[18] A. Koujelev, M. Sabsabi, V. Motto-Ros, S. Laville, and S. L. Lui, *Laser-induced breakdown spectroscopy with artificial neural network processing for material identification,* Planetary and Space Science **58**, 682 (2010).

[19] C. Haisch, U. Panne, and R. Niessner, *Combination of an intensified charge coupled device with an echelle spectrograph for analysis of colloidal material by laser-induced plasma spectroscopy,* Spectrochimica Acta Part B: Atomic Spectroscopy **53**, 1657.

[20] J. P. Singh and S. N. Thakur, *Laser-induced breakdown spectroscopy* (Elsevier, 2007).

[21] D. E. Lencioni, *The effect of dust on 10.6-μm laser-induced air breakdown,* Applied Physics Letters **23**, 12 (1973).

[22] F. Weritz, D. Schaurich, A. Taffe, and G. Wilsch, *Effect of heterogeneity on the quantitative determination of trace elements in concrete,* Analytical and Bioanalytical Chemistry **385**, 248 (2006), weritz, F Schaurich, D Taffe, A Wilsch, G 3rd Euro-Mediterranean Symposium on Laser Induced Breakdown Spectroscopy Sep 06-09, 2005 Aachen, GERMANY.

[23] C. Lopez-Moreno, S. Palanco, and J. J. Laserna, *Stand-off analysis of moving targets using laser-induced breakdown spectroscopy,* Journal of Analytical Atomic Spectrometry **22**, 84 (2007).

[24] C. Bohling, K. Hohmann, D. Scheel, C. Bauer, W. Schippers, J. Burgmeier, U. Willer, G. Holl, and W. Schade, *All-fiber-coupled laser-induced breakdown spectroscopy sensor for hazardous materials analysis,* Spectrochimica Acta Part B: Atomic Spectroscopy **62**, 1519 (2007).

[25] D. A. Cremers, J. E. Barefield, and A. C. Koskelo, *Remote elemental analysis by laser-induced breakdown spectroscopy using a fiber-optic cable,* Appl. Spectrosc. **49**, 857 (1995).

[26] S. Florek, C. Haisch, M. Okruss, and H. Becker-Ross, *A new, versatile echelle spectrometer relevant to laser induced plasma applications,* Spectrochimica Acta Part B: Atomic Spectroscopy **56**, 1027 (2001).

[27] F. Weritz, D. Schaurich, and G. Wilsch, *Detector comparison for sulfur and chlorine detection with laser induced breakdown spectroscopy in the near-infrared-region,* Spectrochimica Acta Part B: Atomic Spectroscopy **62**, 1504 (2007).

[28] B. Praher, V. Palleschi, R. Viskup, J. Heitz, and J. D. Pedarnig, *Calibration free laser-induced breakdown spectroscopy of oxide materials,* Spectrochimica Acta - Part B Atomic Spectroscopy **65**, 671 (2010).

[29] M. Hoehse, D. Mory, S. Florek, F. Weritz, I. Gornushkin, and U. Panne, *A combined laser-induced breakdown and raman spectroscopy echelle system for elemental and molecular microanalysis,* Spectrochimica Acta - Part B Atomic Spectroscopy **64**, 1219 (2009).

[30] M. Sabsabi and P. Cielo, *Quantitative analysis of aluminum alloys by laser-induced breakdown spectroscopy and plasma characterization,* Appl. Spectrosc. **49**, 499 (1995).

[31] D. A. Cremers and L. R. Radziemski, *Handbook of Laser-Induced Breakdown Spectroscopy*, 1st ed. (Wiley, New York, 2006).

[32] C. W. Ng, W. F. Ho, and N. H. Cheung, *Spectrochemical analysis of liquids using laser-induced plasma emissions: Effects of laser wavelength on plasma properties,* Appl. Spectrosc. **51**, 976 (1997).

[33] K. Novotny, A. Stankova, H. Hakkanen, J. Korppi-Tommola, V. Otruba, and V. Kanicky, *Analysis of powdered tungsten carbide hard-metal precursors and cemented compact tungsten carbides using laser-induced breakdown spectroscopy,* Spectrochimica Acta Part B-Atomic Spectroscopy **62**, 1567 (2007).

[34] T. Ctvrtnickova, M.-P. Mateo, A. Yanez, and G. Nicolas, *Characterization of coal fly ash components by laser-induced breakdown spectroscopy,* Spectrochimica Acta Part B: Atomic Spectroscopy **64**, 1093 (2009).

[35] F. Weritz, A. Taffe, S. Dieter, and G. Wilsch, *Detailed depth profiles of sulfate ingress into concrete measured with laser induced breakdown spectroscopy,* Construction and Building Materials **23**, 275 (2009).

[36] K. Sugiyama, T. Fujii, T. Matsumura, Y. Shiogama, M. Yamaguchi, and K. Nemoto, *Detection of chlorine with concentration of 0.18 kg/m3 in concrete by laser-induced breakdown spectroscopy,* Applied Optics **49**, C181 (2010).

[37] M. A. Gondal, Z. H. Yamani, T. Hussain, and O. S. B. Al-Amoudi, *Determination of chloride content in different types of cement using laser-induced breakdown spectroscopy,* Spectroscopy Letters **42**, 171 (2009).

[38] E. Matthies, *Grundlagenuntersuchung der Moeglichkeiten einer Online Analyse mit Hilfe der Laser induzierten Plasmaspektroskopie (LIPS) am Beispiel von Kalkstein*, Ph.D. thesis (2008).

[39] T. Oguri, H. Inoue, S. Tsuge, K. Kitagawa, and N. Arai, *Laser ablation-assisted radiofrequency atomization excitation source for direct determinations of elements in ceramics,*

Journal of Analytical Atomic Spectrometry **12**, 823 (1997), cited By (since 1996): 6 Export Date: 3 October 2011 Source: Scopus.

[40] R. Goldston and P. Rutherford, *Introduction to plasma physics* (Smithsonian Astrophysical Observatory, 1995).

[41] X. K. Shen, J. Sun, H. Ling, and Y. F. Lu, *Spatial confinement effects in laser-induced breakdown spectroscopy,* Applied Physics Letters **91**.

[42] X. Shen, H. Ling, and Y. Lu, *Laser-induced breakdown spectroscopy with high detection sensitivity,* in *Laser-based Micro-and Nanopackaging and Assembly III*, Vol. 7202 (International Society for Optics and Photonics, 2009) p. 72020D.

[43] F. R. Doucet, G. Lithgow, R. Kosierb, P. Bouchard, and M. Sabsabi, *Determination of isotope ratios using laser-induced breakdown spectroscopy in ambient air at atmospheric pressure for nuclear forensics,* J. Anal. At. Spectrom. **26**, 536 (2011).

[44] K. Chang, C. W. Brown, and R. K. Forcé, *Laser-induced fluorescence multicomponent analysis in full spectra and their fourier transforms by principal component regression,* Applied spectroscopy **47**, 1801 (1993).

[45] J. Janucki and K. Kiczynski, *Application of laser induced plasma spectroscopy for remote detection of explosives,* PRZEGLAD ELEKTROTECHNICZNY **87**, 106 (2011).

[46] J. Amador-Hernández, L. García-Ayuso, J. Fernández-Romero, and M. L. de Castro, *Partial least squares regression for problem solving in precious metal analysis by laser induced breakdown spectrometry,* Journal of Analytical Atomic Spectrometry **15**, 587 (2000).

[47] J. L. Luque-Garcia, R. Soto-Ayala, and M. D. L. de Castro, *Determination of the major elements in homogeneous and heterogeneous samples by tandem laser-induced breakdown spectroscopy-partial least square regression,* Microchemical Journal **73**, 355 (2002).

[48] S. M. Clegg, E. Sklute, M. D. Dyar, J. E. Barefield, and R. C. Wiens, *Multivariate analysis of remote laser-induced breakdown spectroscopy spectra using partial least squares,*

principal component analysis, and related techniques, Spectrochimica Acta Part B: Atomic Spectroscopy **64**, 79 (2009).

[49] J. M. Andrade, G. Cristoforetti, S. Legnaioli, G. Lorenzetti, V. Palleschi, and A. A. Shaltout, *Classical univariate calibration and partial least squares for quantitative analysis of brass samples by laser-induced breakdown spectroscopy,* Spectrochimica Acta Part B: Atomic Spectroscopy **65**, 658 (2010).

[50] J.-B. Sirven, B. Bousquet, L. Canioni, and L. Sarger, *Laser-induced breakdown spectroscopy of composite samples: comparison of advanced chemometrics methods,* Analytical chemistry **78**, 1462 (2006).

[51] J.-B. Sirven, B. Bousquet, L. Canioni, L. Sarger, S. Tellier, M. Potin-Gautier, and I. Le Hecho, *Qualitative and quantitative investigation of chromium-polluted soils by laser-induced breakdown spectroscopy combined with neural networks analysis,* Analytical and bioanalytical chemistry **385**, 256 (2006).

[52] A. Ciucci, M. Corsi, V. Palleschi, S. Rastelli, A. Salvetti, and E. Tognoni, *New procedure for quantitative elemental analysis by laser-induced plasma spectroscopy,* Applied spectroscopy **53**, 960 (1999).

[53] D. Bulajic, M. Corsi, G. Cristoforetti, S. Legnaioli, V. Palleschi, A. Salvetti, and E. Tognoni, *A procedure for correcting self-absorption in calibration free-laser induced breakdown spectroscopy,* Spectrochimica Acta Part B: Atomic Spectroscopy **57**, 339 (2002).

[54] M. Corsi, V. Palleschi, A. Salvetti, and E. Tognoni, *Calibration free laser induced plasma spectroscopy: a new method for combustion products analysis,* Clean Air **3**, 69 (2002).

[55] G. Wilsch, F. Weritz, D. Schaurich, and H. Wiggenhauser, *Determination of chloride content in concrete structures with laser-induced breakdown spectroscopy,* Construction and Building Materials **19**, 724 (2005).

[56] C. D. Gehlen, E. Wiens, R. Noll, G. Wilsch, and K. Reichling, *Chlorine detection in cement with laser-induced breakdown spectroscopy in the infrared and ultraviolet spectral range,* Spectrochimica Acta Part B-Atomic Spectroscopy **64**, 1135 (2009).

[57] D. K. Ottesen, *Detection of contaminants on electronic microcircuit substrates by laser spark emission spectroscopy,* Appl. Spectrosc. **46**, 593 (1992).

[58] *Mineral detection and content evaluation method,* US Patent 6, 753, 957 B1 (June, 2004).

[59] U. Aydin, J. Makowe, R. Noll, and V. D. I. Berichte, *Fast identification of light metal alloys by laser-induced breakdown spectroscopy for material recycling - development of a demonstrator for automatic sorting of aluminium scrap,* in *Photonics in Measurement*, Vdi Berichte, Vol. 1844 (2004) pp. 401–412.

[60] R. Noll, I. Moench, O. Klein, and A. Lamott, *Concept and operating performance of inspection machines for industrial use based on laser-induced breakdown spectroscopy,* Spectrochimica Acta - Part B Atomic Spectroscopy **60**, 1070 (2005).

[61] M. Gaft, I. Sapir-Sofer, H. Modiano, and R. Stana, *Laser induced breakdown spectroscopy for bulk minerals online analyses,* Spectrochimica Acta - Part B Atomic Spectroscopy **62**, 1496 (2007).

[62] L. M. Cabalin, A. Gonzalez, J. Ruiz, and J. J. Laserna, *Assessment of statistical uncertainty in the quantitative analysis of solid samples in motion using laser-induced breakdown spectroscopy,* Spectrochimica Acta Part B: Atomic Spectroscopy **65**, 680 (2010).

[63] P. Werheit, C. Fricke-Begemann, M. Gesing, and R. Noll, *Fast single piece identification with a 3D scanning LIBS for aluminium cast and wrought alloys recycling,* Journal of Analytical Atomic Spectrometry (2011).

[64] H. Wiggenhauser, M. Salzmann, G. Wilsch, and D. Schaurich, *Analysis of concrete with laser induced breakdown spectroscopy (libs),* (1995) pp. 529–537.

[65] A. V. Pakhomov, W. Nichols, and J. Borysow, *Laser-induced breakdown spectroscopy for detection of lead in concrete,* Applied Spectroscopy **50**, 880 (1996).

[66] H. Wiggenhauser, G. Wilsch, D. Schaurich, and J. Wostmann, *Analysis of concrete using libs (reprinted from non-destructive testing civil engineering, april, pg 407-414, 2000),* Insight **42**, 436 (2000), wiggenhauser, H Wilsch, G Schaurich, D Wostmann, J.

[67] A. Taffe, G. Wilsch, D. Schaurich, and F. Weritz, *Einsatz der Laser-Induzierten Breakdown Spektroskopie (LIBS) im Bauwesen - Teil 1: Verfahrensbeschreibung und Durchfuehrung von Zementanalysen,* Beton- und Stahlbetonbau **99**, 693 (2004).

[68] A. Taffe, G. Wilsch, D. Schaurich, and F. Weritz, *Einsatz der Laser-Induzierten Breakdown Spektroskopie (LIBS) im Bauwesen-Teil 2: Ermittlung von bauschädlichen Salzen,* (2004).

[69] K. Kagawa, N. Idris, M. Wada, H. Kurniawan, K. Tsuyuki, and S. Miura, *Carbon analysis for inspecting carbonation of concrete using a tea co(2) laser-induced plasma,* Applied Spectroscopy **58**, 887 (2004).

[70] F. Weritz, S. Ryahi, D. Schaurich, A. Taffe, and G. Wilsch, *Quantitative determination of sulfur content in concrete with laser-induced breakdown spectroscopy,* Spectrochimica Acta Part B: Atomic Spectroscopy **60**, 1121 (2005).

[71] K. Tsuyuki, S. Miura, N. Idris, K. H. Kurniawan, T. J. Lie, and K. Kagawa, *Measurement of concrete strength using the emission intensity ratio between $Ca(II)$ 396.8 nm and $Ca(I)$ 422.6 nm in a Nd : YAG laser-induced plasma,* Applied Spectroscopy **60**, 61 (2006), tsuyuki, K Miura, S Idris, N Kurniawan, KH Lie, TJ Kagawa, K.

[72] A. Taffe, M. Pohl, W. Roeser, and B. Schwamborn, *Concrete corrosion at sewage plants caused by sulphuric acid innovative damage analysis,* Beton- und Stahlbetonbau **102**, 691 (2007), taffe, Alexander Pohl, Markus Roeser, Wolfgang Schwamborn, Bernd.

[73] M. Bruns, M. Raupach, C. D. Gehlen, R. Noll, G. Wilsch, and A. Taffe, *High speed chemical analysis of concrete surfaces using the LIBS method within the ILCOM project,* (2009) pp. 225–226, bruns, M. Raupach, M. Gehlen, C. D. Noll, R. Wilsch, G. Taffe, A. 2nd International Conference on Concrete Repair, Rehabilitation and Retrofitting Nov 24-26, 2008 Cape Town, SOUTH AFRICA.

[74] A. Taffe, D. Schaurich, G. Wilsch, and F. Weritz, *Development of a portable libs-device for quality assurance in concrete repair,* (2009) pp. 223–224.

[75] A. Mansoori, B. Roshanzadeh, M. Khalaji, and S. H. Tavassoli, *Quantitative analysis of cement powder by laser induced breakdown spectroscopy,* Optics and Lasers in Engineering **49**, 318 (2011).

[76] M. Gondal, A. Dastageer, M. Maslehuddin, A. Alnehmi, and O. Al-Amoudi, *Sensitivity enhancement at 594.8 nm atomic transition of Cl I for chloride detection in the reinforced concrete using libs,* Journal of Environmental Science and Health, Part A **46**, 198 (2011).

[77] M. A. Gondal, M. A. Dastageer, M. Maslehuddin, A. J. Alnehmi, and O. S. B. Al-Amoudi, *Detection of chloride in reinforced concrete using a dual pulsed laser-induced breakdown spectrometer system: comparative study of the atomic transition lines of Cl I at 594.85 and 837.59 nm,* .

[78] G. Wilsch, D. Schaurich, and H. Wiggenhauser, *Imaging laser analysis of building materials—practical examples,* AIP Conference Proceedings **1335**, 1315 (2011).

[79] M. Belyaeva and V. Trofimov, *Remote laser spectroscopy of building materials,* Optics and Spectroscopy **112**, 638 (2012).

[80] T. Kratochvil, M. Pouzar, K. Novotnỳ, V. Havránek, T. Černohorskỳ, and M. Zvolská, *The use of laser-induced breakdown spectroscopy for the determination of fluorine concentration in glass ionomer cement,* Spectrochimica Acta Part B: Atomic Spectroscopy **88**, 26 (2013).

[81] M. O. Vieitez, J. Hedberg, O. Launila, and L. E. Berg, *Elemental analysis of steel scrap metals and minerals by laser-induced breakdown spectroscopy,* Spectrochimica Acta - Part B Atomic Spectroscopy **60**, 920 (2005).

[82] R. Noll, V. Sturm, U. Aydin, D. Eilers, C. Gehlen, M. Hohne, A. Lamott, J. Makowe, and J. Vrenegor, *Laser-induced breakdown spectroscopy-from research to industry, new frontiers for process control,* Spectrochimica Acta Part B-Atomic Spectroscopy **63**, 1159 (2008).

[83] E. Tognoni, G. Cristoforetti, S. Legnaioli, and V. Palleschi, *Calibration-free laser-induced breakdown spectroscopy: State of the art,* Spectrochimica Acta - Part B Atomic Spectroscopy **65**, 1 (2010).

[84] W. T. Chan and R. E. Russo, *Study of laser-material interactions using inductively coupled plasma-atomic emission spectrometry,* Spectrochimica Acta Part B: Atomic Spectroscopy **46**, 1471 (1991).

[85] R. Gaudiuso, M. Dell'Aglio, O. de Pascale, G. S. Senesi, and A. de Giacomo, *Laser induced breakdown spectroscopy for elemental analysis in environmental, cultural heritage and space applications: A review of methods and results,* Sensors **10**, 7434 (2010).

[86] A. C. Tam, W. P. Leung, W. Zapka, and W. Ziemlich, *Laser-cleaning techniques for removal of surface particulates,* Journal of Applied Physics **71**, 3515.

[87] C. Fricke-Begemann, *Fast and flexible,* AT MINERAL PROCESSING ENGLISH EDITION **51**, 2 (2010).

[88] C. Fricke-Begetnann, P. Jander, H. Wotruba, and M. Gaastra, *Laser-based online analysis of minerals,* ZKG International **63**, 65 (2010), export Date: 31 August 2011 Source: Scopus CODEN: ZKGIF Language of Original Document: English Correspondence Address: Fricke-Begetnann, C.; Fraunhofer Institute for Laser Technology, Aachen, Germany.

[89] E. G. M. Kleijn *et al.*, *Materials and energy: a story of linkages*, Ph.D. thesis (2012).

[90] *Advanced Technologies for the Production of Cement and Clean Aggregates from Construction and Demolition Waste (C2CA),* `http://www.c2ca.eu/`, accessed: 2016-06-30.

[91] F. DiMaio, P. Rem, S. Lofti, S. Serranti, G. Bonifazi, M. Hu, V. Burganos, E. Skouras, F. Cucchietti, and M. Vázquez, *Cement and Clean Aggregates from CDW: The C2CA Project,* (International Conference on Solid Waste Technology and Management, 2012) pp. 11–14.

[92] W. de Vries, P. Rem, and P. Berkhout, *Adr: a new method for dry classification,* in *Proceedings of the ISWA International Conference, Lisbon*, Vol. 12 (2009).

[93] S. Lotfi, J. Deja, P. Rem, and et. al, *Mechanical recycling of eol concrete into high-grade aggregates,* Resources, Conservation and Recycling **87**, 117 (2014).

[94] S. Lotfi, M. Eggimann, E. Wagner, and et. al, *Performance of recycled aggregate concrete based on a new concrete recycling technology,* Construction and Building Materials **95**, 243 (2015).

[95] *European Committee for Standardization, EN 933-11: Tests for Geometrical Properties of Aggregates - Part 11: Classification Test for the Constituents of Coarse Recycled Aggregate,* (2009).

[96] *European Committee for Standardization, EN 12620+A1: Aggregates for Concrete,* (2008).

2

PHYSICS OF NANOSECOND LIBS

2.1. TRANSIENT PROCESSES AND MODEL ASSUMPTIONS

2.1.1. ACCOUNT OF THE MAIN PROCESSES BEHIND LIBS

This section presents a qualitative account and timing of the main processes associated with a nanosecond pulsed laser experiment on a solid material. This is not a quantitative account of all the fundamental physics involved, if only because it is the subject of ongoing research. Instead, it provides a basic understanding of the possible processes behind a LIBS experiment according to the governing physical insights in the literature. This account serves as a point of departure for the models and experimental methodologies introduced further on in this thesis. To that end possible processes are discussed for both types of solid that can be found in demolition concrete: non-metals (e.g. minerals) and metals. The focus is on processes that are likely to occur within the achievable ranges of our laser setup: 1064 nm, pulse duration 10 ns, power density 0.5-8 GW/cm^2, fluence 5-80 J/cm^2.

$t < 0$ ***Seed electrons:***

1. All non-metals contain some free moving electrons, for example due to cosmic radiation, tunnelling effect (thermal electrons), material impurities or crystal defects. These are the seed electrons that are needed to initiate nonlinear laser light-matter processes. In metals there is already an abundance of free moving electrons.

$t \geq 0$ ***Start of laser pulse and ionization:***

2. The subsequent sequence of events require that the laser intensity and fluence lie above material dependent threshold values. Otherwise only linear photonic processes

occur, commonly characterized by reflection and absorption parameters. Ionization of the material may occur by multiphoton absorption and/or tunnelling [1]. Depending on the laser intensity, wavelength and ionization energy of the species involved, the Keldysh parameter γ indicates if multiphoton ($\gamma \gg 1$) or tunnelling ($\gamma \ll 1$) plays the bigger role [2]. Energetic electrons can ionize heavy species (ions, atoms, molecules) by impact to free more electrons. If the free electron energy is boosted by the laser field it takes just a few seed electrons to trigger an avalanche of impacts [1, 3], which appears to work better using infrared radiation [4]. For example, for silica (SiO_2) the main process leading to avalanche is multiphoton absorption while for silicon it is single photon absorption [4]. Inverse Bremsstrahlung [5] may also enhance the kinetic energy of free electrons and initiate avalanche.

$t > t_T$ ***Thermalization and ablation:***

3. In the plasma plume thermalization is due to repeated collisions between hot electrons and the heavy species, which can take in the order of 1 ns for the plasma to reach a uniform temperature [6]. With a delay determined by relaxation time t_T the free electrons can transfer energy to the molten or solid material by electron-phonon collisions [7]. This initiates heat diffusion and it initiates detectable vibrations in the solid sample. Typical values for t_T are in the order of 1-10 ps for metals [8, 9], but for non-metals it could be as long as 1 μs [10].

4. Process 3 may coincide with the initiation of a shockwave [7] into ambient air with supersonic velocity [8, 11, 12]. The high compression wave front carries charged hot matter from the first few atom layers of the material surface. Behind the wave front the much denser plasma plume develops as ablation continues. Different zones may be distinguished in the plume, among which a rarefaction wave [13].

5. In the ablation zone the temperature and vapour pressure build up and reach a peak [11, 14] when also the ablation rate reaches a maximum. The process in which a material surface is effectively cooled by release of hot surface material is called ablation. In case the surface breaks up in pieces during the heating process is called thermal spallation, which is not desired as it causes random variations in the observable spectrum when comparing repeated LIBS experiments. The mechanisms behind ablation may

be explained more easily from thermodynamic principles. This led to identification of different possible mechanisms for ns-pulse laser ablation, complying with different thermodynamic pathways.

i: Evaporation is the ablation mechanism if the temperature stays below the liquid-vapour critical temperature [15].

ii: At higher fluence than needed for evaporation [15], or short pulse duration with higher laser intensity [16], the matter goes through a supercritical solid-liquid state to a metastable liquid-vapour state. Then the matter stabilizes by phase explosion, also called explosive boiling, which is essentially phase separation. Here, stabilization is characterized by instantaneous nucleation and growth of vapour bubbles, ending up as vapour (plasma) and liquid droplets. The droplets may then evaporate in the laser beam. This ablation mechanism is also classified as spinodal decomposition, where the spinodal is a thermodynamic boundary where matter becomes mechanically instable [17].

iii: Spallation may occur if fluence and matter temperature lie within certain limits [18]. This mechanism is driven by large mechanical strains (tension) produced by a rarefaction wave in reaction to the compressive air shockwave. Fortunately, these conditions are not likely to arise in our LIBS experiments.

iv: At higher fluence or long pulse duration the matter can be brought to a supercritical state near thermodynamic equilibrium. If the matter cannot expand fast enough it stabilizes by trivial fragmentation to end up as liquid droplets [8, 19], which may then evaporate in the laser beam.

An equivalent point of view is that these ablation mechanisms depend on the degree of inertial confinement of the irradiated material [16], meaning the matter accumulates energy faster than it can be expelled by ablation. Whichever the ablation mechanism, plasma is expelled at an initial supersonic velocity [12]. In ambient air a thin Knudsen layer develops at the ablation zone that allows the velocities of the hot matter to assume the equilibrium Maxwellian distribution [13, 20, 21], after which the plasma expands adiabatically. The plasma may carry droplets or even small molecular fragments, which also explains the higher rate of ablation of phase explosion compared

to evaporation [22, 23]. On the downside, such a coarse ablation mechanism may cause non-repeatable variations in plume ionization levels, temperature and even in the elemental composition compared to the original sample where it concerns trace elements.

6. Processes 2, 3, 5 continue during the laser pulse.

7. As the plasma plume expands it absorbs significant incoming laser energy through inverse bremsstrahlung and photoionization [9]. This is called shielding and it boosts plasma ionization levels and temperature, though it reduces the mass ablation rate.

$10 ns$ ***End of laser pulse:***

After $1\ ns$ the electrons and heavy species in the plume reach a common temperature. At this stage the plume expand freely and emits a continuous spectrum in which high-energy bremsstrahlung dominates [14]. Such hot plasma is generally characterised as optically thin, meaning that the mean free path for the dominant part of radiation is larger than the dimensions of the plasma and self-absorption can be neglected. In this case collisional processes dominate over radiative ones and LTE is obtained [24]. Unfortunately, the continuous spectrum cannot be traced back quantitatively to specific species in the plume and is therefore rarely used in LIBS applications.

Thermal equilibrium (TE) for either all the species in the plume or for just one particular type of species means that, averaged over a certain relaxation time, all energy transitions of the species can be linked to a unique temperature. More specifically, there is no net exchange of energy taking place between the species or between the species and the surroundings so the temperature remains constant. It may be intuitively clear that TE does not apply during the laser pulse. But after the pulse the plume expands adiabatically and shows internal convection due to different temperature zones. If one adds to that ion recombination and radiation into ambient air it seems unlikely that TE can be assumed in a time window that is of any practical use for LIBS.

Local thermal equilibrium (LTE) for all species in the plume or for just one particular type of species means that there is a unique temperature that can be found in just a part of the plume, whereas the temperature is allowed to vary slowly from point to point in the plume.

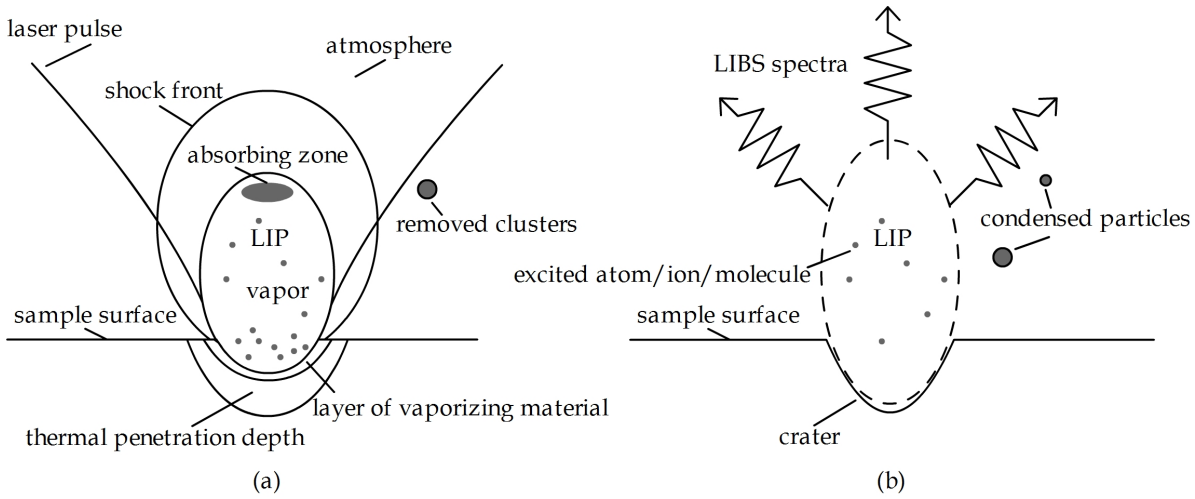


Figure 2.1: (a) Laser-matter interaction stage. (b) Cooling down stage.

As the hot plume expands against the air molecules [23] it loses momentum and slows down [12]. In the meantime the plasma ionizes air molecules that can enter the plasma and influence the LIBS result [7]. When the expansion has reduced to subsonic velocity it releases acoustic waves that propagate freely into the ambient air [25]. High wave frequencies are quickly absorbed by air molecules but low wave frequencies persist. Moving at air velocity (340 m/s) they may be audible at several meters distance from the ablation spot. Above steps are described in Fig. 2.1a.

$t > t_A$ ***Start acquisition atomic/ionic spectra (typically*** t_A ***=1*** μs***):***

8. At this later stage the plume is cooler and still expanding (cf. Fig. 2.1b). It now emits atomic/ionic spectral radiation that dominates over bremsstrahlung [14], in which case the kinetic collisions between particles dominate and determine the temperature to which also the radiation is linked. For high densities of a specific species (element) in the plume, the plasma behaves like an optically thick medium. Driven by the temperature and density gradient along the plasma volume, the radiation of the interior hot parts of plasma is absorb by the exterior cold parts due

to self-absorption effect [26]. Self-absorption may prove significant in which case the plasma is no longer optically thin. In that case the radiation and the species themselves may have different temperatures, and it could even vary between different species (elements). This implies that for high-density species there is less LTE in the plume. Practically speaking this means that in those cases the assumption of LTE will lead to less reliable measurements of the electron density and plume temperature. However, a small degree of self-absorption is no reason to immediately abandon the assumption of LTE. It can only be determined by tests when the assumption of LTE becomes inaccurate for LIBS. The maximum allowable window is linked to the species relaxation factors (cf. integration time in Sec. 3.2). These relaxation factors must be determined experimentally and depend on the material, laser setup and ambient conditions. The acquired spectra allow measurement and calculation of quantitative plume parameters such as temperature and electron density.

The spectral emissions carry quantitative information on the types and amounts of elements in the plume. They are radiated when an exited ion or atom falls back to a lower energy state. In particular, in spectrometry the emissions due to a transition to the ground state are known as resonance lines. Self-absorption in the plume causes a deviation from linearity between photon counts and the content of a certain element, and this increases for increasing density of the element in the plume. Also disturbing for detecting emission lines is line broadening, as caused by Resonance broadening and Stark effect [27]. Other types of radiation such as ion-recombination fall in the UV range ($> 4\ eV$ or $< 300\ nm$). This high energy radiation is absorbed very quickly in air and has limited applicability in the stand-off applications of the industry.

The exact relation between photon emissions and the elements (atoms, ions) is documented in [27]. For quantitative LIBS measurements calibration is required, mainly due to self-absorption and deviations from stoichiometric ablation. The latter means that the plume composition may not be an exact representation of the ablated sample. And noting that single shot ns-pulse ablation creates holes of a few micrometre deep (cf. Fig. 3.19), a surface sample may not be representative for the

composition of the sample volume. These complications may make it necessary to average multiple spectra of repeated LIBS experiments to get a more accurate result.

$< 1\ ms$ ***End of acquisition***

2.1.2. IMPLICATIONS FOR APPLICATION OF LIBS

The dominant processes that initiate breakdown in a solid (i.e. destruction of irradiated material) and sustain its ablation (i.e. removal of hot material into a plasma plume) depend first on whether it is a metal, an opaque non-metal or a transparent non-metal. They also depend on the laser power intensity and fluence delivered by the optical system of laser and lenses. Threshold values for the energy of the pulse should be exceeded to initiate breakdown and to sustain ablation. The thresholds vary mainly with the type of material, surface conditions, laser wavelength and intensity. Metals generally have a lower breakdown threshold than non-metals. For ns pulses the ablation of both metals and non-metals tends to be more efficient at shorter laser wavelengths [3, 28, 29], and for metals the total ablated mass tends to increase with pulse duration [9, 30]. The infrared laser used in this work provides a relatively high fluence, which also helps to ablate more mass in order to provide better reproducible emission spectra from rough or dirty waste samples. The crater left in the sample surface after a LIBS experiment is commonly a bit wider than the cross section of the laser beam [9], for which there is as yet no conclusive explanation. The threshold fluence at which phase explosion occurs for a 1064nm, nanosecond laser pulse has been determined experimentally for a few materials. For example metals: aluminium 15 J/cm^2 [28], silicon 3 J/cm^2 [31], niobium 15 J/cm^2 [22], and non-metals: graphite 22 J/cm^2 [22] a ceramic superconductor 17.5 J/cm^2 [22], and carbon 55 $J/cm2$ [29]. The fluence threshold for trivial fragmentation is far less explored in literature. For our laser setup with fluence $5-80\ J/cm^2$ the likely mechanism for metals is phase explosion or trivial fragmentation [17]. For non-metals it is most likely evaporation or phase explosion. In any case, with a sufficient ionization level all three ablation mechanisms produce a plasma that is suitable for LIBS application.

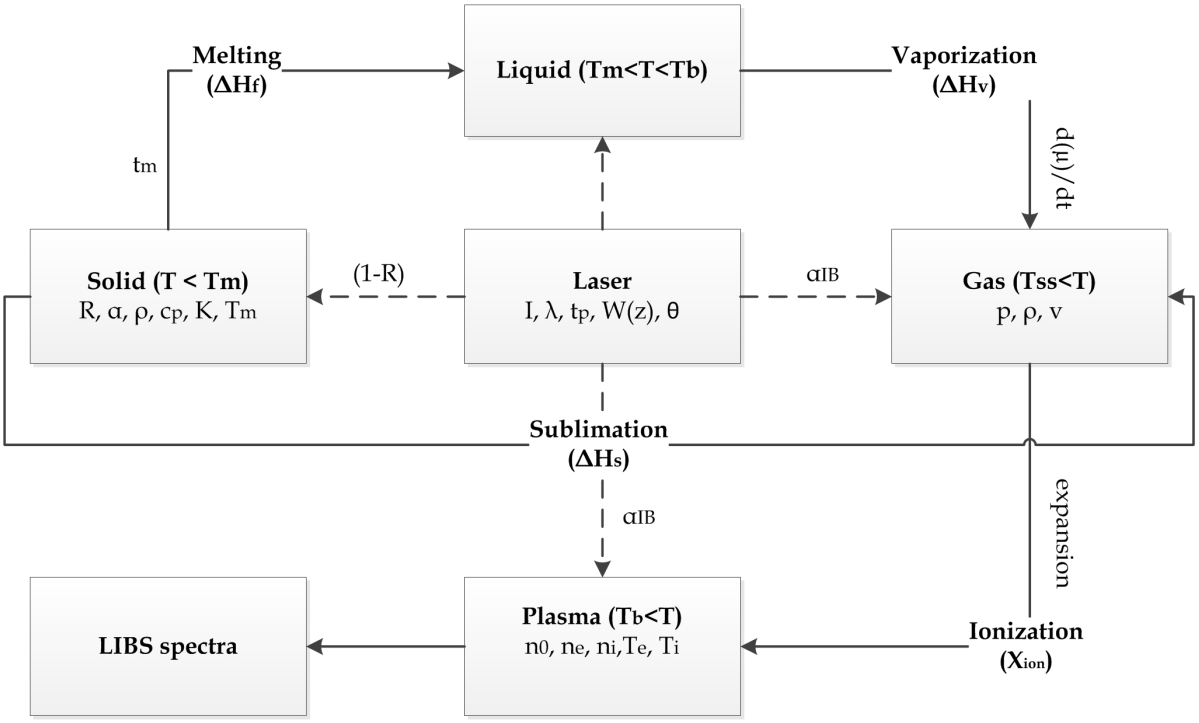


Figure 2.2: Modelled linear and non-linear processes and associated phase transitions in a LIBS experiment.

2.1.3. ASSUMPTIONS AND PARAMETERS IN THE MODEL

Per nanosecond an electron in a conductive or highly ionized material encounters $10^4 - 10^5$ collisions with other electrons and lattice phonons [32]. The energy absorbed and carried by electrons may therefore be assumed to be passed on practically instantaneously to the lattice. This implies that (localized) equilibrium conditions can exist by which a few thermo-dynamical variables are already sufficient to fully describe the state. Each transient process in the laser experiment is assumed to be dominated by a single material phase, while an energy approach is taken when time-overlapping processes, such as vaporization and ionization, are analyzed as separate processes as depicted in Fig. 2.2. The temperature is related to a local thermal equilibrium and can be described by piecewise continuous functions. Reversible processes (e.g. condensation) and non-equilibrium processes (e.g. shock wave, Knudsen layer) are assumed to play a minor role in the energy balance and are not accounted for. The laser beam is treated as Gaussian (confirmed by measurement) by which it may be characterised by maximum power density I_0 $[W/cm^2]$ at wavelength λ, pulse duration t_p, incidence angle θ, beam waist radius W_0 and Rayleigh length z_0. The laser energy absorption by the material during the pulse is a function of effective power density that depends on focusing conditions and linear and nonlinear electromagnetic

material responses, such as reflectivity, emissivity, transparency and ablation.

In this analysis, the solid material phase is characterized by constant factors, e.g. the reflectivity R, absorption coefficient α, mass density ρ, specific heat capacity c_p and heat conductivity K. In the liquid phase ($T > T_{melt}$), the latent heat of fusion ΔH_f accounts for the phase transition. The same types of constant parameters as in the solid phase are used to characterize the melt. Above boiling temperature T_b the latent heat of vaporization ΔH_v accounts for the phase transition, and is characterized by vapor pressure p_v, density ρ_v, mass removal flux rate $\dot{\mu}$ (ablation rate) and vapor velocity v_v. During expansion the $(i+1)\ th$ order ionization energy χ_{i+1} represents the degree of ionization of the vapor. The laser-induced plasma is characterized by electron density, number of ions and atoms, ionized fraction ($n_e,\ n_i,\ n_0$), and electron and ionic temperatures T_e and T_i.

2.2. MODELLING THE LASER EXPERIMENT

2.2.1. HEATING AND MELTING

The volume density [cm^{-3}] and flux rate [$cm^{-2}s^{-1}$] are used in the following conservation laws. Consider a quantity Φ per unit volume (dv) in a space V enclosed by the surface S that changes due to an outward flow through the boundary S. The global conservation law is:

$$\frac{d}{dt}\int_V \Phi dv = -\int_S \vec{F}\cdot d\vec{a} \tag{2.1}$$

$\vec{F}$ is the power density [$J/cm^2/s$] of dimension Φ per unit area ($d\vec{a}$) and time (dt), where $d\vec{a}$ is normal to the surface S and points outwards by convention. Applying Gauss's theorem, eq. 2.1 may be rewritten in a local differential form as:

$$\frac{d\Phi}{dt} = -\nabla\cdot\vec{F} \tag{2.2}$$

Assuming heat is the only energy form, and the heat equation is obtained by substituting $\Phi = \rho c_p T(z,t)$ as the energy density [J/cm^3] and $\vec{F} = -K\nabla T$ as the power density [W/cm^2] in eq. 2.2 as follows:

$$\rho c_p \frac{\partial T(z,t)}{\partial t} = \nabla\cdot(K\nabla T) \tag{2.3}$$

ρ denotes the mass density $[g/cm^3]$, c_p specific heat capacity $[J/g/K]$ and K thermal conductivity $[W/K/cm]$. To simplify the model without losing essential properties, the former parameters are assumed isotropic ($|\vec{F}_z| = |\vec{F}_{xy}|$). In the laser experiment the heat conduction in the vertical (z) direction dominates, since the spot size ($2W_0$) is much wider than the thermal diffusion length (l). This specifies eq. 2.3 as a one dimensional parabolic equation:

$$\rho c_p \frac{\partial T(z,t)}{\partial t} = K \frac{\partial^2 T(z,t)}{\partial^2 z} \tag{2.4}$$

The heat source, a Gaussian laser beam, is introduced through a boundary condition at $z = 0$ and $t = 0$. The free air Gaussian power density $[W/cm^2]$ can be written as a product of a spatial, temporal and attenuation terms in accordance with Beer's absorption law:

$$I(r,z,t) = I_0 \left(\frac{W_0}{W_z}\right)^2 \cdot exp\left[-\frac{2r^2}{W^2(z)}\right] \cdot \frac{1}{\sigma\sqrt{2\pi}} \cdot exp\left[-\frac{(t-t_0)^2}{2\sigma^2}\right] \cdot exp(-\alpha z) \tag{2.5}$$

r is the horizontal distance from the origin, I_0 is the input power density (spatial and temporal integral) and W_0 is the beam waist radius at $z = 0$, $W(z)$ is the beam radius at z, t_0 is the time of peak power density, σ is the standard deviation (full width, halve pulse magnitude, FWHM) as $\tau_p = 2\sqrt{ln4} \cdot \sigma$, and α $[cm^{-1}]$ is the absorption coefficient [33]:

$$\alpha = 4\pi \cdot k/\lambda \tag{2.6}$$

by which I attenuates to $e^{-1} \cdot I_0$ at $z = 1/\alpha$. Here k denote the extinction coefficient. Assuming $z \ll l$[1], where l is the thermal penetration depth $[cm]$, and the boundary conditions for eq. 2.4 are:

$$\begin{aligned} T(l,t) &= T_R, \frac{\partial T(z,t)}{\partial z}\Big|_{z=l} = 0 \\ (1-R)\bar{I}(t) &= -K \frac{\partial T(z,t)}{\partial z}\Big|_{z=0} \\ \int_0^t (1-R)\bar{I}(t)dt &= \rho c_p \int_0^{l(t)} T(z,t)dz \end{aligned} \tag{2.7}$$

T_R (298 K) is the room temperature and $\bar{I}(t)$ $[W/cm^2]$ is the source term related to a cross section of the Gaussian beam. The bottom equation describes the balance of flu-

[1] This assumption holds for metals (cf. Tab. 2.1) and for ionized minerals with abundance of free electrons in the ablation zone.

ence $[J/cm^2]$ when the laser energy is transformed instantaneously to heat. For the case where the power density is uniform in time a solution of eq. 2.5 and 2.7 is given by Hassan et al. [34]. To this end the time-averaged power density is defined first.

$$\left.\begin{aligned} \bar{I}_t &= \tfrac{1}{t}\int_0^t \bar{I}(\tau)d\tau \\ T(z,t) &= T_s(t)\left[1-\tfrac{z}{l(t)}\right]^3 \end{aligned}\right\} t < t_p \tag{2.8}$$

t_p is the laser pulse duration. The penetration depth is linked to the diffusivity [34]:

$$l(t) = \sqrt{12\kappa t}, t < t_p \tag{2.9}$$

$\kappa = K/\rho c_p$ is thermal diffusivity $[cm^2/s]$. The surface reaches a temperature:

$$T_s(t) = \frac{(1-R)\bar{I}_t}{K}\left(\frac{4}{3}\kappa t\right)^{1/2}, t < t_p \tag{2.10}$$

This temperature differs by a factor 4/3 in the square root from other work [35–37]. The melting temperature at the surface is reached when:

$$t_m = \frac{3}{4\kappa}\left[\frac{KT_m}{(1-R)\bar{I}_t}\right]^2, t < t_p \tag{2.11}$$

Substituting $t = t_m$ in eq. 2.9 and dividing using eq. 2.11, the average thermal relaxation velocity is found as:

$$\bar{v}_{rel} = \frac{l}{t_m} = 4\kappa \cdot \frac{(1-R)\bar{I}_t}{KT_m}, t < t_p \tag{2.12}$$

Based on the fluence balance in eq. 2.7 a melting damage threshold may be determined, based on the fluence F_{th}^d required to melt the surface at time t_m:

$$F_{th}^d = \int_0^{t_m} \bar{I}_t dt = \frac{\sqrt{12\rho c_p K t_m}}{1-R} T_m, t_m < t_p \tag{2.13}$$

This expression is similar to a threshold defined in [38]. It provides a good lower limit of the breakdown threshold, which is expected to occur almost immediately upon melting, which strongly increases the absorption of the surface and strongly lowers the linear reflectivity R. At high fluence ($F >> F_{th}$), a high temperature and electron density plasma is formed and the laser energy can be absorbed effectively into the target surface even if the initial reflectivity is high [39]. Reflectivity only plays a role when the very front thin layer is not molten or vaporized. Plasma shielding causes that part of the laser pulse energy is directly absorbed in the plume, and does not contribute to ablation.

2.2.2. VAPOUR PLUME FORMATION

During evaporation certain parts of the target material that are not directly exposed to the laser beam may melt. The energy needed to melt material may be neglected if the enthalpy of fusion ΔH_f (latent energy) is small compared to the energies of heating, boiling and evaporation. Thus, the energy required to bring the solid to the boiling stage may be assumed proportional to the difference in temperature between boiling and room temperature. The time required to bring the surface temperature to the boiling point, just before vaporization, is determined as [35]:

$$T_b = T_s(t_b) = \frac{(1-R)\bar{I}_t}{K}\left(\frac{4}{3}\kappa t_b\right)^{1/2} \tag{2.14}$$

Just one step further in energy the main process is the onset and flow of hot vapour, which removes liquid (evaporation) or solid (i.e. sublimation) material from the surface. The vaporization leads to a Knudsen layer, just several free particle lengths thick, where the vaporized particles have considerable interaction with the solid surface interface. Due to the onset of vapour flow and multitude of possible energy transfer levels for interacting particles this thin layer does not comply with conditions for LTE. However, the main effect of the particle-surface interactions in the Knudsen layer is that it increases the pressure at the surface interface, thereby increasing the partial vapour pressure. As a result, vaporization occurs at higher pressures and may be produced by phase explosion [21, 40]. It is noted that after the laser pulse the Knudsen layer is still present and tends to inhibit vaporization by the same rules. As a result, vaporization stops abruptly after the pulse and the pressure at the interface is mainly determined by the low rarefaction wave pressure.

The ablation rate is denoted as $\dot{\mu}$ $[g/cm^2/s]$. This rate is assumed to be generated by the ideal gas laws ($pV = nN_A kT$, $\rho = mnN_A/V$), where n is the amount of substance $[mol]$, m is the average mass of an ablated species and N_A is the Avogadro constant $[6.02 \times 10^{23}\ mol^{-1}]$, neglecting the electron number density. This leads to:

$$\dot{\mu} = \alpha_K \rho_s^V \bar{v}_s^V,\ \bar{v}_s^V = \sqrt{\frac{k_b T_{ss}}{2\pi m}} \tag{2.15}$$

where $\bar{v}_s^V$ is determined for a Maxwellian distribution. The influence of the Knudsen layer is accounted for by the factor α_K, which increases the vapour pressure as $1/\alpha_K$. Here, the

average vapour velocity at the surface is chosen as the expectation value according to the one-dimensional Maxwell distribution [41], where $k_b = 1.38 \times 10^{-16}$ $[g \cdot cm^2/s^2/K]$ is the Boltzman constant and T_{ss} denotes the surface temperature [35, 42], except here it is defined as the temperature at the interface of the Knudsen layer and the expanding vapours where LTE exists. To obtain an expression for the onset of ablation the integral form of the Clausius-Clapeyron equation [41, 43] is invoked to describe the phase transition from boiling to vapour:

$$p_s^V(T_{ss}) = p_0 \cdot exp\left[-\frac{M \cdot \Delta H_v}{R}\left(\frac{1}{T_{ss}} - \frac{1}{T_b}\right)\right] \tag{2.16}$$

The ambient pressure is assumed $p_0 = 1$ bar $[10\ N/cm^2]$. T_{ss} is the surface temperature corresponding to p_s^V and T_b is the boiling temperature. The mass removal rate may now be specified by the Hertz-Knudsen equation as:

$$\dot{\mu} = \alpha_K \frac{p_s^V m}{k_b T_{ss}} \sqrt{\frac{k_b T_{ss}}{2\pi m}} = \alpha_K p_0 \sqrt{\frac{m}{2\pi k_b T_{ss}}} exp\left[-\frac{M \cdot \Delta H_v}{R}\left(\frac{1}{T_{ss}} - \frac{1}{T_b}\right)\right] \tag{2.17}$$

M is the molar mass $[g/mol]$, ΔH_v is heat of vaporization $[J/g]$ at the boiling point and R is the universal gas constant $[J/K/mol]$. The temperature T_{ss} may be determined by measuring the mass removal rate. The boundary condition with imposed laser power density at the moment when the plasma starts to form ($t_b < t_v < t_p$) at the surface $z = 0$ is written as:

$$(1-R)\bar{I}(t) = -K \frac{\partial T(z,t)}{\partial z}\Big|_{z=0} + \dot{\mu}\Delta H_v \tag{2.18}$$

If we assume the transition of material from solid to gaseous phases is by sublimation, similar to eq. 2.13, a threshold for sublimation F_{th}^s $[J/cm^2]$ under which no vaporization takes place can be estimated when the deposited energy exceeds the heat of sublimation:

$$F_{th}^s = \rho \cdot \Delta H_s \sqrt{12\kappa t_v},\ t_v < t_p \tag{2.19}$$

t_v is the time needed to reach the point of vaporization. The above physical ns-LIBS ablation model (Eqs. 2.9-2.19) is applied on selected materials listed in Tab. 2.1 using corresponding linear optical properties [2] and thermal dynamic parameters at room temperature

[2] $R_{Sb} = 0.67$ calculated using the normal incidence reflectivity from the air onto the sample surface $R = [(1-n)^2 + k^2]/[(1+n)^2 + k^2]$ with $n = 3.46$, $k = 4.69$ from [44] and $R_{Si} = R(reflectance) + T(transmittance) = 0.93$ calculated using $T = exp(-\alpha_{Si} \cdot l) = 0.61$ where $\alpha_{Si} = 4\pi \cdot k/\lambda = 11.4\ cm^{-1}$, $l = 430\ \mu m$ (measured), $k = 9.65 \cdot 10^{-5}$ and $R = 0.32$ from [33]

(298 K). We assume that $H_s = H_f + H_v$ for, e.g. Sb, of which H_s is not available.

2.2.3. TRANSMISSION OF INCIDENT LASER LIGHT

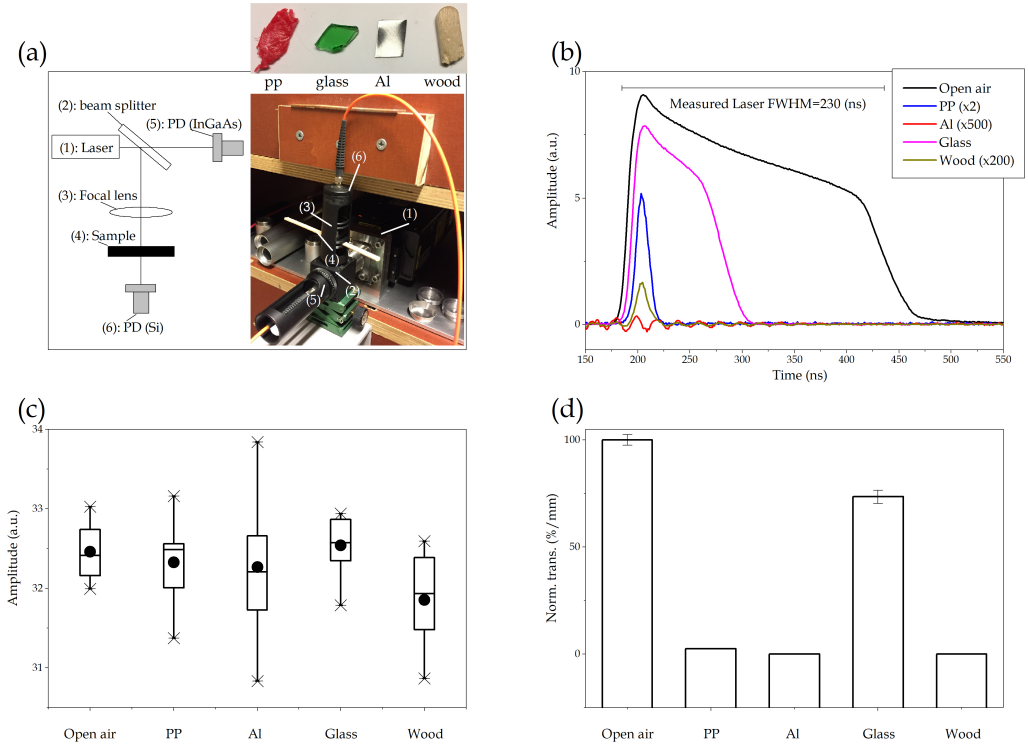


Figure 2.3: (a) Experimental setup to measure the transmission of incident laser pulse through open air and four waste materials (pp, glass, Al and wood). (b) Measured pulse shapes of the incident laser pulse and the transmitted light through the samples. pp, Al and wood are amplified with a factor of 2, 500, and 200, respectively. (c) Boxplots of measured incident laser energy (integral of its temporal shape): the upper and lower limits of the box indicate 25% and 75% percentiles, the horizontal line within the box marks the median value, the upper and lower crosses stand for the 99% and 1% percentiles, the top and bottom horizontal lines outside the box represent the maximum and minimum values, and the circle for the mean value. (d) Normalized transmission of waste materials.

In this subsection, we investigate the laser transmission coefficients through different representative waste materials. This is an indirect way of measuring the absorption coefficient that can be used to derive the optical penetration depth. Fig. 2.3a shows the experimental setup, where the incident laser is split into two beams. One beam propagates through the polarizer beam splitter (VBA05-1064: variable beamsplitter/attenuator for 1064 nm, Thorlabs) and is detected by the a InGaAs fast diode (SM05PD5A, Thorlabs). The other beam gets reflected by the beam splitter and penetrates towards the sample. Another Si fast diode (SM05PD1B, Thorlabs) is placed underneath the sample to measure the transmitted light. First, we measure the transmission of the collimated laser beam without a lens between the beam splitter and the sample surface. Fig. 2.3b shows the measured time traces (oscilloscope with 50 ohm impedance, Lecroy) of the incident laser

Table 2.1: Thermal dynamic parameters at room temperature (298 K) calculated for nine selected materials. ρ $[g/cm^3]$, c_p $[J/g/K]$, K $[W/cm/K]$, κ $[cm^2/s]$, T_m $[K]$, T_m $[K]$ [45], H_v $[kJ/mol]$, H_s $[kJ/mol]$, χ_{1st} $[kJ/mol]$, M $[g/mol]$ [46], R [47], n and k[33], α $[\mu m^{-1}]$ (cf. eq.2.6), l $[nm]$ (cf. eq.2.9), t_m $[ps]$ (cf. eq.2.11), $\bar{v}_{rel}$ $[km/s]$ (cf. eq.2.12), F^d_{th} $[J/cm^2]$ (cf. eq.2.13), v_p $[bar]$ (cf. eq.2.16), $\dot{\mu}$ $[mg/cm^2/s]$ and $\dot{\mu}_{mol}$ $[10^{-3}\ mol/cm^2/s]$ (cf. eq.2.17), F^s_{th} $[J/cm^2]$ (cf. eq.2.19).

	Al	Cu	Mo	Ni	Sb	Si	Ti	W	Zn
ρ	2.70	8.93	10.20	8.90	6.68	2.42	4.50	19.30	7.14
c_p	0.89	0.39	0.25	0.44	0.21	0.71	0.38	0.19	0.39
K	2.37	4.01	1.38	0.94	0.24	1.49	0.22	1.74	1.16
κ	0.98	1.16	0.54	0.23	0.18	0.86	0.13	0.48	0.42
T_m	933.47	1357.77	2883.15	1728.15	903.15	1687.15	1941.15	3695.15	692.68
T_b	2792.15	2835.15	5833.15	3186.15	1653.15	3538.15	3560.15	5828.15	1180.15
H_v	294.00	300.40	598.00	377.50	193.43	359.00	425.00	806.70	123.60
H_s	326.40	337.70	664.00	394.98	213.22	450.00	469.00	851.00	130.92
χ_{1st}	577.27	745.14	684.00	736.79	830.20	786.15	658.51	758.41	905.98
M	26.98	63.55	95.94	58.69	121.75	28.00	47.87	183.84	65.38
t_m	51.22	262.69	302.15	117.27	2.84	75.25	14.64	884.20	15.85
l	245.81	604.96	442.08	180.69	24.49	279.32	47.23	714.40	89.28
$\bar{v}_{rel}$	4.80	2.30	1.46	1.54	8.63	3.71	3.23	0.81	5.63
R	0.91	0.99	0.57	0.74	0.67	0.93	0.63	0.58	0.58
n	1.23	0.35	2.30	2.80	3.50	3.50	3.30	3.03	1.98
k	10.60	6.70	4.00	5.00	4.70	$9.65 \cdot 10^{-5}$	3.30	3.80	4.20
α	125.19	79.13	47.24	59.05	55.51	$1.14 \cdot 10^{-3}$	38.97	44.88	49.60
F^d_{th}	0.61	28.38	0.76	0.48	0.01	1.16	0.04	2.27	0.04
v_p	1.40	1.15	1.06	1.18	1.10	1.33	1.21	1.04	1.19
$\dot{\mu}$	3.19	4.03	4.52	3.96	5.32	3.07	3.67	6.16	4.19
$\dot{\mu}_{mol}$	0.12	0.06	0.05	0.07	0.04	0.11	0.08	0.03	0.06
F^s_{th}	3.55	5.60	5.68	3.16	0.54	3.96	1.72	6.79	1.01

pulse and the transmitted light through four different waste materials, i.e. polypropylene plastic (pp, 1 mm thick), glass (2.1 mm thick), aluminum (0.25 mm thick), and wood (2.2 mm thick). A reference measurement is performed in open air without a sample between the beam splitter and Si photo diode. It is noted that both the amplitude and pulse width of the transmitted light decrease [3]. Also noticeable is the latency 7 ns of the transmitted light wrt. incident. To further quantify the transmission coefficients, we use the integral for transmitted light, and normalized to the varying incident laser energy (integral of the incident laser trace) to compensate for the pulse-to-pulse variations as shown in Fig. 2.3c. As a result, the glass , pp, and wood use in this experiment have a transmission coefficient of 73 %/mm, 2.5 %/mm and 0.016 %/mm, respectively, wrt. the transmission through open air. A metal like Al has no measurable transmission.

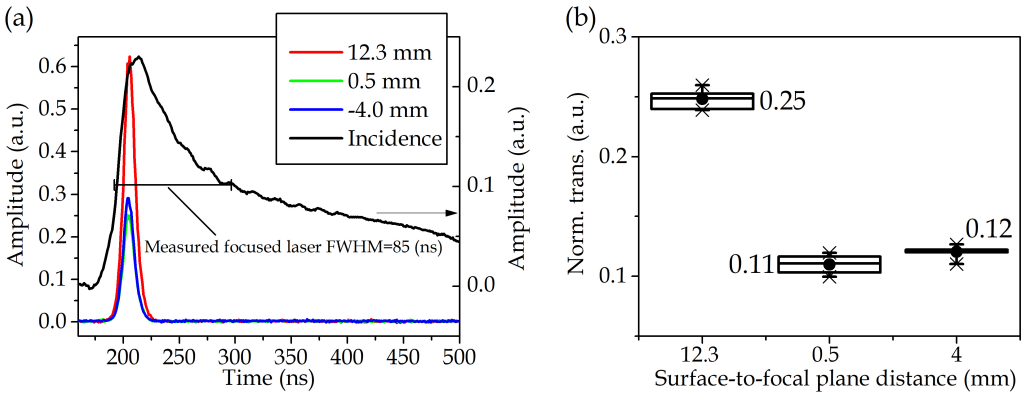


Figure 2.4: Through focus measurement: (a) Time traces of incident laser, and the transmitted light through the wood sample at three different focal plane-to-sample surface distances and (b) the measured transmission rates.

Next, we measure the transmission for a focused laser beam by inserting a focusing lens (30 mm focal length) between the beam splitter and the sample surface. The lens is first de-focused with a 17.7 mm lens to the sample surface distance, which corresponds to 12.3 mm distance between the focal plane and the sample surface. Then the lens is moved away from the surface, so the surface is illuminated at the focal plane and plasma is generated. Last, the lens is moved further away from the surface to de-focus it with a -4 mm sample surface to focal plane distance [4]. Fig. 2.4a shows the time traces of incident laser and the transmitted light through the wood sample at three different sample surface-to-focal plane

[3] The measured pulse width is much larger than the original pulse width, due to bandwidth filtering effect of the large junction capacitance of the photo diode.

[4] We did not perform a reference measurement, because of the risk of burning the photo diode without a sample between the lens and the diode.

distances. Note that at 0.5 mm distance and closest to the focal plane, the transmission signal is smallest in both amplitude and pulse width. Fig. 2.4b shows the measured transmission energy integral of the time trace normalized to the incident laser energy. The transmission closest to the focal plane is 0.11, as compared to 0.25 measured at the 12.3 mm surface-to-focal plane distance. If we assume this latter value is comparable with the transmission of the collimated light as shown in Fig. 2.3d for the wood sample, the transmission coefficient at the focal plane should be 0.007%/mm, which is clearly negligible.

To conclude, waste materials demonstrate the same behaviour as a metal in that the laser energy is mainly absorbed in a surface layer. In other words, the optical penetration depth seems sufficiently small to be heated to breakdown and form plasma. The major difference between metal and other waste materials is the initial electron density and the diffusion of heat. As soon as the incident laser intensity exceeds the breakdown threshold, the induced free electrons absorb the incident laser energy similar to a metal.

2.2.4. SHOCK WAVE AND ELASTIC ENERGY

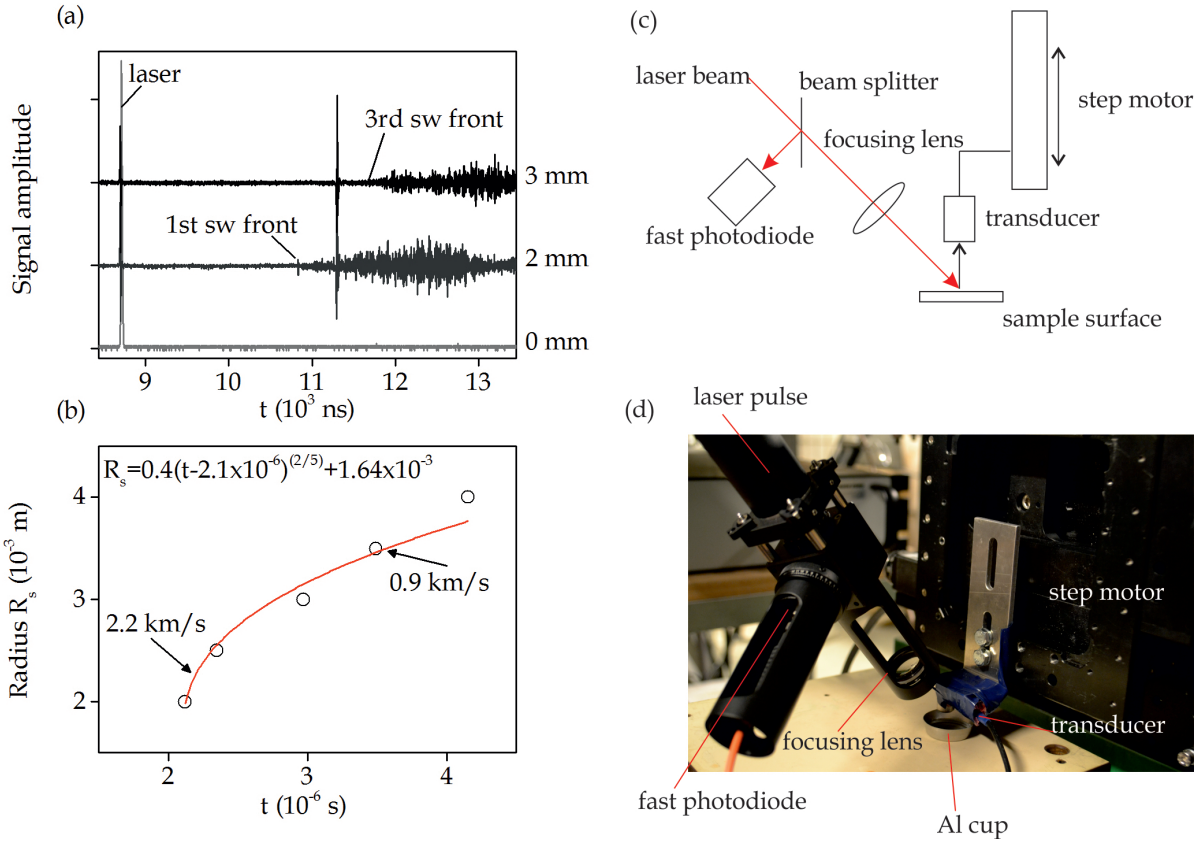


Figure 2.5: (a) Raw data of shock wave at 2 mm and 3 mm after laser firing from focused laser spot on a Al sample surface. (b) Results using point explosion model eq. 2.20. (c) Schematic and (d) experimental setup for laser-induced shock wave detection.

A laser-induced shock wave expands in a gaseous background with decreasing velocity. This phenomenon can give information on the laser energy that the material absorbs. In an analogy, the total explosion energy of the first atomic bomb was successfully estimated in 1950 using the Taylor-Sedov relationship [48]. It describes the expansion of a shock wave front over time t, based on which the initial energy deposited to create the shock wave could be estimated [49–51]:

$$R_s(t) \propto \gamma_g (E_0^{ab}/\rho_o)^{1/(2+\beta_d)} t^{2/(2+\beta_d)} \tag{2.20}$$

$R_s(t)$ denotes the distance between the sample surface and the shockwave front, E_0^{ab} the initial absorbed energy, γ_g the ratio of the specific heats, ρ_g the density of air, and β_d the dimensionality of shockwave propagation. Fig. 2.5 shows a time signature of a shock wave front detected with a piezoelectric transducer (OLYMPUS 805271 central frequency of 175 ± 50 MHz). The first data point is located at ca. 2 mm above the Al surface, as limited by the size of the transducer. The following four data points are measured at steps of

0.5 mm as the transducer is moved upwards from the sample surface. The measured speed of the shockwave decreases from ca. 2.2 km/s at 0.5 mm to 0.9 km/s at 2 mm above the surface, and the measured absorbed laser energy $E_{ab} = 2.3\ mJ$, using $\rho_{air} = 1.225\ kg/m^3$ and $\gamma_g = 1.4$. These values may underestimate the real velocity because the transducer is bandwidth limited.

The vapour pressure exerted during laser ablation causes the material (solid or liquid) underneath to be compressed, by which part of the laser energy is converted to work. This well-known effect of the laser pulse is utilized to induce elastic waves in the solid for the purpose of non-contact material inspection [52, 53]. It is of interest to estimate the work. The force impulse exerted by the ablation process may be estimated using eq. 2.15, and rewritten to obtain an average applied pressure P:

$$P = \rho_s^V (\bar{v}_s^V)^2,\ t < t_p \tag{2.21}$$

The fastest possible time for elastic compression to take place is causally limited to the highest acoustic wave speed available, i.e. the compressional wave speed C of the solid. As the laser pulse exerts pressure only during the laser pulse, the maximum forced displacement d and work E done in a laser experiment cannot exceed these values:

$$d = C t_p,\ E = PAd \tag{2.22}$$

Calculations for Al and Fe ($\rho_s^V = \rho,\ T = 15 \cdot 10^3\ K$) both indicate a maximum elastic energy of 0.5 mJ. This is conservative estimation as the real vapour density will be lower (most likely the saturated vapour pressure at surface temperature in the Knudsen layer) while the laser reheating of the vapour reduces the effective ablation time. Nevertheless, this upper limit indicates the work done by the laser energy on the solid may be neglected compared to the available laser energy.

2.2.5. VAPOUR EXPANSION

So far the discussion was limited to phenomena close to the material surface. To gain insight into the expanding vapour plume the conservation of mass, momentum and energy must be considered. Departing from the linear description in eq. 2.1, the one dimensional

equations for mass, momentum and energy conservation are written as:

$$\frac{\partial \rho}{\partial t} = -\frac{\partial \rho v_z}{\partial z}$$

$$\frac{\partial}{\partial t}(\rho v_z) = -\frac{\partial}{\partial z}(p + \rho v_z^2) \tag{2.23}$$

$$\frac{\partial}{\partial t}(\rho u) = -\frac{\partial}{\partial z}\rho v_z \left(u + \frac{p}{\rho}\right) + I_{ab} - \varepsilon_{rad}$$

Introduced are the pressure p $[N/cm^2]$ where the vapour is a highly ionized gas for which a modified gas law must be applied; internal energy u $[J]$ of which the detailed form depends on the energy partition by the different species; average particle velocity v_z $[cm/s]$, absorbed laser power density I_{ab} $[W/cm^2]$ that depends on the specific laser absorbtion mechanism; and thermal radiation losses ε $[W/cm^2]$ which depend on the type of radiation in the time window. The interaction between vapour and laser light is highly dynamic, because every variable is a function of time and space. A way to better understand this interaction is to obtain $I_{ab}(t,z)$ in the 3rd term of eq. 2.23 by performing time- and space-resolved measurements on the other variables. This task is outside the scope[5] of our current research and, hereafter, we will ignore dynamic vapour-laser light interactions.

2.2.6. OPTICAL EMISSION SPECTRA

The hot vapour is highly ionized. Upon cooling by radiation and expansion, the ionization level will decrease due to recombination by which the plasma eventually degenerates to the status of a hot gas. In an optically thin plasma the free electrons distribute heat and momentum effectively among the rest of the matter through collisions, which facilitates local thermal equilibrium (LTE) in the plume. The early plasma is characterized by a continuous emission spectrum due to the large number of possible energy transitions available, for example, free-free and free-bound recombination and fluorescence, but also due to Stark broadening. As the plume cools the level of ionization reduces. At this later stage the plume reveals the characteristic emission lines connected to bound-bound energy transitions, i.e. electron transition in an ion or atom, which is of interest for quantitative interpretation

[5] To perform a time measurement of laser absorption, a photo electro-magnetic detector is needed to measure the absorbed laser energy with ns resolution, and to measure the spatial distribution of laser absorption during a dynamic laser-induced plasma process, a fast camera with an integration time window of ns is needed.

of the species contents of the plume. Also the free-bound recombination may still occur, i.e. free electron recombination with an ion to form an atom, but this is in the UV range or even higher energy, which is not considered in this research.

The emission line intensity related to bound-bound is a measure of the expectation value of the corresponding energy transition, i.e. it is the multiplication of transition probability and number of corresponding energy transitions present in the plume. In this work, the intensity of an emission line is assumed to obey the Einstein's theory of electronic transition, where the electron population obeys the Boltzmann distribution law. Similarly, the relation between different ionization levels of an element is assumed to obey the Saha-Boltzmann relation under LTE. Detailed setup of this framework is discussed in detail in Chap. 5.

REFERENCES

[1] S. Hashmi, *Comprehensive Materials Processing: Laser Machining and Surface Treatment*, Vol. 9 (Elsevier Science, 2014).

[2] D. T. Lloyd, K. O'Keeffe, and S. M. Hooker, *Comparison of strong-field ionization models in the wavelength-scaling of high harmonic generation,* Optics express **27**, 6925 (2019).

[3] M. Cao, J. Cao, M. Liu, Y. Sun, M. Wu, S. Guo, and S. Gao, *Wavelength dependence of nanosecond laser induced surface damage in fused silica from 260 to 1550 nm,* Journal of Applied Physics **123**, 135105 (2018).

[4] P. Pronko, P. VanRompay, C. Horvath, F. Loesel, T. Juhasz, X. Liu, and G. Mourou, *Avalanche ionization and dielectric breakdown in silicon with ultrafast laser pulses,* Physical Review B **58**, 2387 (1998).

[5] D. Wiggins, C. Raynor, and J. Johnson III, *Evidence of inverse bremsstrahlung in laser enhanced laser-induced plasma,* Physics of Plasmas **17**, 103303 (2010).

[6] D. Salzmann, *Atomic physics in hot plasmas*, 97 (Oxford University Press on Demand, 1998).

[7] B. Campanella, S. Legnaioli, S. Pagnotta, F. Poggialini, and V. Palleschi, *Shock waves in laser-induced plasmas,* Atoms **7**, 57 (2019).

[8] P. Lorazo, L. J. Lewis, and M. Meunier, *Thermodynamic pathways to melting, ablation, and solidification in absorbing solids under pulsed laser irradiation,* Physical Review B **73**, 134108 (2006).

[9] A. Semerok, C. Chaléard, V. Detalle, J.-L. Lacour, P. Mauchien, P. Meynadier, C. Nouvellon, B. Sallé, P. Palianov, M. Perdrix, *et al.*, *Experimental investigations of laser ablation efficiency of pure metals with femto, pico and nanosecond pulses,* Applied Surface Science **138**, 311 (1999).

[10] M. S. Brown and C. B. Arnold, *Fundamentals of laser-material interaction and application to multiscale surface modification,* in *Laser precision microfabrication* (Springer, 2010) pp. 91–120.

[11] Z. Chen, D. Bleiner, and A. Bogaerts, *Effect of ambient pressure on laser ablation and plume expansion dynamics: A numerical simulation,* Journal of applied physics **99**, 063304 (2006).

[12] M. Cirisan, J. Jouvard, L. Lavisse, L. Hallo, and R. Oltra, *Laser plasma plume structure and dynamics in the ambient air: The early stage of expansion,* Journal of applied physics **109**, 103301 (2011).

[13] S. I. Anisimov and V. A. Khokhlov, *Instabilities in laser-matter interaction* (CRC press, 1995).

[14] M. Aghaei, S. Mehrabian, and S. Tavassoli, *Simulation of nanosecond pulsed laser ablation of copper samples: A focus on laser induced plasma radiation,* Journal of Applied Physics **104**, 053303 (2008).

[15] X. Xu and D. A. Willis, *Non-equilibrium phase change in metal induced by nanosecond pulsed laser irradiation,* J. Heat Transfer **124**, 293 (2002).

[16] D. Perez, L. J. Lewis, P. Lorazo, and M. Meunier, *Ablation of molecular solids under nanosecond laser pulses: The role of inertial confinement,* Applied physics letters **89**, 141907 (2006).

[17] L. J. Lewis and D. Perez, *Laser ablation with short and ultrashort laser pulses: Basic mechanisms from molecular-dynamics simulations,* Applied Surface Science **255**, 5101 (2009).

[18] V. Mazhukin, M. Demin, and A. Shapranov, *High-speed laser ablation of metal with pico-and subpicosecond pulses,* Applied Surface Science **302**, 6 (2014).

[19] K. Sugioka, M. Meunier, and A. Piqué, *Laser Precision Microfabrication*, Springer Series in Materials Science (Springer Berlin Heidelberg, 2010).

[20] S. Tao, Y. Zhou, B. Wu, and Y. Gao, *Infrared long nanosecond laser pulse ablation of silicon: Integrated two-dimensional modeling and time-resolved experimental study,* Applied surface science **258**, 7766 (2012).

[21] A. Bogaerts and Z. Chen, *Nanosecond laser ablation of Cu: modeling of the expansion in he background gas, and comparison with expansion in vacuum,* Journal of Analytical Atomic Spectrometry **19**, 1169 (2004).

[22] N. Bulgakova and A. Bulgakov, *Pulsed laser ablation of solids: transition from normal vaporization to phase explosion,* Applied Physics A **73**, 199 (2001).

[23] F. Vidal, T. Johnston, S. Laville, O. Barthélemy, M. Chaker, B. Le Drogoff, J. Margot, and M. Sabsabi, *Critical-point phase separation in laser ablation of conductors,* Physical review letters **86**, 2573 (2001).

[24] J. Cooper, *Plasma spectroscopy,* Reports on Progress in Physics **29**, 35 (1966).

[25] H. Chae and S. M. Park, *Microphone detection of laser ablation,* Review of scientific instruments **68**, 4627 (1997).

[26] F. Rezaei, P. Karimi, and S. Tavassoli, *Effect of self-absorption correction on libs measurements by calibration curve and artificial neural network,* Applied Physics B **114**, 591 (2014).

[27] *Nist physical measurement laboratory,* `https://physics.nist.gov`, accessed: 2020-02-20.

[28] M. Stafe, I. Vladoiu, and I. Popescu, *Impact of the lasr wavelength and fluence on the ablation rate of aluminium,* Open Physics **6**, 327 (2008).

[29] J. Hoffman, J. Chrzanowska, S. Kucharski, T. Moscicki, I. Mihailescu, C. Ristoscu, and Z. Szymanski, *The effect of laser wavelength on the ablation rate of carbon,* Applied Physics A **117**, 395 (2014).

[30] A. H. Lutey, *An improved model for nanosecond pulsed laser ablation of metals,* Journal of Applied Physics **114**, 083108 (2013).

[31] V. Craciun, N. Bassim, R. Singh, D. Craciun, J. Hermann, and C. Boulmer-Leborgne, *Laser-induced explosive boiling during nanosecond laser ablation of silicon,* Applied surface science **186**, 288 (2002).

[32] J. Ready, *Effects due to absorption of laser radiation,* Journal of Applied Physics **36**, 462 (1965).

[33] D. Lide, *CRC Handbook of Chemistry and Physics, 90th Edition* (Taylor & Francis, 2009).

[34] A. Hassan, M. El-Nicklawy, M. El-Adawi, and A. Hemida, *A general problem of pulse laser heating of a slab,* Optics & Laser Technology **25**, 155 (1993).

[35] D. Rosen, J. Mitteldorf, G. Kothandaraman, A. Pirri, and E. Pugh, *Coupling of pulsed 0.35-μm laser radiation to aluminum alloys,* Journal of applied Physics **53**, 3190 (1982).

[36] M. El-Adawi and E. Elshehawey, *Heating a slab induced by a time-dependent laser irradiance - An exact solution,* Journal of applied physics **60**, 2250 (1986).

[37] H. Carslaw and J. Jaeger, *Conduction of Heat in Solids*, Oxford science publications (Clarendon Press, 1986).

[38] R. Wood, *Laser induced damage thresholds and laser safety levels. Do the units of measurement matter?* Optics & Laser Technology **29**, 517 (1998).

[39] L. Cabalin and J. Laserna, *Experimental determination of laser induced breakdown thresholds of metals under nanosecond q-switched laser operation,* Spectrochimica Acta Part B: Atomic Spectroscopy **53**, 723 (1998).

[40] A. V. Gusarov, A. G. Gnedovets, and I. Smurov, *Gas dynamics of laser ablation: influence of ambient atmosphere,* Journal of Applied Physics **88**, 4352 (2000).

[41] P. Atkins and J. Paula, *Atkins' physical chemistry*, 8th ed. (W. H. Freeman and Company, 2006).

[42] R. J. Harrach, *Analytical solutions for laser heating and burnthrough of opaque solid slabs,* Journal of Applied Physics **48**, 2370 (1977).

[43] A. Bogaerts, Z. Chen, R. Gijbels, and A. Vertes, *Laser ablation for analytical sampling: what can we learn from modeling?* Spectrochimica Acta Part B: Atomic Spectroscopy **58**, 1867 (2003).

[44] A. P. Lenham, D. M. Treherne, and R. J. Metcalfe, *Optical properties of antimony and bismuth crystals,* J. Opt. Soc. Am. **55**, 1072 (1965).

[45] A. Bejan and A. Kraus, *Heat Transfer Handbook*, Heat Transfer Handbook No. v. 1 (Wiley, 2003).

[46] J. Speight, *Lange's Handbook of Chemistry, 70th Anniversary Edition* (McGraw-Hill Education, 2005).

[47] W. Steen, *Laser Material Processing* (Springer London, 2013).

[48] G. Taylor, *The formation of a blast wave by a very intense explosion. II. The atomic explosion of 1945,* in *Proceedings of the Royal Society of London A: Mathematical, Physical and Engineering Sciences*, Vol. 201 (The Royal Society, 1950) pp. 175–186.

[49] G. Taylor, *The formation of a blast wave by a very intense explosion. I. Theoretical discussion,* Proceedings of the Royal Society of London. Series A, Mathematical and Physical Sciences , 159 (1950).

[50] X. Zeng, X. Mao, S.-B. Wen, R. Greif, and R. E. Russo, *Energy deposition and shock wave propagation during pulsed laser ablation in fused silica cavities,* Journal of Physics D: Applied Physics **37**, 1132 (2004).

[51] L. Sedov, M. FRIEDMAN, and M. Holt, *Similarity and Dimensional Methods in Mechanics* (London, 1959).

[52] Y. Tsukahara, *Analysis of the elastic wave excitation in solid plates by phase velocity scanning of a laser beam,* Applied physics letters **59**, 2384 (1991).

[53] P. Cielo, F. Nadeau, and M. Lamontagne, *Laser generation of convergent acoustic waves for materials inspection,* Ultrasonics **23**, 55 (1985).

3

EXPERIMENTAL STUDY IN LASER DEPLOYMENT AND DATA QUALITY

LIBS is a technique for measuring the composition of a sample or for characterizing the type of material. In either case, it is necessary to decompose the vapour plume emissions using a spectrograph and to achieve a good signal-to-noise ratio (SNR). For example, for quantitative elemental analysis one commonly selects the well identifiable ionic and atomic emission lines, which are dominant when the plasma plume has cooled down and is optically thin for this radiation. Under those conditions the photon count may be considered proportional to the concentration of a certain element in the plume and, supposedly, in the sample. In principle all plume emissions carry some information about the target material, but besides the aforementioned spectra the direct relation to the original sample material contents is not quantifiable. Nevertheless, these mostly continuous and broadened spectra are causally related to the sample material and may offer at least opportunities for classification, which is employed in physical fingerprinting.

The choice of laser, optics and control of ambient conditions (air, material surface) prove to influence the quality of the corresponding optic data. The LIBS hardware used in this work is shown in Fig. 3.1, consisting of laser unit, laser power supply and controller, laser directing focusing optics, laser induced plasma emission collection optics, heat sink and water cooling, frequency generator, sample mountings/holders (e.g. step-motor), compressed air and air suction, spectrometer and PC. The total power consumption of this system is ca. 2 kW. It is designed to control experimental conditions and record the

response obtained through optic mirrors and a spectrometer. The setup's main functionalities are sample positioning and alignment, sample presentation to the laser beam (static or moving), optic control of laser beam delivery, optic collection of photonic emissions, dispersion over wavelengths and recording intensities. The real-time data acquisition was programmed in Delphi, and the synchronization and signal processing in Matlab. The schematic of the LIBS setup shown in Fig. 3.3 is used to study the relation between setup parameters and data quality [1].

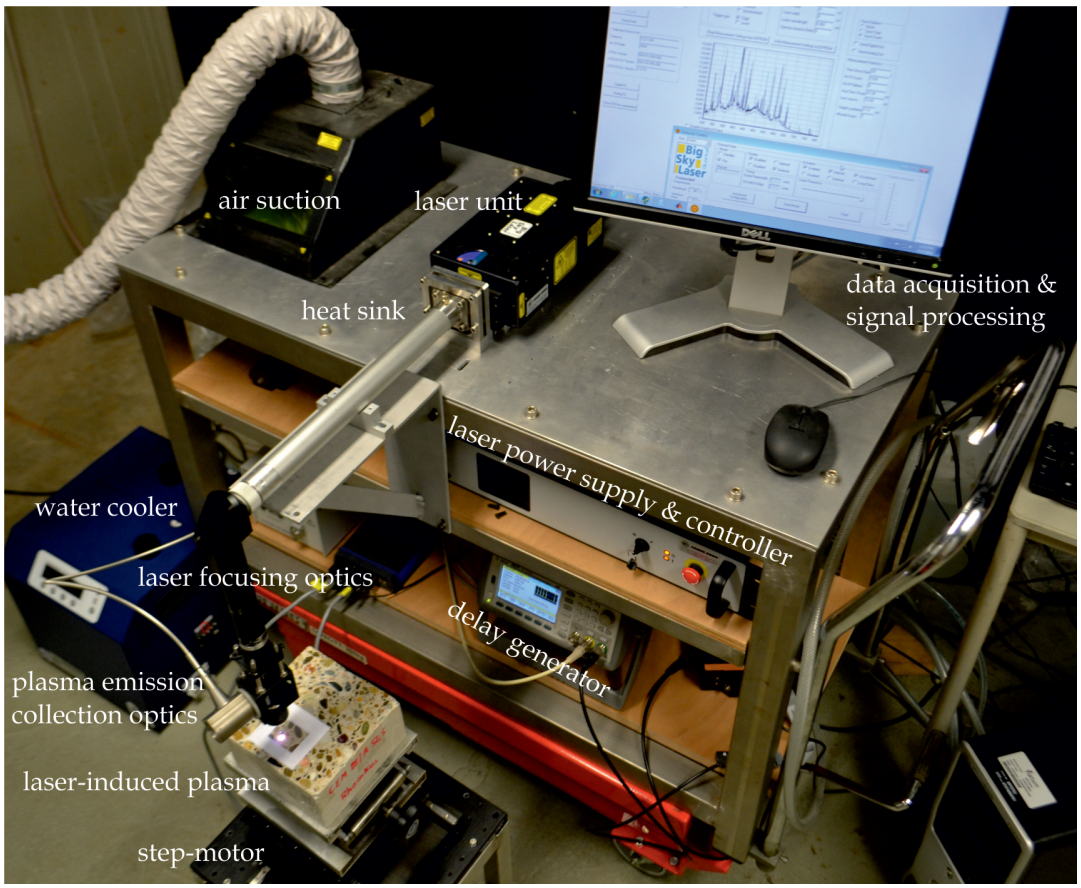


Figure 3.1: Hardware used in this work. Here, the laser-induced plasma is produced on a concrete cube.

3.1. ADAPTIVE OPTICS AND LIGHT COLLECTION FROM THE PLASMA PLUME

The optic fibres, focusing lenses, filters and reflecting mirrors used in an optic setup may impact the signal strength in various ways.

- Coupling of light in- and out of an optic fibre causes signal loss. First because of limited spatial aperture (20 degrees field of view from a cut fibre) the fibre only collects a

[1] The main results of this chapter have been published in [1]

part of the light that a plasma plume radiates in all directions. Second, because of the efficiency by which light couples from ambient air in and out of a glass fibre. The latter depends on the angle of coupling and wavelength of the incident light, resulting in multiple possible modes of propagation of the electromagnetic waves inside the fibre. Waveguide dispersion (geometrical wave confinement) and signal loss (for the short fibres in LIBS usually of much less importance) make multimode propagation even more complex. Fortunately, the acquired spectrum is essentially an accumulation of photons over time and the modes do not change the photon energy. However, the coupling efficiency depends on the mode and that does affect signal loss. Fibre coupling could be improved by connecting a small lens to the fibre end, but unfortunately lenses themselves limit the useful bandwidth.

- A filter is a layered material that reflects and absorbs certain ranges of wavelength in the incident spectrum much stronger than others, resulting in bandlimited transmitted light. Also the transmitted wavelengths are suppressed to some degree and delayed in phase.r.t. to the incident light, which has to be accounted for in case of light-coherent processing (not common in LIBS).

- Focusing lenses transmit light, which means aberration (distorted refraction and poor focusing due to geometrical imperfections) and chromatic aberration (refraction and focus dependent on wavelength due to material type and lens geometry) may affect optic performance. A parabolic mirror reflects to achieve focusing and therefore does not suffer from chromatic aberration like refracting lenses, though they may be affected by geometric aberration. Also, mirrors absorb and lenses reflect and absorb a small part of the light, which may be minimized by applying a reflective or transmitting coating, specified for the range of wavelengths used. In case of guiding and focusing the laser beam, lenses and mirrors should be able to withstand the high-power laser pulses used in LIBS.

- Industrial surroundings cause random vibrations that can modulate the path length between elements, the light modes inside an optic fibre, as well as the alignment of the coupled optic parts. The more parts are used, the more this can cause variations in the observed spectrum. The optic number of parts should be kept to a minimum

and be shielded from strong vibrations.

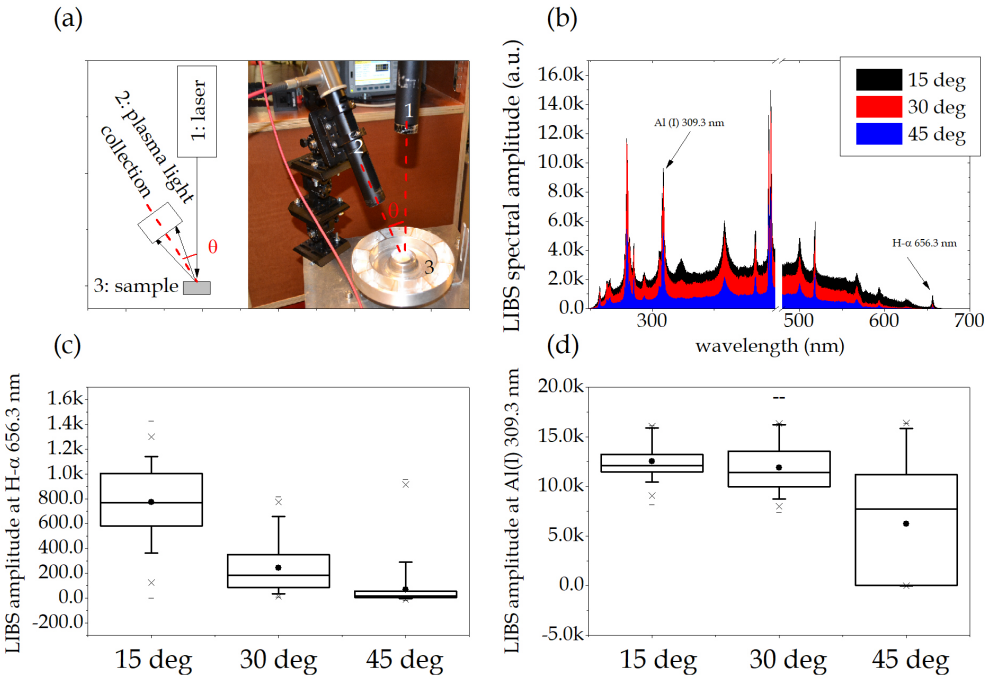


Figure 3.2: (a) Experimental setup for acquiring plasma emissions under θ wrt. the incident light angle. (b) LIBS raw spectra collected at three different tilt angles of plasma light collection optics. (c) Boxplot of $H(-\alpha)$ 656.3 (nm) emission line and (d) Al(I) 309.3 (nm) line. The upper and lower limits of the box indicate 25% and 75% percentiles, the horizontal line within the box marks the median value, the upper and lower crosses stand for the 99% and 1% percentiles, the top and bottom horizontal lines outside the box represent the maximum and minimum values, and a circle the mean value.

3.1.1. ANGLED LIGHT COLLECTION

To find out what the optimum plasma emission light collection angle is, we perform the following experiment shown in Fig. 3.2a, in which a laser pulse is focused (200 mm focusing lens) normal to a Al sample to generate plasma, and light collection optics is tilted under different angles using a mounted stage with adjustable angles wrt. the sample normal (incident laser direction). Emissions are collected using a 100 mm focal lens combined with a Al enhanced parabolic mirror to the spectrometer with 10μs integration time and 1μs delay time w.r.t. the laser pulse trigger. As shown in Fig. 3.2b, at 15° tilt angle, the LIBS raw spectrum is dominated by continuous background emission with slightly low signal-to-background ratio. This indicates that the incident laser energy is mainly absorbed by the top region of the plume where the electron density and plasma temperature are higher than the lower regions of the plume. Therefore, more air molecules

and atoms are excited and merged into the plasma. This effect is also observable in Fig. 3.2c, in which the $H(-\alpha)$ 656.3 (nm) emission amplitude and standard deviation decrease with tilt angle. Our main focus here is the target Al emission line Al(I) 309.3 (nm). It is noted in Fig. 3.2d that Al(I) 309.3 (nm) line has the largest amplitude and smallest standard deviation at 15° and, therefore the best signal-to-noise ratio.

For a tilt angle 0° we obtain the co-focal design shown in Fig. 3.3, which is convenient for optical alignment. Another important key performance indicator (KPI) is the optical observation depth, which is discussed in details further on.

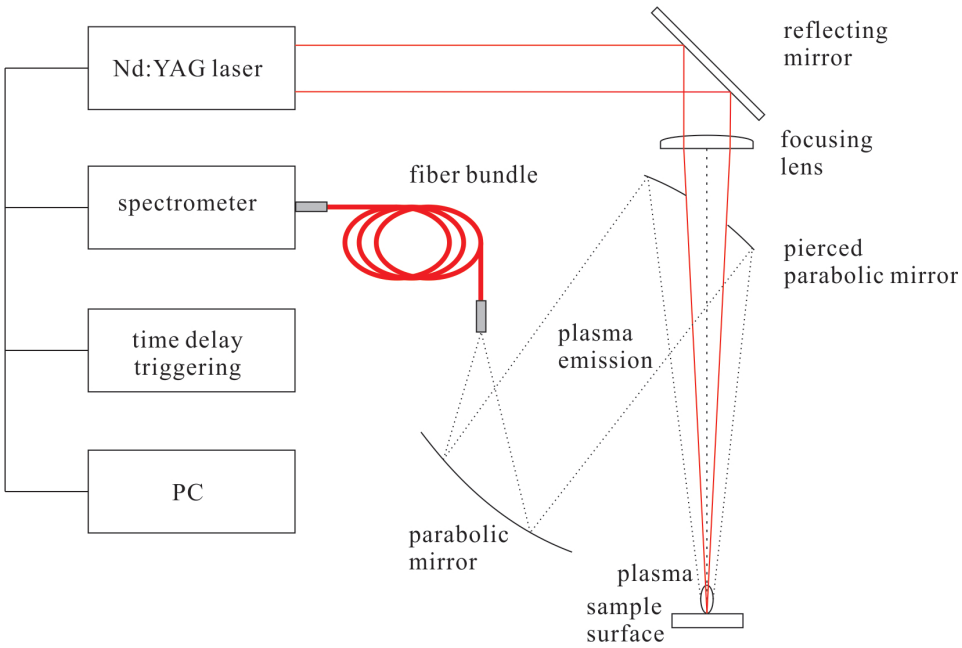


Figure 3.3: LIBS setup in which a pair of parabolic mirrors are used to focus the laser-induced plasma emission light onto the fibre bundle. The 1st parabolic mirror is pierced so the incident laser beam can pass through uninterrupted.

A laser-optical design serves to optimize and stabilize the collection of (selective) plasma emissions under variable environmental and material conditions, such as changes in air moisture, or sample size and shape. Two important variables are laser power and the numerical aperture (NA) of the optics for the purpose of laser focusing or plasma light collection:

$$NA = nsin(\theta) \sim n\theta, \text{ if } \theta \rightarrow 0 \tag{3.1}$$

where n is the refraction index of the medium where the optics (lens, mirror or filter) is and θ is the half-angle of the maximum cone of light that can either enter or exit. For a mirror

in open air, $n \approx 1$ and $sin(\theta) \approx D/2f_n$ if θ is sufficiently small. Here, D is the diameter illuminated by the incident light beam and f_n the focal length for a concave mirror as measured in open air. The laser beam distribution around the focus depends on the NA of the laser focusing optics and optimum positioning of the light collection optics. We first look at plasma emissions from a point of the plume and model the emitted light using classical ray theory.

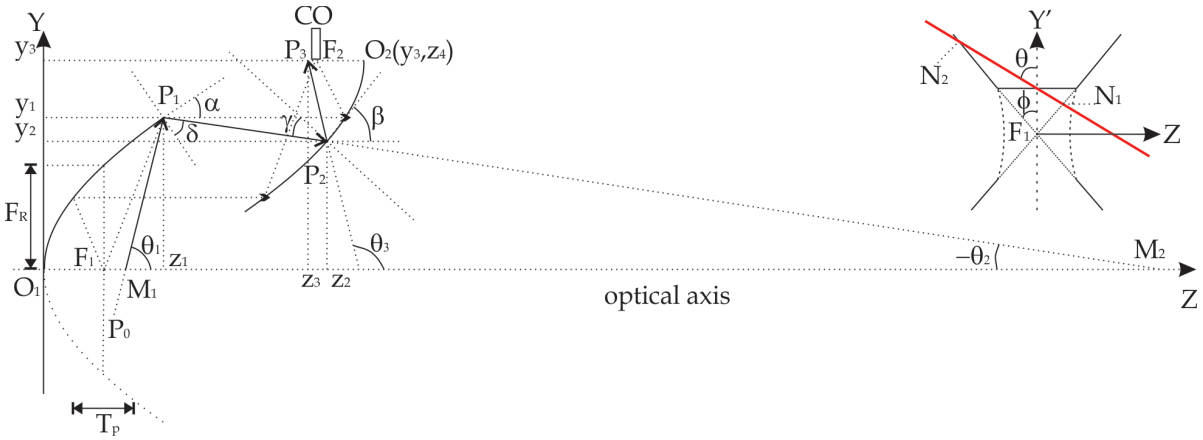


Figure 3.4: A pair of parabolic mirrors guides a ray of light from a point source at P_0 to P_3. The source lies in the focus of the 1st mirror, and the point of entrance of the collection optics (CO) lies in the focus of the 2nd mirror. Note that P_3 is not in the focus of 2nd mirror. Insert: a zoom-in of the region near F_1 where a finite light emitting flat surface (red line) is tilted under angle θ w.r.t. the local Y'-axis and partly falls within the focusing cone of the 1st parabolic mirror with angular range $\pm\phi$

3.1.2. RAY TRACING FOR PARABOLIC MIRRORS

We use ray tracing to gain insight into the light collection efficiency of the parabolic mirror pair shown in Fig. 3.4. For this purpose we need to define a focal length F_R and aperture T_P. These are defined at the points where the vertical ray hits the mirror and the angle between the points where the reflective coating starts and P_1. It is noted that there is no coating near the vertex. These points define the maximum solid angle of light collection according to:

$$d\Omega = 4\tan^{-1}(T_P/2F_R) \tag{3.2}$$

Assuming a uniformly emitting point light source, the ratio of the collected to the total emitted optical power is:

$$r_{op} = \tan^{-1}(T_P/2F_R)/\pi \tag{3.3}$$

If in Fig. 3.4 the plasma plume would be a point source in F_1 the rays within the solid angle will be collected in the focal point F_2 (i.e. in the CO). However, the plasma plume is a

few millimetre in diameter. To account for size we regard another point of the plume as a point source $P_0(y_0, z_0)$, which is chosen to the right and beneath $F_1(0, p_1)$. The arriving rays reflected from the 2nd mirror carry and deliver an energy distribution over the aperture of CO, determined by the NA of the optic fibre bundle. The incident ray path $\overline{P_0P_1}$ is inclined by θ_1 that is also the maximum angle of illuminance for the 1st mirror. The ray crosses the optical axis Z at M_1 and is reflected first at $P_1(y_1, z_1)$. It then follows the path $\overline{P_1P_2}$ and is reflected by the 2nd mirror at $P_2(y_2, z_2)$. Finally, the ray follows the path $\overline{P_2P_3}$ to arrive at $P_3(y_3, z_3)$, just to the left of the CO in the focal point $F_2(y_3, z_4 - p_2)$. The questions to be answered next are: what is the relation between the offset of the ray path $\overline{P_2P_3}$ w.r.t. the focal point F_1, and what is the deviation of the output ray path $\overline{P_2P_3}$ w.r.t. to F_2? Considering only the positive part, the 1st parabola may be described as:

$$y = f_1(z) = \sqrt{4p_1 z} \tag{3.4}$$

The factor $4p_1$ is part of the definition of the parabola. The path $\overline{P_0P_1}$ is described by:

$$y = (z - z_1)\tan\theta_1 + y_1, \quad (y_0 + y_1)/(z_1 - z_0) \leq \tan\theta_1 \leq \theta_{\min} \tag{3.5}$$

Here $\theta_{\min}$ is determined by the small non-coated area near the vertex. With the reflection angle δ, the inclination of the path $\overline{P_1P_2}$ w.r.t. Z-axis is determined by the relation and leads to an expression for the angle $-\theta_2$:

$$-\theta_2 = \theta_1 - 2\alpha \tag{3.6}$$

Here $\alpha = \tan^{-1}(f_1'(z_1))$. It is noted that angle θ_2 has a minus sign to give the reader a geometrical sense of direction, because the ray is traveling downwards w.r.t. the Z axis on path $\overline{P_1P_2}$. The latter path is the ray path to the second parabola, describe by:

$$y = (z - z_1)\tan(-\theta_2) + y_1, \quad \theta_{\min} \leq \tan(-\theta_1) \leq (y_0 + y_1)/(z_1 - z_0) \tag{3.7}$$

The ray travels in this example a distance $z_2 - z_1/\cos(-\theta_2)$ to arrive in P_2. Considering only the negative parts, the 2nd parabola is generally described by $4p_2(z_4 - z) = (y - y_3)^2$, and specified to the lower branch:

$$y = f_2(z) = -\sqrt{4p_2(z_4 - z)} + y_3, \; z \leq z_4 \tag{3.8}$$

The factor $4p_2$ is part of the definition of the parabola. Now the preceding process can be repeated. With a reflection angle γ, the output ray path $\overline{P_2P_3}$ makes an angle:

$$\theta_3 = -\theta_2 + 2\beta \tag{3.9}$$

Similar as for the first parabola, $\beta = \tan^{-1}(f_2'(z_3))$. The offset between P_3 and F_2 is:

$$F_2P_3 = z_3 - z_4 + p_2 \tag{3.10}$$

A numerical study on F_2P_3 for variations in both z_0 and y_0 is shown in Fig. 3.5. All values are negative, which means that P_3 always stays to the left of CO. With y_0 fixed, the absolute offset F_2P_3 increases almost linearly with z_0. Moreover, it proves the signal is much more sensitive to variations in depth z_0 than to the lateral position of the point source (e.g. plume) y_0. Apparently the configuration in Fig. 3.4 is more robust towards light sources which position varies in height (here along the Y-axis).

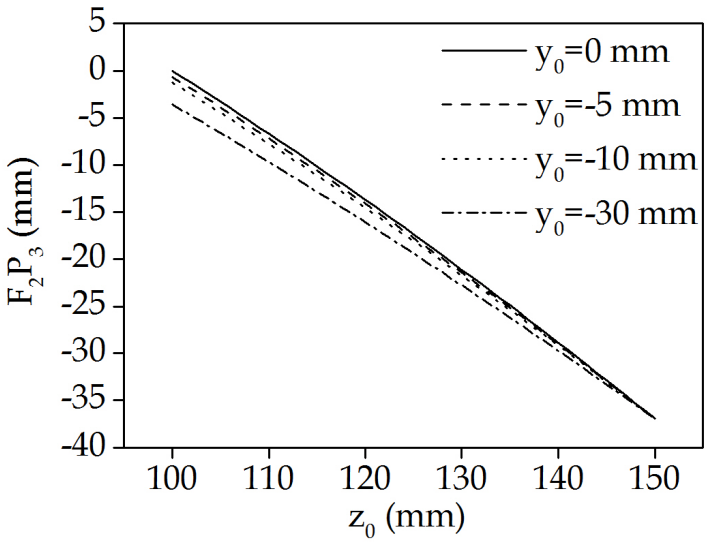


Figure 3.5: The departure F_2P_3 over z_0 and y_0. Minus means on the left side of CO.

In the preceding analysis we assumed the plume is a point light source, but a real plasma plume has a finite size. Mathematically, any light emitting surface may be thought of to consist of a distribution of point light sources. Thus, the total amount of light that can be collected from a finite source may be estimated by integrating over the part of the surface from which point sources are capable of emitting rays that can be guided by the parabolic mirrors to the light collection optics.

In a LIBS experiment the optimum focal point of the laser is just below the sample surface, which limits air-breakdown and promotes material ablation. The optimum focal point for light collection is less clear. Though a large aperture is clearly of advantage for a strong signal, it does not necessarily mean a strong signal-to-noise ratio of the peak ion-atomic emissions w.r.t. spectral continuous radiation and other background noise. There is some evidence in literature that there are two stages to which the optics have to be spatially adapted if all the ionic-atomic emissions from the plume are to be acquired. A few nanoseconds after the end of the pulse the plume is still very hot and radiates mainly continuous radiation bands (e.g. bremsstrahlung) and high energy photons from ion recombination. Though the plume is probably still optically thin for this radiation, it is almost quite certainly not for the evolving ionic-atomic emissions that will only dominate upon further cooling, say > 1 μs after the pulse. This means that for such an early stage of acquisition the collecting lens should be focused on the boundary of the plasma plume. At a later stage when the plume becomes optically thin (or at least much thinner) for the more dominant ionic-atomic emissions, the lens focus should lie inside the plume. Dynamic focusing is technically challenging because the plume still expands quite rapidly just after the laser pulse. As a compromise, a fixed focal point may be used to one side of the plasma plume in angled optic collection, or just on top of the plume given the size it has when data collection starts in the early stage. As the plume expands the focus will be emerged, as desired.

The insert in Fig. 3.4 shows the $Y' - Z$ plane where the local axis Y' is parallel to the global Y axis and runs through the focal point of the 1st parabolic mirror. Depicted is the realistic situation where the rays are not strictly focused at F_1 but, instead, meet around the Z-axis at different points to form a 3D envelope, called a caustic. In the insert of Fig. 3.4 the caustic is depicted by dashed curves in a cross section view to the left and right of F_1. To simplify the following analysis, all rays are assumed to meet exactly in F_1 under which conditions the parabolic mirror focusses within a cone with a half-angle ϕ. For a finite light emitting surface (the part which fits within the maximum optical focussing cone) at a distance a from the origin and for a focal length $f > a$ the collected optical power within the projected aperture at the origin is proportional to the area:

$$\pi\big((f-a)\tan\phi\big)^2 \tag{3.11}$$

As a next case, referring again to the insert in Fig. 3.4, we let a light emitting flat surface cross the cone through the focal point under an angle θ w.r.t. the Z-axis in the points N_1 and N_2 with (y', z) coordinates N_1 and N_2, where a is the distance along the Y' axis between the light emitting surface and the focal point. According to trigonometry, the light emitting length between points N_1 to N_2 within the cone is:

$$L = |N_1N_2| = \begin{cases} \infty, & 0 \le \theta < \phi \\ \frac{[f - a\tan\theta/(\tan\theta+\tan\phi)]}{\cos\theta}, & \phi \le \theta < \tan^{-1}(D/2/(f-a)) \\ \frac{2a\tan\phi\tan\theta\sec\theta}{\tan^2\theta-\tan^2\phi}, & \tan^{-1}(D/2/(f-a)) \le \theta < \pi/2 \end{cases} \tag{3.12}$$

where

$$N_1 = \left(\frac{a\tan\theta}{\tan\theta+\tan\phi}, -\frac{a\tan\theta\tan\phi}{\tan\theta+\tan\phi}\right)$$
$$N_2 = \left(\frac{a\tan\theta}{\tan\theta-\tan\phi}, \frac{a\tan\theta\tan\phi}{\tan\theta-\tan\phi}\right)$$

Here f is the focal length of the collection optics (e.g. a fibre bundle, lens, or mirror) and D is its maximum diameter that still fits inside the optical collection cone. The total collected light will scale linearly with L if each point light source on the emitting surface contributes the same amount of light inside the cone. The setup shown in Fig. 3.3 is designed to achieve the largest possible L by minimizing the angle ϕ and maximizing the Rayleigh length of the laser beam using a laser lens with a longer focal length.

The light emitting length L in eq. 3.12 is representative for the trends in more complex 3D plume shapes within the light collection cone. It is noted that it allows for the realistic case that the luminescence may vary over the light emitting surface by scaling the ray amplitude. The results of a numerical study are shown in Fig. 3.6. Figure 3.6a shows that L decreases quite rapidly for small angles θ, independent of the constant a. Figure 3.6b shows that L

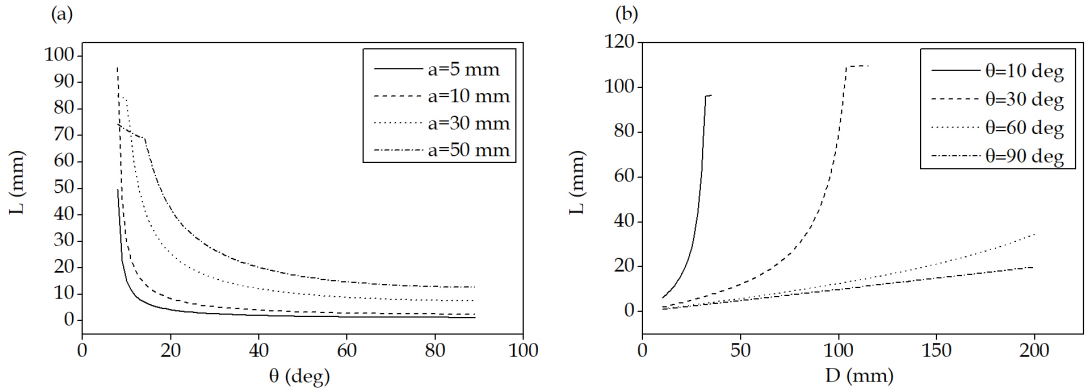


Figure 3.6: Calculations of the light emitting length L for $f = 100\ mm$ as function of θ (a) and D (b).

tends to increase with D, and quickest for $\theta < 45°$. In conclusion, to find the optimum parabolic setup that will guide the most rays from the plasma plume to the light collection optics the following steps should be taken.

1. Required input parameters: coordinates of a point of the plume $P_0(y_0, z_0)$, parabolic mirrors (p_1, F_{R_1}, T_{P_1}, $O_1(0,0)$, p_2, F_{R_2}, T_{P_2}, $O_2(y_3, z_4)$), boundary z_1 and geometrical parameters.

2. Reconstruct the ray path from the plume point to the 1st parabolic mirror.

3. Determine the reflection angle θ_2 using α.

4. Reconstruct the ray path $\overline{P_1P_2}$ to the 2nd mirror and calculate z_2 and θ_3 using γ.

5. Reconstruct the ray path $\overline{P_2P_3}$ to the collection optics (CO) and calculate z_3.

6. Determine if the arriving ray falls within the aperture of the CO (calculate the offset P_3F_2).

7. Scale the received light (energy) to the luminosity of the plume point.

8. Go to step 1 for the next point of the plasma plume, or go to 9 if ready

9. Calculate the total collected optical power by summation over all rays.

3.1.3. TESTING LIGHT COLLECTION FROM A PARABOLIC MIRROR

We test a light collection optics using the pierced parabolic mirror (cf. Fig. 3.3) shown in Fig. 3.7a. The objective is to increase the range of the observable LIBS emission line

Si (*I*) 251 nm of a Si wafer, which is very weak due to the low sensitivity of the spectrometer at the edge of the detectable range (cf. Fig. 3.8a). Fig. 3.7b shows that by moving the pierced parabolic mirror upwards approaching the focal point of the laser by a distance $L = 26\ mm$ the observable range decreases from about 30 mm to ca. 10 mm, while the maximum intensity increases from 160 to 600 photon counts. This demonstrates a basic idea to compensate for the varying sample surface-to-light collection optics distances in practical applications without having to resort to an expenstive auto-focusing unit.

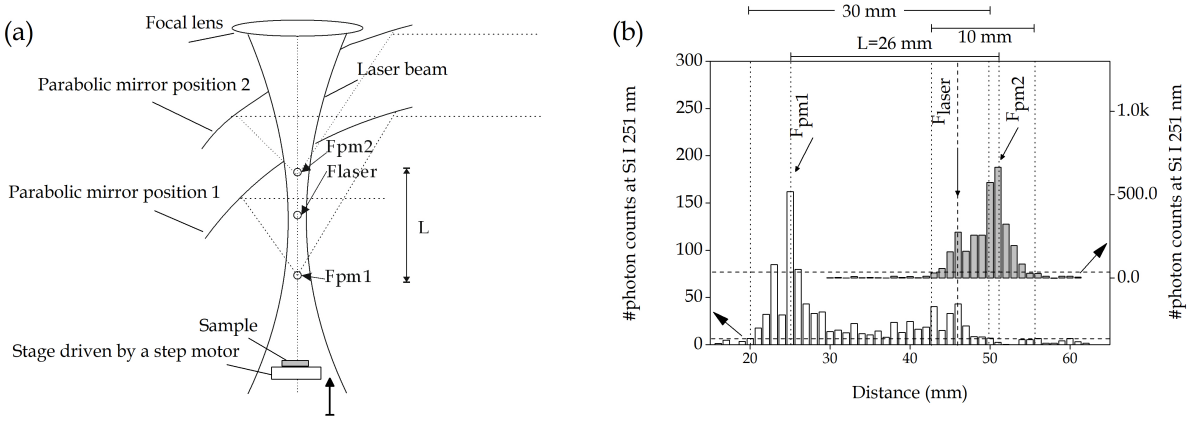


Figure 3.7: (a): A laser pulse focused by a lens with a focal point at F_{laser}. A pierced parabolic mirror was first mounted of which the focal point at the position F_{pm1} and then at F_{pm2}. The sample was moved by a step motor from below and out of the focus of the parabolic mirror to collect the laser-induced plasma emission light. The distance between the two focal points is *L*. (b): The LIBS photon counts at *Si* (*I*) 251 nm when moving the pierced parabolic mirror upwards approaching the F_{laser}. Every data point is the average of five single shots.

3.1.4. SPECTROMETER CALIBRATION

The integrated spectrometer with CCD detector is chosen in a compromise between resolution, sensitivity, wavelength range, noise and value for money. The entrance slit of 10 μm is a trade-off between resolution (0.3 nm) and achievable SNR. Figure 3.8a shows the spectral correction factor of the detector measured using a standardized deuterium lamp for the range 200 – 400 nm and a standardized halogen lamp for the range 350 – 900 nm after a warming up of 40 min when a thermal equilibrium of the lamp can be assumed. The light emission was collected by an optic assembly of 50 mm focal lens coupled with a parabolic mirror to a fibre bundle and finally to the spectrograph. For model-based quantitative analysis (cf. chapter 5), the raw spectrum is first multiplied with this calibration curve. It is noted that our CCD detector is enhanced in the visible range which leaves the sensitivity

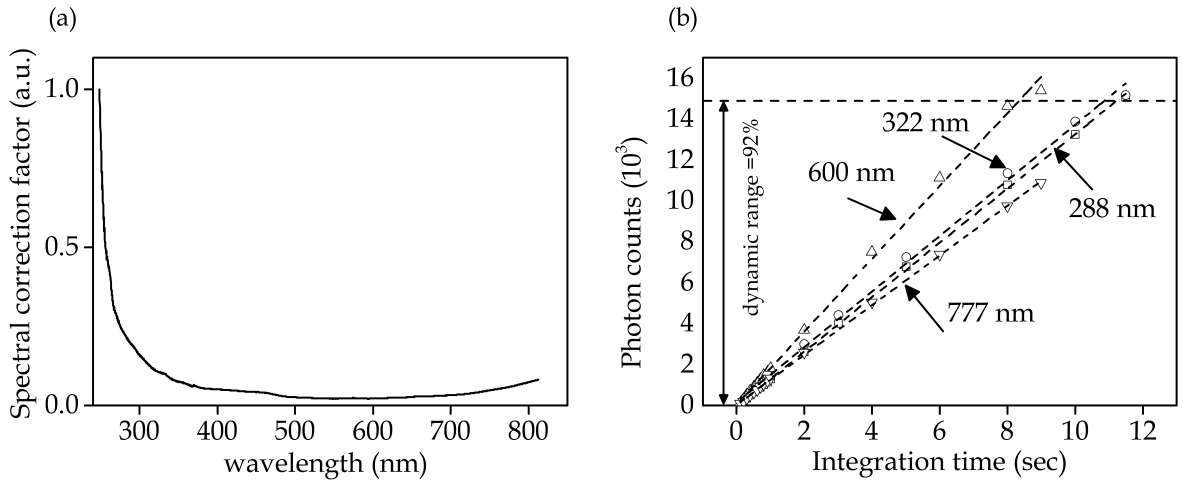


Figure 3.8: (a) Spectral correction factor of CCD normalized to it maximum. (b) Linearity of the CCD.

at UV and NIR relatively lower. Fig. 3.8b shows the linearity with integration time of the CCD detector at four representative wavelengths. The dynamic range (i.e. maximum linear range) is 92% (14-bit gives maximum 16383 photon counts) with a noise level of 30 photon counts (3σ).

3.2. SYNCHRONIZATION OF LASER PULSE AND ACQUISITION WINDOW

The spectrograph used throughout this work delivers the best linear response in the so-called pre-scan mode. This means that the data of the first scan is always discarded to remove the electrical charges from the CCD that remain from previous scans. This slightly complicates the triggering procedure. First because the spectrograph must now be triggered before the laser fires, so the start of the recorded scan coincides with the start of the desired time window of integration. Second, two delays occur between the TTL level trigger to the laser diode and the actual laser Q-switch output. The first delay is needed to pump the laser to the desired population inversion, and the second internal delay is needed to complete the Q-switch action. These initially unknown delays are determined by recording the trigger and by optic-electronic sampling of the laser pulse using a polarizing beam splitter (VBA05-1064, Thorlabs) connected with 1064 nm laser line filter (FL1064-10, Thorlabs) and a fast-response photodiode (DET025AFC/M, Thorlabs). The time between the laser trigger and opening trigger of the Q-switch was 177 μs and the Q-switch delay time to optic output 62 ns. The triggering and synchronization of laser and spectrograph

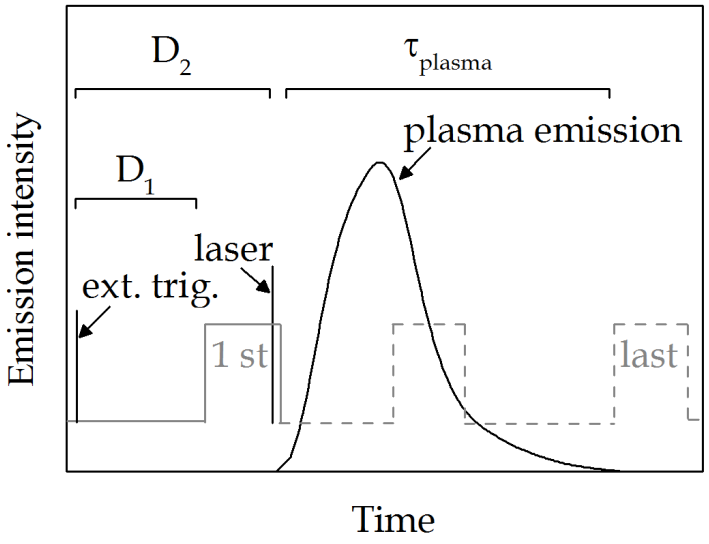


Figure 3.9: Timing of the ion-atomic emission spectrum.

was performed by an external dual-signal generator. For common LIBS applications the optimum start of the time window of integration is in the range $0.1 - 10\ \mu s$ after firing the laser. Time-resolved averaged data are obtained by varying the start of the time window (D_1 in Fig. 3.9) from 0 to 40 μs while using a fixed pre-scan delay ($D_2 = 3.54\ ms$ in Fig. 3.9). The duration of the time window is set to the spectrograph minimum allowable value of 10 μs.

The development of the plasma emissions is much faster than this 10 μs integration time. Instead, we investigate the decay of plasma emissions that is much slower. By continuously shifting the start of the time window the observable LIBS lifespan τ_{obs} can be determined. It is defined as:

$$\tau_{obs} = \tau_{gate} + \tau_{plasma} \tag{3.13}$$

where τ_{gate} is the time window and τ_{plasma} is the plasma decay time down to the moment when the signal intensity has dropped to e^{-1}. An average spectral intensity is defined as a function of the stepped delay time $t_d = m\Delta t$, $m = 1, 2, 3...$, as:

$$I_{avg}(t_d) = \frac{1}{N}\sum_{n=1}^{N} I(\lambda_n, t_d) \tag{3.14}$$

Here $I(\lambda_n, t_d)$ is the photon count accumulated during the integration time of a selected

emission line at wavelength λ_n $[nm]$, and t_d is the stepped delay time that is to be optimised for the emissions of the corresponding element and N is the total number of wavelengths taken into account.

Assuming a normal exponential decay of the spectrum radiated by the plasma plume and according to Beer's law, the above average spectral intensity may be curve-fitted after eliminating the offset intensity for $t > t_0$:

$$I(\lambda_n, t) = \varepsilon^{eff}(\lambda_n) \cdot I^{plume}(\lambda_n) \cdot e^{-(t-t_0)/\tau_n} \tag{3.15}$$

Here ε^{eff} is the effective emissivity, $I^{plume}(\lambda_n)$ is the emission intensity at the wavelength λ_n from the plasma plume, and reference time t_0 is the moment when the emissions are at maximum. The detected peak amplitude $I(\lambda_n, t_0)$ for each emission line (or excited species) occurs after the compromise time delay $t = t_0$, at which stage the plume is hottest and the most species are excited. Note that we assume LTE for which all emissions decay with a singular plasma temperature and therefore with time. The plume intensity in Eq. 3.15 depends on the plasma temperature, on the probability of the energy transition, and is proportional to the number of elements that can give rise to this emission. The effective emissivity depends on the wavelength as it accounts for self-absorption in the plume (possibly indicating a deviation from LTE), and is therefore linked to the concentration of the corresponding element in the plume. It is most likely also linked to radiation directionality of the plume due to its shape and temperature zones. The relaxation time for an emission depends on to the rate of cooling of the plasma and on the rate of decreasing probability that the element can be excited again to the corresponding species.

Eq. 3.15 shows that each emission line should ideally be integrated during approximately $3\tau_n$. This is why one would ideally like to set a wavelength dependent integration time and delay time, which unfortunately is not possible with the present generation spectrometers. It also shows that with time certain energy transitions become less probable and finally vanish. As long as the number of available energy states does not decrease too much within the window of integration one may still assume LTE (cf. 2.1.1). The maximum allowable window is linked to the species relaxation factors (cf. Chap. 3) and thus to

Table 3.1: Fitting results using eq.3.15 for selected materials.

	Si	W	Al	Ca	Zn	CEM	PVC	DC
$t_0[\mu s]$	10.51	10.39	10.51	10.55	10.10	10.46	10.38	10.54
$\tau_{plasma}[\mu s]$	2.12	2.33	2.35	2.50	2.78	2.93	3.21	3.67

how quickly emissions decay. A possible approach is to employ multiple time windows to ensure LTE in each, and calculating the temperature in each case. The downside is that the SNR will be smaller in each time window as fewer photons are integrated.

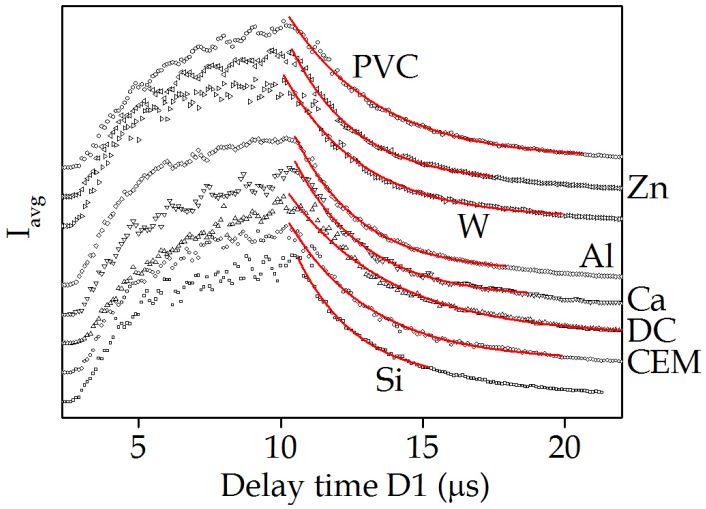


Figure 3.10: Plasma decay times for selected materials. Each data point is the average of ten shots.

In our spectrometer, one fixed integration time window is allowed for each LIBS measurement and it has a minimum setting of 10 μs. Therefore, we adopted Eq. 3.15 for the average emission intensity over the whole spectrum per material with an average decay time. Fig. 3.10 shows data points and fitted curves of metals and minerals and Tab. 3.1 shows the corresponding fitted parameters (CEM=cement, DC=demolition concrete). It is observed that minerals and plastics have longer decay times which may be caused by other elemental/molecular emissions.

3.3. CHARACTERIZATION OF THE LASER BEAM

3.3.1. LASER BEAM PROFILE

An accurate description of the laser beam is important for the interpretation of LIBS data and paramount in case of quantitative goals such as measuring the breakdown threshold of a material. Main parameters are the spatial distribution in free air, the temporal signature,

pulse energy and angle of incidence. The angle and free air spatial distribution strongly influence the power density and fluence levels at the sample, whereas the temporal distribution strongly influences the processes of ablation and plasma plume formation as described in chapter 2. During ablation, the heat distribution and effective heat transfer

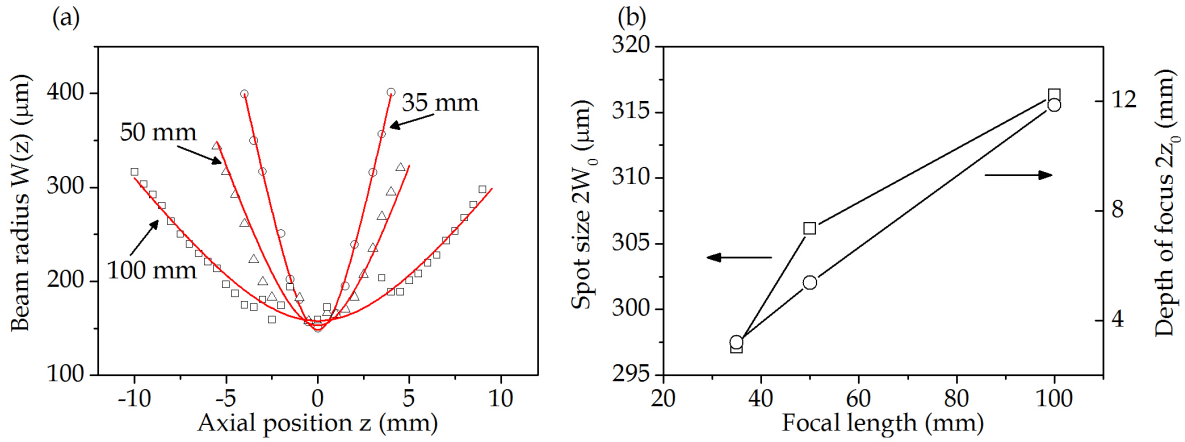


Figure 3.11: Maximum heat affected zone using burn paper for three focal lengths. (a) Beam waist radius in axial direction; (b) hole size (squares) and depth of focus (circles).

from the laser beam to the sample cannot be fully described using only the laser beam and linear absorption and reflection factors at the solid surface. This is because the hot plasma effectively poses very different interface conditions which are difficult to quantify. Unfortunately, due to the highly transient nature of the experiment ($< 10\ ns$) it was not possible in our laboratory to measure or predict accurately the effective heat zone for the range of targeted materials. Instead, as an estimate, we determine the maximum hole diameter using burn paper of 0.5 mm thickness, which has a lower breakdown threshold than any of the targeted materials. The beam profile is matched to the resulting diameter of the hole for different distances between the paper surface and the laser focus. Three focal lengths are tested and the resulting holes are analyzed using microscopy image analysis. Fig. 3.11 shows the measured maximum beam waist, hole size and depth of focus.

We compare these results with the Gaussian beam model according to [2]:

$$W(z) = W_0\sqrt{1+(z/z_0)^2} \tag{3.16}$$

W_0 is the beam waist radius, the spot diameter is $2W_0$, z_0 is the Rayleigh length, the depth of focus is $2z_0$ and the beam divergence is $\theta = W_0/z_0$. W_0 and z_0 are fitted to burn paper

data in Fig. 3.11a. Close to the focus the beam profile is strongly curved, while further away eq. 3.16 reduces to $W(z) = W_0 z/z_0$, which is known as the far-field of the laser showing the familiar plane wave profile. The minimum diffraction limited spot size d_{min} for a plane from circular multimode beam is calculated as [3]:

$$d_{\text{min}} = 0.64 \times M^2 \lambda / NA \tag{3.17}$$

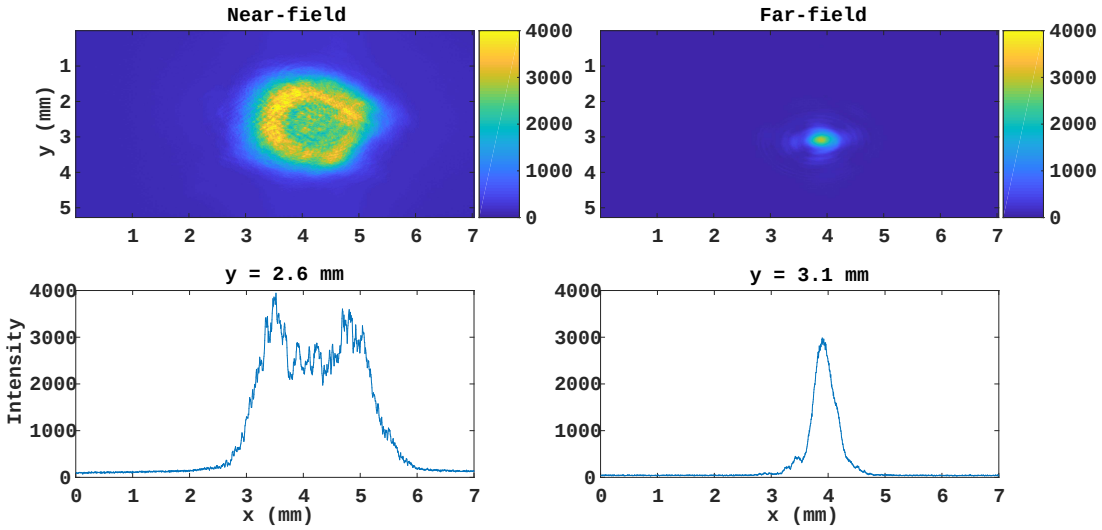


Figure 3.12: Near- and far-field laser beam profiles of our ns-laser.

M^2 is the beam quality factor, which parameter allows a multimode laser beam to be compared to the Gaussian laser beam and NA is the numerical aperture of the focusing optics. Eq. 3.17 predicts 292.6, 146.3, and 102.4 μm for the 100 mm, 50 mm and 35 mm lens, respectively. For the 100 mm lens, the formula predicts a slightly smaller spot size than observed in the experiment, while for the 35 mm and 50 mm lenses it predicts a much smaller spot size. Probable causes are radiation from the beam focus and combustion of the calorific paper.

Even though burning paper proved not a good comparison for concrete materials, the equations 3.16 and 3.17 can be used reliably to predict the beam width.

When a laser beam propagates in free air, the intensity is dominated by a diffraction pattern. The near field intensity distribution is described by Fresnel diffraction and the far-field by Fraunhoffer diffraction. The boundary between these is estimated by the

so-called Fresnel number:

$$N_F = r_a^2/(\lambda d) \tag{3.18}$$

Here r_a is the aperture radius and d is the distance of the observation plane to the aperture. N_F determines the boundary between the near ($N_F > 1$) and far field ($N_F < 1$). For a white light source the near field is characterized by a high curvature wave front but for a laser source it is associated with complex interference patterns. The corresponding far field for white light is a low curvature wave front and for the laser case it is a wave field decaying with distance as the wave energy spreads in space. Fig. 3.12 shows the near- (left) and far-field (right) laser output multimode laser beam intensity profiles measured by a camera beam profiler. The former was measured by 1 : 1 imaging using a 1 m focal-length lens at the laser output aperture. The diffraction pattern is a perfect shadow of the laser output aperture where a characteristic top-hat multimode distribution is present ($N_F > 1$, Fresnel diffraction). The latter was measured at 2 m from the laser output aperture where Fraunhofer diffraction ($N_F < 1$) dominates.

3.3.2. 1064 NM LASER LIGHT DISSIPATION

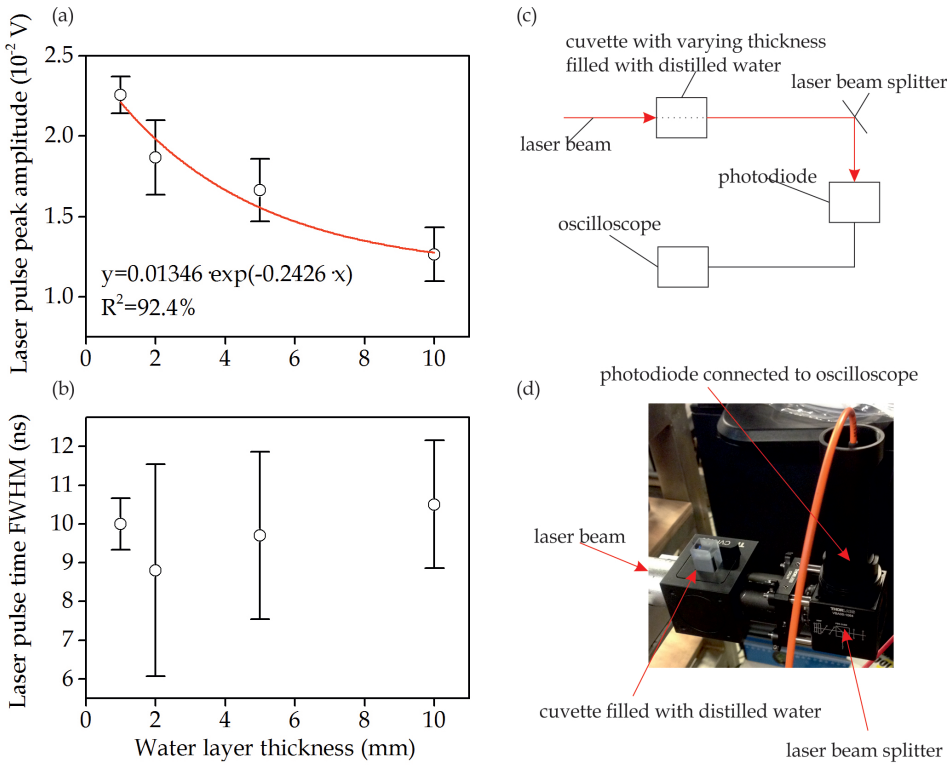


Figure 3.13: Laser pulse dissipation in distilled water. (a) Laser pulse intensity fitted by an exponential function; (b) laser pulse FWHM over 10-single-shots. (c) Schematic and (d) experimental setup for the measurement.

For many practical applications the target materials are wet or moist, and water affects the LIBS measurement. In particular, the dissipation at 1064 nm is mainly caused by the absorption from $-OH$ molecular bonds. Here we investigate the dissipation of the unfocused laser light pulse through distilled water. As shown in Fig. 3.13c and d, we detect the intensity of the residual laser pulse that passes through a glass cuvette filled with distilled water with varying thickness ($1 \sim 10$ mm) using a photodiode connected to an oscilloscope. Ignoring nonlinear effects of water such as self-focusing, the absorption coefficient of the laser energy in distilled water is 0.24 mm^{-1} and the average laser intensity dissipation rate is ca. -5% mm^{-1} (cf. Fig. 3.13a) over 10 single-shots with $\pm 10\%$ RSTD for the intensity and with 10 $ns \pm 19\%$ (RSTD) for the temporal FWHM (cf. Fig. 3.13b). This indicates that a laser pulse ($11-12$ mJ) will be completely absorbed after traveling through a water layer of thickness larger than 20 mm. This is much more than the water layer on wet saturated concrete aggregates, which is less than 50 μm. Furthermore, the effect of a thin water layer near the focal plane of a focused laser pulse is different, as the breakdown takes place at the interface of the air and water layer. This effect on the recorded plasma emission spectra is investigated in the following section.

3.4. OPEN AIR SHOT STABILITY AND DATA QUALITY

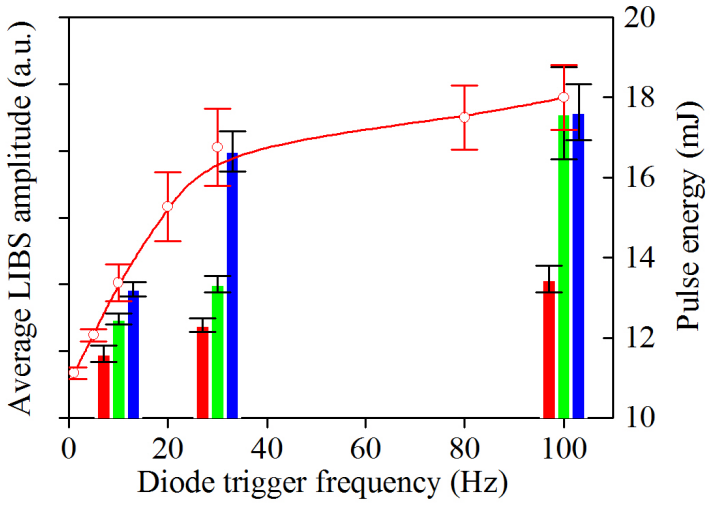


Figure 3.14: Pulse energy (red curve) versus diode trigger frequency (shot rate), and related average intensity for plastic (red), glass (green) and gravel (blue). Error bars comply with 1 STD for a total of 100 laser shots.

We first investigate the influences of shot to shot laser energy variations. The output laser energy varies depending on the shot rate, which in turn is determined by the optical

oscillator, laser cavity working temperature and diode pumping efficiency. In Fig. 3.14 the laser energy curve is compared with the average intensity for different diode trigger frequencies (shots per second) on plastic (polypropylene), glass and gravel. The laser efficiency apparently improves with shot rate because the energy increases per shot. The signal strength ratios for the different materials vary slightly with the exception of glass. Glass ablates best at the highest shot rate and thus highest energy output as a result of its transparency and dependence of breakdown on multi-photon absorption. The magnitude of the error bars for laser energy and signal amplitude indicate by good approximation a material independent, constant relative STD.

Next we investigate the influences of air absorption and surface moisture on the data quality in terms of the emission line abundance. The abundance is the number of detectable emission lines in a spectrum that is related to either the target material or to air breakdown. This also classifies the undesired air emission lines w.r.t. to the targeted materials. To this end, a thousand spectra in air (i.e. incl. dust and other fine particles and without target material) were recorded and all emission lines that occur in more than 500 of them are identified as air emission lines. Fig. 3.15a shows the abundance of the spectra in terms of the numbers of identified material and air emission lines using three focusing lenses with the laser shot rate at 1 Hz (11 $mJ/shot$). With increasing focal length the abundance decreases while the air emissions remain relatively constant. The decrease in abundance is due to the increase in Rayleigh length (cf. Fig. 3.11) by which the power density of the laser beam and temperature of the plasma decreases. The observation that the air emissions remain relatively at the same level can only be explained from the fact that the hot focal zone expels air molecules. This implies that air emissions originate mainly from the boundary of the focal zone. If we assume for simplicity that the focal zone is spherical, a doubling of the focal length triples the focal volume and, assumedly, the ablated mass and emissions. However, the boundary of the focal zone only doubles and so do the air emissions. This explains why the abundance improves with respect to the level of air emissions if the focal length increases. A large focal length is obtained using a lens with larger focal distance. Therefore, if the laser lens also serves to collect the plasma light, the collection aperture decreases with increasing focal length and with it the SNR

of the detected emissions. On the other hand, a longer Rayleigh length facilitates a larger LIBS observation depth for rough surfaces. The focal lens should therefore be determined in a compromise between focal length and desired spectral abundance. Apparently the air breakdown happens just as easy with all three lenses because their level remains practically constant. This implies that the laser power density and fluence is high enough in each case to cause air breakdown. To compare the spectrum quality for wet and dry materials we use one thousand particles of each. Each material is put in a bucket and first well shaken before it is moved though the laser beam while LIBS spectra are acquired. In this fashion many particles are sampled. After elimination of the miss-shots a total of 5000 useful spectra are acquired for both dry and moist materials. For signal robustness and good statistics, the 100 mm lens is used to provide a laser fluence of 102 J/cm^2. The

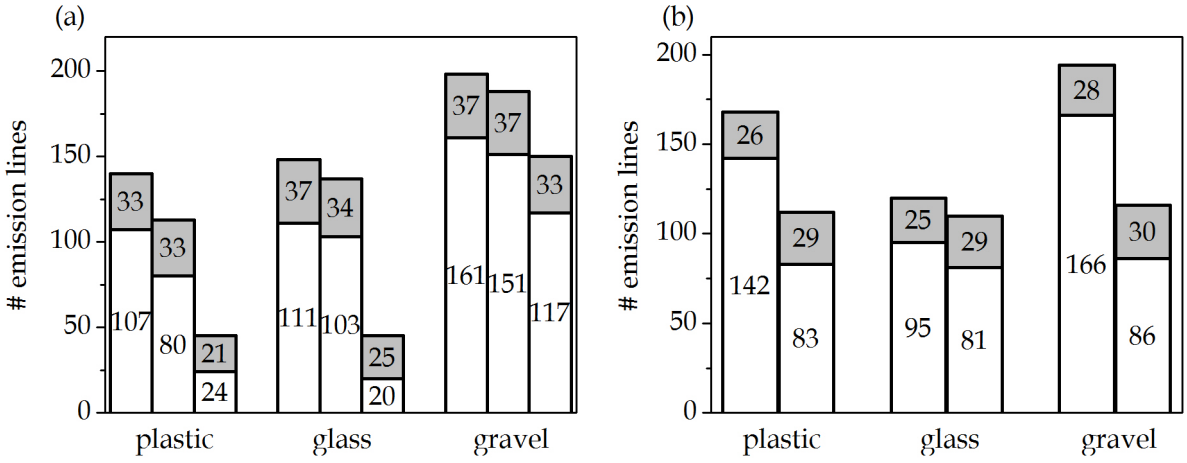


Figure 3.15: Emission line count for plastic, glass and gravel (white bars) and air (grey bar tops). (a) Shot rate 1 Hz, material groups left to right: 35 mm, 50 mm, 100 mm focal lens. (b) Shot rate 100 Hz (18 $mJ/shot$), 100 mm lens; material groups left to right: dry and moist surfaces.

spectral abundance for air and the selected materials for dry and moist surfaces are shown in Fig. 3.15b. Compared to the corresponding case for the 100 mm focal lens in Fig. 3.15a, considerably more emission lines are present for all materials due to the higher laser energy. The abundance for air remained practically the same as for the lower laser energy setting, showing that higher laser energy settings are favourable. The abundance is lower in the presence of surface moisture, which may be attributed to a partial absorption or reflection of the laser energy. But more importantly, the moisture does not prevent the acquisition of good quality spectra. It is noted that the amount of moisture, its physical distribution (a water layer or just droplets) and water absorbing capability of a material

surface has significant influence, and depends on parameters such as wettability, porosity and permeability.

3.5. LIBS OBSERVATION DEPTH AND LASER ANGLE

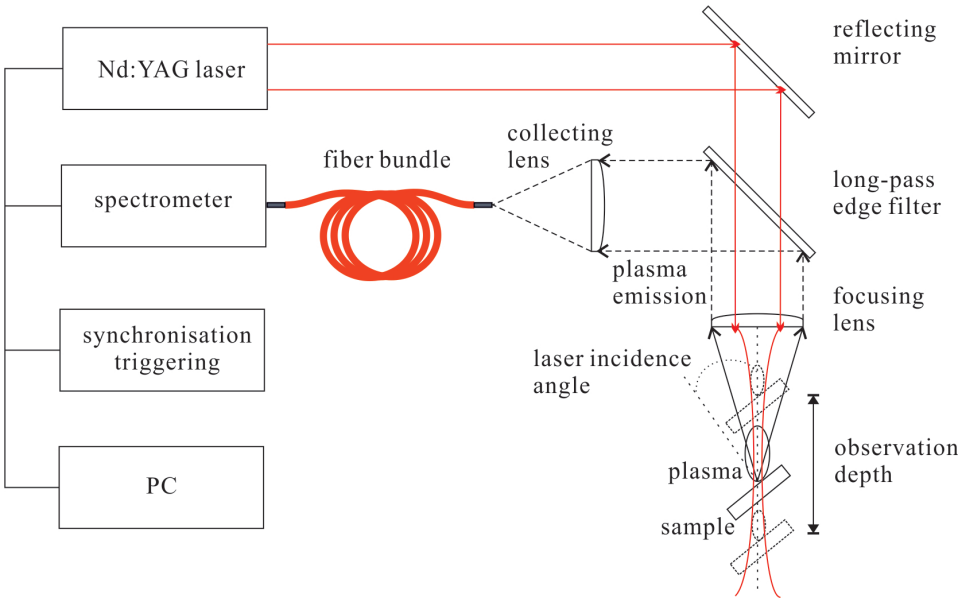


Figure 3.16: The LIBS setup with fixed collection optics and sample is moved up- / downwards in small steps.

The breakdown threshold of a material may in principle be determined by increasing the laser power and observe when non-linear effects set in, such as ablation and spectral emissions. To that end, we determine at which distance from the focus the emissions show up or vanish. Figure 3.16 depicts the methodology. The laser and the light collection optics are fixed while the sample is moved upwards into and through the focal region of the laser beam. The maximum distance over which the emissions remain detectable is called the observation depth (OD). It will be shown in this section that the OD is also closely linked to the ablated mass and the strength of the observable LIBS emission spectrum.

In the setup, the laser beam is focused behind a long pass edge filter (800 nm cut-off) that is transparent to 1064nm laser light. The incoming plasma emissions are guided anti-parallel to the laser path and reflected sideways by the long pass filter. A second plano-convex lens is placed behind this filter to focus the incoming light on the entrance of a bundle of optical fibres. This angled optical setup is robust against spatial variations in plasma plume size and position, and is also less affected by possible obscuring of the

plume by airborne particles. The window of integration is set to 1 ms and the limit of detection is set to 15 dB above the noise level. Samples were mounted on a 2D motorized stage, which height varied in steps of 0.5 mm. The OD is listed in Tab. 3.3 for plastic, glass and gravel, and is measured with three different lenses. The air influence is noticeable in N and H lines of the plastic, creating on average a larger OD than for the carbon emissions. For glass and gravel the OD for air is comparable with that for the target materials. Outside the OD range the air spectra dominate and seriously degrade the quality of the spectrum. It is therefore paramount to stay within the OD as determined by the material. It proved that more abundant spectra can be acquired with 35 mm and 50 mm lenses, but at the disadvantage that the OD becomes smaller and less controllable. All subsequent tests were therefore conducted with the 100 mm lens.

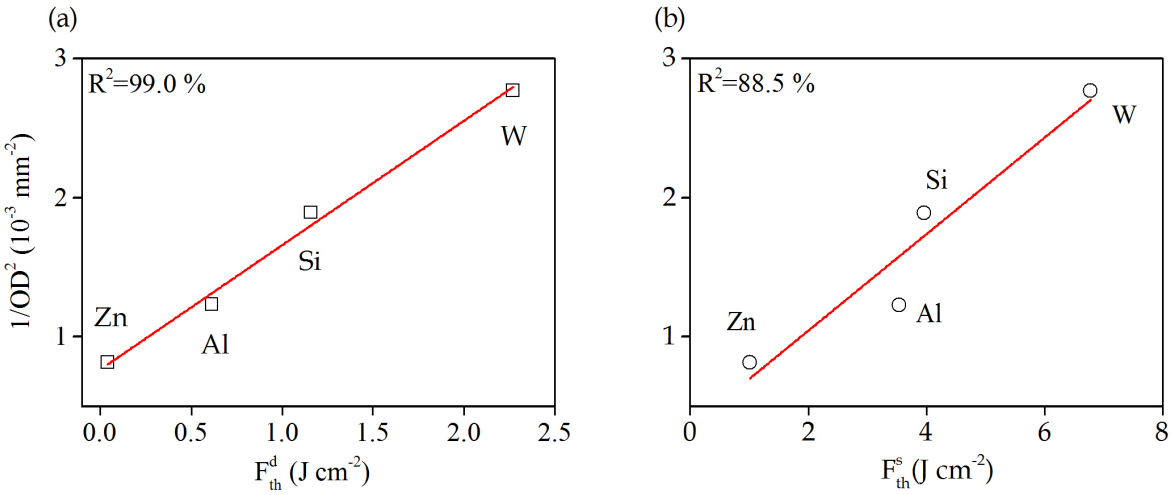


Figure 3.17: Relation between the measured OD and the calculated melting damage threshold fluence F^d_{th} (a) and the sublimation threshold fluence F^s_{th} (b) for pure materials.

Next we relate the measured OD to the fluence breakdown thresholds for solid-liquid and solid-vapor calculated in equations 2.13 and 2.19, respectively. As a first trial test we use perfectly flat samples of pure metal to validate the assumed linear relation between the thresholds and the OD for metals. When validated, it will offer a robust method to also determine the threshold for mineral and other waste materials. To that end, the OD directly provides the required estimation for the area of the laser beam where breakdown starts to occur, based on the Gaussian beam approximation in eq. 3.16, so that the breakdown fluence may be calculated.

Using the LIBS setup with fixed laser focus and collection optics shown in Fig. 3.16, the sample surface is moved up- / downwards in small steps from below the laser focus into the focus to determine the OD, and related fluence. Figure 3.17a shows the data points for OD^{-2} against the calculated melting threshold fluence F_{th}^{d} (cf. eq. 2.13) in a linear fit with $R^2 = 99.0\%$. Fig. 3.17b shows the data points for the calculated sublimation threshold fluence F_{th}^{s} (cf. eq. 2.19) in a linear fit with $R^2 = 88.5\%$. The additional thermodynamic parameters used in these calculations are listed in Tab 2.1. The laser fluence is 14 J/cm^2, which means that sublimation of these metals takes 25% (Al), 28% (Si), 48% (W), and 7% (Zn) of the total applied laser fluence. From these figures it may be concluded there is a satisfactory linear relation between OD^{-2} and both types of threshold for metals.

Table 3.2: Dependence of observation depths (OD in mm) on the laser incident angle (LIA). Shown are the OD for selected emission lines from Al, Si, W and Zn samples and for air breakdown emission lines of N, H and O.

LIA (°)	Target material emission lines			Air emission lines		
	Al (309 nm)	Al (394 nm)		N (567 nm)	H (656 nm)	O (777 nm)
0	26.5	28.5		22.5	16.5	17
15	26.5	28		22.5	17	17
30	26	27		22	16.5	16
45	24	26		20.5	15.5	15
60	21.5	23		18	13	14
	Si (288 nm)	Si (385 nm)	Si (390 nm)	N (567 nm)	H (656 nm)	O (777 nm)
0	17	22.5	23	19	11.5	15
15	18.5	22	22	18.5	11	15
30	17	21	21	18	9.5	14
45	16	21	21.5	17.5	10	14
60	12	19	19	16.5	8	13
	W (357 nm)	W (400.7 nm)		N (567 nm)	H (656 nm)	O (777 nm)
0	18	19		17	14	14
15	17.5	18.5		16	14.5	14
30	17.5	19		17	14	14
45	16.5	17		15.5	13	14.5
60	14.5	15		14.5	11.5	12.5
	Zn (328 nm)	Zn (467.8 nm)	Zn (636 nm)	N (567 nm)	H (656 nm)	O (777 nm)
0	33.5	35	32.5	22.5	19	19
15	33.5	34.5	32.5	22	19	18
30	32.5	34	32	21.5	19.5	18
45	32.5	33.5	31	21.5	19	18.5
60	30	30.5	29	20	18	18

We further investigate the breakdown threshold of these four metals by varying the laser incident angle (LIA) in Tab. 3.2. Most emission lines of both target materials and air prove little sensitive to the LIA (0-45 °) and OD for air emission lines is similar to that of target materials which is is favorable for practical applications. Air emission lines might be used as normalization references for emission lines of target materials to compensate for shot-to-shot variations caused by LIA. More favourable, Tab. 3.2 shows that the linear

relation between the breakdown thresholds and the OD^{-2} persists in case of varying LIA.

Next we calculate the breakdown threshold of plastic, glass and gravel based directly on the measured OD as an estimate for the area of the laser beam where breakdown starts to occur. We use the OD in Tab. 3.3 for the 100 mm lens. After substituting these OD values for z in eq. 3.16, the breakdown threshold fluences calculated are 10.3 (polypropylene plastic), 8.61 (glass) and 6.64 J/cm^2 (gravel).

Table 3.3: Average observation depths (OD) in mm for selected emission lines from plastic, glass, gravel and air breakdown using a 35, 50 and 100 mm lens.

target	air	Emission line [nm]	Lens (different focal length)		
			35 mm	50 mm	100 mm
plastic		386, 387, 388 (CN), 516 (C_2)	2.8	3.5	5.3
	N	463, 500, 504, 568 (N II)	3.5	3.8	7.8
	H_20	656 ($H\alpha$)	3.5	4.0	6.5
	O	777 (O I)	2.0	2.5	-
glass		279 (Mg II), 393 & 397 (Ca I), 589 (Na I)	3.0	3.8	7.8
	N	463, 500, 504, 568 (N II)	3.3	4.5	6.0
	H_20	656 ($H\alpha$)	3.0	4.0	-
	O	777 (O I)	3.0	3.5	0.5
gravel		279 (Mg II), 288 &385 & 390 (Si I), 634 (Si II), 393 & 397 & 422 & 445 & 616 & 644 & 646 (Ca I), 309 (Al I), 455 & 493 (Ba II)	4.3	4.5	12.0
	N	463, 500, 504, 568 (N II)	4.3	5.5	13.0
	H_20	656 ($H\alpha$)	4.0	5.5	5.5
	O	777 (O I)	4.0	6.0	9.5

A further investigation of the effects of LIA is done by inspecting the signal strengths in Fig. 3.18a-c, showing the strength of selected emission lines within the OD relative to the average spectrum I_{avg}. In all cases the continuous background is subtracted first. Because the emission lines are quite strong the amplitudes in Fig. 3.18 were scaled down by a factor 15 (CN 388 nm), 35 (Na 589 nm), 4 (Mg 279 nm) and 10 (Al 309 nm). The LIA ranged from 0° (straight incidence) to 60°. For each LIA the signal starts and ends in accordance with the material dependent OD.

The threshold amplitude for acceptance of an emission line is determined from the average spectrum. It is shown as a horizontal dashed line in Fig. 3.18: 16 (plastic), 42 (glass) and 72 (gravel). This threshold is also a suitable criterion for detecting anomalous spectra. There is no clear monotonic trend in the dependence on LIA, as also reported in

[4], and also no common trend between the different materials. Main issue is that even for relatively large LIA there still appears to be sufficient signal strength, which is mandatory for application of LIBS to granular materials.

To better understand the dependence of the spectral amplitude and observation depth on the LIA we use a model where the average spectrum is assumed to be directly proportional to the ablation hole volume $V_h = A_h \cdot z_h$ where z_h is the depth of the ablated hole and $A_h = \pi W_0^2[1 + (z_{max}/z_0)^2]$ is the ablated area with z_{max} the maximum axial distance of the plasma emission. The latter can be estimated using the Beer-Lambert absorption law for fluence $[J/cm^2]$:

$$F_B = F_z \cdot exp(-\alpha_{ab} \cdot z_h) \tag{3.19}$$

$F_B = E_P/A_h$ is the breakdown threshold fluence $[J/cm^2]$, $F_z = E_p/A_L$ is the incidence fluence at the axial position z, α_{ab} is the absorption coefficient $[cm^{-1}]$ of the incident laser by the target material. The LIA angle Φ enters through the projected beam surface $A_L(\phi_{LIA}) = A_{L0}/cos(\phi_{LIA})$ where $A_{L0} = W(z)^2$ is the cross section area of the incidence laser beam at the axial position z. Thus, assuming constant incident fluence, even at a $\phi_{LIA} = 60°$ only $6dB$ signal would be lost. As a result, the hole volume V_h is described by:

$$V_h = \frac{A_h}{\alpha_{ab}} \cdot \ln\left(\frac{F_z}{F_B}\right) \tag{3.20}$$

Here we assume that $A_h = \beta A_L$ and F_B are independent of the LIA. Combined with eq. 3.16, eq. 3.20 can be rewritten as a function of axial position z and LIA:

$$V_h(z, \phi_{LIA}) = \frac{\beta \cdot A_{L0}}{\alpha_{ab} \cdot \cos(\phi_{LIA})} \cdot \ln\left\{\frac{E_P \cdot F_B \cdot \cos(\phi_{LIA})}{\pi W_0^2[1 + (z/z_0)^2]}\right\} \tag{3.21}$$

The effective laser fluence on the sample surface is different if the focus is above (in mid-air) or below material surface (inside the material). To investigate we use a flat plastic flake, a flat piece of glass and a flat piece of gravel and set the laser angle (LIA) to six angles 0 to 60 deg and manually control the distance between the sample surface and the laser focus. Note that the laser focus is also the centre of light collection (cf. Fig. 3.16). Fig. 3.18a-c show the average intensity of the spectrum (black dash) and the amplitude of one

or two (red and blue) selected emission lines for plastic (a), glass (b), and gravel (c). For each LIA, the sample upper surface is moved downwards in steps of 0.5 mm per laser shot from roughly 5mm above the laser focus (focus inside material) to 5 mm below the laser focus (focus in mid-air). The horizontal axis in Fig. 3.18a-c count the total number of shots over the six LIAs. It is noted that the 10 mm vertical range of the sample lies within the OD of the setup.

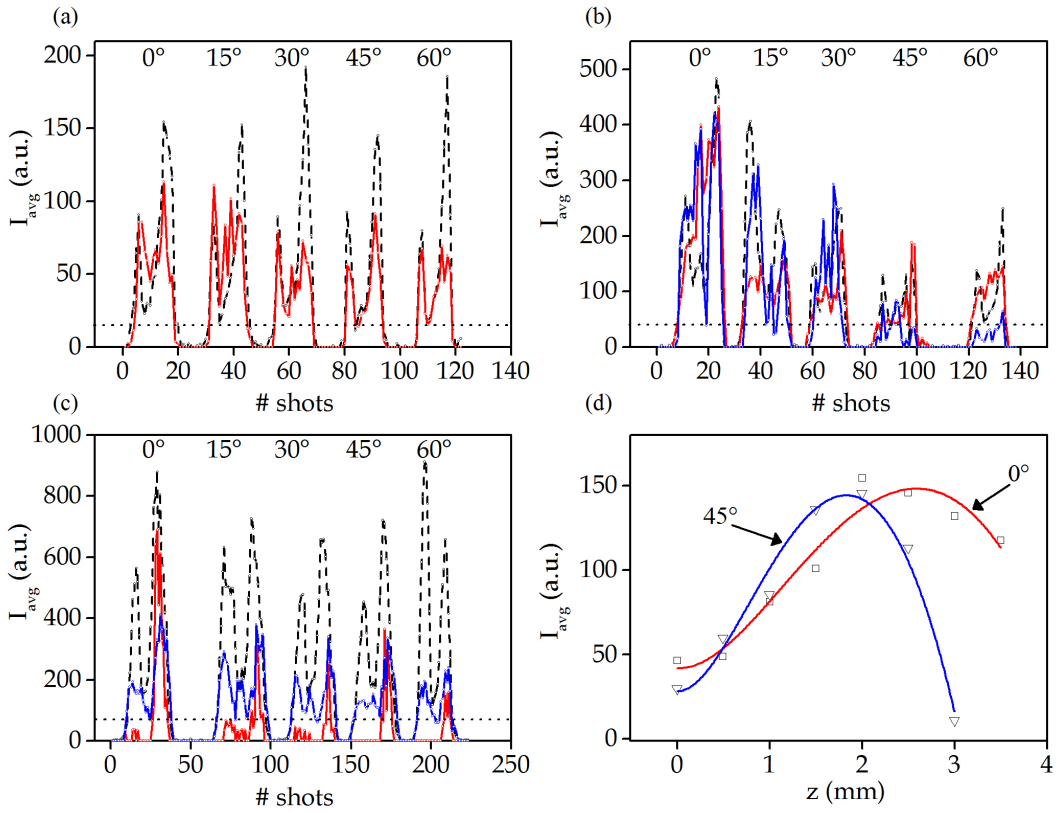


Figure 3.18: Intensity of selected emission lines and average spectrum (black dash) for five LIAs using single shot spectra. Accepted emissions exceed the threshold (straight line). The controlled offset between the sample surface and laser focus is counted as 0.5 mm per laser shot (~ 20 shots per LIA). Samples and selected emission lines are: (a) Plastic, CN 388 nm (red); (b) Glass, Na 589 nm (red) and Mg 279 nm (blue); (c) Gravel, Si 288 nm (red) and Al 309 nm (blue). (d) Average intensity data points from Fig. 3.18a for two laser angles as a function of the offset between the sample-surface and the laser focus. For z=0 the focus is on the surface and for z>0 the focus is in mid-air.

All the average spectra in Fig. 3.18a-c show a sharp dip roughly half way the range, at which position the focus is assumed to be on the sample surface, because that is where we may expect the most change. It should be noted that we base the laser focus on free space calculations in eq. 3.16 and 3.17. This is probably correct when the focus is in mid-air but for a focus near and below the sample surface the focus diameter may be affected to unknown degree by shielding and/or self-focusing effects of the ablated, ionized matter.

Nevertheless, the observable dips may partly be contributed to a mismatch between the laser focus and the best optical centre for collecting emissions. After all, it is well known that by the time of data acquisition the plasma plume extends approximately a millimetre into the air away from the ablated surface. The sharpness of the dip indeed suggests a distance mismatch of just a few millimetres as the average intensity reaches a maximum when the sample surface lies just a few millimetres below the focus.

A pertinent question is if it is just the mismatch or if the emissions are also less strong because less mass is ablated when the focus is on the sample surface? To answer this we plotted the data points of the average spectrum intensities (black dash) in Fig. 3.18a for the LIA 0 deg and 45 deg as a function of the offset between the sample surface and the laser focus. For z=0 the focus is on the sample surface and for z>0 the focus is further up in mid-air. In Fig. 3.18d we added two continuous curves calculated using the ablation hole model eq. 3.21. The OD decreases most visible with laser angle, and the signal strength initially increases with ablated mass as the focus is moved a few millimetre away from the sample surface (larger z). This strongly suggests that not only there is a potential mismatch between the centre of optic data collection and the focus on the sample surface, but also that less mass is ablated in that case.

Another two factors may play a role in the observed emissions. First, when the focus is on or inside the material the laser energy is probably applied more efficiently for ablation and that means that either the plasma is potentially hotter and/or the ablated mass is larger. But to take full advantage the focus of the collection optics should not coincide with the laser focus as in Fig. 3.16. Second, when the focus is in mid-air the air emissions dominate the spectrum, which is highly undesirable. Overall, judging from the maxima to the left of the dips in Fig. 3.18a-c, the optimum focal point for the laser is a distance OD/4 below the material surface.

3.6. RELATION BETWEEN LASER FLUENCE AND ABLATED MASS

In the preceding section we silently assumed that the ablated mass (or hole volume in the sample surface) is proportional to laser fluence, provided the laser power density is high

enough to cause breakdown. This assumption seems to be in line with the experimentally verifiable trend that the strength of the observed LIBS signal is proportional to laser fluence. In fact, this proportionality is the basis for the common practice of normalizing the acquired spectrum to the spectral integral. However, above the breakdown threshold and under fixed laser fluence, the observable emissions can still vary with chemical and physical properties of the sample material. This is relevant as many seemingly similar building waste materials may have different material properties, and because the surface properties may slightly differ from those in the bulk of the material. The chemical and physical variations may cause changes in thermodynamic processes and states as the laser energy partitions differently between ionization, evaporation and other possible processes. The emphasis in this work is on single-shot experiments, which rules out the possibility of averaging out all kinds of material effects. This is why the dependence of the LIBS spectrum on laser fluence and ablated mass needs to be investigated more closely. To this end two types of experiment were performed. In type 1 experiments the laser energy per shot is constant while the irradiated surface is varied to obtain different levels of fluence. In type 2 experiments the laser energy is varied to obtain different levels of fluence and the irradiated surface is kept the same.

1. The upper sample surface is varied through the laser beam in 0.5 mm steps, thereby firing one shot (11.5 mJ) in a fresh position in each step (cf. Appendix Tab. 2).

2. For a fixed sample surface the laser shoots five times with a different energy in five fresh positions. The laser energy is varied by increasing the Q-switch delay from 165 (default) to 175, 180, 185 and 190 μs. The time delays for the spectrometer were increased by the same to maintain a constant integration time of 10 μs. The plasma light was collected using a 50 mm lens in combination with a parabolic mirror connected to an optic fibre bundle. It is noted that varying the Q-switch delay slightly alters the beam profile, which effects are neglected (cf. Appendix Tab. 3).

In all experiments a laser focusing lens of 50 mm was used. The geometry of the resulting hole (cf. Fig. 3.19) is measured using a white light interferometry (WLI) microscope (Contour $GT-K1$, Veeco Instr. Inc.). This revealed the ablated depth, area, volume and cross-section profile of the hole. A $20X$ objective optics and ± 50 μm forward- and back-

scanning were used. A disturbance with the white light method is the regular occurrence of light shielding and light absorption in a hole by which the light signal cannot be detected, which is reported as not-a-number notation (NaN) in the data set. A second disturbance is that the sample surface is not perfectly horizontal on the sub-millimetre scale, which slightly distorts the observed hole geometry.

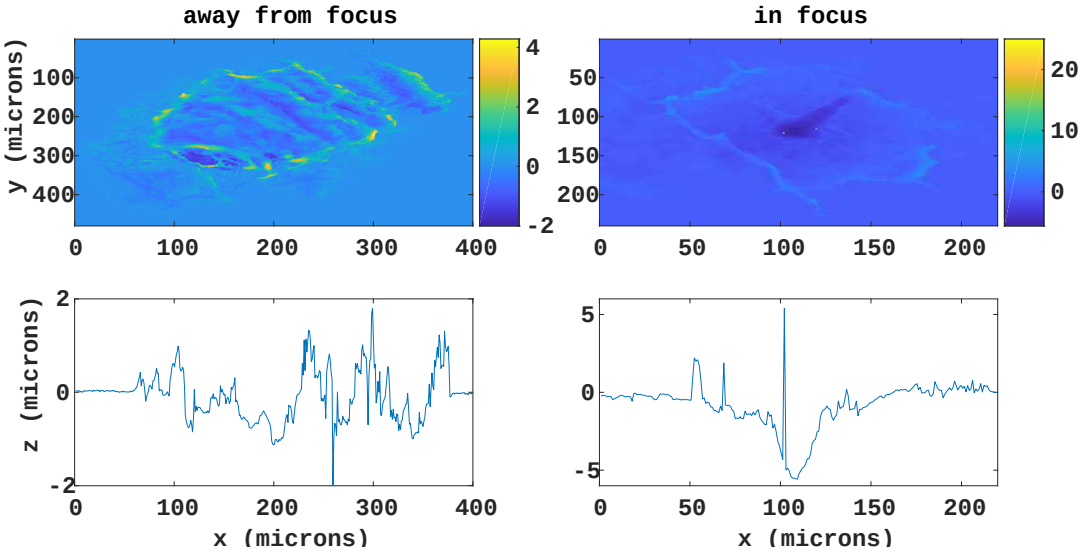


Figure 3.19: Surface mapping and profiling using white light interferometry on a Si wafer. Left: away from the focus. Right: in the focus. The colour bar corresponds to height (μm).

The samples were round silicon wafers used for production of microchips with a thin layer of Sb ($\sim 3\ \mu m$), Ni ($\sim 1.5\ \mu m$), Mo ($\sim 1.5\ \mu m$), Ni ($\sim 1.5\ \mu m$) and Cu ($\sim 1.5\ \mu m$). These layers were created on n-type Si-wafers (100) using a physical vapour deposition (PVD) system (Trikon Sigma 204 magnetron) with RF discharge plasma under Ar background gas and controlled flow rates at $25-350^{\circ}C$ in a sputter chamber.

The white light image (WLI) raw data was processed with the following procedure:

1. Determine a bounding box and define the surface reference using four lateral corners.
2. Interpolate the missing NaN points linearly along the columns.
3. Interpolate the missing NaN points linearly along the rows.
4. Assign all NaN the smallest value from steps 2 and 3.
5. Determine a surface reference for the profiling.

6. Reconstruct the surface matrix of normally distributed random numbers using the average of the reference and the STD.

7. Calculate the hole parameters.

The hole correlation parameters are defined as follows:

- S_{std}: surface roughness ($\pm 3STD$)
- A_1: deposited surface area (sum of pixels of which height is larger than surface mean+$3STD$)
- Avg_h: average deposited height
- V_1: deposited volume
- Max_h: maximum deposited height
- $R_{dep} = \sqrt{A_1/\pi}$: deposited area effective radius
- A_2: ablated surface area (sum of pixels of which height is smaller than surface mean$-3STD$)
- Avg_d: average ablated depth
- V_2: ablated volume
- Max_d: maximum ablated depth
- $R_{ab} = \sqrt{A_2/\pi}$: ablated area radius
- $A_{tot} = A_1 + A_2$: total area (deposition + ablation)
- $V_{tot} = V_1 + V_2$: total volume (deposition + ablation)

We calculated the correlation coefficients of the datasets in Tab. 2.1 and those in Appendix Tab. 2, and focus on correlation coefficients larger than 90%. Fig. 3.20a shows that the total area A_{tot} is proportional ($R^2 > 95\%$) to the square of the optical penetration depth (α^{-2}) using the average and STD of 6 single-shots for each material. Each shot was taken at height different of 0.5 mm between the laser beam focal plane and sample surface. It implies that the absorption of the first laser pulse by the flat sample surface (on the lateral

XY-plane) depends on its optical property , i.e. $A_{tot} \sim 1/\alpha^2$. Assuming that each single-shot (12 mJ) is completely utilized for fusion, vaporization, sublimation and ionization (cf. Tab. 2.1), the corresponding ablated material volumes are calculated in Fig. 3.20b. It indicates that the measured ablated volume is merely a fraction of the calculated values, e.g. <1.3% for Sb and ca. 24% for Mo. It also indicates that the shot-to-shot variations in ablated volume (6 shot average) ranges from 17% for Si wafer and >100% for Sb.

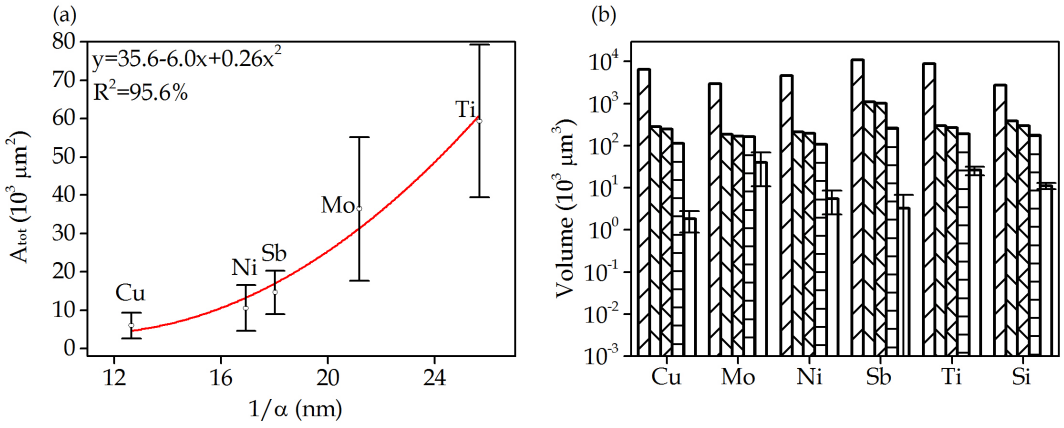


Figure 3.20: (a): Total area A_{tot} $[\mu m^2]$ over the optical penetration depth α^{-1} $[nm]$. Fitting is performed according to $A_{tot} \sim \alpha^{-2}$. (b): Volumes $[10^3\ \mu m^3]$ represented by 5 bars for each material (from left to right), are respectively, four calculated volumes assuming all the laser energy absorbed for fusion, vaporisation, sublimation and ionization, and measured ablated volumes over 6 single-shots.

Linear correlation coefficients were determined to learn more about the possible dependencies between hole formation and corresponding LIBS spectra. For this we used the resonance line $Si\ (I)\ 251\ nm$ that corresponds to the transition $(3s^2 3p4s\ ^3P^0 -> 3s^2 3p^2\ ^3P)$ from the excited state to the ground state, while the line $Si\ (I)\ 288\ nm$ corresponded to the transition $(3s^2 3p4s\ ^1P^0 -> 3s^2 3p^2\ ^1D)$ from a high to a lower excited state. It is noted that the resonance lines are affected strongest by self-absorption in the plume.

Next we correlate forenamed twelve parameters from WLI with the LIBS spectra. A threshold of $|C_{corr}| \geqslant 0.5$ is applied to the absolute correlation coefficients shown in Tab. 3.4. For Cu, A_1 is correlated with the $Cu\ (II)\ 254\ nm$ line ($C_{corr} > 0.8$) from which the bands originated ($C_{corr} > 0.65$); Avg_h is inversely correlated with bands ($C_{corr} < -0.85$); Avg_d is a good representative to describe the laser ablation process as it is inversely correlated with the bands ($C_{corr} < -0.95$). The stronger the band emissions the smaller Avg_d, which means the residual energy after ionization contributed to the formation of

the ablated hole. Also R_{ab} correlates reasonably well ($C_{corr} > 0.8$). The atomic data for Mo is very limited due to its dense band structure, but even this atom may show continuous atomic band emissions. Again, Avg_h correlates with $Mo\ (II)\ 393\ nm$ ($C_{corr} > 0.84$), V_1 correlates with bands ($C_{corr} > 0.95$) and inversely correlates with $Mo\ (I)\ 268\ nm$ ($C_{corr} < 0.90$) which means that the deposited volume may be correlated with the ionization process that partitioned the absorbed energy from atomic emissions. Avg_d correlates with the $Mo\ (II)\ 393\ nm$ line which implies there may be an electromagnetic force active during the ionization process that is responsible for removing molten material from the hole. Contrary to Cu, the $Ni\ (I)\ 507\ nm$ line correlates with Max_h and Max_d for Ni. This implies either that the laser ablation on Ni as described by Max_h and Max_d is more of an atomization process, or that the ionization process may take place earlier than the observation time window. For Si the parameters A_1, V_1 and R_{dep} correlate with the $Si\ (II)$ lines and bands ($C_{corr} > 0.90$). The parameters Avg_h and Avg_d correlate with the $Si\ (I)$ lines, which means the deposition area or volume is more likely to be driven by the ionization process while the height or depth is more dependent on the residual energy after ionization.

REFERENCES

[1] H. Xia and M. Bakker, *Single-shot libs spectral quality for waste particles in open air,* tm-Technisches Messen **82**, 606 (2015).

[2] B. Saleh and M. Teich, *Fundamentals of Photonics*, Wiley Series in Pure and Applied Optics (Wiley, 2013).

[3] W. Steen, *Laser Material Processing* (Springer London, 2013).

[4] R. A. Multari, L. E. Foster, D. A. Cremers, and M. J. Ferris, *Effect of sampling geometry on elemental emissions in laser-induced breakdown spectroscopy,* Applied Spectroscopy **50**, 1483 (1996).

Table 3.4: Correlation coefficients between hole parameters and LIBS spectra for four materials.

Parameter	Cu		Mo		Ni		Si	
	lines	bands	lines	bands	lines	bands	lines	bands
A_1	0.8 Cu II 254	0.65	-	-	-	-	-0.89 Si I 249	0.92
Avg_h	0.56 Cu I 250	-0.85	0.84 Mo II 393	0.65	0.50 Ni I 341		0.90 Si I 251	-0.80
V_1	-0.60 Cu I 250	-	-0.90 Mo I 268	0.95	-	-	0.92 Si II 254	0.90
							0.96 Si II 637	
Max_h	-0.85 Cu I 324	-		-0.60	0.87 Ni I 507	-0.80	-0.50 Si I 288	-0.94
	-0.83 Cu I 250							
A_2	-	0.80	0.70 Mo I 268	-0.80	-	-	-0.98 Si I 251	-
Avg_d	0.64 Cu I 250	-0.95	0.93 Mo II 393	0.70	-	-	0.80 Si I 251	-0.80
R_dep	-0.68 Cu I 249	0.75	-	-	-	-	-0.80 Si I 251	0.94
V_2	-	0.73	0.90 Mo I 268	-0.87	-	-	0.60 Si I 259	-0.60
Max_d	-0.8 Cu I 324		-0.50 Mo II 393		0.81 Ni I 507	-0.70	-	0.90
	-0.86 Cu I 522							
A_{tot}	-	-0.77	0.60 Mo II 393	0.60	-	-	-0.80 Si I 249	0.60
V_{tot}	-	-0.70	0.80 Mo II 393	0.95	-	-	-0.60 Si I 249	0.95
			-0.95 Mo I 268					
R_{ab}	-	0.80	-0.93 Mo II 393	-0.80	-	-	-0.98 Si I 251	-

4

PROPERTIES OF LIBS SPECTRA

LIBS is essentially a spectroscopic methodology and as such it offers similar possibilities and encounters similar limitations as other spectroscopic techniques such as NIR and HSI when translating spectral data to target material parameters. The major advantage is that, as a technique, LIBS physically samples some of the material and brings it into a standardized state (plasma phase) before LIBS emission spectral data is collected, i.e. it is vaporized and partly ionized into atoms, ions and electrons. This way the collected spectrum is more likely to represent the target material and is less sensitive to surface conditions such as roughness, moisture, oxides and dust than an optical method such as NIR.

The translation from spectral data to material parameters may be based on statistical signal processing, a physical model or a combination of both. The latter is favoured in this work, because there is normally insufficient information on reference standards (e.g. calibration or training) and variables for a purely physical model in recycling. The suppression of intra-class variation and enhancement of inter-class distance play the key role in statistical LIBS analysis. To this end, one tries to employ all possible information sources related to the target material, while at the same time trying to minimise interfering factors. Traditionally, spectral calibration of element contents is based on reference measurements from prepared samples that closely match the target sample matrix. Unfortunately, the calibration is sensitive to the exact physical and chemical properties of the matrix material which affect the plasma plume processes of ablation, ionization and optical emission.

This is what essentially constitutes the so called matrix effects. These seemingly illusive sensitivities and related spectral variations are the subject of this chapter.

First, we investigate the possible origins (laser unit, spectrometer slit size and laser fluence) for shot-to-shot spectral variations using prepared samples. Second, we define raw spectrum processing schemes for various applications. As case studies, schemes are tested for the differentiation of monetary coins with well-defined metal composition, the production of calibration curves in different matrices measured at different time delays for quantitative element analysis; and the extraction of LIBS spectral information that correlates with product quality.

4.1. STUDY OF VARIATIONS IN LIBS SPECTRA

Averaging is an effective solution to suppress random electronic noise and other non-correlated disturbances in the spectra of repeated experiments. Unfortunately, for a laser with a maximum shot frequency, the economic disadvantage is that fewer particles can be inspected per second compared to single-shot data. Every source of disturbance may generate its own specific average and variation levels in LIBS spectra, which offers a possibility to quantify, identify and perhaps eliminate it. Moreover, when building a LIBS data set using a sample in independent spots one can determine the correlated variations that are particular to that material, and one can also experimentally determine to which conditions the variation is most sensitive. In this way the variation, usually considered a nuisance, becomes a useful indicator to improve the performance of LIBS-based methods.

It is noted that the statistical concept for correlated disturbances reaches even further. The variation in different emission lines in a LIBS data set may characterize a material in a way that may not be intuitive. In that case correlated variations may be associated with information, where more variation indicates more information. This is the topic of Chapter 6.

Here we first determine how many repeated spectra (N) are minimally needed to span the average and variation of emission line amplitudes. We first define the ensemble average,

which is the average amplitude of the emission line $s_i(\lambda)$ over an ensemble of N spectra, and the ensemble fluctuation [1] (page 9), which is the ensemble sum of the square of the variations w.r.t. the ensemble average:

$$\langle s_i(\lambda)\rangle = \frac{1}{N}\sum_{i=1}^{N} s_i(\lambda),\ \left\langle (\Delta s_i(\lambda))^2 \right\rangle = \sum_{i=1}^{N} \left(s_i(\lambda) - \langle s_i(\lambda)\rangle\right)^2 \tag{4.1}$$

Next we define the signal-to-variation ratio (SVR) for any kind ensemble, not necessarily one of repeated spectra, as a ratio of cumulative distributions:

$$SVR(\lambda) = \frac{N\langle s_i(\lambda)\rangle}{\sqrt{\left\langle (\Delta s_i(\lambda))^2 \right\rangle}} \propto \sqrt{N},\ for\ N \geq N_{min} \tag{4.2}$$

Eq. 4.2 indicates that N_{min} is reached when the SVR increases linearly with $\sqrt{N}$. This may be more clear when we use the SVR for an ensemble of repeated spectra. In this case the SVR may be recognised as $\sqrt{N}$ divided by the relative standard deviation (RSTD) for a specific emission line. When the STD and average have converged the ratio becomes proportional to $\sqrt{N}$. Similarly, the signal-to-background ratio (SBR) for an ensemble is here defined as:

$$SBR(\lambda) = \frac{\langle s_i(\lambda) - b_i(\lambda_{BG})\rangle}{\sqrt{\left\langle (s_i(\lambda) - b_i(\lambda_{BG}))^2 \right\rangle}} \propto \pm\sqrt{N},\ for\ N \geq N_{min} \tag{4.3}$$

Parameter b_i denotes an average background signal to the emission line s_i, determined from several wavelengths λ_{BG} in the neighbouring of λ. Eq. 4.3 is valid if the signal and its background are strongly correlated. The SBR can be positive or negative, depending whether the signal or the background accumulates faster.

As a test case we investigate single-shot LIBS spectra from pure silicon by using a round, flat wafer such as commonly used in the production of electronic chips. This pure and ideally flat sample allows us to selectively investigate the spectral variances due to sources of disturbance that are part of the LIBS system. We use the $Si\ (I)\ 288\ nm$ emission line. The laser angle is 45° (cf. setup in Fig. 1.6). The main system settings are time delay 400 ns and integration time 10 μs. The silicon wafer is moved by a step motor that triggers a laser shot each second. A total of 2500 single-shot LIBS spectra are collected from as many fresh positions on the Si-wafer. Fig. 4.1a shows the SVR as a function of $\sqrt{N}$. At first the trend is decreasing, showing that the variation increases w.r.t. to the average signal. At 169

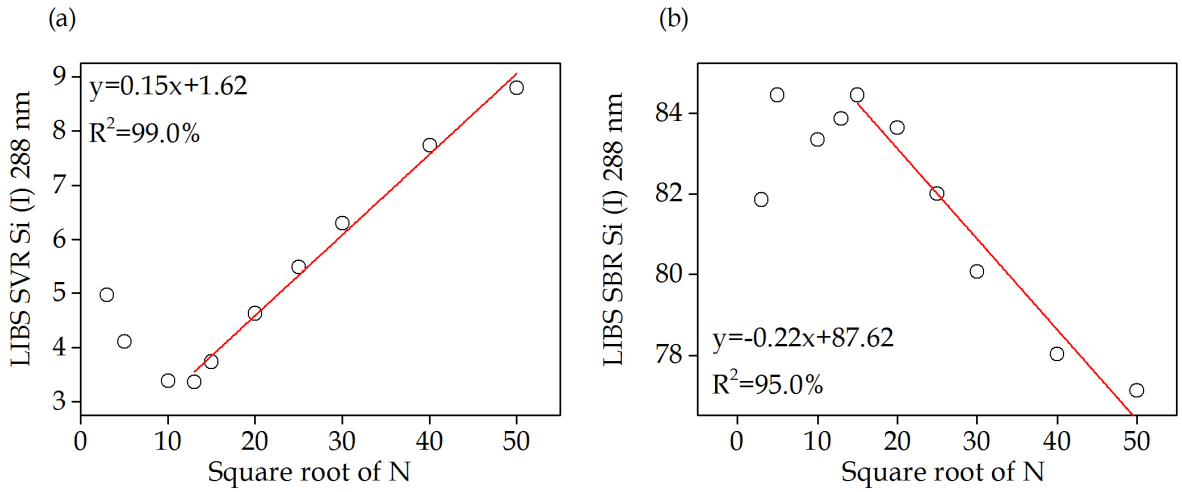


Figure 4.1: LIBS spectral variation caused by laser unit: (a) SVR and (b) SBR of $Si\ (I)\ 288\ nm$ emission line over 2500 single-shots. The background is averaged over 30 wavelength pixels on each sides of 288 nm, respectively.

shots the SVR starts the linear trend upward, showing that the average signal and variation remain comparable from that point on. In other words, the total detectable variation in repeated experiments of the emission line $Si\ (I)\ 288\ nm$ can be captured by acquiring at least 169 LIBS spectra.

Where the SVR provides information about the variation of the signal, the SBR provides information about the variation of the signal w.r.t. its background. This is shown in Fig. 4.1b. The SBR is positive and relatively stable around 82-85 for the first 255 shots. This shows the signal is stronger than the background and that both remain at the same relative levels. However, since the $\sqrt{N}$ behaviour would tend to lower the SBR we also conclude that the absolute levels of the emission line and its background increase to the same degree. This stops at 255 shots, at which point a downwards trend is set in. In other words, the total variation detectable in repeated experiments of this emission line w.r.t. to its background can be captured by acquiring at least 255 LIBS spectra.

The growth of the emission line and its background infers that the (effective) laser energy is increasing during the first 255 shots. A probable cause is that the laser energy, and perhaps also the laser beam quality (M^2 factor, which influences focussing), was settling. This may be attributed to the fact that the laser is operated at the lowest possible rate of 1 Hz and it apparently takes 255 shots before the laser cavity temperature, the laser

inversion conditions, and/or Q-switch operation has stabilized.

4.1.1. VARIATION CAUSED BY OPTICAL THROUGHPUT

Besides the laser unit itself, variations between different emission lines has several other causes. The first is that the hot plume is not a homogeneous distribution for all the species. It is bound to have a direction sensitive radiation pattern, rather than a spherical symmetric pattern. The second is when using two different laser fluences on the same material the spectra will vary according to the total ablated mass and the achieved plasma temperature. While all signals tend to be stronger for higher laser fluence, the photon counts generally will not scale the same for all emission lines.

These causes of spectral variations may also be material-dependent. In fact, by capturing these variations in an ensemble of spectra and processing them using statistical correlation, it may be possible to use the information to our benefit and improve the inter-class distance. The method is to create the variation artificially for one of these two causes while keeping everything else constant.

First, the influence of the plasma radiative throughput on variance in collected spectra is investigated. To this end the amount of light collected with a fibre bundle at 45° w.r.t. the vertical axis of the plasma was controlled using an additional slit with variable opening diameter. This way the variations in the spectra may be analyzed without influencing the temperature and electron density of the plasma. It is noted that the slit opening is optimized for each material to prevent signal saturation of the CCD and also being able to detect the smaller emission lines. Some 5-10 slit openings per material are tested and for each an ensemble of 10 shots are collected to account for possible shot-to-shot variations. Thus, for a selected emission line, the correlation coefficient for the ensemble of 5x10 spectra can be calculated. Here we select the $Si\ (I)\ 288\ nm$ and the $Ca\ (I)\ 616\ nm$ emission lines from pure Si and CaO samples.

Figure 4.2a-b shows correlation coefficients for varying slit openings, while targeting $Si\ (I)\ 288\ nm$ and $Ca\ (I)\ 616\ nm$ and the other spectral parts of CEM and DC. It shows

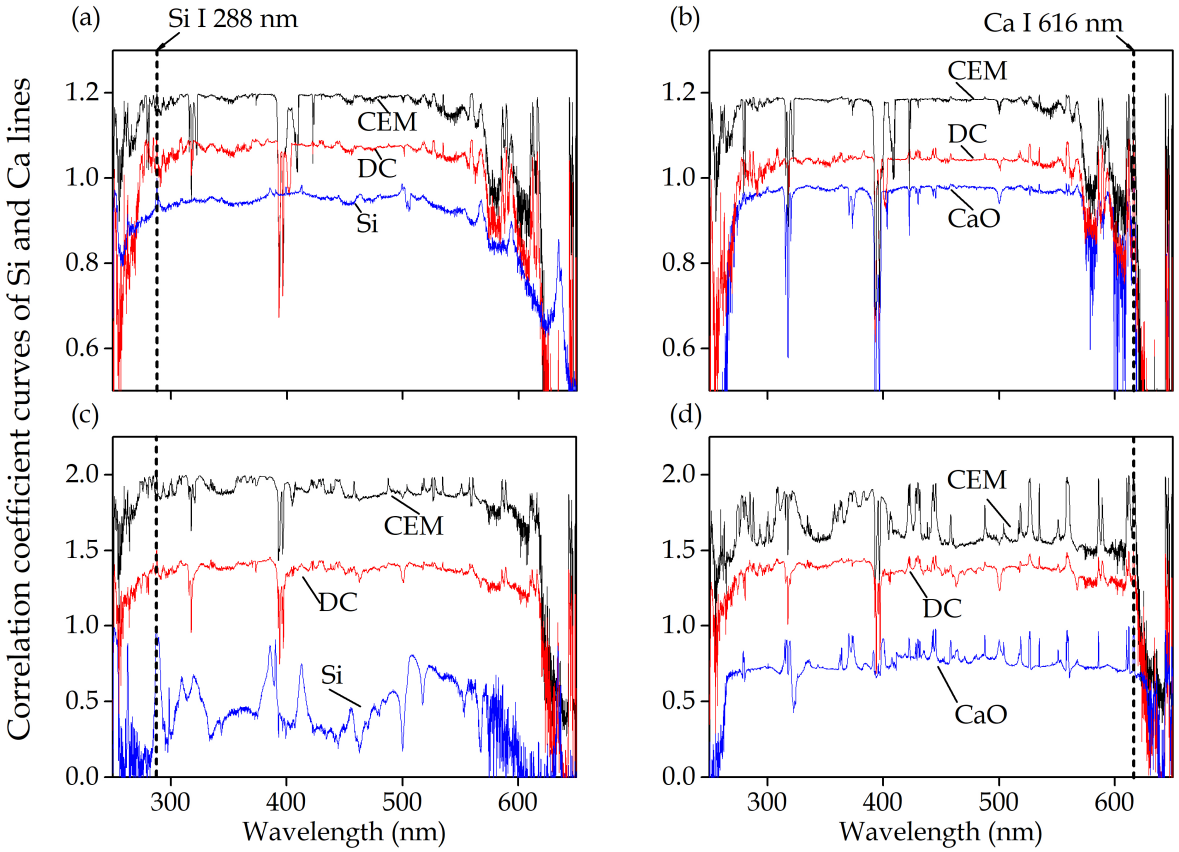


Figure 4.2: Shot-to-shot correlation coefficients of emission lines $Si\ (I)\ 288\ nm$ (left rows) and $Ca\ (I)\ 616\ nm$ (right rows) with the rest of spectra in CaO, CEM, DC, and Si matrices. (a)-(b): LIBS spectra are collected with varying slit opening (curves are offset by 0.2 for clarity) and (c)-(d) laser fluence (curves are offset by 1.0).

that the two emission lines are highly correlated with other atomic lines as well as with continuum bands between $300-500\ nm$. This indicates there is equilibrium for the atomic energy levels (which are normally close) and continuum levels. The two atomic emission lines also correlate with ionic emission lines (e.g. Ca II: 315.8, 317.8, 370.5, 373.4, 393.2, 396.6 nm) to a smaller degree. This may indicate that the number of atomic lines increase as the number of ionic lines decrease due to ion-electron recombination.

The high levels of inter-correlation among spectral lines may cause an ill-conditioned regression model that is unstable (cf. Chap. 6). This could be improved by normalization, e.g. to the correlated continuum bands, or the background at the emission line of interest. Fig. 4.3 shows 8 data points using 8 different slit opening applied to Ca and Si emission lines from demolition concrete and cement. For each material the amplitude of the emission line is shown as the ensemble average for 10 shots per slit opening. The two selected

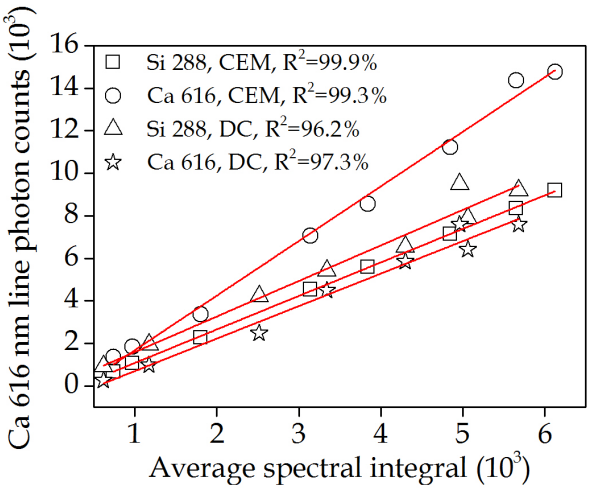


Figure 4.3: Emission line average amplitudes (average of 10 shots) for increasing slit size, plotted as a function of the ensemble-average of the spectral integral. Sample TS1CEM, Holcim: Si I 288 nm (squares) and Ca I 616 nm (circles). Sample demolition concrete: Si I 288 nm (triangles) and Ca I 616 nm (stars).

emission lines are $Si\ (I)\ 288\ nm$ and $Ca\ (I)\ 616\ nm$. These data points are plotted as a function of the ensemble-average of the spectral integral according to eq. 3.14.

It is noted the slit opening was varied between 5 and 12 mm, though the number of times the slit opening was used is different for the four curves in Fig. 4.3. This choice of axes produced curves with a similar trend for both materials, in which the slit opening is proportional to a higher spectral integral value. The slope for an emission line in the plot depends on the target material. The LIBS spectra from CEM and DC samples are dominated by the Ca species of which the emission lines-to-continuous bands ratio is higher than that of Si (cf. Fig. 4.4). Consequently, as the slit opening increases, more Ca emissions are collected compared with those from Si. Note that the plasma temperature and ionization rate may be assumed constant in these plots. The linearity between emission line amplitude and spectral integral indicates that the normalization according to eq. 3.14 is effective and compensates for the shot-to-shot variation caused by different slit openings.

4.1.2. VARIATION CAUSED BY LASER FLUENCE

The influence of plasma temperature variation on the LIBS spectrum is investigated by varying the laser fluence. To this end different laser focal lens-to-sample surface distances

are employed while the light collection optics are fixed at 45° w.r.t. the laser incident angle to maintain constant collection efficiency. Single-shot LIBS spectra are acquired using $t_d = 300\ ns$ and $t_{int} = 10\ \mu s$.

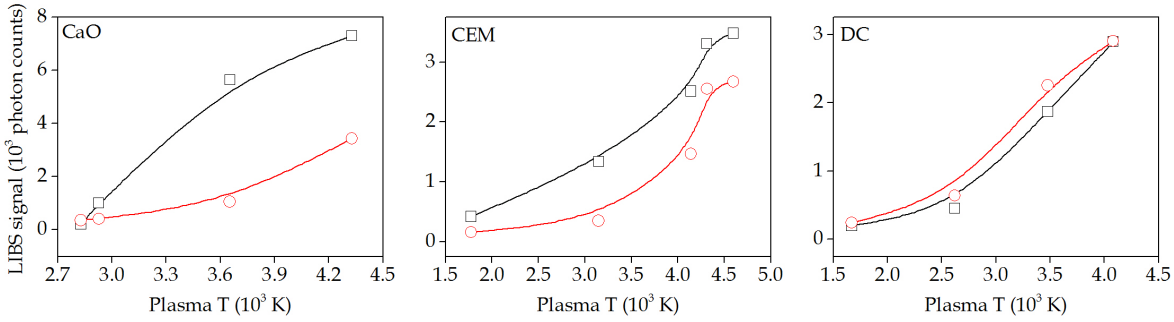


Figure 4.4: Ca (I) 616 nm emission line amplitudes (black curves) and average spectral integrals (red curves) over plasma temperatures determined by Ca (I) 616 nm to Ca (I) 644 nm ratios in different material matrices: (a) calcium oxide CaO (b) cement CEM and (c) demolition concrete DC.

To study the correlation coefficients, we applied a time delay of 100 ns. Fig. 4.2c-d shows the correlation coefficients of $Si\ (I)\ 288\ nm$ and $Ca\ (I)\ 616\ nm$ line amplitudes with all other emissions. Compared with the R in Fig. 4.2a-b, the R of $Si\ (I)\ 288\ nm$ is reduced by 60% for at the continuum bands for Si wafer, and the R of $Ca\ (I)\ 616\ nm$ is reduced by 40% for the cement and CaO samples. The concrete sample is less effected. Overall, the variation caused by laser fluence is much stronger than the variation due to the optical throughput.

To further explain the phenomenon shown in Fig. 4.3 in more detail, we investigate the Ca (I) 616 nm emission line and the average spectral integral amplitudes as a function of the plasma temperature. The plasma temperature is determined using the ratio of the line amplitudes of Ca (I) 616 nm and 644 nm in the model described in Chap. 5, assuming local thermal equilibrium (LTE). Parameters[1] such as transition probability, upper energy level, statistical weight are taken from [2]. The plasma temperature range calculated in Fig. 4.4 is obtained by adjusting the 100 mm laser lens from 98 mm to 120 mm above the sample surface. It proves that the resulting temperature ranges for the different materials are comparable. Nevertheless, it does show that the temperature starts out highest for CaO at the lowest fluence and ends highest for cement at the highest fluence. The

[1] For Ca 616 nm, $E_k = 31539\ cm^{-1}$, $g_k = 3$, $A_{ki} = 0.48\ \pm 25\%$, and for Ca 644 nm, $E_k = 35897 cm^{-1}$, $g_k = 9$, $A_{kj} = 0.53\ \pm 50\%$. Readers are kindly referred to Chap. 5 for detailed explanation.

Ca (I) 616 nm (weak line) amplitudes are largest for CaO where the curve shows signs of self-absorption towards the highest laser fluence. Overall, the two curves for Ca in the plots of Fig. 4.4 converge for more complex matrices, concrete being the most complex. Concrete has perhaps only half the Ca content of cement, but the measured intensities are quite comparable. This indicates that also for higher elemental contents the pressure cooker effect may be effective in increasing the number of exited species in the plume (cf. subsection 4.2.3). It should be noted that compensation for the variation caused by varying laser fluence becomes less effective with with increasing Ca content and when applying a normalization to the whole spectral integral as in eq. 3.14.

Normalization of emission line intensity from major elements to the average spectral integral can compensate for the laser shot-to-shot variations. To produce a calibration curve for each analyte on a sample dataset[2], the following steps are to be conducted:

1. Choose the dataset measured at one selected time delay (e.g. 2100 raw spectra over 3648 wavelength pixels)
2. Normalize the single-shot LIBS spectral data-set according to eq. 3.14.
3. Determine the wavelength where the signal has the highest correlation with the analyte concentration array. The result is the analyte emission line.
4. Normalize the signal at selected wavelength to the signal at all the other wavelengths and find out the next wavelength to which the ratio of the analyte signal has the highest correlation with the analyte concentration array.

This procedure was used for the calibration curves shown in subsection 4.2.3.

4.2. CASE STUDY USING NORMALIZED LIBS DATA

4.2.1. CLASSIFICATION OF COINS USING SINGLE SHOT DATA

We test the potential of LIBS spectra for classifying standardized metal alloys, i.e. the 1 €, 20 and 5 eurocent European monetary coins. The main alloy composition is listed in Tab. 4.1 [3] and the coins are shown in Fig. 4.5a. In these tests we use single shot data for classification of the alloys, where each shot is on a fresh position of the coin surface. The

[2] As an example, here we first measure each sample out of seven at 21 time delays ($0-10$ μs with 0.5 μs time interval), and collect 100 single-shot LIBS spectra at each time delay. In total, a 3648x14700 dataset is obtained for each sampleset consisting of seven samples

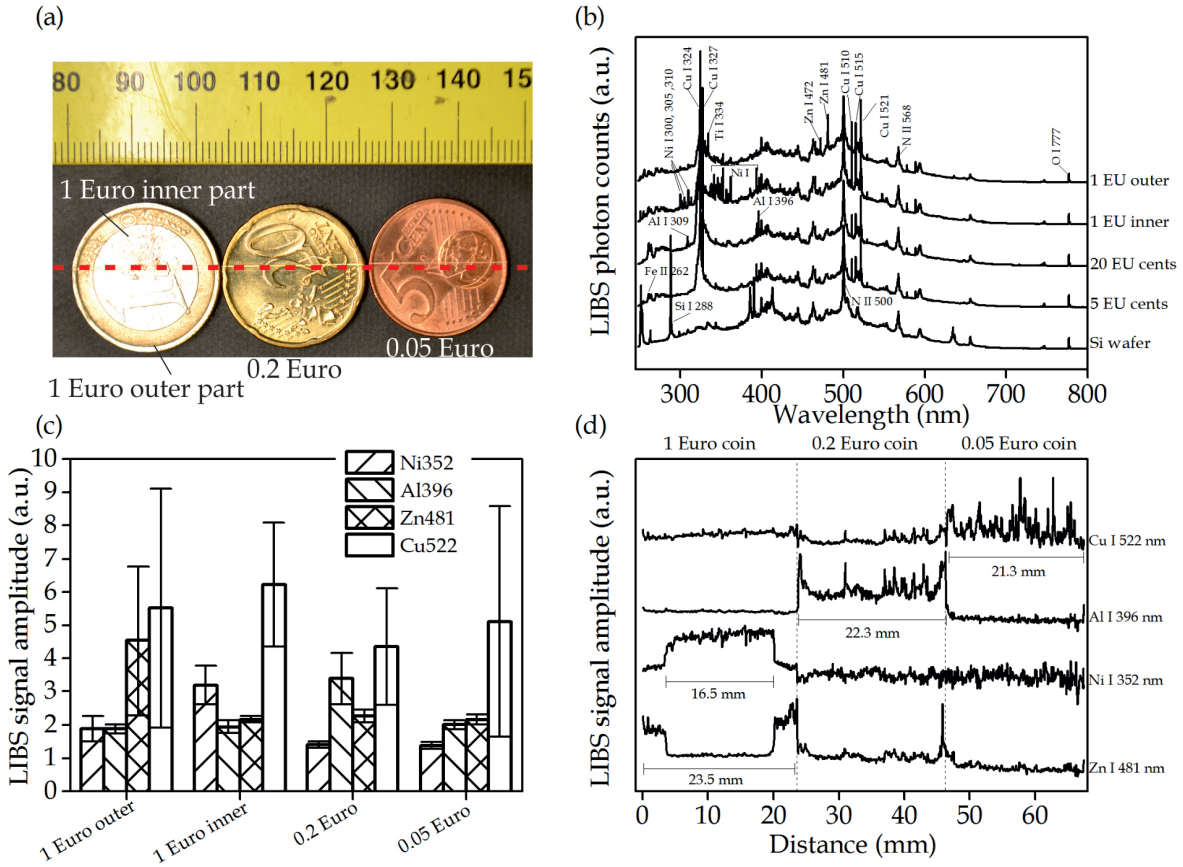


Figure 4.5: LIBS classification of European coins (a) used coins and the single file scanning line in red; (b) raw LIBS spectra for each coin on different parts; (c) 200 shots average amplitudes and STD of those emission lines of training dataset and (d) measured dimension for each coin using selected LIBS emission lines (normalized to the maximum amplitude of each emission line).

Table 4.1: Termed diameter $\oslash_t$ and composition of tested monetary EU coins in comparison with the measured diameter $\oslash_m$ using LIBS.

Coin [€]	Surface layer material	Emission lines	Location	$\oslash_t$ $[mm]$	$\oslash_m$ $[mm]$
1	Cu(75wt%)-Zn(20wt%)-Ni(5wt%)	Zn (I) 481	Outer	23.25	23.5
1	Cu (75wt%)-Ni(25wt%)	Ni (I) 352	Inner	-	16.5
0.2	Cu(89wt%)-Al(5wt%)-Zn(1wt%)	Al (I) 396	-	22.25	22.3
0.05	Cu(100wt%) covered Steel	Cu (I) 522	-	21.25	21.3

coins are placed on the flat surface of a silicon wafer, also because coins do not contain Si so the emission line Si (I) 288 nm provides a unique background identifier. The wafer is moved along the LIBS unit by a step motor at 12.2 mm/s. The shot rate was 100 Hz by which we collected a training dataset of 200 spectra at random surface positions by using repeated line scanning at various offsets. The testing dataset was acquired along the scanning line shown in Fig. 4.5a. The potential of LIBS for characterisation is proven if LIBS can at least detect the boundary (diameter) of each coin. A few raw training spectra are plotted in Fig. 4.5b. The following procedure extracts distinguishing emission lines that can characterize the coins:

1. Normalize the single-shot LIBS spectral dataset according to eq. 3.14.

2. Choose non-overlapped strong emission lines for each of the major elements in a coin as characterized by percentile occurrence, which is defined as the percentile ratio of the number of shots (spectra) with characterizing emission lines and the total number of shots (spectra).

3. The 5 cent coin has a surface composition comparable to other coins due to the dominance of Cu. This necessitates we use a combination of two or more emission lines to get in combination a more unique signature for this coin.

Step 2 was performed using the spectral background subtraction procedure described in [4, 5] [3]. In Tab. 4.2, the selected strong and non-overlapped emission lines (orthogonal lines) with occurrence >90% are listed.

Table 4.2: Characteristic emission lines and occurrence (%) for Euro coins. Robust emission lines that are absent in other target coins are in boldface.

1 Euro outer ring		1 Euro inner part		20 EU cents		5 EU cents	
wavelength	%	wavelength	%	wavelength	%	wavelength	%
Cu (I) 324.54	100	Ni (I) **310.00**	99	Al (I) **396.00**	100	Cu (I) 324.54	100
Cu (I) 327.19	100	Cu (I) 324.54	100	N (II) 500.24	99.5	Cu (I) 327.19	100
Ti (I) **334.30**	100	Cu (I) 327.19	100	Cu (I) 515.22	96.5	N (II) 500.24	99.5
Zn (I) **480.91**	100	Ni (I) **341.23**	100	Cu (I) 521.70	100	Cu (I) 521.70	100
N (II) 500.24	99.5	Ni (I) **351.28**	100	N (II) 567.59	96	N (II) 567.59	97.5
Cu (I) 510.34	99.5	Ni (I) **352.27**	100			O (I) 777.18	98.5
Cu (I) 515.22	100	Ni (I) **361.80**	100				
Cu (I) 521.70	100	N (II) 500.24	99				
N (II) 567.59	98	Cu (I) 510.34	100				
O (I) 777.18	95.5	Cu (I) 515.22	100				
		Cu (I) 521.70	100				
		N (II) 567.59	99				
		O (I) 777.18	96				

Fig. 4.5c shows the average signal amplitudes with STD of the selected orthogonal emission lines. A classification error may occur if we assign a threshold value to emission peaks that overlap within one STD. For a 1 € coin we use the Zn (I) 481 nm and Ni (I) 352 nm lines to scan its outer (23.5 mm) and inner (16.5 mm) diameter, as shown in Fig. 4.5d. The diameter (22.3 mm) of 20 cents coin is determined using the Al (I) 396 nm

[3] Here we reproduced the continuous background of a LIBS spectrum using Matlab functions in 4 steps. 1: using "sgolayfilt.m" (polynomial order 5, window size 7) to smooth the raw spectrum; 2: "findpeaks.m" to locate emission peaks of the smoothed spectrum, 3: "interp1.m" to interpolate and fit (method: 'pchip') the residual spectrum excluding peaks and 4: "sgolayfilt.m" (polynomial order 5, window size 101) to smooth the final background

line. Unfortunately, there is no unique emission line for the 5 cent coin as its surface is Cu, which is also present as alloying element in the other coins. Thus, by combining the Al (I) 396 nm and Cu (I) 522 nm lines can we determine the 5 cent coin diameter as 21.3 mm.

Using the Zn (I) 481 nm line causes errors if we exchange the position of the 1 € and 20 cent coins, because the spectrum of the edge of the 20 cent coin also contains this emission line. It is a challenge to minimize also the chance of classification errors caused by the coincidental arrangement of samples.

To resolve this issue we would modify Step 3 in the above emission line selection procedure and use multi-variate analysis, which is a topic of Chapter 6.

4.2.2. CLASSIFICATION OF BINARY MIXTURES

A classic scenario in quality inspection or materials sorting of waste is to distinguish one type of material from the rest and effectively regard the batch as a binary mixture. Thus, only the target material has to be recognised by LIBS while the rest of the materials may go unrecognised. Classification of multiple targeted materials (multi-classification) may be approached as a sequence of binary mixture cases, though there are also algorithms that can perform multi-classification in a single run (cf. Chap. 6). The major challenge for multi-classification using LIBS spectra is that the number of independent characterizing emission lines (or, in mathematical terms, orthogonal identifiers) for each targeted material decreases quickly if some of the other materials have a similar elemental composition. In those cases the single emission line approach is prone to generating classification errors.

There are two types of error to consider when LIBS is used to recognise a targeted material. To clarify we will use the example of a binary mixture of a pollutant material in natural gravel, which is also the experimental test case in this chapter. Here the pollutant is targeted by LIBS. A false negative (FN) is when a piece of pollutant material is not recognised and passes as a piece of gravel. A false positive (FP) is when a piece of gravel is erroneously recognised as a piece of pollutant. These are two different errors, each with a probability of occurrence that depends on: condition and cleanliness of the materials;

the careful method of presenting the materials to the LIBS unit; laser and optics; ambient conditions such as air humidity and vibration of the optics; and how distinguishable the target material actually is from the others when viewed as LIBS spectra.

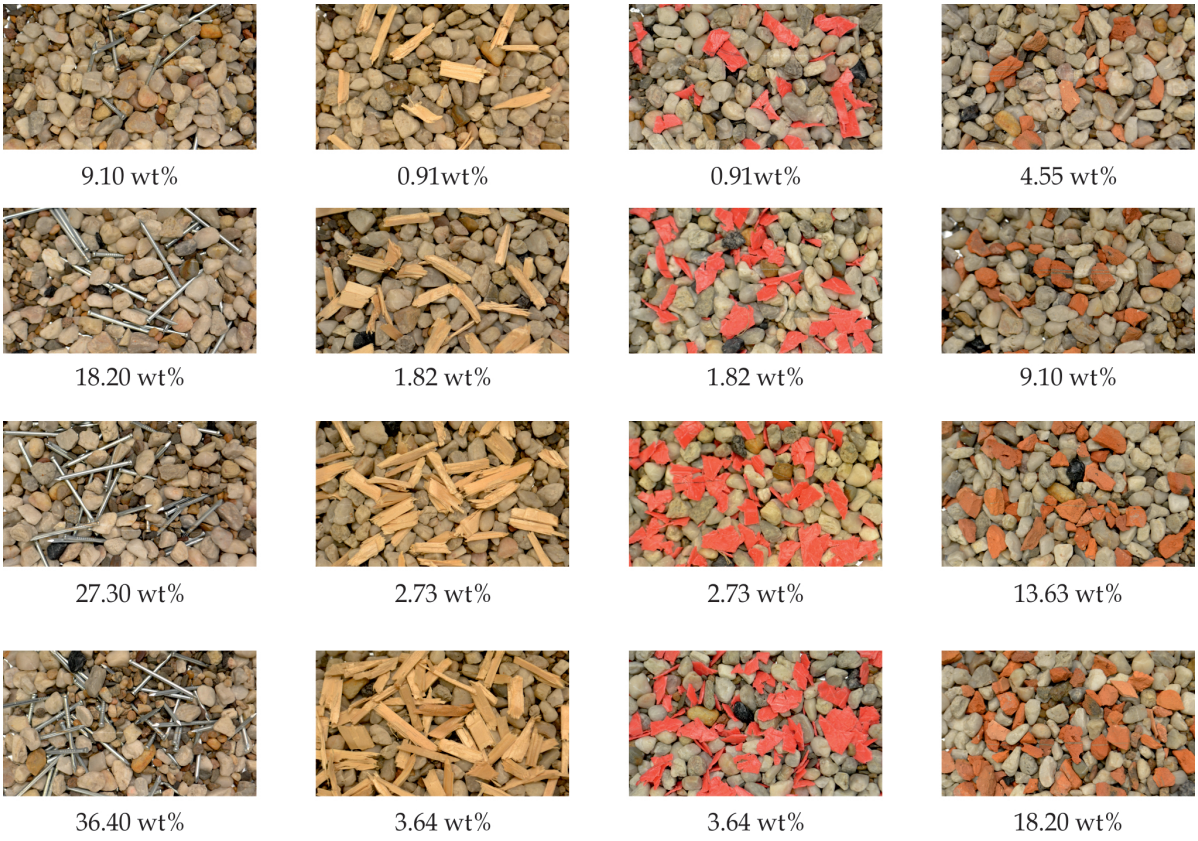


Figure 4.6: Binary material mixtures: Contaminants in natural gravel. From left to right: nail, wood, plastic and brick as contaminants; from top to bottom: different contamination levels for each contaminant.

An additional challenge for LIBS inspection is to convert the positive counts to the pollutant contents in terms of the unit contents determined in norms. For pure mixtures with very high quality demands the allowable pollutant content may be specified as a particles ratio. For example, if only 1 out of every 100000 particles is allowed to be a pollutant, this translates into very small allowable FP errors that pose a major challenge for any sensor-based quality inspection technology. But not in all cases will it be sufficient to just count the number of targeted particles. For example, the allowable content of brick in recycled concrete aggregate is determined in Dutch norms by a mass percentage. This requires the translation of LIBS counts to total brick mass, e.g. through an average brick particle mass obtained by calibration. For a volume-based norm the approach is slightly different. For example, the allowable amount of wood particles in recycled concrete

aggregates is determined in Dutch norms by a volume percentage per kilogram aggregates. This requires the translation of LIBS counts to total wood volume, e.g. through an average wood particle volume obtained by calibration, and a measure of the mass of the aggregates in the inspected waste batch.

If the target material is a minority, which is often the case in quality analyses, the FP is more critical than the FN. For example, if the probability of FN=0 % and FP=1 % while 2 % of the particles in a binary mixture are targets, the target particle number content is overestimated by 49 %. For the reverse case, FN=1 % and FP=0 %, the target number content is underestimated by only 1 %.

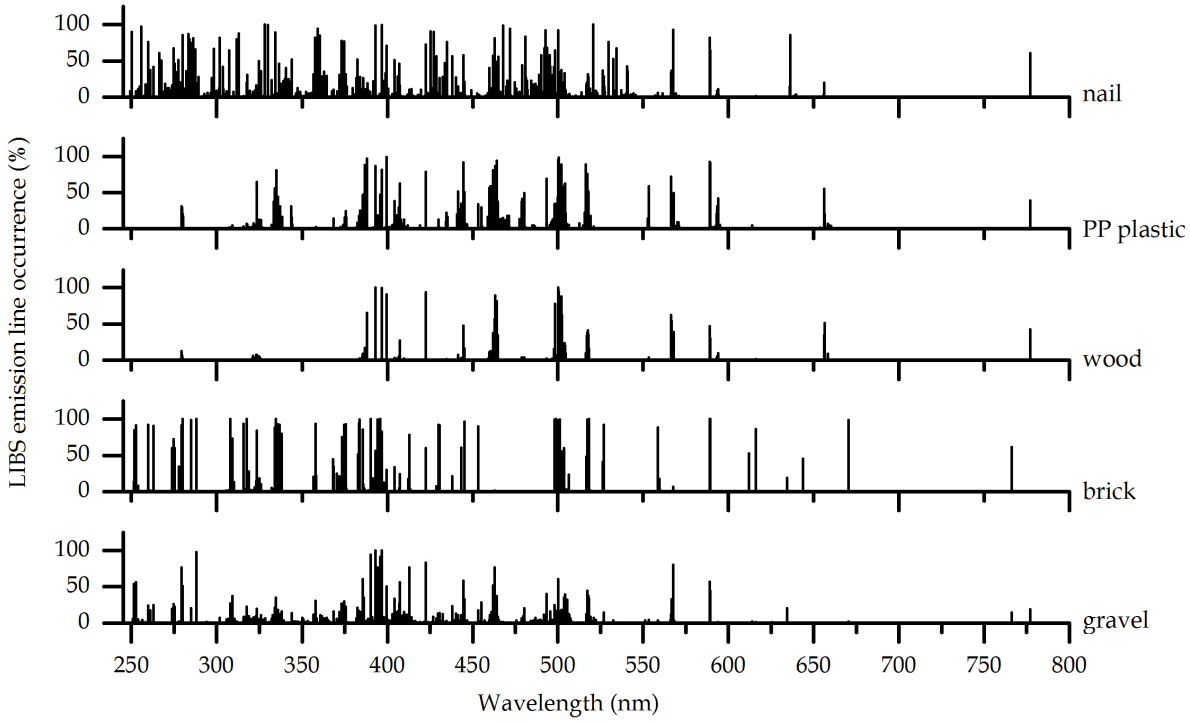


Figure 4.7: LIBS emission line occurrence [%] of nail, plastic (PP), wood, brick and gravel for training.

To test the probability of the classification errors with our LIBS setup we prepared binary mixtures of natural gravel (2-8 mm) with four types of pollutant with varying composition: steel nails, polypropylene (PP) flakes, wood and brick particles. The relatively clean binary mixtures are shown in Fig. 4.6. The training data set consisted of 700 LIBS single shots spectra. The raw spectra were translated to the occurrence spectra, which are shown in Fig. 4.7 as a function of wavelength.

The steel produces the highest occurrence with most of the emission lines originating from Fe, Zn and Cr. Because the LIBS is operated in air the N and O lines are observable in all spectra. Wood and PP appear quite similar in composition (C, H, O) though wood spectra are much less abundant w.r.t. to air emissions due to its porous nature. Brick has a similar spectrum as gravel but its emission lines have higher occurrence. We selected robust emission lines that are unique for the targeted pollutants with >90 % occurrence (cf. Tab. 4.3).

Table 4.3: Robust emission lines (>90% occurrence) for target pollutants and in natural gravel for each binary mixture. Lines are sorted by occurrence in descending order.

Steel nail against gravel	
Steel nail	Zn (I) 328.0, Cr (I) 520.6, Zn (I) 330.0, Zn (I) 467.8, Zn (II) 255.9, Fe (II) 359.2, Zn (I) 472.2, N (II) 567.6, N (II) 500.2, Zn (II) 492.6, Cr (I) 425.3, Fe (II) 250.3
Gravel	Si (I) 288.0, Si (I) 390.4, Al (I) 396.0
Plastic against gravel	
Plastic (PP)	N (II) 399.5, N (II) 500.6, CN 388.1, 500.2, 464.0, Na (I) 589.0, 444.5, Na (I) 589.6
Gravel	Ca (II) 393.2, Ca (II) 396.6, Si (I) 288.0, Si (I) 390.4, Al (I) 396.0
Wood against gravel	
Wood	N (II) 500.2, N (II) 500.6, Ca (I) 422.6, N (II) 399.5
Gravel	Si (I) 288.0, Si (I) 390.4, Al (I) 396.0
Brick against gravel	
Brick	Mg (II) 280.0, Al (I) 308.0, Ca (II) 317.8, Ti (II) 334.6, N (II) 499.0, Mg (II) 518.2, Na (I) 589.0, Na (I) 589.6, Al (I) 394.2, Ti (I) 498.0, Mg (I) 517.1, Mg (I) 383.7, Ti (I) 501.2, Mg (I) 285.0, N (II) 500.6, Li (I) 670.6, Ca (I) 445.3, Mg (I) 383.2, Fe (I) 357.9, Ca (II) 315.8, Fe (I) 375.7, Cr (II)335.8, Fe (I) 374.6, Cr (II) 336.9, Fe (II) 259.7, Ca (I) 430.0, Ca (I) 526.8, Mg (II) 279.3, Ti (I) 430.5, Fe (II) 252.7, Fe (II) 262.9, Ti (I) 453.3
Gravel	No robust emission lines from gravel because they're all present in brick with >90% occurrence

There were no robust emission lines from gravel, because all the emission lines with >90 % occurrence were also present in brick to the same degree. Each binary batch was mixed homogeneously and sampled by LIBS using the same settings as used in subsection 4.2.1 (100 Hz shot rate, 10 mm/s scanning speed). In total 700 LIBS spectra were collected for each of the four types of binary batch. In an attempt to minimize the errors we established the following procedure:

1. Select a robust emission line for each pollutant type. Combine several lines if there are no unique emission lines for a pollutant type.

2. Determine the average and STD of these emission lines over all the sampled spectra.

3. Set an amplitude threshold for classification.

4. Calculate the resulting number of FP and FN.

5. If the errors are minimum keep the threshold value, otherwise go back to step 3

Table 4.4: Training influence on false negative (fn) and false positive (fn) classification errors [%] for steel nail (691 qualified spectra) in gravel (553 qualified spectra) over threshold values set to different times of STDs above average emission line amplitudes of gravel using different robust lines.

	1STD		**3STD**		**5STD**		**10STD**	
Steel line [nm]	fn	fp	fn	fp	fn	fp	fn	fp
328.0	0	6.33	0	2.71	0	1.08	0.72	0
520.6	0	11.39	0.43	0.90	3.76	0	20.98	0
330.0	0	12.66	0	0.72	0	0.18	0	0
467.8	0	13.92	0	0	0	0	0.29	0
255.9	0	16.27	0	0.90	0.14	0.36	1.74	0
359.2	0.14	17.36	7.38	0.54	31.26	0	89.44	0
472.2	0	12.66	0	0	0	0	0	0
567.6	100	11.21	100	0.18	100	0	100	0
500.2	100	16.27	100	0.18	100	0	100	0
492.6	0.43	13.02	8.68	0	61.22	0	99.42	0
425.3	19.83	14.10	44.86	0	71.92	0	98.26	0
250.3	0.43	16.64	1.88	0.72	6.66	0	87.99	0

Tab. 4.4 lists the false negative (FN) and false positive (FP) classification errors for the binary mixture of steel nails and gravel, and for different choices of robust emission lines from the 700 LIBS spectra taken from the mixture. Threshold values for gravel varied from 1, 3, 5 to 10 STD above the average amplitude of the corresponding emission lines. The two orthogonal lines Zn (I) 330.0 and Zn (I) 472.2 nm were selected because these are not present in natural gravel. If the threshold increases the FN increase as more steel spectra are not recognised as steel and thus pass as gravel spectra. The FP decrease as fewer gravel spectra are mistaken as steel spectra. Also noteworthy are the N (II) 567.6 and N (II) 500.2 nm emission lines which amplitudes for gravel outweigh those for steel. Therefore, with these emission lines none of the steel spectra are recognised (FN=100 %) but fortunately also none of the gravel spectra are mistaken for steel spectra (FP=0 %). This choice of emission lines is clearly useless for targeting steel nails. It would be useful for targeting gravel, provided that is the minority material in a binary mixture. Fig. 4.8a shows the Zn (I) 472.2 nm line amplitudes in the training samples for steel nails (in black) and gravel (in red). The dashed line is a selected threshold value. As long as the orthogonal emission line amplitudes in the steel nails are significantly larger than those of gravel, and the threshold value is smaller than the minimum line amplitude in steel nail, the probability for both the classification errors is zero. It is not possible to find a threshold value giving zero errors using the

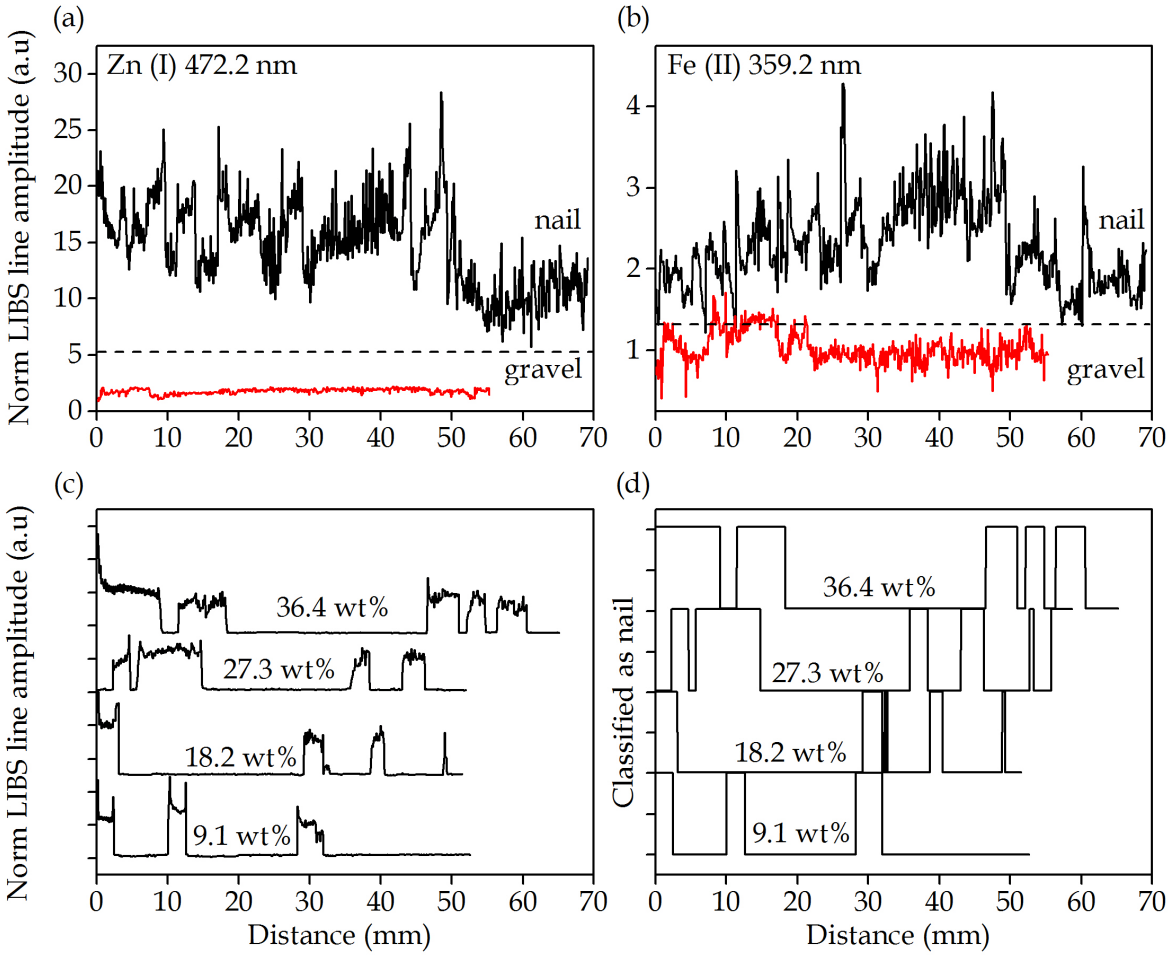


Figure 4.8: Normalized LIBS amplitudes of (a) Zn (I) 472.2 nm line and (b) Fe (II) 359.2 nm in training for steel nail and gravel. (c) Normalized LIBS amplitudes of Zn (I) 472.2 nm line in and (d) classified steel shots (using a threshold value of 6.) in four testing binary mixtures. Materials were moved at 10 mm/s speed and were measured by LIBS at 100 Hz.

Fe (II) 359.2 nm, because those emission line amplitudes overlap in steel and gravel. Next, we set a threshold value of 6 (>3STD of gravel) using the Zn (I) 472.2 nm line for the four testing mixtures (cf. Fig. 4.8c). Above the threshold the material is classified as steel nail (1), and below as gravel (0). The results are shown in Fig. 4.8d. The detected width of a nail agrees with the known nail diameter of 2 mm. However, this depends on the orientation of a nail w.r.t. the laser beam. The spectrum distortion occurs at the nail edge, where part of the plasma emissions may be shielded ($LIA > 40°$). Therefore, the emission line amplitude from the nail edge is significantly smaller and that it may lead to a false negative.

For the other binary mixtures no single orthogonal emissions lines (occurrence<90%, fn=fp=0) were found (cf. Tab. 4.5). In steel we used emission lines that minimized the sum

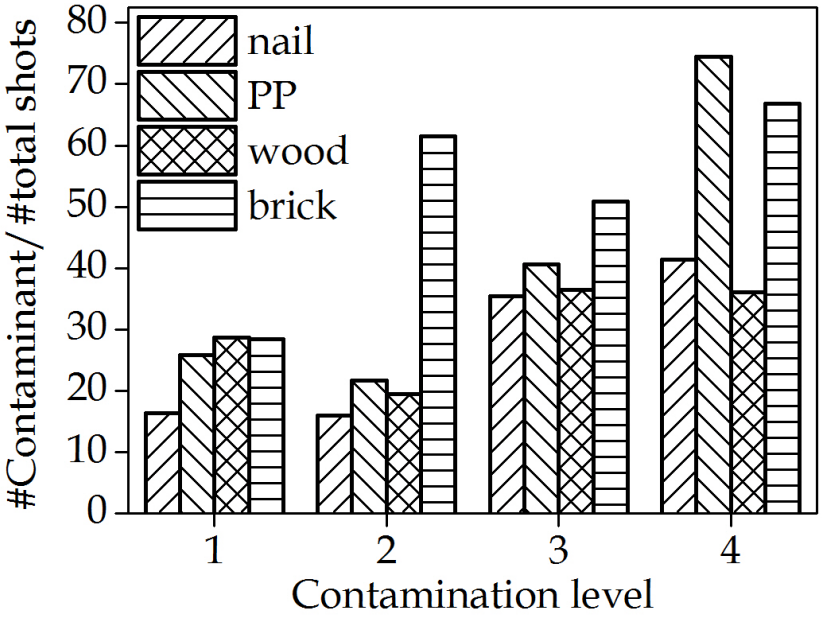


Figure 4.9: Binary classification of nail, wood, plastic and brick against natural gravel at 4 different contamination levels (cf. 4.6).

Table 4.5: Training false negative (fn) and false positive (fn) classification errors [%] of PP plastic, wood and brick in gravel over threshold values set to different times of STDs above average emission line amplitudes of gravel using different robust lines.

	1STD		2STD		3STD	
Material (line [nm])	fn	fp	fn	fp	fn	fp
PP (CN 388.1)	0.8	15	2	1.3	3.17	0.2
Wood (CN 388.1)	3	15	33.4	1.3	74	0.2
Brick (Li 670.6)	0.3	11.8	17	3.1	80	1.6

of classification errors, as based on training datasets. Fig. 4.9 shows the ratios of classified shots of pollutant and the total number of shots for four overall levels of contamination (cf. Fig. 4.6):

- Steel nail (Zn (I) 472.2 nm, occurrence=95%, threshold>6)
- PP (CN 388.1 nm, occurrence=97%, threshold>2STD=2.4)
- Wood (CN 388.1 nm, occurrence=66%, threshold>1STD=2.2)
- Brick (Li (I) 670.6 nm, occurrence=99%, threshold>1STD>0.67)

In the above case, the orthogonality of Zn (I) 472.2 nm line holds among all five materials, but the CN 388.1 nm line amplitudes also appear in plastic (PP) and wood. This leads to classification errors when plastic is to be recognised and distinguished from wood.

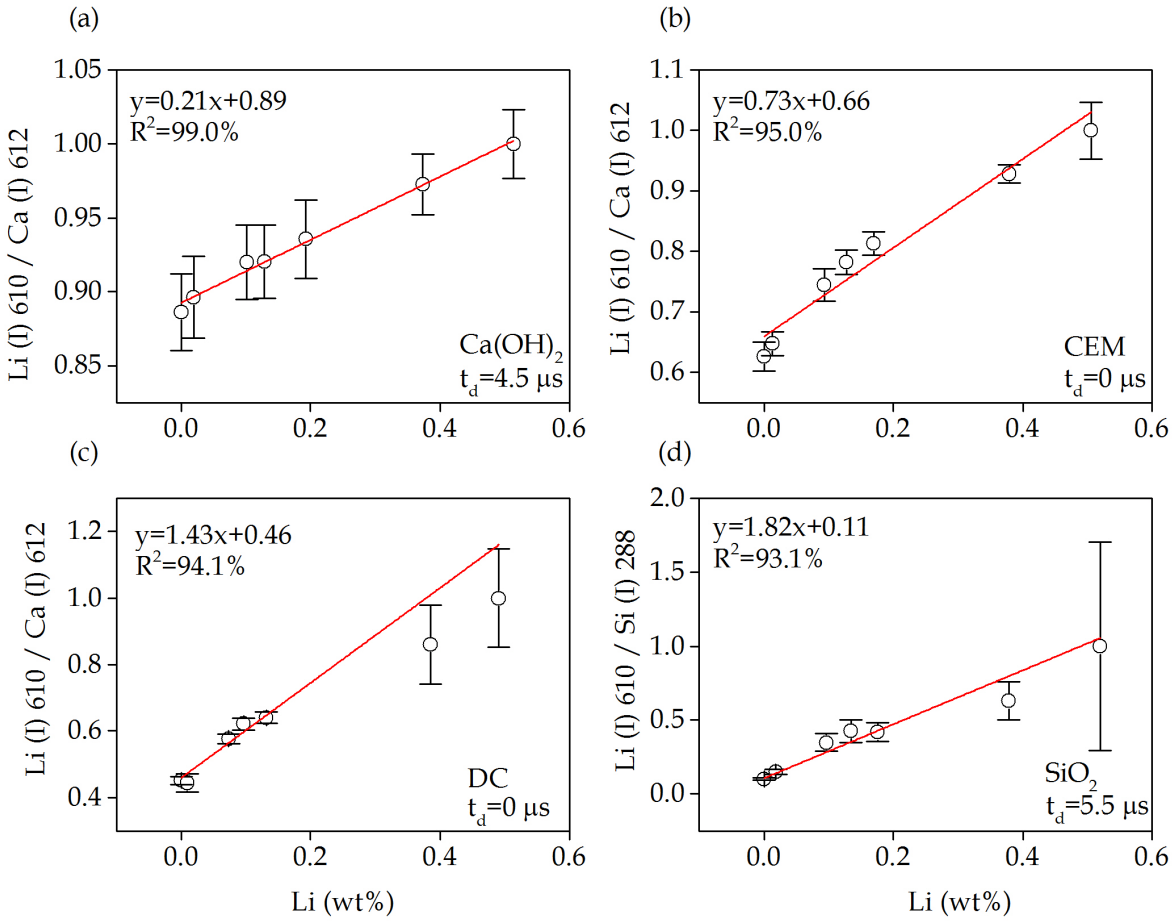


Figure 4.10: Calibration curves for the *Li* (*I*) 610 *nm* in four matrices: (a) $Ca(OH)_2$ (Ca=54wt%, Si=0wt%); (b) cement paste (CEM, $Ca = 54wt\%$, $Si = 17wt\%$), demolition concrete (DC, $Ca = 21wt\%$, $Si = 33wt\%$) and silica (SiO_2, $Si = 47wt\%$, $Ca = 0wt\%$). For each curve, every LIBS signal intensity is normalized to the maximum intensity from the 7th sample. The sensitivity for the minor compound increases with the Si content, demonstrating the 'pressure cooker effect'.

4.2.3. MATRIX EFFECT: TRACKING LITHIUM IN DIFFERENT MATRICES

Here we study the influence of a small concentration of the easily ablated salt lithium nitride in four matrices. This leads to a type of matrix effect which we called 'the pressure cooker effect' [6]. We distributed $LiNO_3$ in: $Ca(OH)_2$, cement paste (CEM), demolition concrete (DC) and silica (SiO_2). Main concept of the pressure cooker effect is that when the matrix breaks down at a higher threshold, the salt crystals with their low threshold will already be vaporized. This gives the disassociated minority species during ablation a higher probability of reaching a highly excited state in the plasma plume. As Fig. 4.10 demonstrates, the stronger the matrix (proportional to Si content) the higher the sensitivity (slope of the calibration curve) for the minor salt compound, in agreement with the proposed pressure cooker effect.

Table 4.6: Four sets of pressed pellet samples with varying lithium contents $wt‰$ in different matrices, i.e. $Ca(OH)_2$, hydrated cement paste (CEM), demolition concrete (DC) and silica SiO_2.

Sample#	Li $(wt\%)$ in $Ca(OH)_2$	Li $(wt\%)$ in CEM paste	Li $(wt\%)$ in DC	Li $(wt\%)$ in SiO_2
1	0.00	0.00	0.00	0.00
2	0.20	0.14	0.10	0.18
3	1.02	0.93	0.73	0.96
4	1.28	1.27	0.96	1.35
5	1.93	1.70	1.31	1.76
6	3.73	3.80	3.85	3.79
7	5.14	5.05	4.91	5.19

For each matrix type, an amount of 4 g was milled (Retsch ball mill) and then mixed with lithium nitride (cf. Tab. 4.6) together with distilled water (8 g). These samples are dried and then milled again at 20 Hz for 1 minute. Under identical milling conditions, the hardness of the matrix material determined how fine we could make the final powder grain size. This influences the matrix porosity after it is pressed into a pellet using 20 $tons$ of hydraulic pressure for 2 minutes.

The calibration curves of the LIBS signal intensity against lithium contents at selected times in $Ca(OH)_2$, CEM, DC and SiO_2 matrices are shown in Fig. 4.10 as a best linear fit $y = ax + b$ in Tab. 4.6. For the first three matrices the Li (I) 610 nm line intensity is normalized to the Ca (I) 616 nm line intensity. For SiO_2 it is normalized to the Si (I)288 nm line intensity. The slope related to the concentration y and signal intensity x is defined as:

$$b = R_{xy}\frac{\sigma_y}{\sigma_x} \tag{4.4}$$

where b is the intercept, σ_x and σ_y are the standard deviations of x and y, and R_{xy} is the standard correlation coefficient:

$$R_{xy} = \frac{\mathrm{cov}(x,y)}{\sigma_x \sigma_y} \tag{4.5}$$

Here $\mathrm{cov}(x,y)$ is the covariance between x and y. Fig. 4.11 shows the temporal evolution of the normalized correlation/regression coefficients of Li (I) 610 nm. Each calibration curve has its own optimum time delay: $t_d < 4$ μs for both CEM and DC, 2 $\mu < t_d < 6$ μs for $Ca(OH)_2$ and 5 $\mu < t_d < 7$ μs for SiO_2 matrices. Because the temporal evolution varies over samples we focus on the average per sample set. For pure matrices, the optimum time delay was reached later than for complex (composite) matrices that allows for many more available excited energy levels.

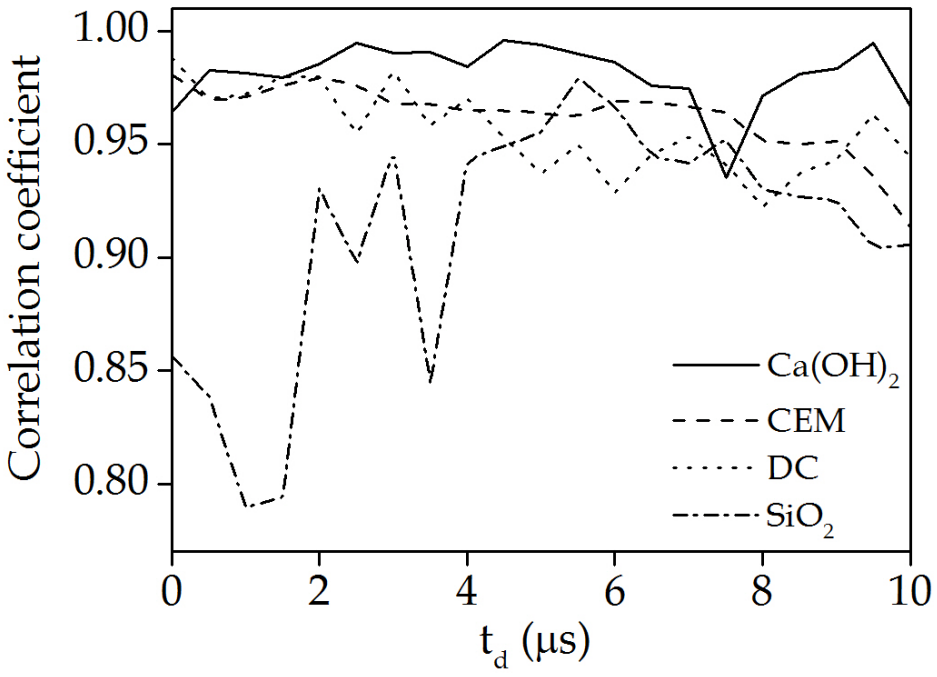


Figure 4.11: Regression coefficients of Li (I) 610 nm on four sample sets (7 samples per set) measured at 21 different time delays.

The average RSTDs over seven samples of the LIBS signal intensity are 2.67 %, 3.11 %, 6.52 %, 23.16 %, respectively, which corresponds to $Ca(OH)_2 < CEM < DC < SiO_2$). It is noted that a higher SiO_2 content complies with a coarser grain size. Also noticeable in Fig. 4.10 is the concentration effect, namely the RSTD grows with the Li contents in matrices except for $Ca(OH)_2$.

4.2.4. SENSITIVE DETECTION OF A THIN CALCIUM LAYER ON SAND GRAINS

We test the sensitivity of our LIBS system for small amounts of a mineral by detecting the presence of a very thin (submicron) layer of $CaCO_3$ adhered to sand grains. This capability is tested more quantitatively by detecting for a flattened surface of sand particles how much $CaCO_3$ is adhered and whether the layer is uniform over all the surface grains. This sensitivity test is relevant for practice as well. For example, it is a challenge to determine how much cement stone is adhered to broken old concrete that is going to be reused as gravel replacement in new mortar production. This is important because porous cement stone influences the strength of the cured concrete through the water to cement ratio of the wet mortar. To our knowledge there is no inline sensor-based measurement technique capable of verifying the thickness and homogeneity of a cement stone layer. The alternative

is a laboratory test such as an acid test or high-temperature treatment, which may be used to determine the total amount of attached cement stone in a small batch. To establish a relation between LIBS data and the presence of a thin surface coating is not straightforward, which is why we test two signal processing methods:

1. Use the emission line ratio of Ca over Si; a peak value indicates the presence of $CaCO_3$.

2. Classify single-shot LIBS spectra as Ca vs. sand, using principal component analysis (PCA, cf. Chap. 6) and then count the number of positively classified shots. The classification boundary is determined by the peripheral data points from Si and sand (NS) classes in the PCA plot Fig. 4.12a.

We use clean natural sand and coat it with pure $CaCO_3$ in the following procedure. The dry sand is sieved to the size fractions 0.5-1.0 mm and 1-2 mm. Samples of these fractions are soaked in a heated solution of $Ca(HCO_3)_2$. After different soaking times the samples are dried in an oven at $900°C$ for either two minutes or two hours, after which a crystalline layer of $CaCO_3$ is deposited on the sand particles. The dried samples were put in sample holders and the surfaces were flattened as a preparation for LIBS. The result were a number of samples varying in grain size, soaking time and drying time.

A first visual inspection revealed that the sand particles are still loose, though it could not confirm the overall presence of the extremely thin Ca layer. But the amount of $CaCO_3$ should be proportional to the signal intensity as in method 1. Yet it should also be proportional to how many sand particles are coated to the same degree, i.e. the uniformity of the layering, and thus to the number of positively classified counts of Ca in method 2.

Fig. 4.12b shows that the Ca indication gets stronger with longer soaking time (method 1, blank bars) and that the layer is distributed more homogeneously over the sand surface (method 2, grey bars). This trend is expected because deposition and adherence tends to increase with time inside the solution. Fig. 4.12c shows that the Ca/Si indications in the fine fraction (0.5-1 mm) are higher than for the coarse fraction. This may be attributed to the larger surface area for small particles. The figure also shows that the Ca/Si indication is significantly higher after 2 minutes drying than after 2 hours, while the Ca/Si indication

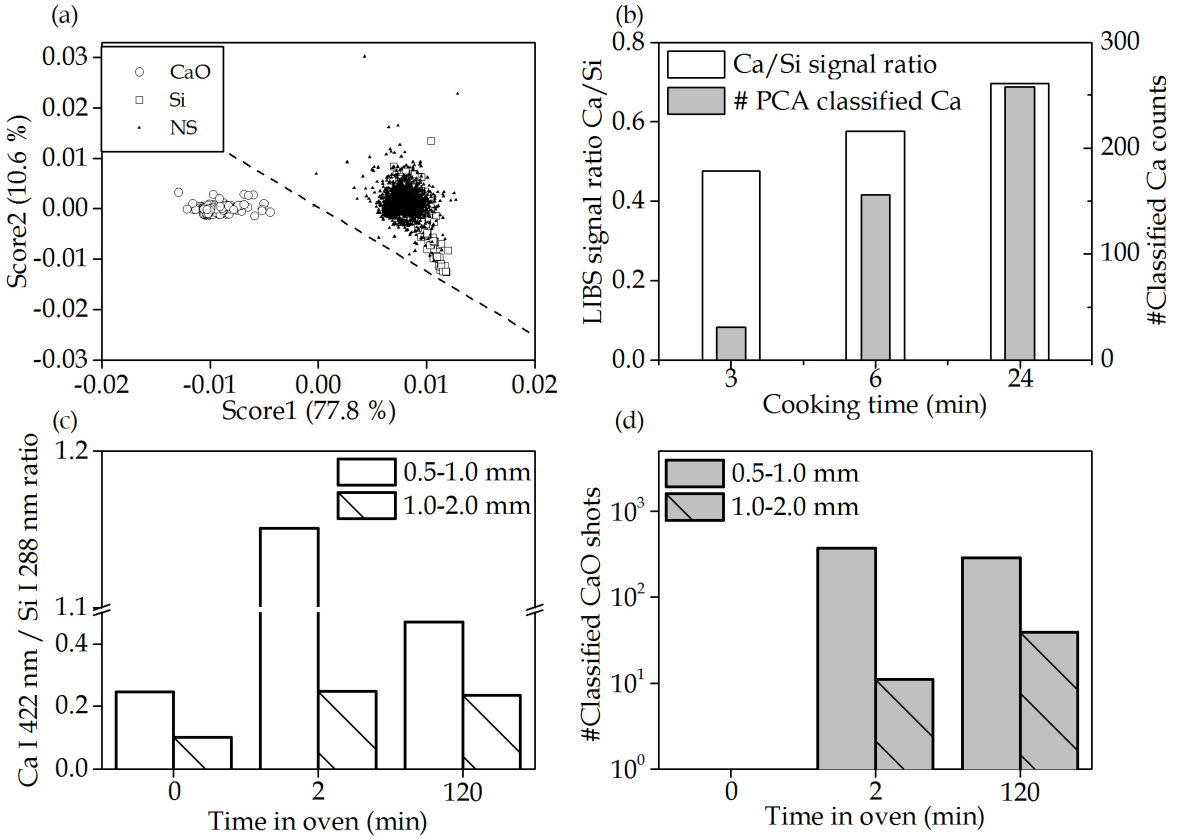


Figure 4.12: LIBS data correlated with surface treatment parameters. (a): Boundary for PCA classification into Ca-rich layer (CaO), silica (Si) and natural sand (NS); (b) relation between Ca/Si LIBS signal ratios using two signal processing methods with soaking time; relation between Ca/Si LIBS signal ratio using method 1 (c) and method 2 (d) with heating time.

for the coarse fraction (1-2 mm) is more or less stable after 2 minutes drying. This may be caused by the fact that the brittle Ca coating on a small, sharp edged sand grain is mechanically less stable than for a larger and smoother sand grain. Specifically when cooling the sample the thermal strains may cause the coating to let loose and percolate through the sand where it is out of reach of the LIBS laser. Fig. 4.12d shows that in the coarse fraction more sand grains are coated if the sample is left for 2 hours in the oven, according to expectation. The number of positively classified Ca-spectra in the fine fraction decreases with oven time, which is attributed to the same cause as the decline in the Ca/Si ratio. We may conclude that our LIBS system is quite sensitive as it can detect a submicron surface layer of a Ca mineral on sand grains, and even confirm if the thickness of this layer is uniform over all the sand grains.

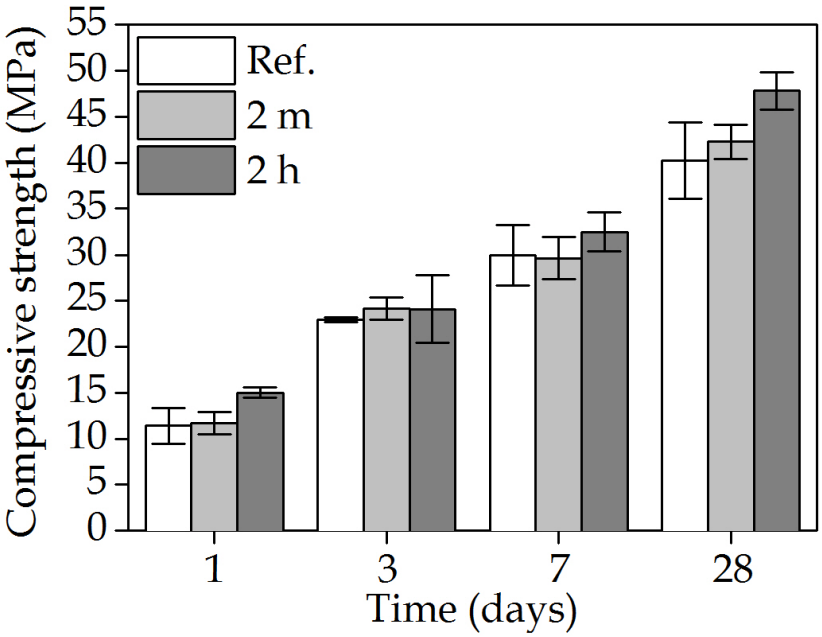


Figure 4.13: Compressive strength tests on mortar using coated sand. STD are obtained from three mortars per day test. White bar: reference mortar using 100% natural sand, light grey bar: mortar using sand heated at 900 degrees for 2 minutes, dark grey bar: mortar using sand heated for 2 hours.

4.2.5. RELATION BETWEEN LIBS SPECTRA OF SAND AND CONCRETE STRENGTH

In the preceding subsection we prepared two size fractions of sand and coated them with $CaCO_3$. These size fractions were dried in an oven at 900°C for either 2 minutes or 2 hours. Here, the size fractions for each drying time are mixed to size fractions 0.5-2 mm and used to make mortar with a water to cement ratio W/C=0.5. Reference mortars are made using the same W/C ratio but with uncoated virgin sand in the same size range. The wet mortars are poured into moulds to make prisms that are subsequently left to cure under moist atmosphere. The development of the compressive strength is tested after 1, 3, 7 and 28 days of cure. For each test three repeat samples are used to get an average and STD as shown in Fig. 4.13. Compared with the reference specimens, the Ca coated sand that was oven heated for 2 hours shows the highest compressive strength after 1 day; 32 % higher than reference. This becomes a trend with 8.6 % higher than reference after 7 days and 20% higher than reference after 28 days. The Ca coated sand that was oven heated for 2 minutes also shows a higher than reference strength after 28 days. A possible explanation for the higher strength of the prisms with Ca coated sand is the occurrence of Ca-Si reactions at the sand grain surfaces which become manifest above 800°C. Such matching interface could improve the bond between the cement, essentially a Ca-Si compound, and the pure

silica grains. With these tests we demonstrated a difference in the compressive strength of concrete resulting from differently treated batches of sand. Point is that these differences in raw material properties were sensitively detected and even quantified in terms of uniformity of distribution using LIBS. This reveals the potential of LIBS spectra for characterizing raw materials and to correlate these characteristics with the main engineering properties of the final product for which they are used.

REFERENCES

[1] L. Landau and E. Lifshitz, *Statistical Physics*, v. 5 (Elsevier Science, 2013).

[2] J. Reader, C. Corliss, W. Wiese, G. Martin, U. S. N. B. of Standards, and C. for Radiation Research, *Wavelengths and transition probabilities for atoms and atomic ions*, NSRDS-NBS No. pts. 1-2 (U.S. Dept. of Commerce, National Bureau of Standards : for sale by the Supt. of Docs., U.S. G.P.O., 1980).

[3] European Central Bank, *The EURO Coins,* (Last accessed on 01.06.2016).

[4] H. Xia and M. Bakker, *Quality of open air, single-shot libs spectra from waste particles,* in *OCM 2015-Optical Characterization of Materials-conference proceedings* (KIT Scientific Publishing, 2015) p. 169.

[5] H. Xia and M. Bakker, *Single-shot libs spectral quality for waste particles in open air,* tm-Technisches Messen **82**, 606 (2015).

[6] M. C. Bakker and H. Xia, *Laser-induced breakdown spectroscopy for identification of solid recycled materials,* SPIE Newsroom, Sensing & Measurement (2015), 10.1117/2.1201505.005950.

5

MODEL-BASED SINGLE-SHOT LIBS

The translation from raw LIBS spectra to material compositions is affected by shot-to-shot variations due to the heterogeneity of material properties (physical and chemical), varying experimental settings and ambient conditions. This is the reason that element contents are commonly determined by means of a statistical method based on a large number of measurements. To reduce the costs of LIBS data scanning in the envisioned recycling application it is desirable to make every shot count, which culminates in the ideal case of single-shot LIBS. It is also preferable to calculate the element contents without labour intensive training programs such as the supervised training required for chemometric methods (cf. chapter 6). This goal can be achieved with the help of a self-contained physical model that can explain each LIBS spectrum separately. The main objectives of this chapter are therefore to investigate the possibilities of deriving such a model and its potential for quantitative LIBS measurements. To make the highly complicated physics of laser ablation tractable we start from the assumption of thermal equilibrium as described in Chapter 2. This leads to the Boltzmann distribution for the electronic population for each species in the plasma plume, the Saha-equilibrium between different species (e.g. atoms, electrons, ions) and reducing the formation of the high-dimensional LIBS spectrum to a few key variables such as plasma temperature and electron density. These objectives are quite challenging, seeing that this method relies on raw data with an abundance of minor and weak emission lines. This method sets high requirements on the quality of the acquired LIBS spectra where it concerns temporal and spatial sensitivity and resolution, the dynamic range and the spectral bandwidth. In this work we use the extended visible

range 250-750 nm. There, the LIBS spectra from calcium-rich materials are dominated by Ca lines while other major and minor elements (e.g., Si, Al, Fe, Mg, Na, S and Cl) in typical cementitious materials have very few and/or very weak lines. In addition, most observed emission lines are quasi resonance lines that can be prone to self-absorption, even if the element concentration is lower than a few weight percentages. Using simulations based on atomic/ionic spectral databases, the LIBS spectra of different material compositions can be predicted from the part of the integrated spectrum where local thermal equilibrium (LTE) and Saha-equilibrium conditions apply. Practically, the well detectable emission lines in a spectrum for a known sample can be simulated using an appropriate model for the purpose of optimising the experimental setup in terms of range, resolution and sensitivity. The physical model can be verified using samples from cement and demolition concrete to test the accuracy and precision. This can demonstrate if this method can accommodate different material matrices with widely varying ranges of Ca/Si contents. Finally, the LIBS results of demolition concrete samples may be correlated with material processing parameters, which can offer information for process control and possibly shed light on material processing effects in real-time.

The work in this chapter builds on the following simplifying assumptions:

- None of the processes during the time that the laser is active need to be considered in the model (e.g. laser absorption, ablation, laser-plasma interaction).
- Transient processes can be approximated by stationary.
- Time overlapped processes may be modelled separately, assuming no interaction.
- LTE applies due to optically thin conditions in a certain time window in which the radiation of a species decays, which depends on the element and its concentration in the plume.
- The plume and its emitted spectrum can be represented by an average plasma temperature and an average electron density.
- Self-absorption in the plume is not taken into account in the model, but its influence may be quantified using a calibration method.

- The partition functions are independent of ambient influences, such as reduction of ionization energy or plasma energy level shifts. The functions include only those energy levels that are quantified in accessible databases. This assumption mainly effects elements with a quite large number of available excited states, for example Ca.

5.1. SIGNAL PROCESSING FOR MODEL-BASED LIBS: PLASMA ELECTRON DENSITY & TEMPERATURE

To reduce the setup variations all spectra are normalized to their mean spectral integral according to eq. 3.14. A broadened emission line is indicative of specific plume conditions. Line broadening may be caused by Doppler, resonance, Stark effects, and instrument width. We acquire spectra after delay time such that the peak widths of all emission lines of interest are larger than the instrumental width, measured as ~ 0.14 nm, which agrees well with the resolution provided with our spectrometer. Doppler line broadening is due to thermal motions of emitting species, here assume atoms rather than molecules, where the broadening at the observed central wavelength λ_0 in terms of full-width at half-maximum (FWHM) $\Delta\lambda^D$ $[nm]$ may be estimated by [1]:

$$\Delta\lambda^D = \lambda_0 \left[5.55 \times k_b T/(Mc^2)\right]^{1/2} \tag{5.1}$$

where T $[K]$ is the plasma temperature and M $[g]$ the mass of the emitting species. In this work Doppler broadening was in the order of ~ 10 pm[1] and may be ignored compared with the instrumental width.

Resonance lines associated with an electric dipole transition to ground state are also self-broadened with a FWHM $\Delta\ \lambda^R$ $[nm]$ [2]:

$$\Delta\lambda^R = 8.6 \times 10^{-28} (g_i/g_j)^{1/2} \lambda_0^2 \lambda_r f_r N_m^i \tag{5.2}$$

where gi, gj, λ_r $[nm]$, f_r, N_m^i $[cm^{-3}]$ are respectively the lower and higher level statistic weights in the transition, resonance wavelength, oscillation strength and number density of the ground state in species m. In this work, the resonance broadening for $Mg(I)$ 285.2 nm, $Na(I)$ 589.6 nm and $Ca(I)$ 422.7 nm all were in the order of ~ 10 pm

[1] The wavelength resolution of our spectrometer is much larger than picometres.

and therefore also ignored. Consequently, the Stark effect and instrument resolution dominated line broadening. Stark broadening may be expressed in terms of the FWHM value $[nm]$ that is linked to the electron density Ne $[cm^{-3}]$ as [3]:

$$\Delta\lambda^S = 2w\left(\frac{N_e}{10^{16}}\right) + 3.5\alpha_i\left(\frac{N_e}{10^{16}}\right)^{1/4} w[1 - 1.2N_D^{-1/3}]\left(\frac{N_e}{10^{16}}\right) \tag{5.3}$$

Here w and α_i are the temperature dependent electron and ion broadening parameters, respectively [4, 5], and N_D $[cm^{-3}]$ is the number of particles in the Debye sphere according to an numerical estimate [6, 7] with T $[K]$ and N_e $[cm^{-3}]$:

5

$$N_D = 1.3 \times 10^3 T^{3/2}/N_e^{1/2} \tag{5.4}$$

which is in the order of ~ 10 cm^{-3} in this work. The first term in eq. 5.3 is the electron collisional term and the second, is the ion collisional term. The latter is in the order of 10 pm and may be neglected. Stark broadening is therefore mainly contributed by electron collisions and eq. 5.3 is used to explicitly express the electron density in terms of the observed Stark broadening:

$$N_e = \Delta\lambda^S \times 10^{16}/(2w) \tag{5.5}$$

The documented electron Stark broadening parameters for most transitions are only available in the temperature range $5 \times 10^3 - 4 \times 10^4$ K from the literature, within which the electron density is determined by interpolating the documented electron broadening (w) over temperature for a selected emission line (Matlab scripts 'interp1.m' and 'pchip.m'). To simplify the spectral processing we introduce the Lorentz function that approximates the broadened emission line at the central wavelength with three parameters after the background subtraction:

$$L(\lambda) = \frac{L^P}{\pi}\frac{W^2}{(\lambda - \lambda_0) + W^2} \tag{5.6}$$

$2W$ is the FWHM value, L^P/π is the amplitude of the central emission line and WL^P is the total area [2] spanned by the broadened emission line with wavelength λ_0. An iterative procedure is applied to obtain the best fit while simultaneously eliminating the influence of

[2] Using variable substitution $\lambda - \lambda_0 = W \cdot tan\theta$ and $d\lambda = W(1 + tan^2\theta)d\theta$, the peak area is obtained by $\int_{-\infty}^{+\infty} L(\lambda)d\lambda = L^P \cdot \frac{W}{\pi} \cdot \int_{-\pi/2}^{+\pi/2} d\theta = W \cdot L^P$

a possible offset contributed by the continuum background. Due to the limited resolution of the CCD detector, a broadened emission peak is often composed of several overlapping peaks. To determine the Stark FWHM value for each individual peak, first the number of overlapping peaks must be determined and then the instrumental width eliminated. To this end a deconvolution is applied assuming a normalized Lorentz function (Matlab script 'deconv.m', with $2W = 0.14\ nm, L^P = 1,\ \lambda_0 = 0$). In details, after automated detection of the emission lines (Matlab script 'peakfit.m' [8]) the corresponding line broadening can be determined by Lorentz-fitting the lines in the original spectrum. The de-convoluted peak width of two Lorentzian functions equals the difference of their peak widths. In this way, the persistent broadening is subtracted from all measured FWHM values in the model calculations for electron densities.

5.2. DERIVATION OF MODEL-BASED LIBS

Neutral and singly ionized emission lines are the main contributions in the collected LIBS spectra. To understand the ratio of neutral and ionized species in the plasma plume is therefore a condition for effective application of LIBS. The emission line intensity is proportional to the product of the number of emitting species and the transition probability. Here we aim to derive a direct relation between the detected emission line intensity and the content of a species in the plume.

The radiation power density I $[W/cm^3]$ from the plasma at the selected emission line wavelength (λ) contributed by a homogenously distributed species (subscript m) is the product of the transition probability A_{ki} $[1/s]$, the number density of species N_m^j $[1/cm^3]$ and the difference of the upper energy level (superscript j) and a lower level (superscript i):

$$I_m^{ji} = \frac{hc}{\lambda} N_m^j(T) A_{ji} \tag{5.7}$$

The energy corresponding to a detected emission line is modelled by integrating this power density over a representative instrument volume and over the time window Δt during which the photons were accumulated. For simplicity, we assume the volume integration amounts to multiplication with a representative volume, while the time integration

amounts to a multiplication with the time interval. Note therefore that the transient plasma parameters in the real experiment are effectively approximated as constants in eq. 5.7. Again the model describes a stationary process which approximates the true transient power density, next denoted as $I(t)$, and the accumulated photon energy density over time as:

$$\int_{\Delta t} I(t)dt = I_m^{ji}\Delta t \tag{5.8}$$

Further, the receiver volume and time interval are assumed to be the same constants for all single-shot measurements. These may be ignored in the ensuing analysis, because all spectra will be normalized using the same spectral processing step without affecting data acquisition rate or other condition. Therefore, to simplify denotation, from here on I_m^{ji} is interpreted as the total detected photon energy per second $[J/s]$ or, equivalently, the number of photons per selected wavelength and per second. The distribution of the number density of species in eq. 5.7 obeys the Boltzmann distribution law under LTE:

$$N_m^j(T) = N_m g_j exp(-E_j/k_bT)/U_m(T) \tag{5.9}$$

Here N_m is the total number density of species m present in the plasma and g_j is the degeneracy, stating how many different states corresponding to the upper energy level can exist. E_j is the higher state energy and $U_m(T)$ is the temperature-dependent partition function of species m, which is obtained as the summation over all possible excited levels as:

$$U_m(T) = \sum_j g_j exp(-E_j/k_bT) \tag{5.10}$$

The temperature dependency of the partition functions are drawn from literature [9] and interpolated in an analogue fashion as eq. 5.5. Combining eq. 5.7 and 5.9, the energy corresponding to the selected emission line is:

$$I_m^j = \frac{N_m}{U_m(T)}\frac{hc}{\lambda}A_{ji}g_j exp(-E_j/k_bT) \tag{5.11}$$

According to eq. 5.11, the more degenerated the species is, the larger the partition function is and hence, the weaker each transition intensity becomes. The intensity ratio of two different emission lines from one species m only varies with the plasma temperature. For two different species, the ratio for two different emission lines depends also on their tem-

perature dependent partition functions. Therefore, for a calibration sample set the corresponding calibration curve of a species may be linear only if the plasma temperature for each sample is the same. In contrast with forenamed Boltzmann distribution describing electronic population for each species, the Saha-equation is used to describe LTE between different species, for example, neutrals, ions and electrons. In brief, the equilibrium constant K_e at a plasma temperature T [10, 11] is:

$$K_e = \frac{N_{i+1} \cdot N_e}{N_i} = \frac{2}{\Lambda^3} \frac{U_{i+1}(T)}{U_i(T)} exp(-\chi_{i+1}/k_b T) \tag{5.12}$$

$\Lambda = h/\sqrt{2\pi m_e k_b T}$ is the thermal de Broglie wave length for electrons. The factor $2/\Lambda^3 = 2.405 \times 10^{15} T^{3/2}$ $[cm^{-3}]$ may be interpreted as an energy state density function of the free electrons. The de Broglie cube Λ^3 tells how many electrons can be found per unit volume and this number is doubled by the spin degeneracy, as based on the uncertainty principle. As an indication, at $T = 1 \cdot 10^4$ K we find $\Lambda = 0.94$ nm.

The subscript $i+1$ for $i = 0, 1, 2, ...$ refers to higher ionization states. Specifically, subscript 'I' denotes neutral atomic species and 'II' the singly ionized species. Further, m_e is the electron rest mass, N_e is the electron density and χ_{i+1} is the $(i+1)$ th order ionization energy needed to ionize a species. In general, to allow for ionization with practically constant N_e, one has to consider if the thermal energy can provide the ionization energy and to which extent the ions are degenerate compared with the neutral atom. By substituting for $N_{II}(T)$ using eq. 5.12 in eq. 5.11, the intensity of an ionic emission line can be described by the atomic number density and partition function:

$$I_{II} = \frac{N_I(T)}{U_I(T)} \frac{hc}{\lambda} A_{ji} g_j exp[-(E_j + \chi_{II})/k_b T] \frac{2}{N_e \cdot \Lambda^3} \tag{5.13}$$

From eq. 5.11 and 5.13 we calculate the species total number density $N_{tot} = N_I + N_{II}$, for which we could use either a neutral or an ionic emission line. The element concentration is assumed proportional to the total of atomic and singly ionized number densities, thereby neglecting possible higher orders of ionization. It is possible the higher ionized species dominate in a very short time interval, but over the considered time window the plasma cools down with such a rate that we may assume that the emitting species are mainly composed of atoms and singly ionized ions. Substituting for N_I and N_{II} according to eq. 5.11

and 5.13, the total number density of an element is:

$$N_{tot} = N_I + N_{II} = \begin{cases} \frac{\lambda_I}{1-\gamma}\frac{U_I(T)}{hcA_{ji}g_j} exp(E_j/k_bT) & ,atomic\ lines \\ \\ \frac{\lambda_{II}}{1-\gamma}\frac{U_I(T)}{hcA_{ji}g_j}\frac{\Lambda^3 N_e exp[(E_j+\chi_{II})/k_bT]}{2} & ,ionic\ lines \end{cases} \tag{5.14}$$

The ionization fraction $\gamma(T) = N_{II}(T)/(N_I(T) + N_{II}(T))$ is valid under LTE conditions. An auxiliary relation is:

$$\frac{1}{1-\gamma} = \frac{2}{\Lambda^3 N_e}\frac{U_{II}}{U_I} exp(-\chi_{II}/k_bT) + 1 \tag{5.15}$$

5

Here we assume that free electrons in the plasma plume obey a Maxwellian distribution, at the tail of which there are electrons with high enough kinetic energy for ionization by collision. In fact, even at relatively low temperature ($\chi_{II} \gg k_bT$), there is a certain ionized fraction and to check how fast the ionization fraction grows from zero another temperature is defined at the ionization fraction $\gamma = 0.5$:

$$T_{0.5} = \chi_{II} \cdot \left[k_b \cdot ln\left(\frac{2}{\Lambda^3 N_e} \cdot \frac{U_{II}(T)}{U_I(T)} \right) \right]^{-1} \tag{5.16}$$

Assuming the degeneracy term is independent of the temperature in a well chosen temperature interval, eq. 5.16 implies that the more degenerate an ion is with respect to the atom, the lower $T_{0.5}$ is, i.e., the easier it is to ionize the atom. The ionization rate $[K^{-1}]$ at $T_{0.5}$ is:

$$\frac{d\gamma(T)}{dT}\Big|_{T_{0.5}} = \chi_{II}/4T_{0.5}^2 \tag{5.17}$$

Fig. 5.1 shows the ionization fraction of the singly ionized ion for eight representative elements for concrete. These are: Ca, Si, Al, Fe, Mg, Na, S and Cl as a function of plasma temperature ($5 \cdot 10^3 - 1 \cdot 10^5$ K) and electron density ($10^{12} - 10^{22}$ cm^{-3}). The lower density limit of 10^{12} cm^{-3} complies with the minimum electron density required for LTE according to [12]:

$$N_e^{min} = 3\Delta E^3 T^{1/2} \tag{5.18}$$

where ΔE $[cm^{-1}]$ is the largest transition energy. It is noted that for lower density thermalization of the electrons is unlikely due to the low probability of collisions. Although outside

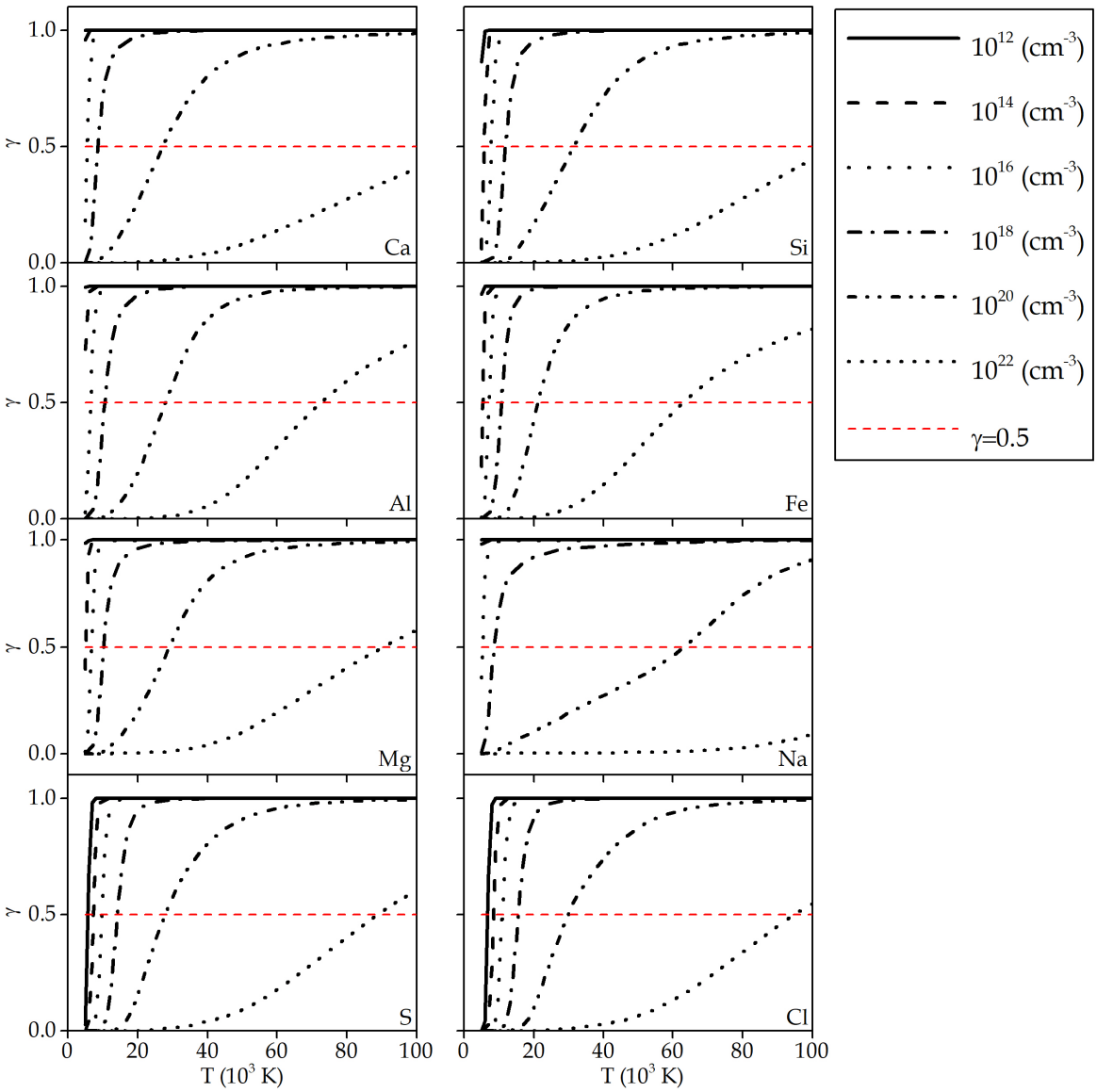


Figure 5.1: Calculated ionization fraction (cf. eq. 5.15 of eight elements as a function of plasma temperature and electron density. Each set of curves corresponds to six electron densities in the range 10^{12} to 10^{22} cm^{-3}.

the present discussion, for completeness we note that the upper density limit of 10^{22} cm^{-3} complies with the critical plasma electron density according to [10]:

$$N_e^{max} = \frac{4.4 \times 10^{28}}{\lambda_{laser}^2} \tag{5.19}$$

Above this electron density the incident laser light will be totally shielded by the plasma, effectively stopping ablation, λ_{laser} is the incident laser wavelength $[nm]$. The general trend in Fig. 5.1 is similar for all elements as the ionization fraction first grows very fast and then starts to saturate before reaching unity. At lower electron density, $T_{0.5}$ is reached

for Ca, Si, Al, Fe below $5 \cdot 10^3$ K. With increasing electron density, the curve starts to flatten. At 10^{22} cm^{-3}, Ca, Si and Na cannot reach $\gamma = 0.5$ even at 10^5 K in contrast with other elements, because their $U_{II}(T)/U_I(T)$ ratios are smaller with increasing temperature. For instance, with $N_e = 10^{16}$ cm^{-3}, $T_{0.5}$ (ionization rate K^{-1}, cf. eq. 5.17) are 5600 $K(0.56 \cdot 10^{-3}$ $K^{-1})$, 8200 K $(0.35 \cdot 10^{-3}$ $K^{-1})$, 6800 K $(0.38 \cdot 10^{-3}$ $K^{-1})$, 7400 K $(0.42 \cdot 10^{-3}$ $K^{-1})$, 7000 K $(0.45 \cdot 10^{-3}$ $K^{-1})$, 5300 K $(0.53 \cdot 10^{-3}$ $K^{-1})$, 10600 K $(0.27 \cdot 10^{-3}$ $K^{-1})$ and 12000 K $(0.26 \cdot 10^{-3}$ $K^{-1})$ for Ca, Si, Al, Fe, Mg, Na, S and Cl, respectively. Compared with the ionization potential in Tab. 5.1, the $T_{0.5}$ is indeed much lower. For some metals such as Al of which $T_{0.5}$ is comparable with that of Na, heating the sample by just a few hundred degrees may enhance the ionic emission line intensity significantly. At constant temperature and electron density, $T_{0.5}$ is proportional to χ_{II} and γ increases with increasing ratio $U_{II}(T)/U_I(T)$. Specifically, at $20 \cdot 10^4$ K and 10^{22} cm^{-3}, only γ_{Fe} is > 0.5 by virtue of its relatively smaller χ_{II} and larger $U_{II}(T)/U_I(T)$.

Table 5.1: Model parameters: g is statistic weight, A [10^8 s^{-1}] is transition probability, E [cm^{-1}] is energy level (in wavenumber units)[9, 13], and χ_{II} [10^3 K] is the first order ionization energy [14].

species	λ [nm]	g_j	A_{ji}	E_i	E_j	T	N_e	N	χ_{II}
$Fe\ (II)$	262.6	10	0.34 ± 0.09	385	38459			✓	91.7
$Si\ (I)$	288.2	3	1.89 ± 0.47	6299	40992		✓	✓	94.6
$Mg\ (I)$	285.2	3	5.3 ± 2.65	0	35051		✓	✓	88.7
$Al\ (I)$	309.3	6	0.74 ± 0.19	112	32437			✓	69.4
$Na\ (I)$	589.6	2	0.62 ± 0.02	0	16956			✓	60.0
$S\ (I)$	921.3	7	0.28 ± 0.14	52624	63475			✓	120
$Cl\ (I)$	837.6	8	0.28 ± 0.14	71958	83894			✓	150
$Ca\ (I)$	616.2	3	0.48 ± 0.12	15316	31539	✓	✓	✓	70.9
$Ca\ (I)$	422.7	3	2.18 ± 0.22	0	23652	✓			
$Ca\ (I)$	430.3	5	1.36 ± 0.34	15316	38552	✓			
$Ca\ (I)$	445.5	7	0.87 ± 0.22	15316	37757	✓			
$Ca\ (I)$	527.0	5	0.5 ± 0.25	20371	39340	✓			

5.3. MODELLING LIBS SPECTRAL LINES

We model LIBS spectral lines based using eq. 5.11 to study the influence of elements and excited species. To this end we take the following steps:

1. Select elements and species and input the plasma temperature and electron density.
2. Calculate species number density ratios based on the Saha-equation (eq. 5.12) and the temperature dependent partition function of each species.
3. Fit the atomic/ionic emission spectrum for each species using the Lorentzian function

(eq. 5.6), and calculate the synthesized element spectrum as a superposition of all element species and then calculate the synthesized spectrum as the superposition of the included elements.

4. Vary the temperature and electron density independently and study dependence trends in the corresponding simulated LIBS emission line intensities.

5. Input the LIBS emission line intensities of each element species and either determine the corresponding number densities or convert them to weight percentages in the (virtual) plume.

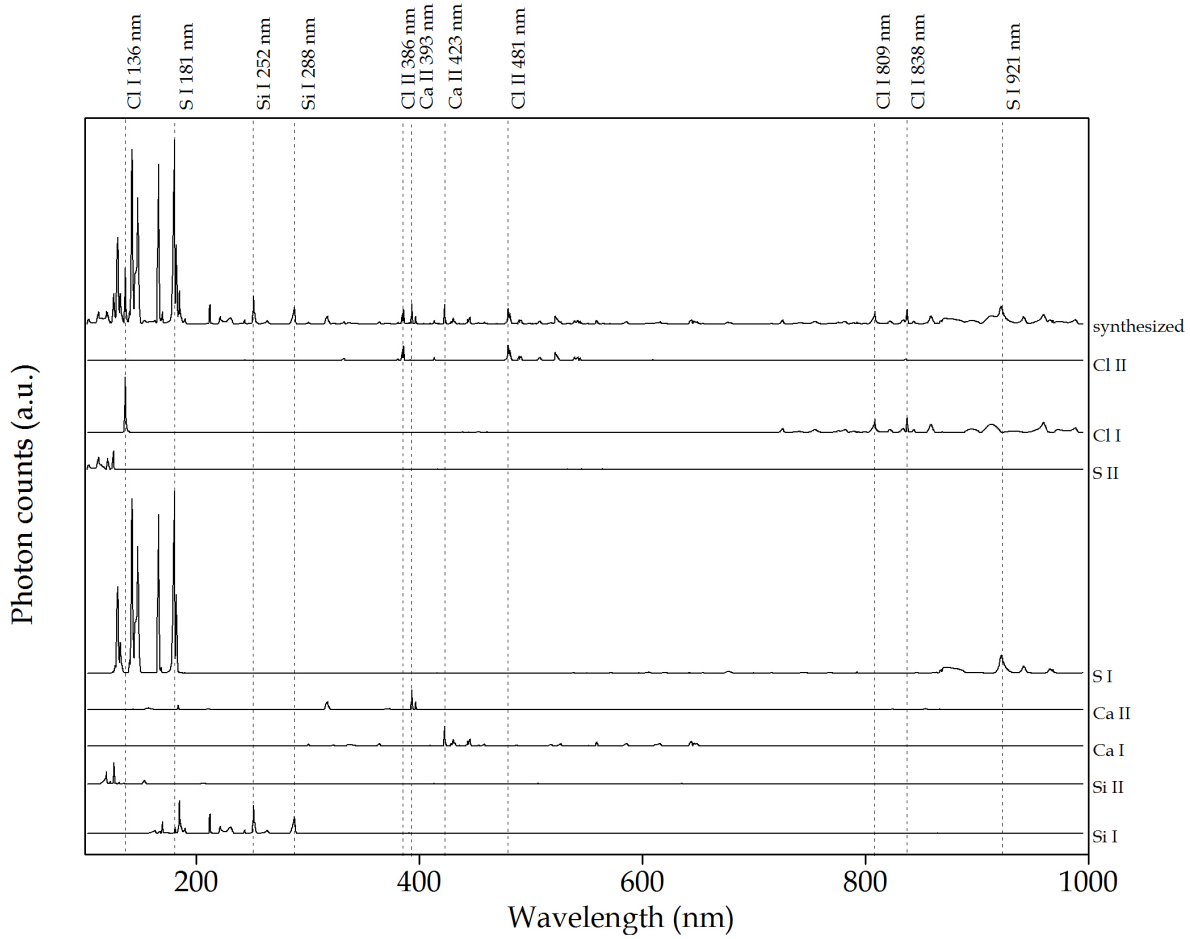


Figure 5.2: Synthetized LIBS spectra composed of Ca $(I\&II)$, Si $(I\&II)$, S $(I\&II)$ and Cl $(I\&II)$.

First we produce a synthesized LIBS spectrum $(100-1000\ nm)$ composed of eight species Ca $(I\&II)$, Si $(I\&II)$, S $(I\&II)$, and Cl $(I\&II)$ (cf. Fig. 5.2) in accordance with eq. 5.11. The number density ratios for six species are chosen to be $13.6:\ 1.13:\ 8.75:\ 1.00:\ 85.5:\ 89.38:\ 147.63:\ 1.56\cdot 10^3$ so that their major atomic/ionic line intensities (between 250 –

800 nm) are conveniently in the same order of magnitude. In total, 910 emission lines and available atomic parameters are taken from the NIST database[9]. These are shown with 106, 57, 98, 86, 174, 289, 70, 46 emission lines, respectively, for $Ca\ I$, $Ca\ (II)$, $Si\ (I)$, $Si\ (II)$, $S\ (I)$, $S\ (II)$, $Cl\ (I)$ and $Cl\ (II)$. The FWHM is set at 0.3 nm and the plasma temperature at $20 \cdot 10^3\ K$. It is observed that the strongest lines are found in the UV range $100-200\ nm$ for which the atomic parameters were documented for ultra-vacuum conditions.

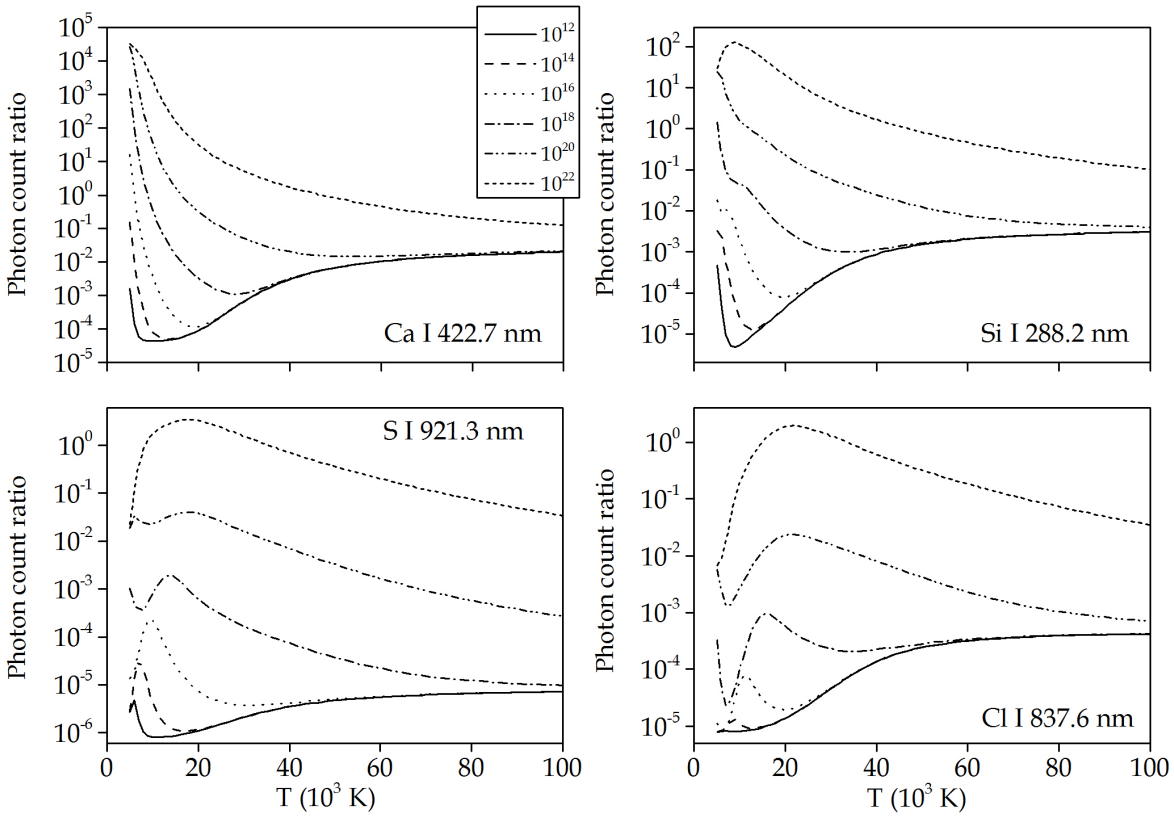


Figure 5.3: Emission line intensity ratios of $Ca\ (I)$ 422.7 nm, $Si\ (I)$ 288.2 nm, $S\ (I)$ 921.3 nm and $Cl\ (I)$ 837.6 nm (from left to right and from up to down). Each set of curves correspond to five electron densities in the range 10^{12} to $10^{22}\ cm^{-3}$ over plasma temperature from 50 to $1 \cdot 10^5\ K$.

Shown in Fig. 5.3 from left to right and from top to bottom are the relative emission line intensity ratios of $Ca\ I$ 422.7 nm, $Si\ I$ 288.2 nm, $S\ I$ 921.3 nm and $Cl\ I$ 837.6 nm to $Ca\ II$ 393.4 nm as a function of plasma temperature. The number density is the same for each element, and the atomic-to-ionic number density ratio for each element is determined by eq. 5.12. The $Ca\ II$ 393.4 nm line has been chosen as the reference because it is the strongest and most persistent line detected in our experimental setup using cementitious samples. In comparison, one can determine which temperature and electron density ranges may be optimum for LIBS and can help increase the SNR of the line under inves-

tigation. In accordance with eq. 5.11, the atomic-to-ionic line ratio for $Ca(II)$ 393.4 nm is:

$$\frac{I_I^m}{I_{II}^{Ca\ II\ 393.4\ nm}} \sim \frac{N_I^m(T,N_e)}{N_{II}^{Ca}(T,N_e)} \cdot \frac{U_I^m(T)}{U_{II}^{Ca}(T)} \cdot exp\left(\frac{E_{upper}^{Ca\ II\ 393.4\ nm} - E_{upper}^{m\ transition}}{k_b T}\right) \tag{5.20}$$

The first ratio N_I^m/N_{II}^{Ca} decreases with T and increases with N_e; while the second ratio depends on the temperature dependent partition functions. Typically, the second ratio decreases and then increases with temperature, except for U_I^{Ca}/U_{II}^{Ca} which increases monotonically with temperature. The exponential term in eq. 5.20 saturates at unity if the temperature is increased infinitely.

This model may be used to predict under which conditions the maximum SNR in the LIBS data can be expected for selected emission lines. For example, there is a maximum amplitude ratio for each of the four atomic emission lines with respect to the dominant $Ca\ (II)$ 393.4 nm line in the range $5000 - 25000\ K$, and this maximum shifts towards higher temperatures for increasing electron density. For instance, at $N_e = 10^{16}$ the optimum temperature is 5000, 8000, 11000 and 15000 K, respectively for $Ca\ (I)$ 422.7 nm, $Si\ (I)$ 288.2 nm, $S\ (I)$ 921.3 nm and $Cl\ (I)$ 837.6 nm.

The model can also calculate the experimental requirements for the spectrograph and subsequent CCD and analogue-digital converter (ADC). For example dynamic range and amplitude resolution. The ratio between the strongest and weakest emission line indicates the required dynamic range, while the desired amplitude resolution for each line gives the required minimum number of bits related to ADC.

The number density for an element in the plume must be determined from the observed LIBS emission lines for the available species. Assuming all these species in the plasma plume are distributed the same way (not necessarily homogenous) during the time window of observation, a normalization factor F may be defined that relates the calculated number density N of element p to its perceived molar percentage M_p in the sample,

according to $M_p = N_p/F$. For a total of P elements we find:

$$\sum_{p=1}^{P} N_p(T) = F \tag{5.21}$$

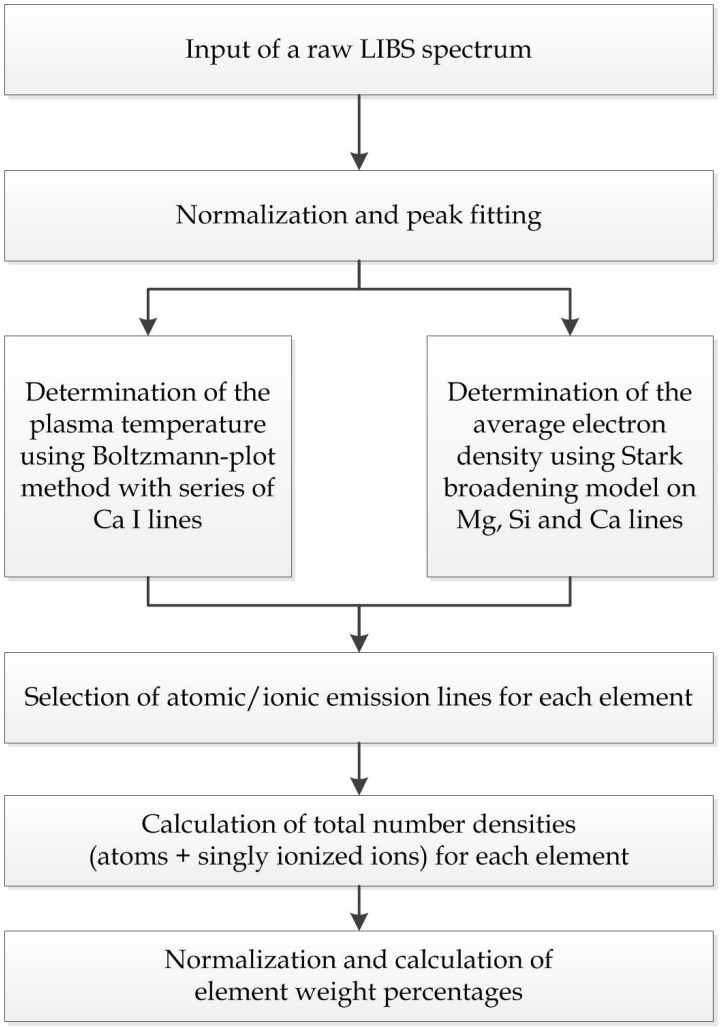


Figure 5.4: Flow chart of the proposed model based LIBS.

A disadvantage of contents normalization is absolute error transfer, in particular if a small measurement error for a major element transfers into a big error for a minor element. The model-based LIBS (MLIBS) flow chart for concrete/cement is shown in Fig. 5.4. For each element an emission line is selected with low transition probability and well-resolved. Up to five Ca (I) lines are used for the Boltzmann plot, and three emission lines from Si, Mg and Ca (limited by available Stark broadening constants) are used to determine the electron density. The desired number densities and molar concentrations follow from eq. 5.14 and eq. 5.21.

Table 5.1 lists the parameters that are used in the model. The emission lines used to determine the plasma temperature T, electron density N_e and element number density N_{tot} are marked with ✓. The S (I) 921.3 nm and Cl (I) 837.6 nm lines could not be detected in our setup. Here, they are listed solely for the benefit of the simulations.

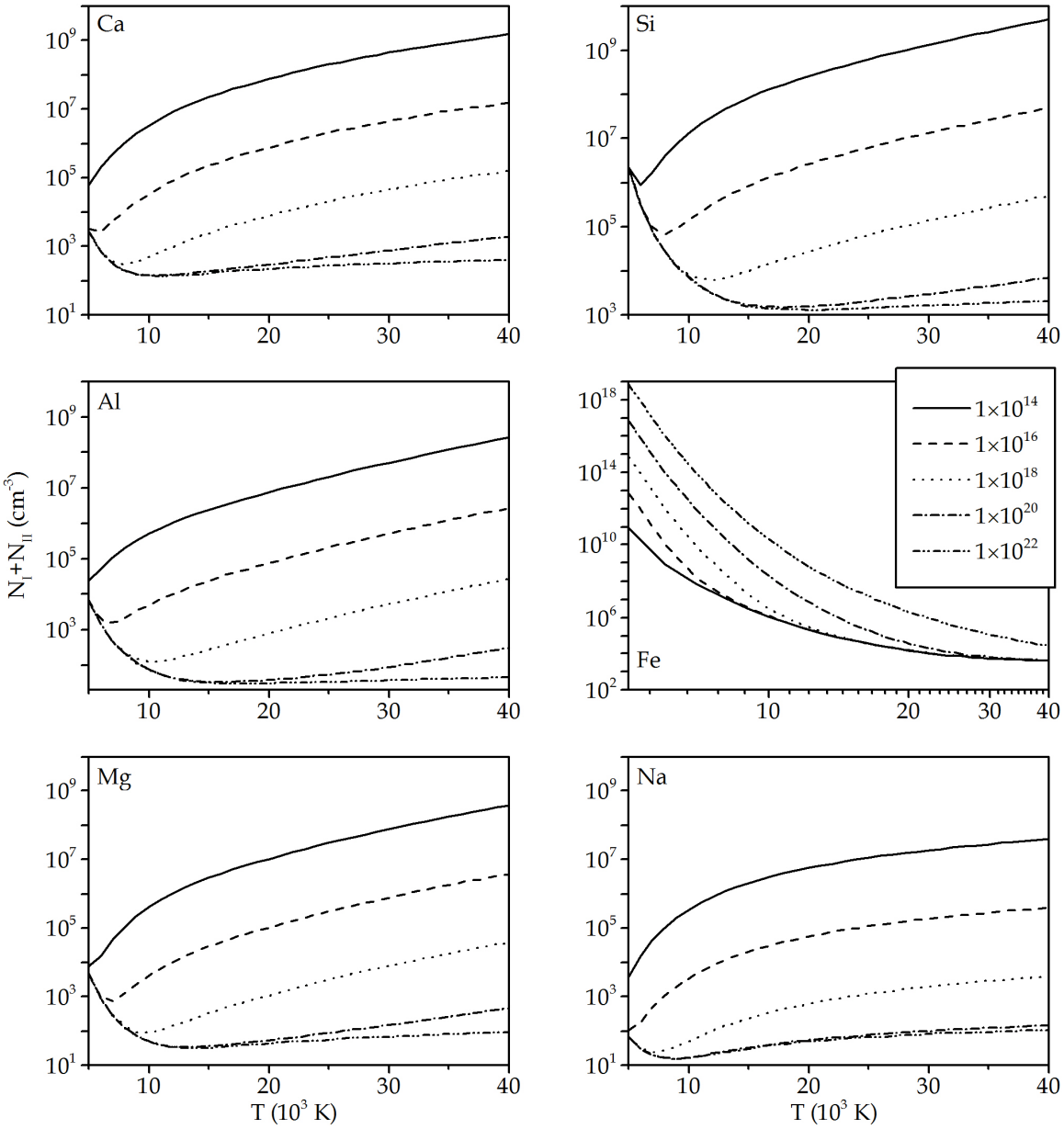


Figure 5.5: Model calculations of the number densities $N_I + N_{II}$ (cm^{-3}) for the concrete contents as a function of plasma temperature. Each set of curves correspond to five electron densities in the range 10^{14} to 10^{22} per cm^3. All emission lines are related to atomic lines (semi-log scale), except for Fe which is related to an ionic line (double-log scale).

Next we study the solution space of the model in Fig. 5.4. This space explains the number

density $N_I + N_{II}$ (cm^{-3}) as a function of plasma temperature and electron density and their sensitivities. Fig. 5.5 shows calculations based on measured LIBS spectral line intensities collected from a concrete sample to study the solution space of the model using LIBS emission line intensities as inputs (cf. eq. 5.14). The start of LTE may differ per emission line, but here $N_{tot} = N_I + N_{II}$ is calculated as a function of temperature for a certain electron density within ranges that are typical for a nanosecond pulsed laser. The atomic curves of Ca, Si, Al, Mg and Na increase monotonically at higher temperatures in complete contrast to the ionic Fe lines. This opposite behaviour is in accordance with the reciprocal electron density term in eq. 5.14 for these two types of emission lines. For a fixed number density of species the electron density tends to increase with temperature, as expected. For a fixed temperature, the number density of species increases with decreasing electron density for atomic lines, while the Fe ionic line shows the opposite trend. The different relative element concentrations with respect to temperature and electron density are caused by the differences in sensitivity for the different elements, as determined by the slope of a curve. This slope depends on the corresponding partition function through temperature, transition probability and statistic weight related to the element at hand.

5.4. MODEL BASED LIBS APPLIED TO CEMENTITIOUS MATERIALS

In this section the reliability and sensitivity of model based LIBS (MLIBS) is tested. For this purpose we make use of reference sample sets of pure cement and pure Si-Ca compounds. Our test samples are demolished concrete (<4 mm or <1 mm) that is processed in different ways with the purpose of concentrating the old cement stone. As a reference technique for the elemental composition of non-certified samples we apply X-ray Fluorescence (XRF). For representative and repeatable reference measurements it is necessary to prepare samples to the highest standards, especially for XRF, but where possible LIBS will be tested with a minimum of sample preparation because that will mimic the inline situation in an industrial setting.

5.4.1. XRF AS A REFERENCE TECHNIQUE

XRF is used as a proven technique to determine the elemental composition of solids, similar to LIBS. However, in LIBS the optical emissions are due to energy transitions mainly

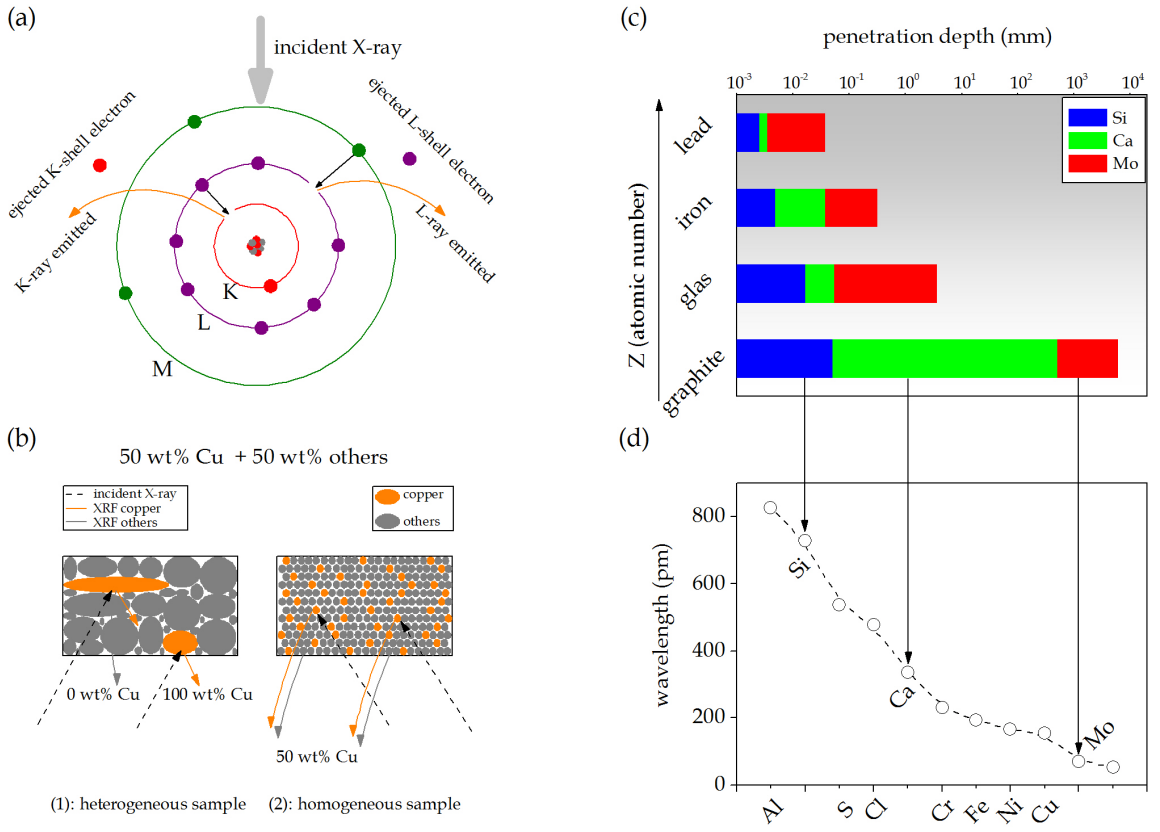


Figure 5.6: (a) XRF principle of photon excitation and (b) sampling bias in a heterogeneous sample versus a homogeneous sample; (c): XRF photon penetration depth in different matrices and (d) examples of different photon wavelengths according to the exited element. Graphs (a), (c), (d) are reproduced from [15]

involving the outer valance electrons that are responsible for chemical bonding in the solid state. XRF, on the other hand, relies on optical emissions due to high energy transitions involving electrons removed from the inner atomic shells. For example the K_α lines, i.e. the first excited upper level to ground level transition, can be used to determine Ca and Si contents (cf. Fig. 5.6a). In view of the high photon energies XRF might be expected to be free of any matrix effect. In contrary, both XRF and LIBS are susceptible to self-absorption and sensitive to material density and conditions of the sample surface. Moreover, if a particulate sample is not finely milled and homogeneous (cf. Fig. 5.6b1) both XRF and LIBS measurements may be affected. As shown in Fig. 5.6c the fluorescent Xray penetration depth decreases with increasing atomic number of the matrix. The denser the matrix, the more likely the fluorescent photons will be absorbed inside the sample. Fig. 5.6d shows that in the same matrix the lightest elements (with weaker Coulomb force by nucleus) correspond to smaller penetration depths of the fluorescent photons. The optimum

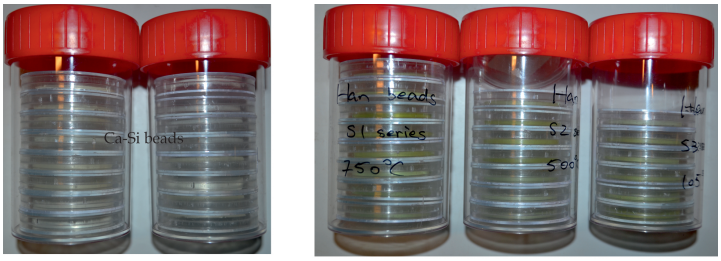
method to minimize these issues is to prepare samples as fused beads using a binder. This homogenizes and dilutes the analyte in a lighter matrix and that reduces self-absorption (cf. Fig. 5.6b2). A drawback is that preparing beads is time consuming. Using a binder and pressing it to a pellet (press pellets) is less time consuming but the associated increase in material density may influence the photon penetration depth compared to loose powder samples.

5.4.2. XRF AND LIBS SAMPLES AND CALIBRATION

We used the following two sets with reference samples:

Table 5.2: Manufacturer calibrated contents [wt%] of the cement reference sample set, normalized to 100%.

Element \ Sample	#100	#101	#103	#105	#106	#107	#108	#109	#110
Ca	74.7	60.2	65.3	75.9	76.4	77.6	75.3	76.6	78.5
Si	15.8	24.7	20.9	15.8	15.3	16.5	15.2	15.4	16.6
Al	4.76	8.15	6.83	3.68	4.89	3.62	3.99	3.63	4.01
Fe	2.97	4.30	2.07	2.85	2.25	1.46	3.36	2.62	0.20
Mg	1.44	1.79	4.46	1.54	0.94	0.68	2.10	1.55	0.63
Na	0.28	0.88	0.41	0.25	0.14	0.22	0.11	0.22	0.06



(a): Pure Ca-Si binary bead sets for XRF calibration

(b): 22 ADR fine demolition concrete beads for XRF measurements

Figure 5.7: Bead samples for XRF measurements. (a): Pure Ca-Si binary bead sets for XRF calibration. (b) 22 bead samples of ADR 0-4 mm products (DC4).

- RS1: A certified cement reference set composed of nine pressed pellet samples (FLUXANA). The elemental composition of the set in Tab. 5.2 is provided by the manufacturer. It is certified by round robin tests using ICP, XRF, titration, gravimetry, EDTA and photometry.
- RS2: 16 binary mixtures of pure Ca-Si compounds. XRF was applied on fused beads (cf. Fig. 5.7a). The resulting XRF calibration curves of the experimental signal intensity as a function of either the Ca or the Si content are shown in Fig. 5.8. The STD for ten

repeated XRF measurements for a selected bead was 0.6 % for Ca and 0.3 % for Si, showing that the XRF measurement for beads is highly repeatable.

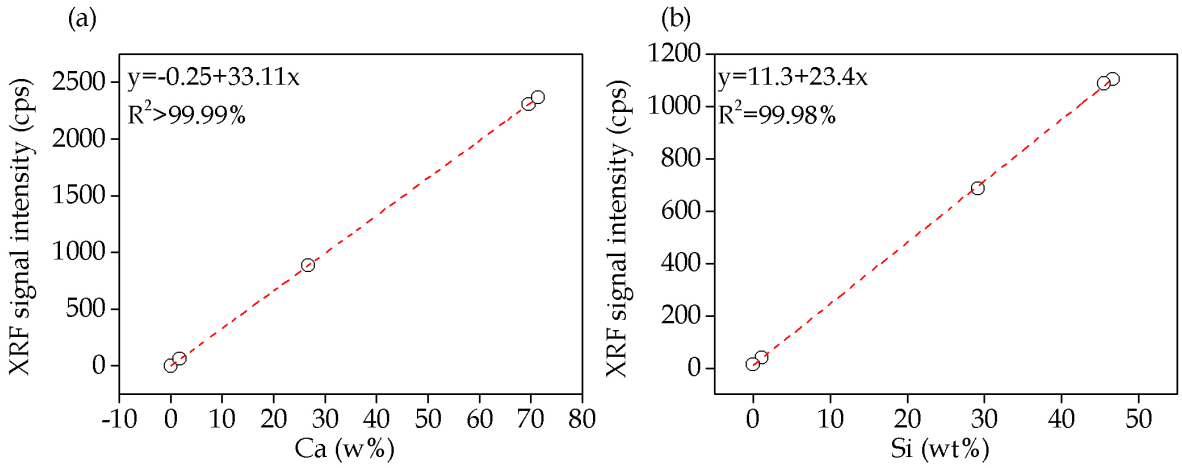


Figure 5.8: XRF linear calibration curves using a pure Ca-Si binary mixture (RS2) and fused beads. XRF signal as photon counts versus the element contents ($wt\%$) for (a) Ca and (b) Si.

The following demolition concrete samples (DC) were taken from a concrete processing plant, which processing steps are shown as a schedule in Fig. 5.9. For all these samples we used three calibration standards for XRF (Omnion, CEM, DC) to average out matrix effects. The predicted XRF average contents and (relative) STD is determined from these three standards. Where press pellets are used with LIBS they were made without binder to prevent corresponding matrix effects and to prevent the elemental composition of the binder to interfere with the targeted spectrum.

Table 5.3: Ten drill core concrete samples for MLIBS test.

#drill core	#building	#room	position	pollutants
3	KB6	12.01	floor	Carpet
4	KB6	12.01	wall	Plaster
7	KB7	2.03	floor	Carpet
8	KB7	2.03	wall	Plaster
9	KB2	0.16	floor	Linoleum
10	KB6	0.15a	floor	Linoleum
12	KB6	0.17	floor	Linoleum
15	KB6	0.36	floor	Linoleum
18	KB4	0.16	floor	Tiles
22	KB4	0.30	floor	Carpet

- DC1: A single grinded ADR sample 0-4 mm, to be used for comparisons between model based and calibration based LIBS methods. For XRF, press pellets with binder were produced. For LIBS, press pellets without binder were produced.

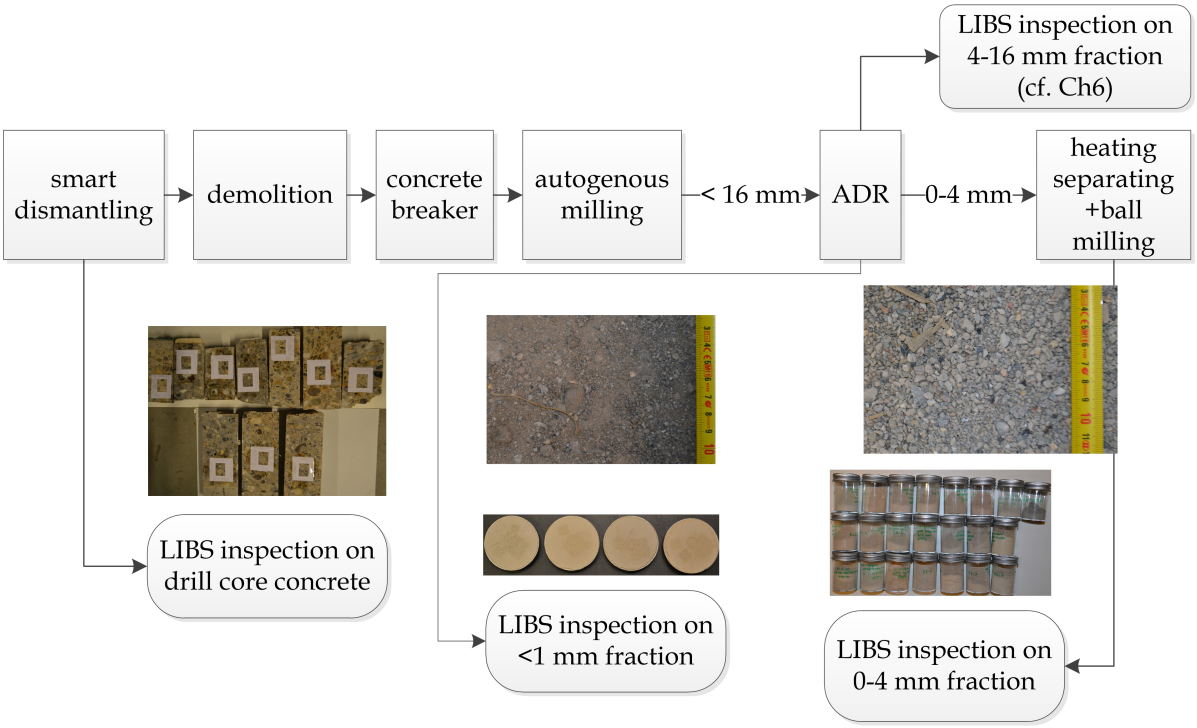


Figure 5.9: Model-based single-shot LIBS inspection on drill core concrete & ADR fine products as traceability study along the whole processing line.

- DC2: 10 concrete drill core samples, cf. Tab. 5.3. These were tested only with LIBS without any surface preparations. The type and exact composition of the cement used in this concrete is unknown; there was no documentation for this old building (dating 1969-1981).

- DC3: 4 ADR samples 0-1 mm, obtained at different ADR feeding rates and milling angles, cf. Tab. 5.9. For XRF, press pellets with binder were produced. For LIBS, press pellets without binder were produced.

- DC4: 22 ADR samples 0-4 mm, processed by different heating temperatures and milling times, cf. Tab. 5.10. For XRF fused beads were produced (cf. Fig. 5.7b). LIBS was applied to the loose powder samples.

The relevance of the various concrete products is that a high Ca content and a low Si content is indicative of a high cement stone concentration. That makes the product a potential substitute for the limestone used in virgin cement production or a potential reactive filler directly in new concrete production. In fact, the additional treatments of the ADR materials (<4 mm) were aimed at concentrating the cement stone and producing a Ca rich fraction.

Here the challenge is to use LIBS and detect and quantify the impact of the different treatments.

5.4.3. SELECTION OF LIBS EMISSION LINES FOR CALIBRATION

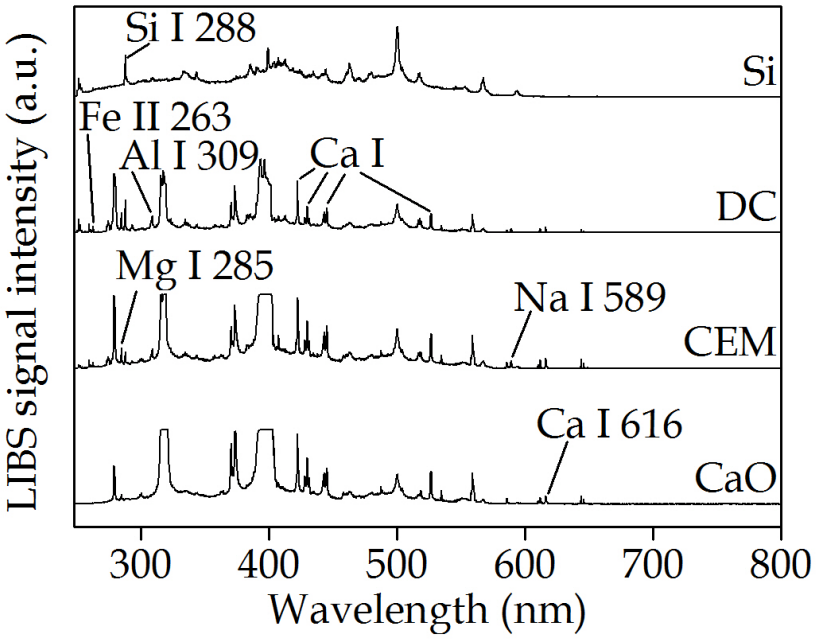


Figure 5.10: Raw spectra of pure CaO, CEM, DC and silicon acquired for zero delay time.

The large dynamic range of LIBS spectra forces a trade-off between detection of the weakest emission lines of interest and to prevent saturation of the strongest. For example, the two lowest spectra in Fig. 5.10 clearly show that the strong Ca (II) lines 317.9, 318.1, 393.4, 396.8 nm are saturated. The detectable emissions of the six main elements in cement and concrete are listed in Tab. 5.4. The LIBS spectral abundance for concrete appears similar to that of cement, but the differences in composition are most clear from the differences in the Si and Ca emissions. For each of the six elements a calibration line was fitted using 10 spectra per sample and testing for the optimum delay time. The emission lines and delay time that produced the best linear calibration of LIBS with the certified contents of the cement reference sample set (RS1) are listed in bold face in Tab. 5.4. It is noted that most of these emission lines correspond to relatively low transition probabilities (cf. Tab. 5.1). Fig. 5.11 shows the best linear fits for the six elements and the optimum delay time.

Owing to the large dynamic range in the LIBS spectra, a trade-off had to be made between

Table 5.4: Detected atomic (I) and singly ionized ionic lines (II) in cement and concrete samples. Bold faced lines are used for quantitative analysis (cf. Tab. 5.1).

Element	Emission lines [nm]
Ca	Ca (I): 422.7, 428.3, 428.9, 430.3, 431.9, 443.5, 445.5, 487.8, 526.6, 535.0, 558.9,
	585.6, 585.8, 610.3, 612.2, **616.2**, 643.9, 645.0, 649.4, 714.9;
	Ca (II): 315.9, 317.9, 370.6, 373.7, 393.4, 396.9
Si (I)	251.6, 252.4, 252.9, **288.2**
Al (I)	308.2, **309.3**
Fe	Fe (I): 258.5; Fe (II): 256.2, 257.3, 259.3, 261.2, **262.6**
Mg	Mg (I): **285.2**; Mg (II): 279.8, 280.3
Na (I)	589.0, **589.6**

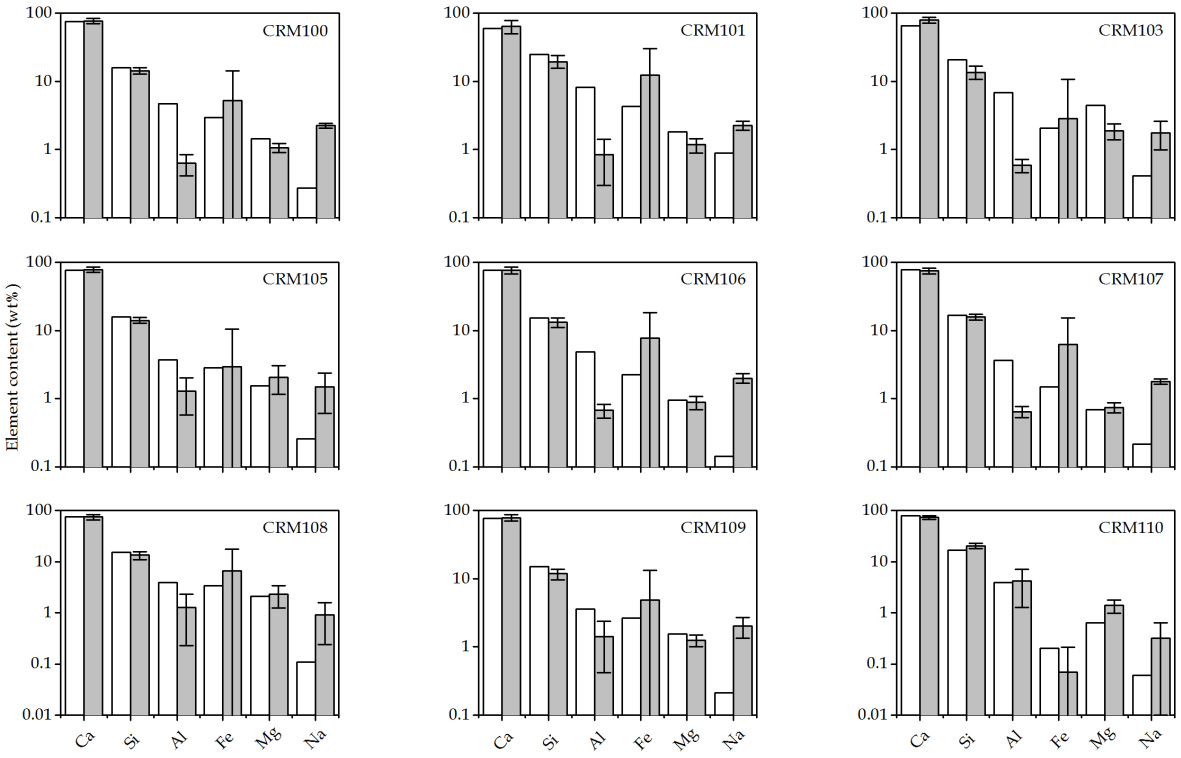


Figure 5.11: MLIBS measurements (grey bars) of the element contents of nine cement samples RS1. Each panel shows the normalized mean and STD for series of ten single shots per cement sample. The certified documented reference contents are shown as blank bars.

proper detection of weak emission lines and risking saturating the strongest ones. For example, Fig. 5.10 shows that the strong Ca (II) lines 317.9, 318.1, 393.4, 396.8 nm were saturated in the three lowest spectra. The detectable emissions of the six elements in cement and DC are listed in Tab. 5.3. The spectral abundance for DC appears similar to that of cement, but their different composition is most clear from the differences in the Si and Ca emissions. For each of the six elements a calibration line was fitted using 10 spectra per sample and testing different delay times. The emission lines and delay times that provided the best linear correlation with the contents of the cement reference samples are indicated

in bold face in Tab. 5.4. It is noted that most of these emission lines correspond to relatively low transition probabilities (cf. Tab. 5.1). Fig. 5.12 shows the best linear fits for the six elements at different optimum delay time for each in the cement samples.

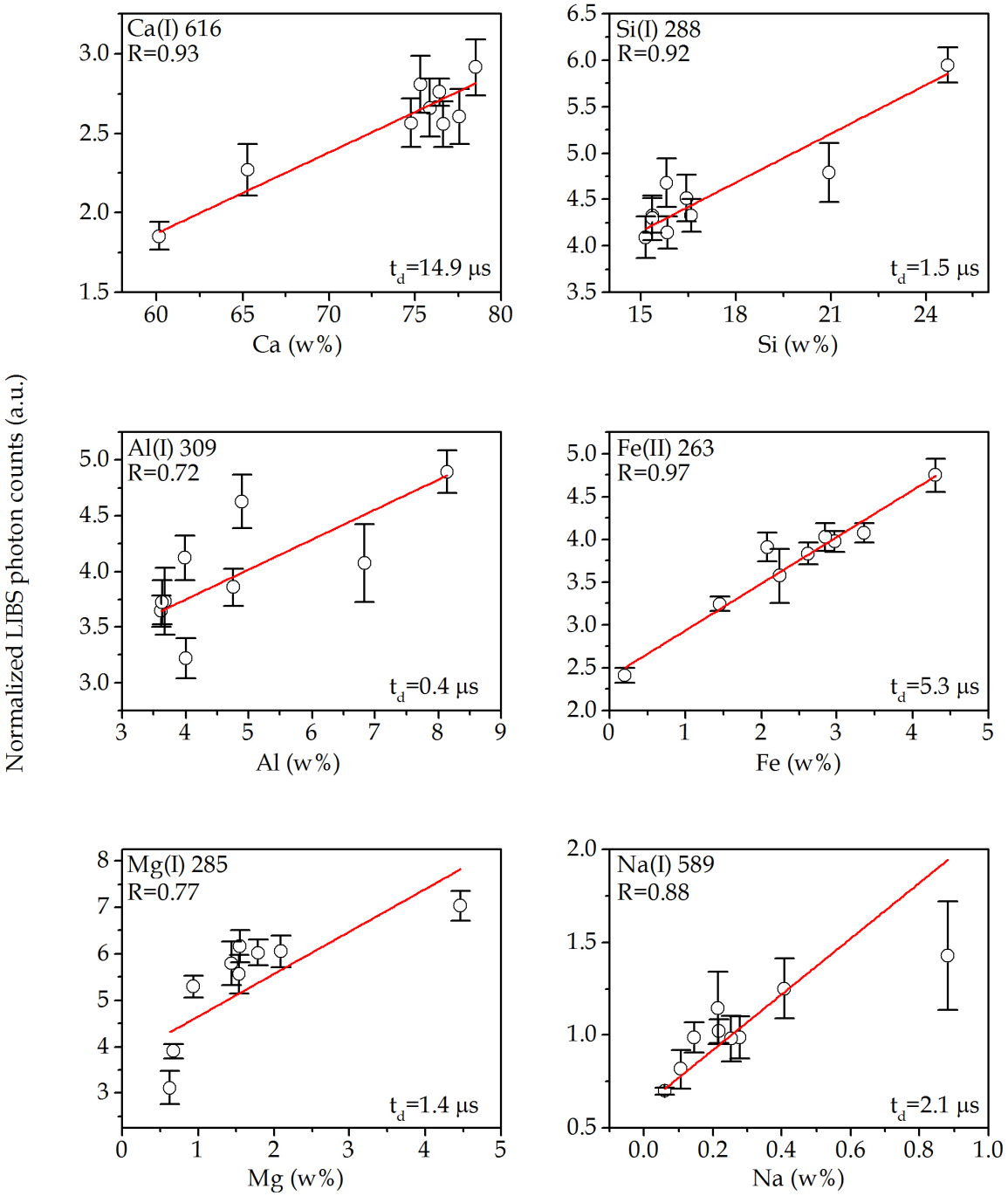


Figure 5.12: Calibration curves for the six elements in the RS1 cement reference sample set. The selected emission line and optimum delay time are indicated.

5.4.4. CALIBRATION BASED LIBS IN A COMPARISON WITH XRF

Tab. 5.5 shows the elemental contents for the concrete sample DC1 as determined by calibration based on LIBS (CLIBS) and XRF. The selected emission lines for the elements are the same as for the cement reference set RS1 and are shown in boldface in Tab. 5.4. Since calibration samples for concrete could not be produced we used the calibration lines shown in Fig. 5.12 that are determined for the cement set RS1. Moreover, where the LIBS content was outside the calibrated range we applied linear extrapolation. The optimum delay times and correlation coefficients of the linear fits are added to Tab. 5.5. The mean and STD for CLIBS is determined from a series of ten single shots. The Na contents proved too low and therefore too inaccurate to determine with CLIBS. It is remarked that the total contents for XRF is normalized to 100% to exclude other elemental contents.

Table 5.5: Comparison of XRF (method 1a, cf. Section 5.4.2) and CLIBS for the elemental contents (wt%) of a DC sample. The XRF results are related to three different reference databases and the CLIBS results are for a series of ten single shots. The CLIBS contents were not normalized. R is the correlation coefficient for the calibrated lines for cement and t_d is the delay time.

	XRF			CLIBS				
	mean	STD	STD%	t_d (μs)	R	mean	STD	STD%
Ca	23.5	4.39	18.7	14.9	0.93	56.8	5.06	8.92
Si	64.7	6.37	9.84	1.5	0.92	46.1	4.94	10.7
Al	6.36	1.35	21.3	0.4	0.72	9.31	1.31	14.1
Fe	3.27	0.26	7.98	5.3	0.97	5.97	0.73	12.2
Mg	2.07	0.46	22.0	1.4	0.77	5.25	1.14	21.7
Na	0.10	0.025	25.1	-	-	-	-	-

The STDs of CLIBS are comparable to those for XRF and for the major elements even smaller. Overall the STD of CLIBS tends to decrease for increasing correlation coefficient, showing that the uncertainty growths with the uncertainty in the calibration. Nevertheless, compared to XRF we have to conclude that the mean contents with CLIBS are quite inaccurate; sometimes they are not even within 3 STD of the XRF result. In fact, all the minor elements are overestimated by a factor 1.5 to 2 and the more so towards the lowest contents (Mg), despite the fact that these contents are inside or very close to the calibrated ranges. Also the major elements are either seriously underestimated (Si) or overestimated (Ca).

These poor CLIBS results point to four possible matrix-dependent effects, which all point to the fact that cement cannot be used as a reference for concrete. First, linear

extrapolation does not take into account the non-linear effect of self-absorption in the plasma plume. For the major elements self-absorption is expected to be considerable, but we cannot rule it out for the minor elements either. Second, concrete contains significantly more silica-compounds than the pure cement that was used here as a calibration for CLIBS. Silica is known to have a higher fluence breakdown threshold than other cementitious compounds. Besides ablated mass this may also affect the plasma temperature, which is a sensitive parameter in relation to the quality of the emission spectrum. Third, depending on the applied fluence and fluence breakdown threshold of the sample material the cement is easier to ablate and may follow a different thermodynamic path than concrete. Seeing both concrete and pure cement are minerals (dielectrics) it may be that concrete is evaporated while the cement was subject to phase explosion before ablation (cooling). The hot matter is expected to follow a different thermodynamic path which implies a different ablated mass and plasma temperature. Fourth, concrete is a heterogeneous material consisting of many different elements, crystals and grains. This may invite a matrix effect we call "the pressure cooker effect". The rationale behind this effect is that some types of crystal, here assumed those with minor elements which properties deviate the strongest from the matrix, are easier to break down than the silica matrix. This means the minor elements are effectively hotter than when they would be exposed under the same laser conditions in the homogeneous material where ablation would have occurred earlier. From the thermodynamic point of view, crystals with minor elements might be subjected to phase explosion while the silica matrix is vaporized. The combination of these two possible pathways apparently increased the ablated mass and plasma plume temperature, because the emission spectrum of the minor elements has clearly improved.

5.4.5. MODEL BASED LIBS, PERFORMANCE AND SENSITIVITY

LIBS spectra of the RS1 cement sample set were acquired with the same 5 μs delay time, which in a compromise minimized the spectral background noise as well as the error between the MLIBS results and the certified contents of the cement samples. Per cement sample ten single shot spectra are averaged to enhance the signal quality. From the average sample spectrum five Ca (I) lines were used in a Boltzmann plot to determine the plasma temperature. Furthermore, from the average sample spectrum the electron density

Table 5.6: MLIBS plasma temperature and electron density for the nine cement reference samples RS1 as the mean for ten single shots. The delay time was 5 μs.

sample	#100	#101	#103	#105	#106	#107	#108	#109	#110
T (10^4 K)	1.92	1.85	2.90	3.40	1.95	1.92	3.47	2.36	5.21
N_e 10^{16} (cm^{-3})	2.96	3.18	2.91	2.85	3.13	3.03	2.92	2.97	2.70

in the plume is determined for each element from the average line broadening of Mg (I) 285 nm, Si (I) 288 nm and Ca (I) 616 nm. The plasma temperature and electron density for all nine RS1 cement samples are presented in Tab. 5.6. The MLIBS contents plotted in Fig. 5.13 are normalized to 100% in a comparison with the certified contents (cf. Tab. 5.2).

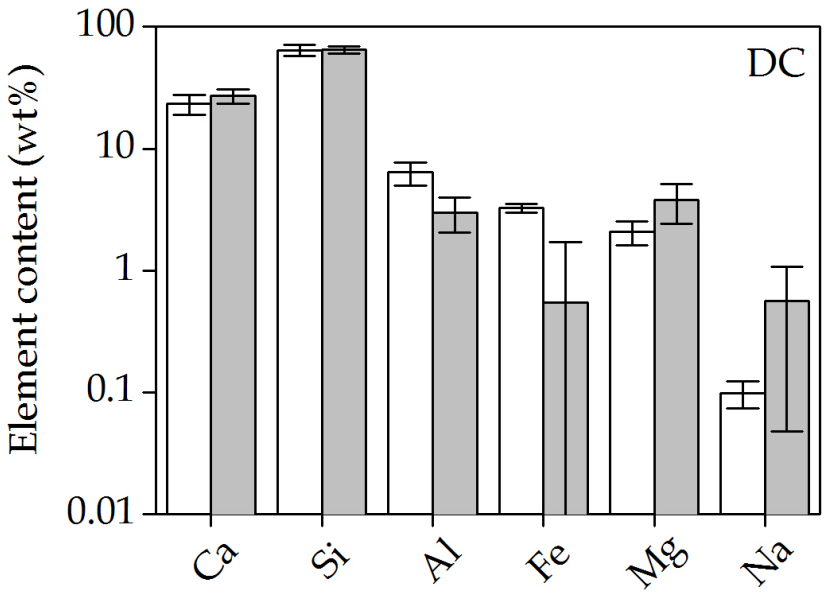


Figure 5.13: MLIBS measurement (grey bars) of the elemental contents of the DC sample DC1, showing the mean and STD for a series of ten single shots. A blank bar indicates the XRF reference contents.

The mean relative error and relative STD over the samples between the MLIBS results and certified contents per element was: Ca 2.72% ± 11.2%; Si −11.6% ± 15.2%; Al −70.0% ± 49.0%; Fe 110% ± 187%; Mg 2.94% ± 27.1%; and Na 632% ± 39.7%. Sample#110 contained very little Na and Fe, which resulted in very noisy emission lines but shows that the STD also accounts for sample to sample variations.

Next we apply MLIBS to the concrete sample DC1. The fixed time delay is now set to 0.3 μs, which gave the best results. We took ten single shot spectra to obtain a mean and STD. Fig. 5.13 shows the STD and mean MLIBS contents, normalized to 100% in

a comparison with XRF. The plasma temperature is determined as 3.72×10^4 K and the electron density as 2.29×10^{16} cm^{-3}. The mean relative error and relative STD between MLIBS and XRF per element was Ca 15.3% ± 13.6%; Si 0.46% ± 6.56%; Al −52.7% ± 31.7%; Fe −83.5% ± 215%; Mg −82.6% ± 35.4%; and Na 460% ± 91.5%. As for the cement samples the MLIBS contents for the major elements Si and Ca compares satisfactorily with the reference.

MLIBS produces some encouraging results for the major elements Ca and Si, arguably the most important in cementitious materials. However, being major elements the question arises why self-absorption does not have a more negative impact on the MLIBS results as it did for CLIBS? After all, the plasma temperature calculation is essentially based on the number of generated photons and an unknown part of those were never detected. This leads to an underestimation of the real plasma temperature and thus to an error in estimated element contents. The likely explanation is that we optimized the time delay (0.3 μs) before starting data acquisition in order to have the best fit with the XRF determined Si-Ca contents. This delay was 0.2 μs earlier than used for the cement sample set RS1. One could argue that this change in delay is justified because the lower Ca contents of concrete means that LTE for the target species is reached earlier and one must therefore also start data acquisition earlier. Nevertheless, a different time delay just means a different photon count over the same time window (usually 10 μs), which may turn out either higher or lower for radiation of a certain element. In this respect, the delay time can effectively be used as a calibration to partly compensate for the nonlinear effect of self-absorption of major elements in MLIBS.

Table 5.7: Sensitivity analysis of MLIBS mean measured contents (wt%) to variations (Var =varied) in either emission line strength (I), plasma temperature or electron density using the concrete sample DC1. The allowable variations are determined from a MLIBS measurement series of ten single shots.

I	T (K)	Ne (cm^{-3})		Ca	Si	Al	Fe	Mg	Na
Var	mean	mean	Mean	27.9	65.4	1.83	1.42	2.34	1.14
			STD%	12.1	6.49	16.6	66.9	20.0	39.5
mean	Var	mean	Mean	24.3	66.3	3.38	2.02	3.53	0.60
			STD%	31.6	11.1	56.0	293	33.8	74.2
mean	mean	Var	Mean	27.2	65.5	1.81	2.10	2.24	1.17
			STD%	0.16	0.16	0.16	7.49	0.16	0.15

The STD in the preceding test cases is mainly due to shot-to-shot variations in the selected

emission lines, the plasma temperature, and the electron density. To determine the dominant cause we test the sensitivity of the MLIBS contents to each of these three variables. To this end we reuse the ten spectra for the DC1 sample but keep two of the three variables fixed at the mean value of the ten spectra. The sensitivity results are shown in Tab. 5.7. We discuss only Fe as an example because all elements show the same trend. The intensity of the emission lines from the six elements varied 19% to 50% and this contributed 67% to the STD of the Fe contents. The plasma temperature varied by 39% and contributed 293% to the STD of the Fe contents. The electron density varied 7.5% and also contributed 7.5% to the STD of the Fe contents. This demonstrates that the plasma temperature is the major contributor to the STD of the MLIBS elemental content and that emission line variation is the second contributor. Errors in electron density calculation may be neglected in comparison. These findings provide useful insights on prioritizing engineering settings.

- To improve the stability of plasma temperature, a water cooling chiller combined with heat sink are applied to maintain a stable laser fluence. Also, more LIBS spectral lines per element are needed to derive more robust plasma temperature using the Boltzmann plot approach.
- To improve the LIBS spectral intensity, optics with larger OD is applied.

5.4.6. MLIBS STUDY OF PROCESSED CONCRETE

Using MLIBS we analyse and compare results for different concrete products. All data were acquired under the same ambient conditions. The integration time was 1 ms to improve the signal-to-noise ratio. The optics-to-sample distance of 200 mm provided a large focal range that made the spectra less sensitive to rough and uneven sample surfaces, especially when the sample is loose powder. The laser fluence was 29 J/cm^2 (15 mJ/shot, focus 0.25 mm diameter). The focus can be comparable or even larger than a part of the sand and cement grains in concrete samples. This means it is inevitable that the laser sometimes ablated cement and sand simultaneously, resulting in a mixed LIBS spectrum. It is not practical to sort or select the correct spectra. In fact, we do not apply supervised training or any other form of pre-classification. The peak fitting algorithm requires that the LIBS emission line intensities (Si (I) 288 nm and Ca (I) 616 nm) are stronger than 200 photon counts. This criterion also screens the LIBS spectra related to pure sand.

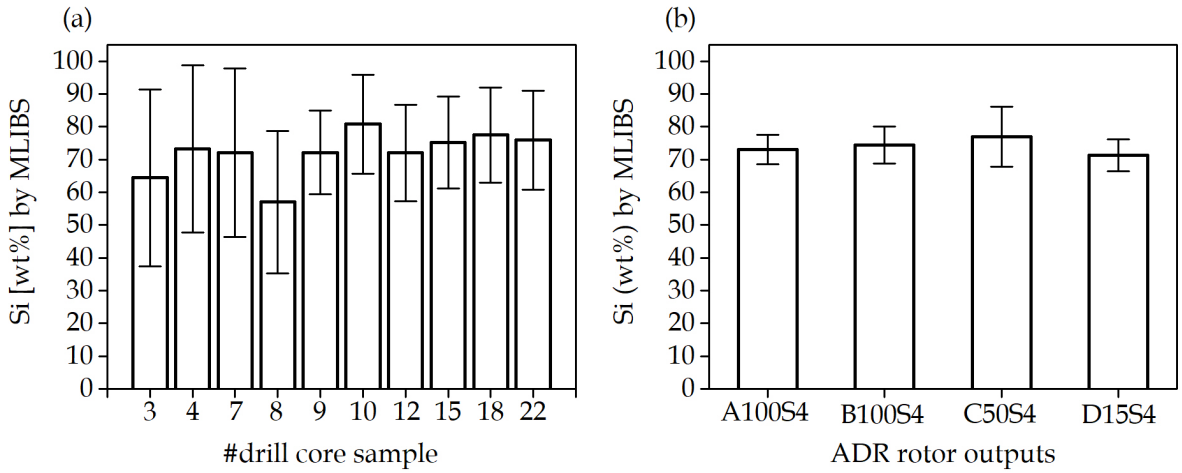


Figure 5.14: MLIBS results of Si (wt%) results on (a) ten concrete drill core samples and (b) four ADR fine product samples (particle size $< 1\ mm$)

Table 5.8: MLIBS results of Ca & Si $[wt\%]$ contents, RSTD%, T $[10^4\ K]$, and N_e $[10^{16}\ cm^{-3}]$ on ten drill core concrete samples (DC2).

#sample	Ca	RSTD	Si	RSTD	T	RSTD	N_e	RSTD
3	35.60	75.86	64.40	41.93	1.56	39.02	2.37	8.85
4	26.75	95.33	73.25	34.81	1.37	39.70	2.40	8.88
7	27.92	91.82	72.08	35.56	1.30	25.71	2.43	8.07
8	43.02	50.56	56.98	38.17	1.53	32.78	2.40	8.08
9	27.86	45.76	72.14	17.67	1.58	29.12	2.29	8.70
10	19.22	78.47	80.78	18.68	1.48	24.30	2.39	13.04
12	28.01	52.46	71.99	20.42	1.66	34.60	2.25	8.46
15	24.78	56.79	75.22	18.70	1.65	38.85	2.50	12.53
18	22.55	64.34	77.45	18.73	1.42	19.45	2.35	10.27
22	24.11	62.36	75.89	19.81	1.63	35.16	2.46	9.24

First we analyse the Si and Ca contents of the ten concrete drilled core samples DC2. They were polished before performing LIBS measurement. The LIBS shots are applied at positions with 1 mm interval in a rectangle of $30 \times 40\ mm$. At each position 5 single-shots were applied to obtain one averaged spectrum. This produced 39×29 averaged spectra, which data can be mapped back to give a spatial distribution of the Si and Ca contents within the rectangular area. The drill core results are compared to those of the ADR samples $0-1\ mm$ DC3 to confirm the concrete or cement-like nature of the ADR samples. Fig. 5.14a shows

Table 5.9: MLIBS results on ADR $0-1\ mm$ (DC3) where the concrete ADR input ($< 16\ mm$) is processed by ball milling with different feeding rate ($f.r.$ $[t/h]$) and milling angle ($m.a.$ $[\circ]$).

#sample	f.r.	m.a.	Ca	RSTD	Si	RSTD	T	RSTD	Ne	RSTD
A100S4	100	7	27.00	16.44	73.00	6.08	1.39	12.74	2.52	9.73
B100S4	100	5	25.57	21.78	74.43	7.48	1.42	20.68	2.47	10.91
C50S4	50	5	22.99	39.98	77.01	11.94	1.42	28.61	2.44	10.71
D15S4	15	5	28.70	16.67	71.30	6.71	1.42	20.91	2.51	9.04

the Si contents of the concrete cores and Fig. 5.14b the Si contents for the ADR samples $0-1\ mm$. The Ca and Si contents, plasma temperature and electron density are listed in Tab. 5.8 for the cores and in Tab. 5.9 for the ADR samples. The ADR samples were relatively homogeneous and the effects of autogenous milling on recovered cement paste are small (cf. STD of Si), seeing that the Si contents are comparable to the concrete core samples.

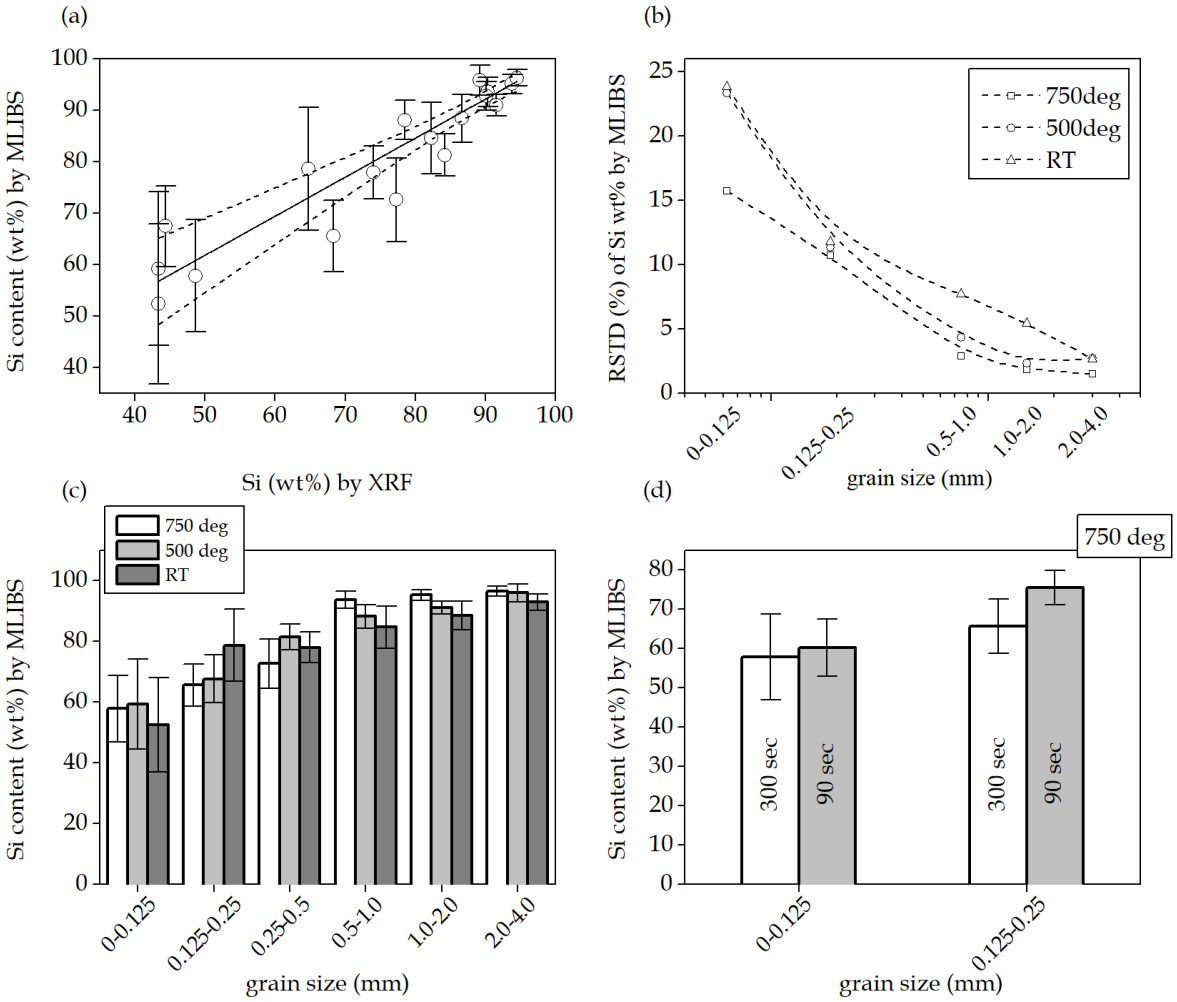


Figure 5.15: MLIBS results for Si (wt%) in ADR $0-4\ mm$ (DC4) after heat-treatment and ball milling: (a) MLIBS results versus XRF. LIBS: 1 STD error bars, solid lines show 95% confidence interval for average of each LIBS series and dashed line complies with 100% correlation with XRF; (b) Uncertainty (1 RSTD%) versus grain size; (c) MLIBS results using different temperatures during heat treatment; (d) MLIBS results at $750°\ C$ for 90 and 300 seconds ball milling times.)

In an attempt to further concentrate the cement stone, ADR materials were exposed to high temperatures and ball milling. The working principle was that heat lowers the bonding strength of the cement stone so a ball mill can remove it more easily from the silica aggregates. MLIBS measurements were carried out on raw ADR 0-4 mm (DC4) powder samples from heat-treated ADR materials. To this end, 100 single-shot spectra are taken

per sample with 10 μs integration time and 0.3 μs delay time. The MLIBS mean contents and STD are plotted against XRF measurements of the Si content in Fig. 5.15. Note that for XRF we used fused beads produced from the ADR 0-4mm samples (DC4). Fig. 5.15a shows a near-linear relation between MLIBS and XRF. Most of the MLIBS data points outside the 95% confidence interval (solid lines) were from the fine sample particles <0.25 mm. This test case demonstrates the major advantage of MLIBS over comparable methods; it can measure the elemental contents over a wide range of concentrations without any time consuming preparations.

Fig. 5.15b shows that the RSTD for LIBS decreases with increasing grain size, which means that the absolute STD decreases very rapidly. In other words, the shot-to-shot variations are smaller when the grain size is larger than the laser focus (0.25 mm). In principle the spectral repeatability may be improved significantly if one applies LIBS to press pellets instead of loose powders, but that is not an option for in-line inspection in an industrial setting. Nevertheless, shot-to-shot variations can also be used positively, as they may carry significant information on the natural surface conditions of a particular material, as demonstrated in Chapter 6.

Fig. 5.15c shows the LIBS results for the DC4 samples ADR 0-4mm in different size fractions that are heat treated at different temperatures before ball milling. The first observable trend is that the Si content is smaller in the finest fractions and higher in the course fractions. This means that the heat treatment and milling have a positive effect, because cement stone is being concentrated in the finer size fractions. Another observable trend is that this effect increases with heating temperature, which was expected. Note that the error bar in the finest size fraction treated at room temperature does not necessarily contradict these trends, despite the average showing a deviating low Si contents. Fig. 5.15d shows the LIBS results for heat treated ADR 0-4mm in two size fractions which were subjected to 90s and 300s of milling time, respectively, and the same heat treatment temperature of 750° C. Here, the only observable trend is that the Si contents decreases in favour of the Ca contents, meaning that the degree of cement stone that is liberated from the silica has increased with milling time. More detailed results are provided in Tab. 5.10

Table 5.10: MLIBS results on ADR fines outputs ($0-4\ mm$) after thermal heat treatment, e.g. heating temperature (h.t. [$^{\circ}\ C$]) and ball milling time (*b.m.*).

grain size	m.t.	h.t.	Ca	RSTD	Si	RSTD	T	RSTD	Ne	RSTD
0-0.125	300	750	41.54	24.94	58.55	15.73	1.60	34.16	1.69	15.06
0.125-0.25	300	750	34.47	20.23	65.87	10.72	1.58	33.70	1.70	12.65
0.25-0.5	300	750	27.55	28.28	72.15	11.04	1.64	29.87	1.58	14.28
0.5-1	300	750	6.89	39.89	92.77	2.87	1.76	26.15	1.65	15.84
1-2	300	750	5.13	33.82	94.87	1.83	1.71	22.57	1.93	13.84
2-4	300	750	3.90	36.19	95.99	1.49	1.79	16.15	2.52	14.55
0.125-0.25	90	750	24.64	18.12	75.36	5.93	1.58	35.49	2.11	11.28
0-0.125	90	750	39.96	18.21	60.30	12.12	1.70	37.86	1.72	11.23
0-0.125	300	500	41.63	32.66	58.00	23.32	1.46	18.97	1.53	25.22
0-0.125	0	500	52.91	28.10	48.53	25.98	1.46	19.98	1.49	22.29
0.125-0.25	300	500	32.53	24.20	67.34	11.32	1.47	21.00	1.81	24.37
0.125-0.25	0	500	22.35	38.23	77.78	10.04	1.48	20.55	1.84	25.90
0.25-0.5	300	500	18.69	22.15	81.32	5.15	1.30	12.61	2.40	15.29
0.5-1	300	500	12.01	31.30	88.04	4.34	1.47	17.42	2.13	18.65
1-2	300	500	9.05	23.45	90.96	2.34	1.54	18.55	2.59	12.98
2-4	300	500	5.85	45.33	94.03	2.75	1.65	11.63	2.05	20.79
0-0.125	300	105	47.85	32.52	54.84	23.81	1.74	33.36	1.49	22.04
0.125-0.25	300	105	24.89	40.55	74.57	11.77	1.98	23.40	1.49	21.56
0.25-0.5	300	105	22.15	23.25	77.90	6.69	1.44	19.75	2.20	19.35
0.5-1	300	105	16.43	39.68	83.27	7.70	1.81	25.42	1.72	21.47
1-2	300	105	12.22	39.12	87.62	5.45	1.78	20.69	1.89	24.08
2-4	300	105	7.51	33.20	92.46	2.69	1.46	14.30	2.47	12.78

such as the calculated plasma parameters.

REFERENCES

[1] I. B. Gornushkin, L. A. King, B. W. Smith, N. Omenetto, and J. D. Winefordner, *Line broadening mechanisms in the low pressure laser-induced plasma,* Spectrochimica Acta Part B: Atomic Spectroscopy **54**, 1207 (1999).

[2] G. Drake, *Springer Handbook of Atomic, Molecular, and Optical Physics* (Springer, 2006).

[3] M. Milan and J. Laserna, *Diagnostics of silicon plasmas produced by visible nanosecond laser ablation,* Spectrochimica Acta Part B: Atomic Spectroscopy **56**, 275 (2001).

[4] H. Griem, *Spectral Line Broadening by Plasmas* (Elsevier Science, 2012).

[5] H. Griem, *Plasma Spectroscopy* (McGraw-Hill, 1964).

[6] G. Bekefi and W. Allis, *Principles of Laser Plasmas*, A Wiley-interscience publication (Wiley, 1976).

[7] M. Sabsabi and P. Cielo, *Quantitative analysis of aluminum alloys by laser-induced breakdown spectroscopy and plasma characterization,* Appl. Spectrosc. **49**, 499 (1995).

[8] T. O'Haver, *Version 6.1, http://terpconnect.umd.edu/ toh/spectrum/toc.html,* (2015).

[9] A. Kramida, Y. Ralchenko, J. Reader, and N. A. Team, *Nist atomic spectra database (ver. 5.2), [online]. available: http://physics.nist.gov/asd [2015, april 9],* (2014).

[10] J. Bittencourt, *Fundamentals of Plasma Physics* (Elsevier Science, 2013).

[11] E. Böhm-Vitense, *Introduction to Stellar Astrophysics:*, Introduction to Stellar Astrophysics (Cambridge University Press, 1992).

[12] R. Huddlestone and S. Leonard, *Plasma diagnostic techniques*, Pure and applied physics (Academic Press, 1965).

[13] J. Reader, C. Corliss, W. Wiese, G. Martin, U. S. N. B. of Standards, and C. for Radiation Research, *Wavelengths and transition probabilities for atoms and atomic ions*, NSRDS-NBS No. pts. 1-2 (U.S. Dept. of Commerce, National Bureau of Standards : for sale by the Supt. of Docs., U.S. G.P.O., 1980).

[14] P. Atkins and J. Paula, *Atkins' physical chemistry*, 8th ed. (W. H. Freeman and Company, 2006).

[15] R. Schramm, *Training Class X-ray Flourescence: Theory, Application Developement and Sample Preparation*, FXMM-0021-01-16.01.2011 (FLUXANA GmbH & Co. KG, HD Elektronik und Elektrotechnik GmbH, 2011).

6

STATISTICAL CLASSIFICATION OF EOL BUILDING MATERIALS

LIBS technology provides data on the elemental composition but the detected spectrum is also influenced by physical properties of the sampled material. This marks LIBS as a broad source of materials information and a technology with high potential for classification. The challenges for the research in this chapter[1] are:

- Investigate LIBS data for statistical quality inspection of materials from demolition.
- Investigate potential and reliability of statistical techniques.

There are two basic challenges for a statistical technique. The first is to determine the optimum space dimensionality to which the primary data are to be reduced before the final classification. The second challenge is to determine optimum boundaries in this multi-dimensional space that define the functional group with the smallest possible error, i.e. without missing too many targeted objects (false negatives) or including too many wrong ones (false positives). A common approach to probing where these boundaries may lie is to apply a training procedure using a collection of known objects (the training set) and tracing their position and clustering in the multi-dimensional space. Training may result in a smaller variance than encountered during the blind tests due to the necessarily size limited set of representative (yet possibly biased) objects tested for each group. On the other hand, the size of the training set and its compositional representation of the group influence the optimum dimensions and the boundaries. The reliability, or robustness,

[1] The major part has been published in [1]

of a statistical technique depends on how well it isolates a cluster of the targeted objects from other clusters. Overlapping clusters are indicative of error, or at least indicative of too high uncertainty in the interpretation of the results. The overlap may be caused by incidental true resemblance of object properties, despite the fact they belonged to different functional groups. In that case, additional independent sensor information is required to separate the clusters more accurately. Noise and experimental errors also tend to increase the variance and to promote the overlap of clusters. On the other hand, the variance in the multi-dimensional space may also be used beneficially as an indicator of specific types of error. In other words, with statistical analysis one is also capable of unravelling non-correlated types of error in a set of repeated measurements.

In this chapter LIBS data is collected from a group of cementitious materials with similar rock forming elements and from several contaminant materials. Chemometric methodology is combined with a statistical model to obtain a more reliable method for classification. The focus is on combinations of Principal Component Analysis & Adaptive boosting (PCA-Adaboost) and Partial Least Squares Discriminant Analysis (PLS-DA) as the promising statistical techniques. For quantitative analysis, the PLS model is trained using a cement reference sample set and the blind tests are performed on demolition concrete samples. It will be shown that statistical processing can be used to recognise commonalities between the data from these related materials and (partly) overcome differences in degree of self-absorption and other LIBS matrix effects identified in Section 5.4.4.

6.1. BASICS OF CLASSIFICATION

$$\begin{bmatrix} x_{11} & x_{12} & \dots & x_{1m} \\ x_{21} & x_{22} & \dots & x_{2m} \\ \vdots & \vdots & \vdots & \vdots \\ x_{n1} & x_{n2} & \dots & x_{nm} \end{bmatrix} \cdot \begin{bmatrix} b_1 \\ b_2 \\ \vdots \\ b_m \end{bmatrix} + \begin{bmatrix} \varepsilon_1 \\ \varepsilon_2 \\ \vdots \\ \varepsilon_n \end{bmatrix} = \begin{bmatrix} y_1 \\ y_2 \\ \vdots \\ y_n \end{bmatrix} \tag{6.1}$$

A classification model is needed to categorize a set of input LIBS spectra into their corresponding target materials. Eq. 6.1 shows a multi-variate linear regression (MLR) model where x_{nm} is an independent variable or LIBS intensity at the m^{th} wavelength for the n^{th} measurement, b is the vector of correlation coefficients, y is the dependent variable or tar-

get label vector that is mostly user defined, e.g. $y = 0$ for gravel, $y = 1$ for wood, $y = 2$ for plastic and etc. For quantitative analysis, y is a continuous number, e.g. $y = 10 - 80\%$ for Ca content. Residual vector ε denotes the discrepancy between y and Xb. It contains variations due to noise and uncertainties in the measurement and ambient conditions. Examples of uncertainties are the variations in air humidity, dust, materials surface conditions, positioning and alignment of equipment, and laser pulse energy. Rewrite eq. 6.1 into the matrix form:

$$Xb + \varepsilon = y \tag{6.2}$$

Ignore the residual vector ε in eq. 6.2 and and multiply it with the transpose of X on both sides, we get:

$$X^T X\tilde{b} = X^T y \tag{6.3}$$

We can derive the approximate solution $\tilde{b}$ for eq. 6.3 as:

$$\tilde{b} = (X^T X)^{-1} X^T y \tag{6.4}$$

where $(X^T X)^{-1} = \frac{1}{det(X^T X)} \cdot adj(X^T X)$. $det(X^T X)$ denotes the determinant of $X^T X$ and $adj(X^T X)$ the adjugate matrix formed by taking the transpose of the cofactor matrix of X.

To obtain an unique set of $\tilde{b_m}$, one needs m independent variables x_m of which $m = n$. However,

1. As demonstrated in Chap. 4, inter-correlation between multiple emission line intensities at different wavelengths is characteristic of a LIBS spectrum. This results in a close to zero $det(X^T X)$ and moreover, the solution $\tilde{b}$ will become instable and sensitive to an insignificant change in $X^T y$. To enhance the determinant of $X^T X$ based on eq. 6.4, we have to orthogonalize X while keeping the maximum info in the co-variance matrix $X^T y$.

2. LIBS requires repetitive measurements per sample, so normally $n \gg m$. As a result, the system is overdetermined and thus non-unique, but a most probable solution might still exist.

This makes MLR a less reliable technique for our purposes and more elaborate solution methods are investigated in the following sections.

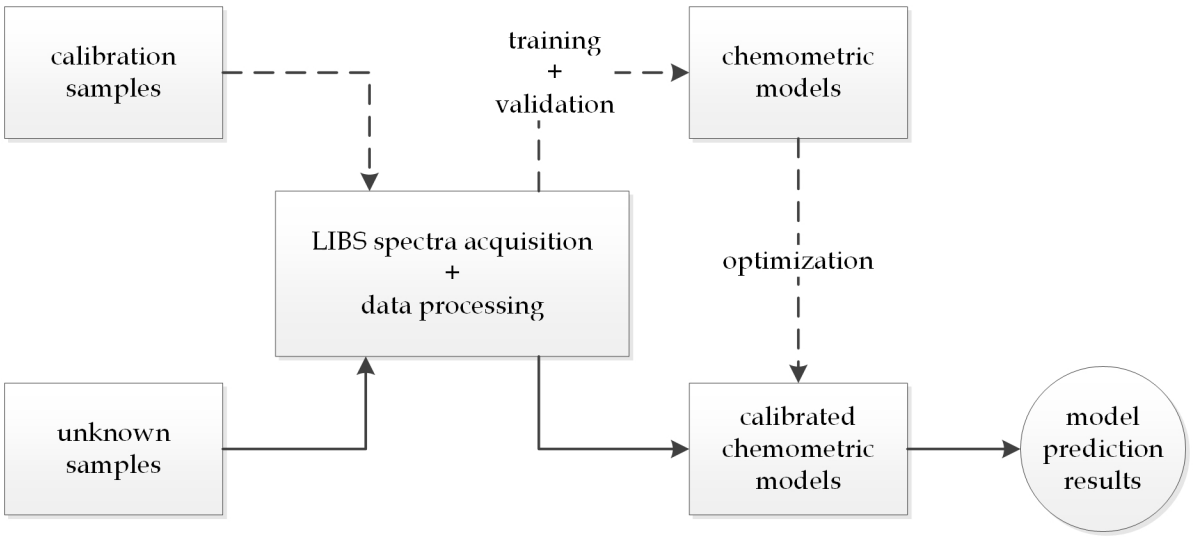


Figure 6.1: Typical classification scheme using a training sample set (dashed lines) to be tested on a blind sample set (solid lines).

A typical scheme is depicted in Fig. 6.1. A training set is first employed to determine the optimum model parameters that suppress redundant spectral information and increase the accuracy and precision of subsequent blind tests. For instance, when classifying the contents of a certain element in a material, the model has to be robust enough to deal with additional sources of variance, such, that the level of invariance associated with the material remains within acceptable intra-class uncertainty and inter-class distances. Some a-priori knowledge is needed to select the minimum number of samples which most likely span the optimum cluster boundaries in latent space before switching to the processing of blind samples. For example, one may choose samples that present upper and lower limits for specified contents, though in practice such samples may not always be available.

6.2. DETAILING OF POTENTIAL STATISTICAL TECHNIQUES

The techniques discussed in this section are based on physically tractable and robust principles, which means efficient for inline sensor applications. They make use of well developed mathematical concepts (mappings) in which a set of matrix equations is solved using nonlinear algorithms which are akin to optimization routines. These algorithms employ the materials information in the dataset (correlations) and suppress noise and data redundancy (repeated data). For a non-supervised method (i.e. not assigning any explicit classes)

as PCA the result is that the dataset is represented in a rotated space (also called "latent" or "virtual" space) using a new set of variables which number is usually smaller than the number of wavelengths in the LIBS spectra. Note the fact that the number of variables is reduced means that information carried by multiple wavelengths in the LIBS data is effectively compressed as it is represented by fewer variables in the non-physical space. In this representation each independent material spectrum is shown as a point in the new space. By utilizing multiple LIBS spectra from the same type of samples a clustering of points can be observed, indicating they have a lot in common. In contrary, if one processes a spectrum of a different sample it will show up as point outside the cluster. For a supervised method such as PLS the result is that a test spectrum is directly assigned to a class. To that end one first has to teach the PLS algorithms by inputting known LIBS spectra for each class and assigning them to the correct class. The result of the teaching procedure is a vector which in an inner product with a test spectrum will produce the class it belongs to. Note that the classes are indicated by a sequence of unique integers. Depending on data quality and on how well the teaching LIBS dataset represents the possible variations in what is considered the same types of samples (coverage), the result of the inner product may deviate from the exact class number. The common approach is to make it more robust by setting the same ranges. For example, if two classes are indicated as 1 and 2 the classes are accepted in the ranges 0.5-1.5 and 1.5 and 2.5. If the deviation is too large the spectrum cannot be correctly classified, meaning that the teaching dataset was inadequate.

6.2.1. PRINCIPAL COMPONENT ANALYSIS (PCA)

Notations specific to PCA:

- $X_0(N \times M)$, N spectra, M wavelengths;
- $L(A \times M)$ is a loading matrix with row vectors $l(M)$, where $A \leqslant min(M, N)$;
- $S(N \times A)$ is a score matrix with column vectors $s(N)$;
- $E(N \times M)$ is the X-residual matrix after deflation.

In PCA the dataset X is projected onto a new space according to the decomposition [2] $X = SL' + E$, where the accent denotes transposition. The dimension of the new latent space is A, spanned by variables called *principal components*. Particular to PCA is that the

decomposition is carried out such that the largest variance is sorted in the first component axis, the second largest in the second component axis, and so on by means of an iterative algorithm. The modulus of the score vector (s) shows how much of X is represented on the corresponding axis represented by the loading vector (l). Thus, redundant, non-correlated information is eliminated and the variance is concentrated in the corresponding component axis. The iterative process to determine principal components is [3]:

1. Mean-centre the data matrix X, set $a = 1$, and initialize residual $E = X$;
2. Assign a score vector: $s_i = E(N \times m)$, where $m = 1 \cdots M$ is user's choice;
3. Compute the corresponding loading vector: $l' = E's$;
4. Normalize l and compute the new score vector: $s_i + 1 = El'$;
5. Check convergence: if $|s_i + 1 - s_i| < \xi|s_i|$ go to step 6, otherwise to 3; in case of poor convergence go to 2 and choose different m.
6. Eliminate the largest variance from the residual: $E_i + 1 = E_i - s_{i+1}l$;
7. Increase the counter a and either go to step 2, or finish.

Another option is to solve the eigenvalues and vectors of the covariance matrix XX', instead of those of X. However, in practice S and L are more efficiently obtained using singular value decomposition, where S is equal to the product of the left singular and diagonal matrices and L is formed by the right singular matrix. For application to classification, the loading matrix L is determined first by using the training dataset, and the score matrix S for blind samples is then obtained as $S = XL$.

6.2.2. PARTIAL LEAST SQUARES (PLS)

Notations specific to PLS:

- $X_0(N \times M)$ is the training data matrix with N spectra and M wavelengths;
- $Y_0(N \times K)$ is the training classification matrix with K classes;
- $W(A \times M)$ is a weight matrix with row vectors $w(M)$;
- $T(N \times A)$ is a X score matrix with column vectors $t(N)$;

- $P(A \times M)$ is a X loading matrix with row vectors $p(M)$;
- $U(N \times A)$ is a Y score matrix with column vectors $u(N)$;
- $Q(A \times K)$ is a Y loading matrix with row vectors $q(K)$;
- $E_X(N \times M)$ is the X residual matrix and $E_Y(N \times K)$ is the Y residual matrix after deflation.

The purpose of PLS is to decompose both the data and class matrices as $X = TP + E_X$ and $Y = UQ + E_Y$ by iteratively reducing the residuals to the level of noise.

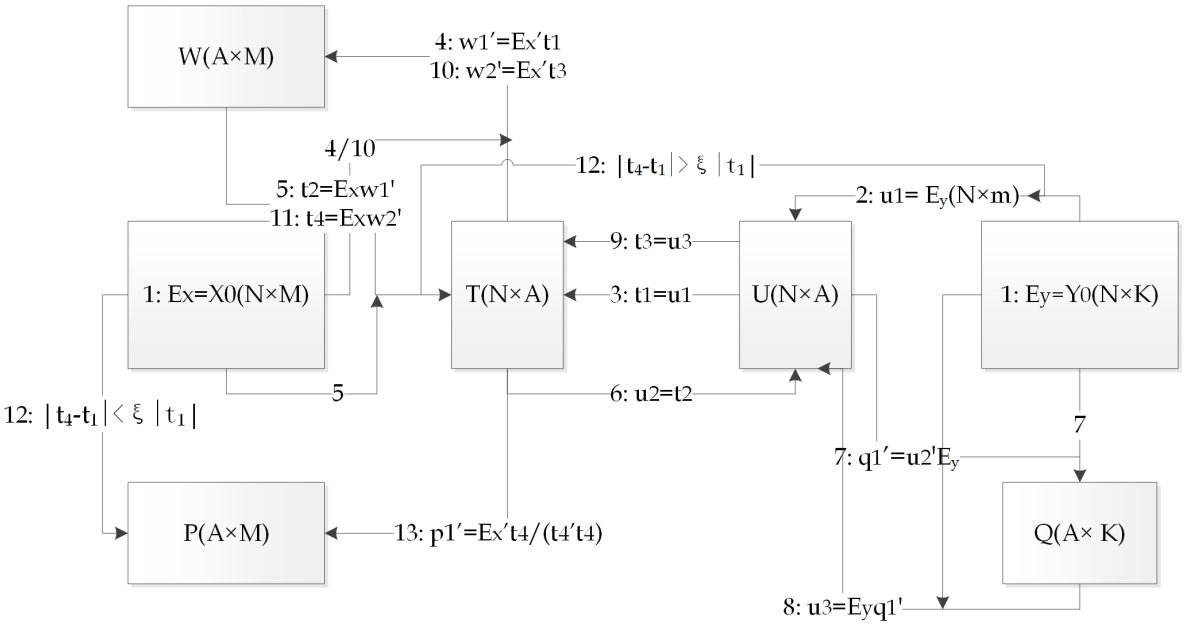


Figure 6.2: NIPALS algorithm proposed by Wold et al. with each step numbered in sequence.

The first PLS algorithm (NIPALS) was proposed by Wold et al. in 1984 [4], who used an iterative procedure to obtain the correlation coefficient between X and Y. To that end, X and Y are deflated to facilitate the build-up of new components used in the reconstruction of X and Y. An advantage of PLS is that it takes the correlation between X and Y into account when new components are being reconstructed. The algorithm in Fig. 6.2 consists of the following steps to build the components $a = 1 \cdots A$:

1. Mean-centre data matrix X, define Y, set $a = 1$, and initialize residuals $E_x = X$ and $E_y = Y$;

2. Assign a Y score vector: $u_1 = E_y(N \times m)$, where $m = 1 \cdots M$ is user's choice;
3. Set the X score vector: $t_1 = u_1$;
4. Compute the weight vector: $w_1' = E_x' t_1$ using the auxiliary relation $T = E_x W$;
5. Normalize w_i and compute a new X score vector: $t_2 = E_x w_1'$;
6. Set the new Y score vector: $u_2 = t_2$;
7. Using $Y = UQ$ compute the E_y loading vector: $q_1' = u_2' E_y$ and then normalize q_1;
8. Re-compute new Y score vector: $u_3 = E_y q_1'$;
9. Set the new X score vector: $t_3 = u_3$;
10. Compute the new weight vector: $w_2' = E_x' t_3$ using the auxiliary relation $T = E_x W$;
11. Normalize w_{i+1} and compute a new X score vector: $t_4 = E_x w_2'$;
12. Check convergence: if $|t_4 - t_1| < \xi |t_1|$ go to step 13, otherwise to 3; in case of poor convergence go to 2 and choose different m.
13. Compute the X loading vector: $p_1' = E_x' t_4 / (t_4' t_4)$;
14. Store vectors t_4, p_1, u_3 and q_1 as t_a, p_a, u_a and q_a in the corresponding matrices;
15. Compute the new residuals: $E_{x;a+1} = E_{x;a} - t_a p_a$ and $Ey; a+1 = E_{y;a} - u_a q_a$;
16. Increase counter a and either go to 2 or finish.

When the counter is large enough the original matrices X and Y should be effectively decomposed as $X = TP$ and $Y = UQ$ where $T = U$ and the residual have supposedly reduced to noise and may further be neglected. The correlation matrix β between X and Y in this case is $Y = UQ = TQ = XWQ$, from which one may infer $\beta = WQ$. During each loop a new component is built via the scores (t_a, u_a), weight w_a, and loadings (p_a, q_a). After each loop, the original X and Y matrices are deflated and the next component is to be built using the residuals E_x and E_y. Finally, the linearly correlated score matrices T and U form the new latent space onto which X and Y are projected. The row-normalized weight matrix W represents X in the latent space. It is been proven by de Jong [5] that W is equal to the left singular matrix after performing singular value decomposition on the cross-product of

$X'Y$ or, equivalently, the eigenvectors combined variance-covariance matrix $X'YY'X$ [6]. Further, P and Q are the non-normalized, orthogonal matrices representing X and Y in the latent space and their modulus contain the main information on X and Y.

6.2.3. ADAPTIVE BOOSTING (ADABOOST)

The Adaboost algorithm in Fig. 6.3 consists of the following specific notations:

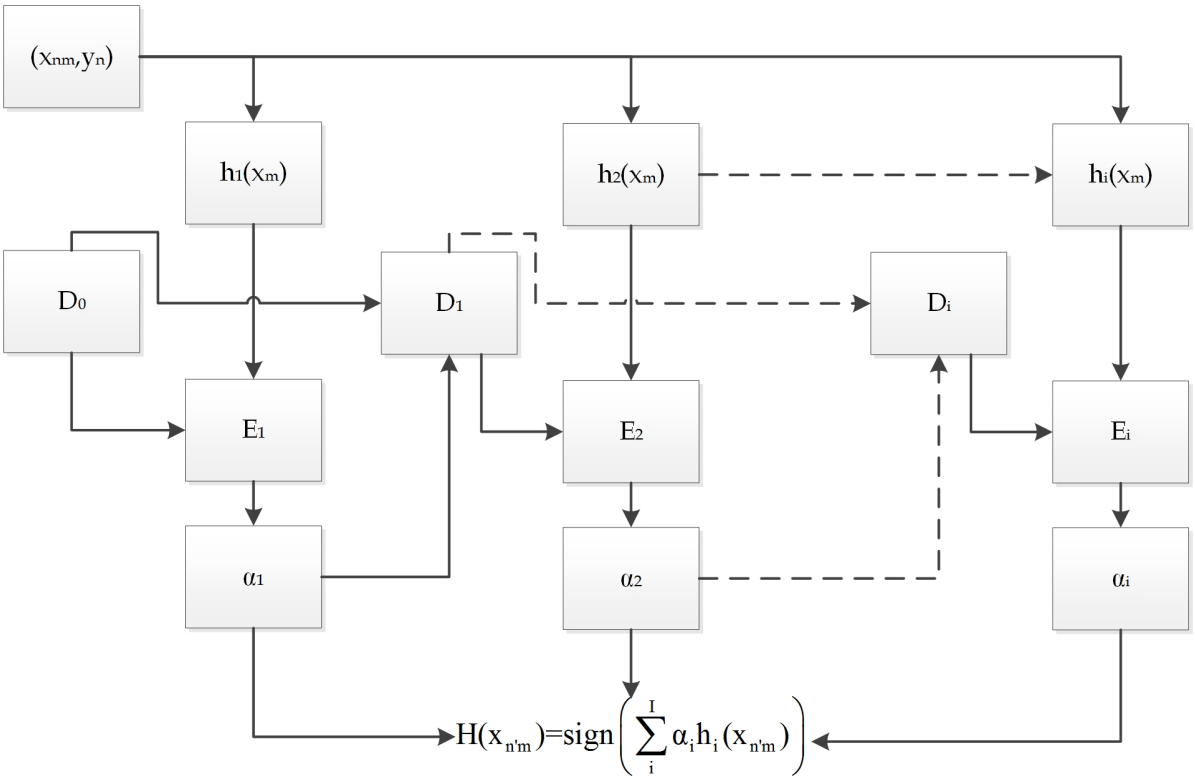


Figure 6.3: Adaboost algorithm in sequence.

- $(x_m, y)_n$: n is training sample identifier, x_m is the m^{th} independent variable or LIBS intensity at the m^{th} wavelength and y is the dependent variable in the binary case 'one-against-all';
- $h_j(x_m)$: a weak classifier to distinguish all samples using independent variable x_m during iteration j;
- $\varepsilon_j(n)$: misclassification error of sample n during iteration j (iteration counter);
- α_j: weight of the weak classifier h_i during iteration j;
- $D_j(n)$: the distribution for sample n during iteration j;

- $\bar{E}_j$: total weighted misclassification error over all samples during iteration j;
- $\bar{E}_{tot}$: total misclassification error over all samples and all iterations;
- $H_{n'}(x_m)$: final strong classifier for blind samples $(x_m, y)_{n'}$ with blind sample identifier n';
- B_E: error bound or upper limit of the error from the training data set using $H_{n'}(x_m)$.

The adaptive Adaboost algorithm is composed of two parts: the introduction of a series of weak classifiers where the next classifier is focused on the main error of the preceding classifier, and a part where the result is generated from the weak classifier in a robust way, the so-called boosting. A weak classifier is defined as having an error < 50%, i.e. always better than a random guess. A virtual distribution of the sample set related to the error as determined by each weak classifier is assumed. If one sample is misclassified by the current weak classifier, the following weak classifier will be adapted to focus more on this sample. The tuneable parameter is the number of iterations during which the weak classifiers are optimized. Finally, a strong classifier is calculated as a weighted combination of all the weak classifiers (boosting). The criterion is the classification error, which depends on both the virtual distribution of the sample set and the reliability of the weak classifiers. In other words, Adaboost only shows its power when each weak classifier shows some classification error, which requires a large sample set. The five Adaboost steps in this work are described as (cf. Fig. 6.3):

1. Initialize the distribution vector with an equal distribution $D_i(n) = 1/N$ for n training samples;
2. Determine the weak classifier $h_i(x_m)$ (+1 or −1) with the minimum total weighted misclassification error E_i over all N samples as the inner product of D_i and a binary vector ε_i, where $\varepsilon_i(n) = 1$ if $h_i(x_{nm}) \neq y_n$ and $\varepsilon_i(n) = 0$ if $h_i(x_{nm}) = y_n$, where y is the user defined yes ($y = +1$) or no ($y = -1$) whether training sample n belongs to a certain class.
3. Compute the reliability of the weak classifier as a monatomic decreasing function of E_i in a nonlinear fashion according to eq. 6.5;

4. The update of the distribution function included the boosting parameter α, according to eq. 6.6;

5. If $E_i < 0.5$ and the maximum number of iterations have not been reached, repeat steps 1-4.

6. Now, the strong classifier H for the samples can be determined from the weak classifiers and applied to the blind samples (n')according to eq. 6.8.

The weight of the weak classifier α_i is calculated as a function of its misclassification error E_i as:

$$\alpha_i = \frac{1}{2} ln\left[(1 - E_i)/E_i\right] \tag{6.5}$$

and the distribution function of each dataset is calculated as:

$$D_{i+1}(n) = \frac{D_i(n)}{F_i} = \begin{cases} exp(-\alpha_i), \ if \ h_i(x_{nm}) = y_n \\ exp(+\alpha_i), \ if \ h_i(x_{nm}) \neq y_n \end{cases} \tag{6.6}$$

where F is a normalization of the sum over D, noting that the final distribution should also be normalized accordingly. If we assign $y_n \in \{+1, -1\}$, eq. 6.6 can be rewritten as:

$$D_{i+1}(n) = D(n) exp\left[-\alpha_i y_n h_i(x_{nm})\right]/F_i \tag{6.7}$$

The final strong classifier (the boosting) is calculated as:

$$H(x_{n'm}) = sign\left(\sum_i \alpha_i h_i(x_{n'm})\right) \tag{6.8}$$

According to eq. 6.5, the larger the weighted total error E_i the less reliable the corresponding classifier is. For example, if $\alpha_i \leq 0$ or $E_i \geqslant 0.5$, it is more probable that $\alpha_i h_i(x_{n'm}) \neq y_{n'}$. These less effective weak classifiers should be eliminated from the final strong classifier by monitoring E_i. On the other hand, according to eq. 6.7, the misclassified sample gets more weight in a next iteration. The final strong classifier is a weighted sum over all weak classifiers according to their reliability α_i. Adaboost is well suited to deal with single-shot LIBS spectral data in view of the wide variance in the data.

6.3. CASE STUDY: CLASSIFICATION OF CEMENT, CONCRETE, AND WASTE POLLUTANTS

We evaluate and compare the performances of PCA-Adaboost and PLS-DA using LIBS spectra. Data are collected from raw materials and products in cement and concrete

production (cf. Fig. 6.4): calcium oxide (Ca), silicate (Si), aluminium (Al) and iron (Fe), limestone (ls), marl (ml), raw meal (rm), clinker (ck), cement (cm), calcium sand (cs) and bauxite (bau). In addition, pollutant materials in concrete waste are classified as is mandatory for quality inspection of demolished concrete.

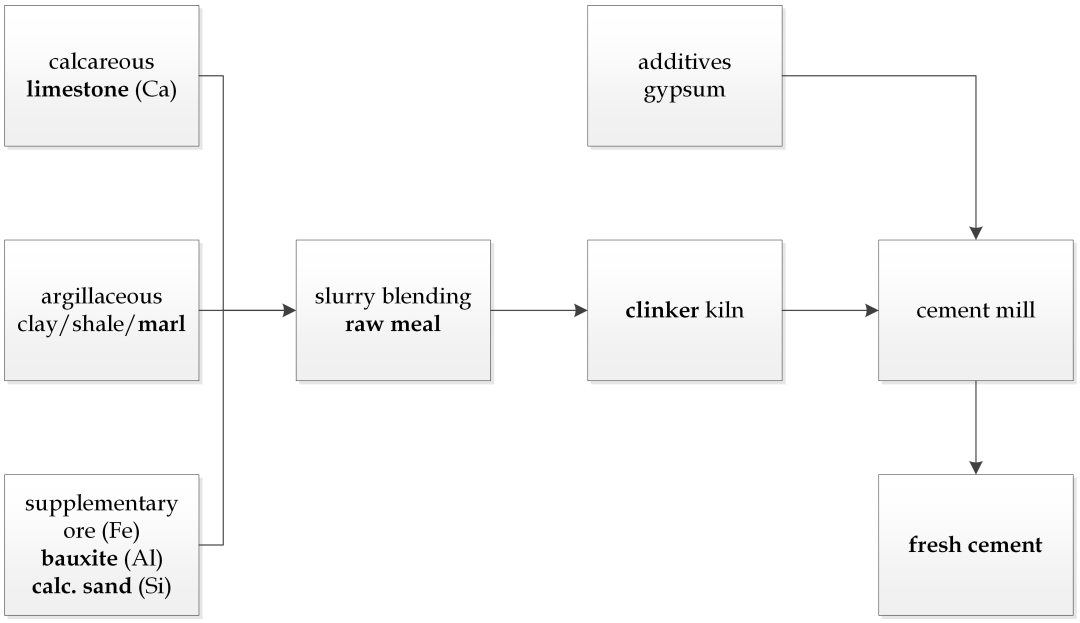


Figure 6.4: Raw materials and steps in the production of fresh cement.

The influence of different approaches to data processing methods using single-shot LIBS spectra will be investigated:

1. Raw LIBS spectra (R): keep original information in X.
2. Normalization to the mean spectral integral as defined by eq. 3.14, (N): compensate for some shot-to-shot variations.
3. Auto-scaling (AS): treat emission at each wavelength equally.
4. Background subtraction as described in Chapter 3 (BG): only take dominant emission line into account.
5. Combination of 4. and 2. (BG+N): compensate for some shot-to-shot variations for dominant emission lines.
6. Combination of 4. and 3. (BG+AS): compensate for some shot-to-shot variations for each emission lines.

7. Raw spectra, but using only specific wavelengths where the selection is performed using the method described in chapter 3 (WS);

The raw spectra and background are shown in Fig. 6.5. It will be demonstrated that the backgrounds in the spectra are also material dependent and, hence, carry distinctive information that can be useful for classification. Auto-scaling gives each wavelength the same weight so that minor peaks are more emphasized, at the risk of emphasizing noise. Background subtraction typically eliminates the continuous emission, absorption bands and non-resolved peaks. According to findings in chapter 4, some parts of the background may be correlated with specific emission lines, but fortunately the shot-to-shot variance of the background is always relatively small.

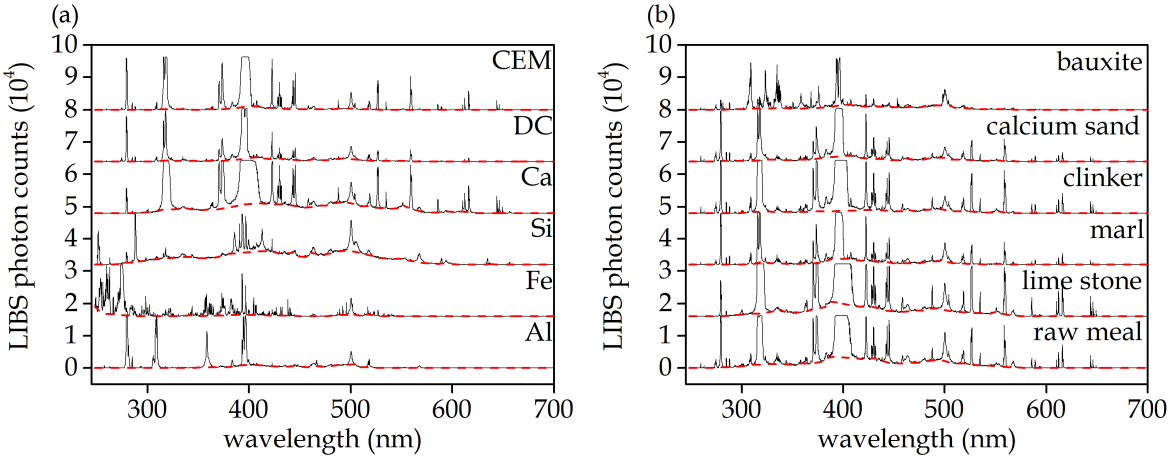


Figure 6.5: LIBS raw spectra (solid lines) with reconstructed background (dashed lines). (a) Products and pure samples. (b) Materials used in cement production.

6.3.1. PCA-ADABOOST

A PCA model should link the data to the unknown material properties. Using pure Ca, Si, Al, Fe as references, all materials are traceable with clear trends w.r.t. reference materials as shown in the PCA score plot (cf. Fig. 6.6a) using training (90 × 12) to testing (10 × 12) spectra ratio of 9 : 1 from 100 single-shots per material. Some quantitative information can be extracted from the PCA score plot on the first two PCs. The demolition concrete, cement, calcium sand and marl clusters are quite close. The cement cluster is separated from the other sample clusters, especially from clinker which is an earlier stage in cement production. Other closely clustered materials are clinker, raw meal, and limestone which are all

calcium-rich materials. Not surprisingly, the bauxite cluster is close to aluminium and iron (magnetite, hematite).

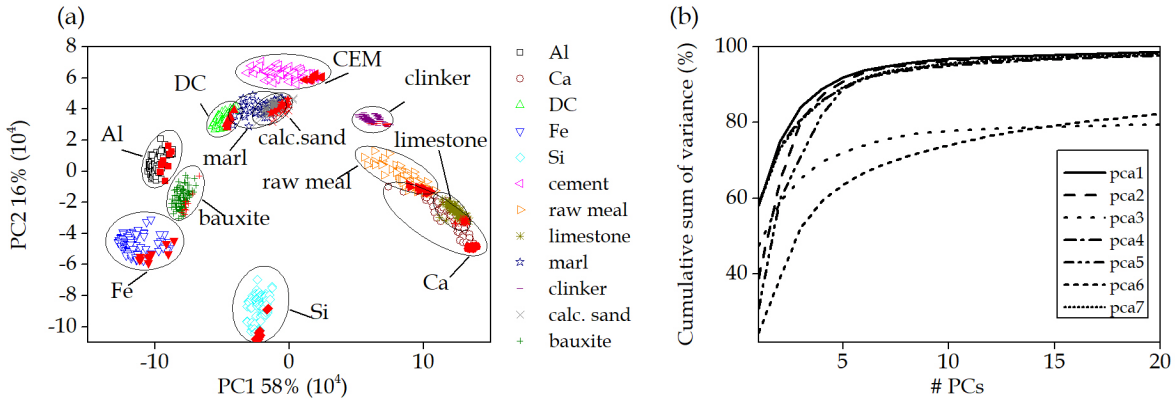


Figure 6.6: (a) PCA score plot on first two PCs with corresponding percentage of variance using raw LIBS data. Colored symbols are samples from the training set and red are sampled from blind tests. (b) Cumulative sum of variance for the seven pre-processing methods.

Figure 6.6b shows the cumulative sum of the variance in the data matrix X. The pre-processing method 1 covers the maximum cumulative variance since it uses the original LIBS spectra in X, followed by methods 4 and 7. The difference between 4 and 7 is related to emission line broadening. The pure reference materials are well distinguishable because they have very different spectral abundances and the emission lines are quite distinguishable by using the first two PCs. In fact, broadening effects as discussed in Chapter 5 result in peak shapes for emission lines and cause overlap of lines. In method 7 only the peak wavelengths are registered and in method 4 the whole peak shape is recorded including peak, shoulder and tail wavelengths. However, their influence indicated that the peak shoulder and tail are well correlated. Methods 2 and 5 show similar trends in that the first few PCs carry less variance compared with method 1 because to some extent they compensate for the shot-to-shot variations, especially for emission lines which variance is mixed in with the variance of the background. Still, the curves for methods 2 and 5 both converge to curve 1, indicating that noise is not the main issue. The auto-scaling methods 3 and 6 both increase slowly and do not reach the same level of variance as the other methods. This indicates that noise does make a difference for methods 3 and 6 or, in other words, the signals contain less material-distinguishing information. The results of the PCA-Adaboost model w.r.t. methods 1 to 7 are listed in Tab. 6.1. Here, misclassification (mc) accounts for both false negatives and positives. Normalization improves the classification at the cost of an

increase in the number of iterations.

Table 6.1: PCA-Adaboost misclassifications (mc) and number of iterations (it) per material (10 testing spectra per material) for the seven pre-processing methods.

Method		Al	Ca	DC	Fe	Si	cm	rm	ls	ml	ck	cs	bau	tot
1: R	mc	1	0	0	0	0	0	0	1	1	0	1	0	4
	it	1	9	3	1	1	1	7	7	9	5	14	1	59
2: N	mc	0	0	0	0	0	0	0	1	0	0	0	0	1
	it	1	9	3	1	1	3	12	11	10	5	13	3	72
3: AS	mc	1	0	3	0	0	4	0	0	2	0	0	1	11
	it	3	5	9	3	3	7	7	6	18	6	13	5	85
4: BG	mc	0	4	1	0	0	0	0	1	1	0	3	0	10
	it	3	14	4	1	1	8	7	12	11	5	13	1	80
5: BG+N	mc	0	2	0	1	0	0	0	0	2	2	1	0	8
	it	1	8	3	1	1	6	10	11	9	10	14	1	75
6: BG+AS	mc	0	4	3	0	5	0	6	1	3	0	1	0	23
	it	5	8	11	1	1	5	9	9	13	5	15	3	85
7: WS	mc	1	2	1	1	0	1	0	1	2	2	0	0	11
	it	3	13	3	1	1	8	9	14	9	4	16	1	82

6.3.2. PLS-DA

Tab. 6.2 shows the results for combinations of the seven pre-processing methods and PLS-DA. Again, the raw single-shot LIBS spectra produce the lowest RMSE% during training with 5-fold cross validation (CV). The numbers of loadings are determined by the minimum RMSE%. The misclassification for blind testing data is zero, except for pre-processing method 6 (BG+AS). It indicates that most of the variance in the blind samples is already covered using 90% of the shots (out of a total 100) for training and 10% for blind testing and 5-fold CV. It is noted that the CV step makes PLS more robust where it concerns the optimum ratio of the size of the training set to that of the blind testing set, where the number of CV also has some influence on the results.

Table 6.2: PLS-DA misclassifications for blind testing data (10% of total spectra), number of loadings (LD) and relative mean square error (RMSE) for the training data (90% of total spectra).

Method	Al	Ca	DC	Fe	Si	cm	rm	ls	ml	ck	cs	bau	#LD	RMSE
1: R	0	0	0	0	0	0	0	0	0	0	0	0	138	10.05
2: N	0	0	0	0	0	0	0	0	0	0	0	0	126	11.79
3: AS	0	0	0	0	0	0	0	0	0	0	0	0	36	29.24
4: BG	0	0	0	0	0	0	0	0	0	0	0	0	154	11.75
5: BG+N	0	0	0	0	0	0	0	0	0	0	0	0	133	13.93
6: BG+AS	0	4	0	0	5	0	0	0	0	0	0	0	77	19.82
7: WS	0	0	0	0	0	0	0	0	0	0	0	0	85	17.66

The cumulative variances in X and Y matrices of PLS represented by each loading is shown

in Fig. 6.7. Similar to the X variance in PCA, the highest represented method is 1, followed by 4, 7, 2, 5, 3 and 6. Because X and Y are inter-correlated in building the PLS model, it is also apparent that the variance in Y w.r.t. the loadings follow a similar trend as X. The main differences in variance between X and Y appear to have been suppressed by the normalization of the weight vectors (w). It is noted that the vectors of Y are orthogonal because the entry for each material of interest is unity while the others are set to zero, which does not change between the seven pre-processing methods. Therefore, the PLS1 model (using one y vector) should give the same results as the PLS2 model (using multiple y vectors).

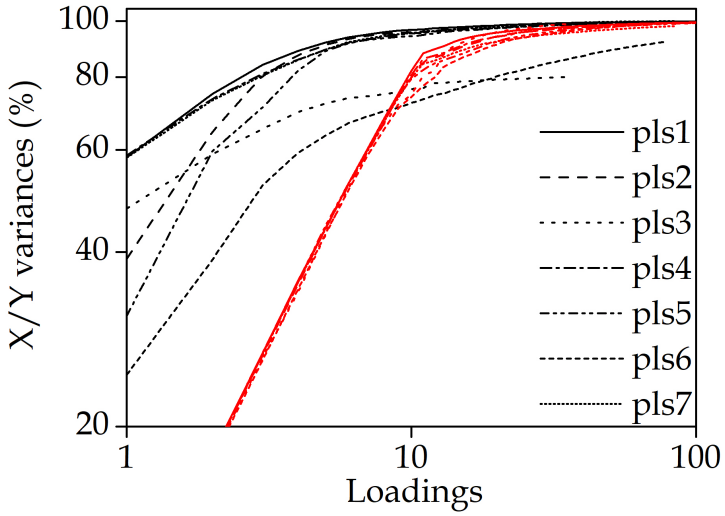


Figure 6.7: Cumulative X (black lines) and Y variance (red lines) represented by the PLS loadings corresponding to the seven pre-processing methods.

6.4. CASE STUDY: CLASSIFICATION OF MOVING WASTE MATERIALS

In this section we investigate moving granular waste materials, simulating the motion on a conveyor belt, and the possible influences this may have on LIBS characterization. We test a range of common building waste materials found in concrete waste and apply different statistical spectral processing methods for comparison.

6.4.1. SAMPLES AND SETUP

We investigate the misclassification error when using PCA-Adaboost and PLS approaches. LIBS spectra are acquired using the setup shown in Fig. 3.16. In particular, the data

processing method 2 (N) from Section 6.3 is compared with method 3 (AS). The moving materials in the concrete waste stream to be tested are contaminants such as wood, PVC, gypsum block, glass, brick, steel rebar, which all can be detrimental for the quality of the recycled products, such as coarse aggregate, fine cement paste and concrete. For each material, up to three different types were considered. For each material, thirty different particles were randomly selected from streams of demolition concrete to represent the materials (cf. Fig. 6.8): cement (CEM I 42.5R HS, CEM II/B-S 52.5 N, CEM III/B 32.5 N), brick (yellow, brown and red), gypsum block (white, blue and red), wood (pine, ash and walnut), PVC plastic (grey, black pipe and grey hard plate), glass (white, green and brown), two of the most common types of aggregate (sandstone and gabbro), and steel rebar, (carbon steel). Each set of thirty particles were evenly divided between the different types to form a total set of two hundred forty particles.

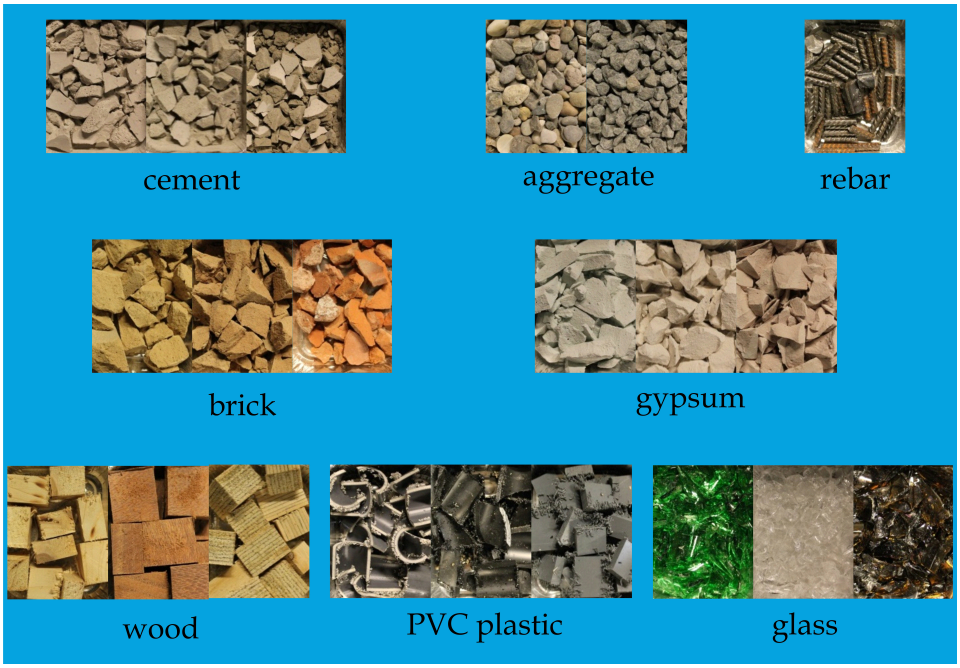


Figure 6.8: Eight waste materials and 21 selected types from a stream of demolition concrete.

Dust was removed from the waste particles using compressed air, which preparation is also quite feasible when the materials are in motion on a conveyor belt. In fact, it may be preferable to the alternatives, such as using a more powerful laser (requiring shorter lifespan flash lamps) or using two lasers where one fires first with the sole purpose of cleaning the surface. In the envisioned application, the moving feed layer of 2-32 mm concrete waste particles



Figure 6.9: Granular materials mounted on a rotating plate. Laser-induced plasma is visible on a brick particle.

will be slightly compressed by a roller to provide a flattened material surface level for the laser to focus on. This avoids the need for an expensive autofocus unit. In our setup (cf. Fig. 6.9), six particles were mounted at a time, rotated and sampled until thirty acceptable (qualified) single-shot spectra per particle were acquired. This process was repeated forty times to the total of two hundred forty particles. Data qualification was applied, where non-qualified spectra were removed from the dataset. To that end, upper and lower limits for the maxima of a spectrum were set, corresponding to 98% and 42% of the dynamic range of the detector, to eliminate the saturated or otherwise poorly delivered spectra. Fig. 6.10 shows how many shots are required for each material to obtain thirty qualified spectra. For most materials between 30% and 45% of all shots are qualified. This means that in practice in a single-shot scenario one would need at least four shots per particle to obtain one qualified shot. The non-qualified ones (ranked in order of decreasing probability) may mostly be attributed to misses (particle spacing), particle edges, surface roughness and porosity, material heterogeneity and high transparency in the case of glass. The steel rebar was quite uniform in material surface properties and shape, which lead to a high percentage of qualified spectra.

The type of cement in concrete demolition waste is of minor interest, because the focus

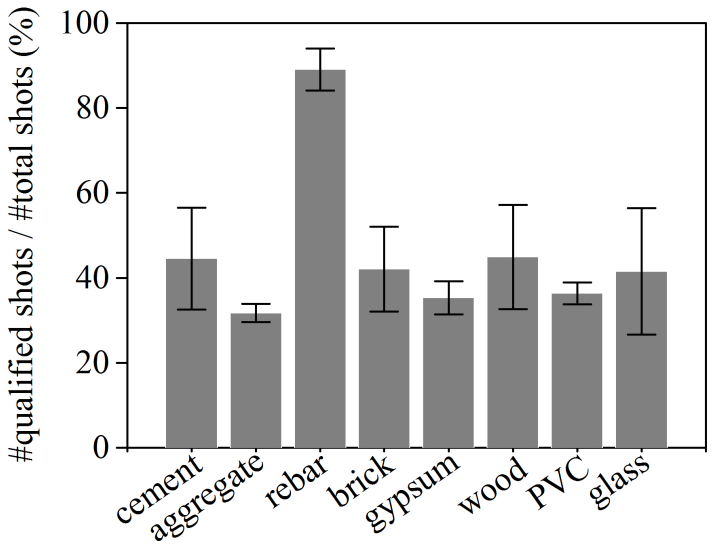


Figure 6.10: The qualified spectra as a percentage of the total number of deployed laser shots. The bar shows the mean for the thirty particles per waste material, and the brackets show the standard deviation.

is here on detecting the waste pollutants. It should also be pointed out that cement stone from demolished concrete is in fact a mixture of sand and cement, where the sand may have a similar geological origin as the coarse concrete aggregate. Of the metals only steel rebar is selected, because other building metals (e.g. aluminium) proved just as easy to discriminate from other waste types as steel. From the large variety of rock types used for concrete aggregate, sandstone and gabbro are arguably the most widely used sources. To emphasize the cement properties instead of the concrete sand, three types of pure cement paste were prepared by mixing cement powder and distilled water to a water/cement ratio of 0.5. It was left to cure for several days to full strength and was then broken into small particles.

6.4.2. LIBS SPECTRA OF EIGHT WASTE MATERIALS

LIBS emissions are primarily produced by the plasma plume, though some emissions may be expected from hot air molecules interacting with the plume, and directly from hot matter at the sample surface. The plume is the result of a sequence of complex physical processes, active during overlapping stages from initiation to extinction of the LIBS experiment as discussed in Chap. 2. As a result, the emissions may be linked to quite different physical processes. To simplify matters we distinguish three types of detectable emissions: continuous radiation, emission bands, and ionic-atomic emissions.

Continuous radiation spans a wide range of wavelengths, linked to as many available energy transitions from ionized species and electrons, e.g. free-free and free-bound transitions [7]. These transitions can occur as long as the plume is hot enough. However, the observed radiation spectra may be quite different for different types of material. This implies that the possible energy transitions and /or most probable emissions depend on the species and degree of ionization of the plume, which in turn are determined by the target material and the effectiveness of laser absorption and the ablation process.

Emission bands arise both in the hottest stage, e.g. Stark broadening and fluorescence shifts, as well as after cooling down of the plume when molecules can start forming. The emission bands are also expected to be highly dependent on the composition of the original target material, how much material is effectively ablated, how hot the plume becomes, and how this particular mix of ionized species eventually condenses.

Complex as the breakdown and ablation processes may be, the continuous radiation and emission or absorption bands may quite well be carrying discriminating information on the target material composition and, quite likely, the specific way in which it has influenced the ablation processes. This implies these spectral contributions may be utilized for materials discrimination, even though it is (at present) not physically tractable and is therefore probably of little use for quantitative measurements. In contrary, ionic-atomic emissions are physically tractable and may, if conditions and calibrations permit it, be used to quantify the elemental concentrations in the target material.

In view of the diversity of potential physical information, it was the logical decision to collect all the types of spectral emissions delivered by the LIBS experiment and let the classification algorithms extract any discriminating information. This way, we also avoid material sensitive calibration procedures and tuning of the time integration window.

Fig. 6.11 shows representative spectra for the waste materials and indicates a few characteristic emission lines and bands. The discriminating emission lines in PVC are Cl (594 nm), CaCl bands (618 nm), CN bands (387 nm) and Ca (422 nm). It indicates the

presence of $CaCO_3$, which is a common type of filler in thermoplastics. Since wood is principally made up of cellulose and lignin, the strong presence of CN, H, O emission lines was expected. Due to the porosity of wood, the laser energy was more prone to be absorbed by air pockets as the spectrum therefore shows strong N emissions. The spectrum of glass shows the expected elements Ca and Si, but it also indicates the presence of Ba, which is a toxic element. The steel rebar shows multiple, well resolved Fe-related emission lines. The gypsum block shows only very weak evidence of S in the 550-556 nm range, while the elemental S content in the gypsum block is estimated as 15 wt%. This confirms the weak emissions of sulfur in the visual range [8].

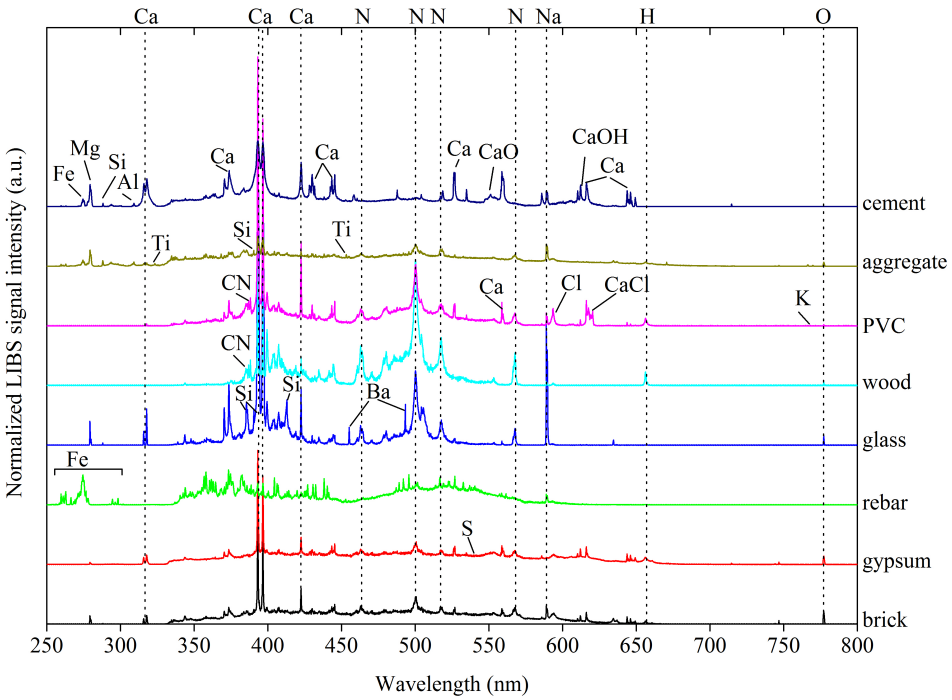


Figure 6.11: Normalized LIBS spectra for eight building waste materials.

The brick and cement share a similar composition as gypsum block where it concerns the elements Ca, Si, Al, Fe, Mg and Na. The similarity for brick and cement is the presence of clay, the main component of brick, and which also used to produce cement in kiln. It is noted that gypsum is added to cement to improve the setting properties of fresh mortar. The CaO and $CaOH$ bands were easiest to observe in cement spectra due to the high Ca content. The continuum contribution to the spectrum appears relatively stronger for the mechanically harder and optically opaque types of material. In this work those are steel

rebar, concrete aggregates and cement. It may be inferred from these comparisons that the LIBS spectra are also sensitive to the optical and mechanical properties of the target materials by virtue of the underlying laser absorption and ablation processes. Judging from the fact that sometimes the most characterizing element emissions are weak or may even be absent for some waste materials, e.g. sulphur in gypsum block, the complete time history provided by LIBS should be utilised to improve the reliability of a classification method.

6.4.3. PLS-DA RESULTS ON EIGHT WASTE MATERIALS

With 72 spectra (each 10 averaged) per material, a 576×3648 predictor matrix is created. Corresponding to X, the response variable Y is a 576×8 label matrix which classifies the materials in a binary way either as a one ("target material") or as a zero ("other material").

The number of PC is a primary parameter in PLS-DA. Selecting too few could result in under-fitting, while too many could result in significant over-fitting in the calibration model. Whereas over-fitting may improve the training, the prediction performance during testing may be poor. Usually, the number of PC is chosen by examining the percentage of variance explained by the model and the relative mean squared error of cross-validation (RMSECV).

With the 9-fold cross-validation the training dataset was partitioned into nine mutually exclusive and equal subsets. Each subset was used as a test set, while a PLS model was trained using the other subsets. The nine results were averaged to produce a single PLS calibration model. This internal validation method makes it possible that each sample can be seen as a test for which the prediction error (RMSECV) can be calculated. Therefore, the resultant model using cross-validation could be better representative for the statistical spread in the data than for example goodness of fit that varies significantly with the choice of training dataset.

Traditionally, the number of PC is determined by the point where the RMSECV is minimal. In this case, the RMSECV estimate for a 9-fold cross-validation reaches a local minimum for both mean centre (1.5% of RMSECV and 99.8% variance in Y) and auto scaling (2.0%

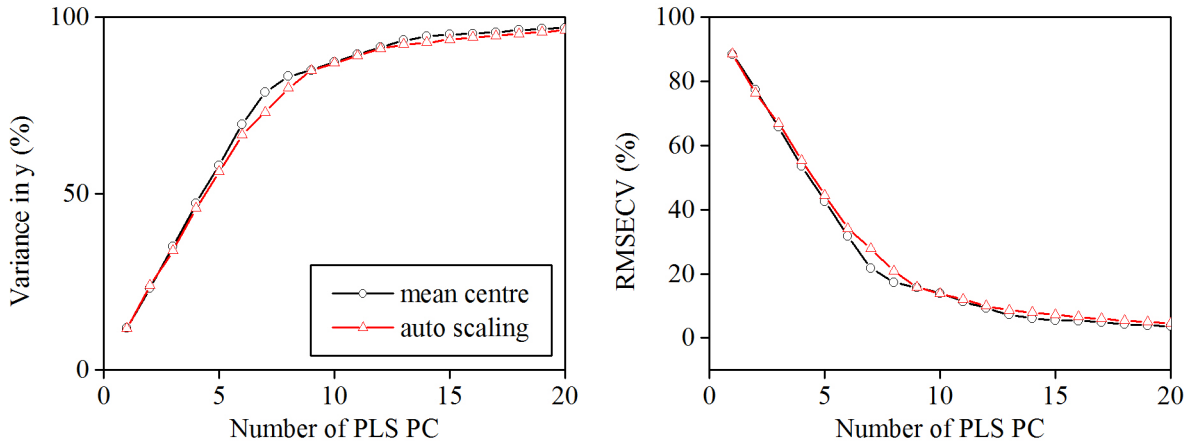


Figure 6.12: Variance explained in the response variable as a function of the number of PLS PC (left) and the RMSECV for 9-fold cross-validation (right) using mean centre and auto scaling.

of RMSECV and 99.6% variance in Y) with the first 59 PC. Mean centre performs slightly better as it shows a higher variance in Y and a lower RMSECV. However, both methods (cf. Fig. 6.12) converge slowly after 17 PCs and the RMSECV is smaller than 5% for 17 PCs using mean centre compared with 6.0% using auto-scaling. We choose mean centre for PLS in the remainder of this section. Cross-validation is mostly applied in quantitative

Table 6.3: Misclassification rates [%] of PLS-DA (with mean centre) during training for increasing number of PC. For each material 72 training spectra were used.

#PC	cement	aggregate	rebar	brick	gypsum	wood	PVC	glass
1	0.0	100.0	100.0	100.0	100.0	0.0	100.0	100.0
2	0.0	100.0	0.0	100.0	95.8	1.4	100.0	0.0
3	0.0	100.0	0.0	16.7	27.8	0.0	100.0	0.0
4	6.9	58.3	0.0	0.0	0.0	0.0	100.0	0.0
5	9.7	97.2	0.0	0.0	0.0	0.0	16.7	0.0
6	9.7	15.3	0.0	11.1	0.0	0.0	16.7	0.0
7	6.9	12.5	0.0	11.1	0.0	0.0	16.7	0.0
8	5.6	5.6	2.8	0.0	0.0	0.0	16.7	0.0
9	5.6	1.4	0.0	0.0	0.0	0.0	16.7	0.0
10	0.0	1.4	0.0	0.0	0.0	0.0	16.7	0.0
11	0.0	0.0	0.0	0.0	0.0	0.0	16.7	0.0
12	0.0	0.0	0.0	0.0	0.0	0.0	16.7	0.0
13	0.0	0.0	0.0	0.0	0.0	0.0	8.3	0.0
14	0.0	0.0	0.0	0.0	0.0	0.0	1.4	0.0
15	0.0	0.0	0.0	0.0	0.0	0.0	0.0	0.0

calibrations, because the error can be accurately calculated as a continuous value. However, cross-validation can overestimate the number of PC required for classification since the classification rules may exaggerate the error. Table 6.3 shows the misclassification rate [%] for increasing PC during training, based on 72 spectra of each material. This approach is also known as 'goodness of fit'. In contrast to the 59 PC determined using

9-fold cross-validation, only 15 PC are shown to provide full classification during training, corresponding to a RMSECV of 5.5%. PVC proves to be the most challenging.

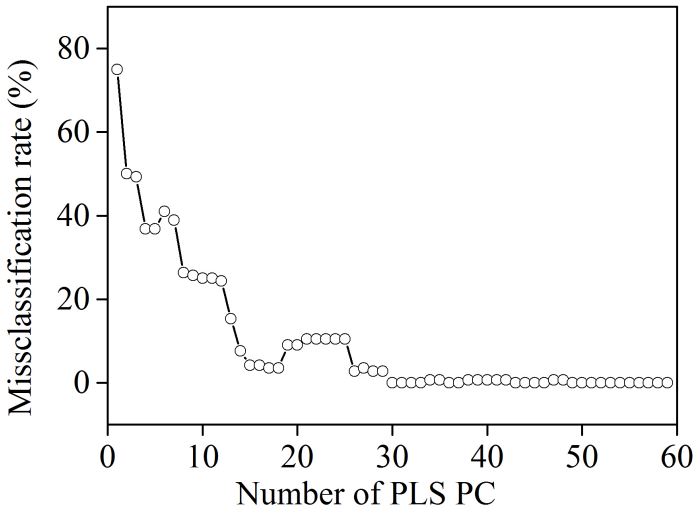


Figure 6.13: Misclassification rate (ratio of misclassified to total number of test spectra).

It is desirable to find a reliable relation between the number of PC as determined by 9-fold cross-validation and goodness of fit. To this end, 18 testing spectra per material are used in two PLS models, which results are compared in Fig. 6.13. Six glass test spectra were misclassified as brick (4), aggregate (1) and gypsum (1), using a PLS model with only 15 PC. Apparently, this error is the result of under-fitting. In this case, addition of PC may help cover a possibly wider spread during testing. Indeed, with 59 PC all 18 spectra for each material are fully classified.

Figure 6.13 shows that full classification is achieved for the first time with 30 PC, corresponding to 2.2% of RMSECV. However, with increasing number of PC, the curve fluctuates until it remains zero at 49 PC (1.5% of RMSCV). This level of correspondence between cross-validation and goodness of fit might vary according to the partition of training and testing datasets. In this sense, cross-validation appears more reliable, even though it introduces here some 10 redundant PC.

To gain same insights into the influence of partition of datasets on PLS performance, 2, 4, 6, 9-fold cross-validation (corresponding to 1, 3, 5 and 8 training to testing datasets ratios)

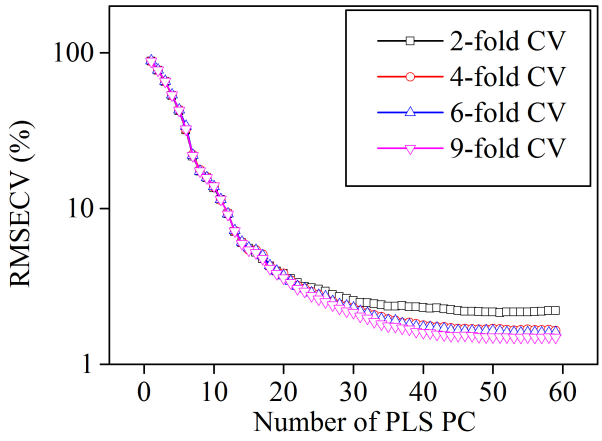


Figure 6.14: RMSECV with increasing number of PLS PC applying different folds of cross-validation in semi-logarithm.

were employed to evaluate RMSECV for increasing PC in Fig. 6.14. The main differences were observed for higher PC. With relatively large training sets the RMSE values are lower, indicating a better classification at the cost of using more PC. It appears a compromise should be made between the number of training samples and the misclassification rate. It is noted that the RMSECV cannot be lower than 2% if the training set is smaller than the testing set. Practically, the PLS algorithm did not converge for all numbers of PC. Fig. 6.14 shows that up to 20 PC the convergence rate does not depend on the relative size of the training set. For more than 30 PC, the convergence rate reduces to a crawl, indicating increasing uncertainty in how many PC will be required for full discrimination.

6.4.4. PCA-ADABOOST ON EIGHT WASTE MATERIALS

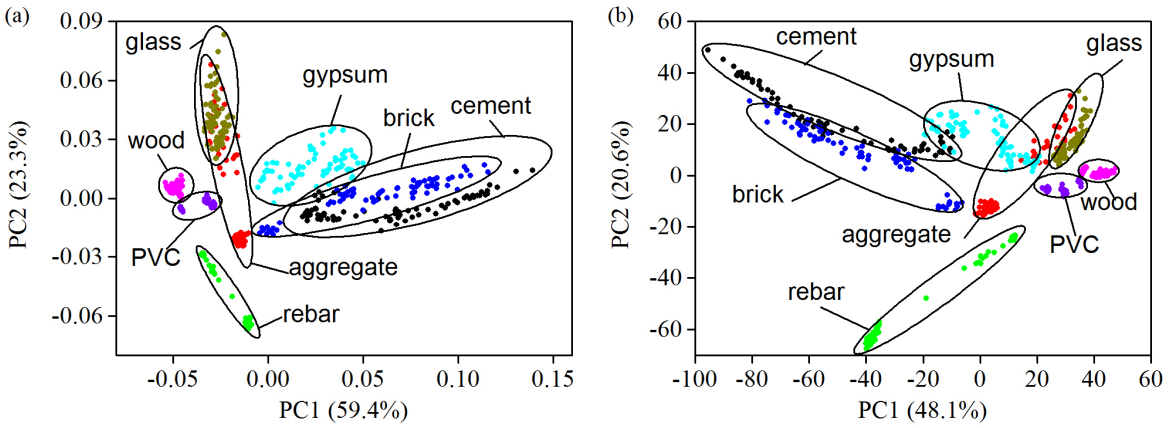


Figure 6.15: Clusters produced by PCA using the first two PC scores. Indicated in the axis label is the PC contribution to the total variance. (a) With mean centre. (b) With auto scaling.

Fig. 6.15 shows PCA clusters for the eight waste materials using the first two PC scores with mean centre (Fig. 6.15a) and auto scaling (Fig. 6.15b), accounting for 83% and 69% of the total variance, respectively. They reveal nicely distinct clusters, regardless of the scales of the PC scores and the direction of the PC1 axis. Glass overlaps with aggregate, while wood, PVC and rebar are already well separated. Cement was better separated from brick using auto scaling.

The PCA scree plot Fig. 6.16 shows that the first five PC account for more than 95% of the cumulative variance in X. Mean centre converges faster than auto scaling, since in auto scaling noise plays a relatively more pronounced role. Next, Adaboost is employed

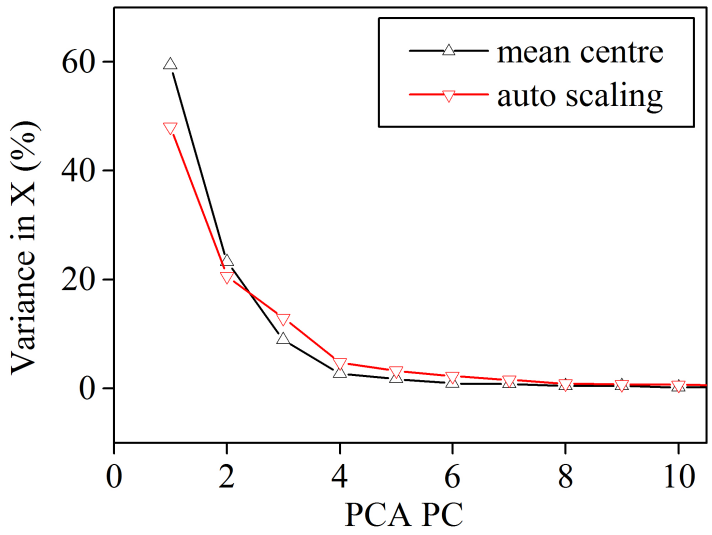


Figure 6.16: PCA scree plot of the percentage of the variance contributed by each PC.

to determine classes using the PCA-PC scores. A few other linear classifiers, reported to be little susceptible to over-fitting, were also tested. The unsupervised types proved less effective, such as K-mean clustering (multi class) and Fischer linear discriminant (binary class). Of the supervised classifiers, Perceptron (multiclass) may perform well for sufficiently resolved classes but it could not find a satisfactory boundary in case of overlapping clusters, similar to the case for cement and brick in Fig. 6.15a.

Since Adaboost is little susceptible to over-fitting, the first 100 PC scores from the PCA algorithm were used as input features, which proved to include all the relevant PC scores as determined by Adaboost. The binary approach was applied, meaning that each single

target material class is determined against the second class, which is the mix containing the other seven waste materials. Fig. 6.17 shows the error bound and weighted error as a function of the number of weak classifiers/iterations using both mean centre and auto scaling. It proves the error bound decreases sharply the first ten iterations, after which it declines quite slowly. At that point of loss of convergence, the weighted error begins to fluctuate, which indicates that the following weak classifiers perform poorly and one should stop. The first few weak classifiers are the most distinctive for classification. Mean centre again outperforms auto scaling in terms of lower error bounds and weighted errors.

Table 6.4: PCA-PC used in Adaboost (one-against-all) during training of 72 spectra and number of misclassifications during testing of 18 spectra. Top two rows relate to mean centre (MC) and two bottom rows to auto scaling (AS). The most distinguishing PC number for the material is in bold face (rb=rebar; wd=wood).

	Cement	aggregate	rb	brick	gypsum	wd	PVC	glass
MC	1,2,3,**5**,10	1,3,**7**,8,10	**2**	1,3,**4**	3,4,**5**,8	**1**	1,2,3,4,6,**7**,8	**2**,3,6,10
misses	1	3	0	1	0	0	0	0
AS	1,2,**6**,7	3,4,7,**8**	**2**	1,**4**,5,7	4	**1**,9	1,2,3,6,9	1,**3**,8
misses	0	6	0	1	0	0	1	17

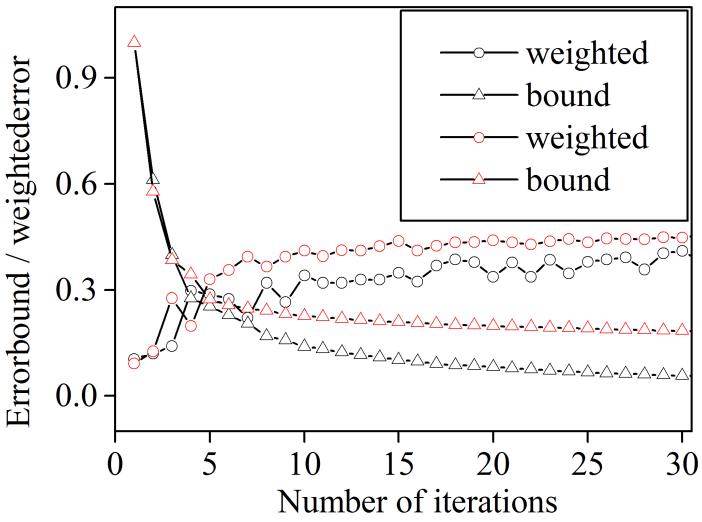


Figure 6.17: Error bound and weighted error during Adaboost training iterations with mean centre (black) and auto scaling (red).

Table 6.4 lists the number of misclassifications using a training set of 72 spectra and a test set of 18 spectra per material. The relevant PC numbers for each target material were determined by Adaboost. It shows that at most only 7 out of 100 PC scores contribute to the classification. Using mean centre, the rebar, gypsum, wood, PVC and glass were fully classified. Five spectra were not classified correctly, meaning the target material was not identified as such, meaning a FN. Using auto scaling the cement, rebar, gypsum and wood

were fully classified. In total, twenty five spectra were not classified correctly. The mean centre approach outperformed auto scaling in terms of total misclassifications and is preferred for PCA-Adaboost.

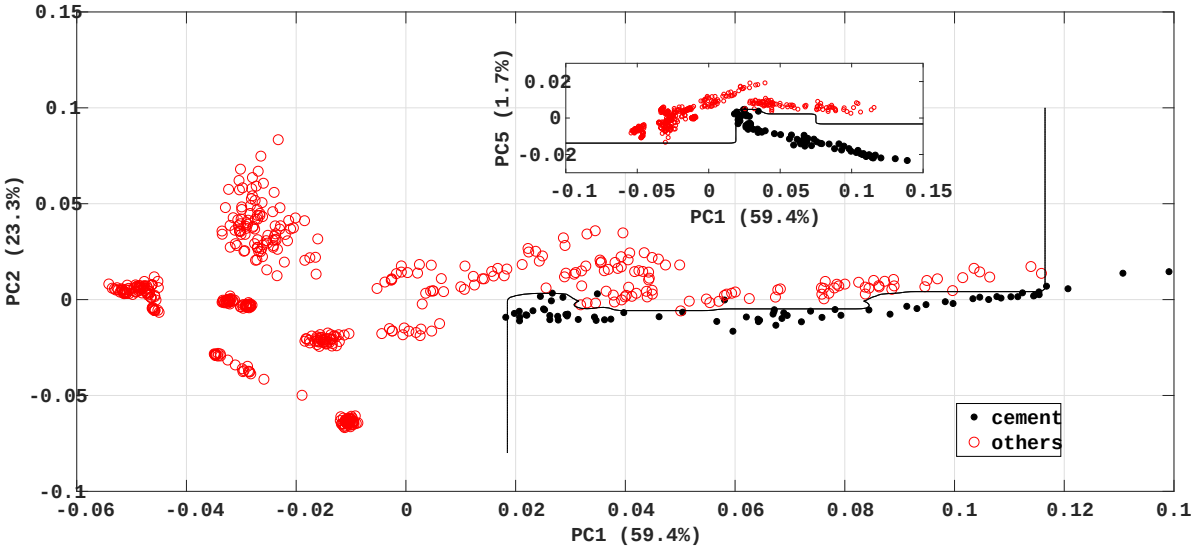


Figure 6.18: Adaboost binary class boundaries for cement against the mix of seven other materials for training. The erratic boundary is for PC scores with high variance coverage and the inset shows a boundary with much smaller variance coverage.

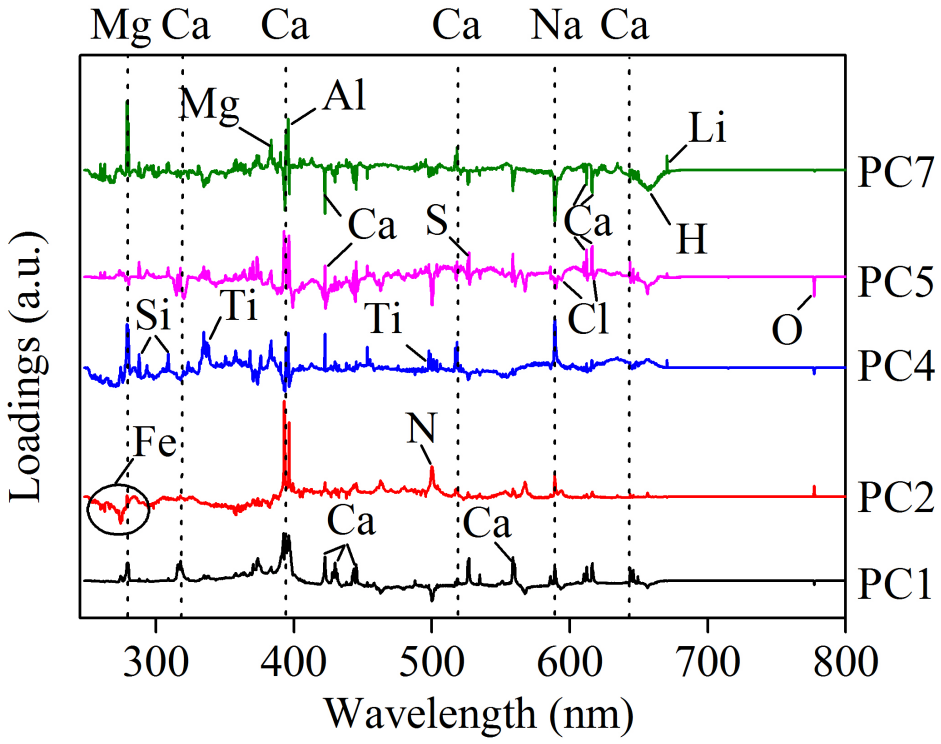


Figure 6.19: PCA loading plot linking the dominant loading vectors to the physical spectra.

Fig. 6.18 shows the typically detailed, seemingly erratic class boundaries produced by Adaboost, in this case for cement against the mix of other materials. For scores PC1 and PC2 the boundary 'surgically' isolates the cement, which explains the success of boosting in producing class boundaries. The inset of Fig. 6.18 details the class boundary in the space spanned by scores PC1 and PC5, where PC5 contributes less than 5% in the variance coverage. This inset shows that the level of PCA variance coverage has no real bearing on the performance of Adaboost for classifying materials.

Based on the results in Table 6.4, a PCA loading plot with the most distinctive PC loading vectors is shown in Fig. 6.19. The parts corresponding to the emission lines and bands mainly responsible for classification of the target material are marked. Rebar was best classified by PC2 in relation to Fe emissions in the UV range, while aggregates were most distinguishable with PC7 due to the Mg, Al and Li emission lines. Brick was most distinguishable with PC4 due to strong Si and Ti emission lines and emission bands.

6.4.5. EFFECT OF ENSEMBLE AVERAGE

Based on lower misclassification rate, the PLS-DA algorithm is preferred when dealing with LIBS spectra from building waste materials. In view of the envisioned application of the proposed methodology, the characterization on the basis of single-shot spectra is highly preferred [9]. First, because averaging lowers the effective sampling and pulsed lasers with high repetition rates are quite costly. Second, because according to Fig. 6.10 some two out of three shots may not contribute to qualified spectra. Since the training set should be representative for the variance in the unknown spectra, the PLS-DA model should also be built using single-shot spectra. To stay consistent with the results in Table 6.3, we applied 720 single-shot spectra per material for the training set and 180 for the test set.

To gain some insight into the relation between the spread in the raw data sets for the different materials and the robustness of PLS-DA, it is instructive to calculate the relation between the average misclassification rate, data averaging and number of PC required to achieve optimal convergence during 9-fold cross-validation for the training process. Fig. 6.20a shows the average misclassification rate in RMSECV as a function of PC for

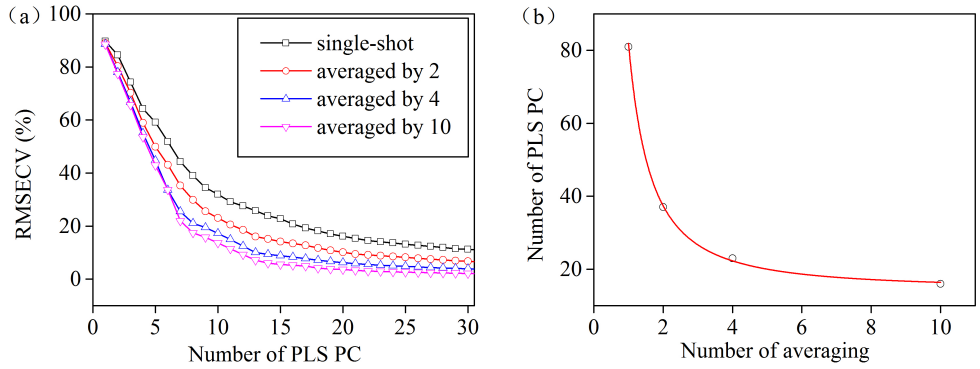


Figure 6.20: (a) Convergence of misclassification rate in RMSECV during 9-fold cross-validation and increasing numbers of data averaging. (b) Number of PC required for less than 5.2% average misclassification rate.

single-shot, 2, 4, and 10 times averaging of all the spectral data, while maintaining the same size ratio of 4 : 1 for the size of the training set and test set. Apparently, data averaging slightly increases the rate of convergence, but for single-shot and averaging two spectra the rate slows down to a crawl after 20 PC. The local minima of RMSECV for the number of averaging spectra are 5.2% (single shot, 81 PC), 3.0% (2 averaged, 80 PC), 2.0% (4 averaged, 74 PC) and 1.5% (10 averaged, 59 PC).

Fig. 6.20b shows the number of PC required to get below 5.2% [2] average misclassification rate as a function of the number of averaged spectra. The fitted smooth curve is $N^{-3/2}$, which clearly shows the rapid convergence for increasing data averaging.

Table 6.5: Misclassifications of PLS during testing of the scenarios: single-shot, 2, 4 and 10 spectra averaging with optimum number of PC, determined during training. For all materials together the number of single-shot spectra (spec) acquired was 5760 for training and 1440 for testing (agg=aggregate; rb=rebar; bk=brick; gp=gypsum; wd=wood; gls=glass).

averaging	PC	spec	cem	agg	rb	bk	gp	wd	PVC	gls
1	81	1440	0	3	0	1	0	0	0	0
2	80	720	0	1	0	0	0	0	0	0
4	74	360	0	0	0	0	0	0	0	2
10	59	144	0	0	0	0	0	0	0	0

For testing, the numbers of PC determined by the local minima of RMSECV during 9-fold cross-validation were used while varying the number of averaged data. Tab. 6.5 lists the classifications using PLS-DA. As a percentage of the tested data set, the misclassifications made up 0.28% (single-shot), 0.14% (2 averaged), 0.56% (4 averaged) and 0% (10 averaged).

Perfect discrimination is achieved only for the last scenario (10 averaged), though it

[2] Best RMSE for signle-shot LIBS spectra w/o averaging.

will keep on improving for increasing numbers of PC. It is important to distinguish between two types of misclassifications. The first is where a target material is not classified as such (false negative), and the second is the consequence, i.e. where one type of material is misclassified as another (false positive). The consequences may be most significant in case of the identification of minority particles in a waste stream if the majority particles create many false positives. For example, if aggregate or cement particles (majority of the stream) would be mistaken for pollutants (minorities).

For 4 averaged data, one glass particle was misclassified as cement and another as PVC. For 2 averaged data, one aggregate was misclassified as glass. For single-shot data, three aggregates were misclassified as cement, wood and glass, respectively, and one brick particle was misclassified as cement. Because pollutant materials form perhaps only 1-5% of the particles in concrete aggregate, for single-shot LIBS, it is paramount to tailor the size and quality of the training set and the number of PC in order to strongly reduce the chance of false positives.

In conclusion, ten times averaged spectra were used first, for which case PLS-DA combined with the mean centre approach gave the most robust results. Continuing with PLS-DA, the relation between data averaging for an optimum number of PC, as required for convergence, was investigated up to the ideal single-shot scenario. Single-shot LIBS constitutes the most promising real-time methodology, but its success depends on the quality of the training set and the implications of the degree of false positives. Another approach to reduce false positives is to accept a spectrum as wood only if it is some factor closer to the center of the cluster than it is to other clusters. This may create false negatives, but this is usually a less problematic error than a false positive for contaminants.

6.5. CORRELATION BETWEEN LIBS DATA AND CONCRETE QUALITY

Allowable types and levels of contaminants in recycled concrete are pragmatically grouped in the EU norms for recycle concrete quality. If a contaminant will sink in water it is part of the "sink fraction", and if it will float it is part of the "float fraction". The influence of these on concrete is quite different and, consequently, they have a different unit for maximum

tolerance in the norms. Floating contaminates, such as wood or foam, are notorious for lowering the strength of concrete as they represent weak pockets within the concrete matrix. For these light particles the volume is more important than mass, and so their norm limit is described as a total particle volume per kg-concrete. In contrary, limits for sinking contaminates are described as a mass per kg-concrete. Some of the sinking materials are known to affect the concrete strength by either chemical reactance (gypsum) or by affecting the water-to-cement ratio (porous brick), which is critical for resulting strength. Metals may corrode and not adhere well to the concrete matrix, while the non-porous and glass particles bond well with concrete and form less of a problem. We prepared coarse concrete batches with 0.6-5 wt% sinking contaminants and 0.2-2 cm^3/kg-concrete floating contaminants. These batches were first inspected for floating and sinking contaminants using PLS-DA. Subsequently these batches are used in the production of five types of concrete samples. The samples are subjected to tests for workability and strength to judge the impact of the varying levels of contaminants.

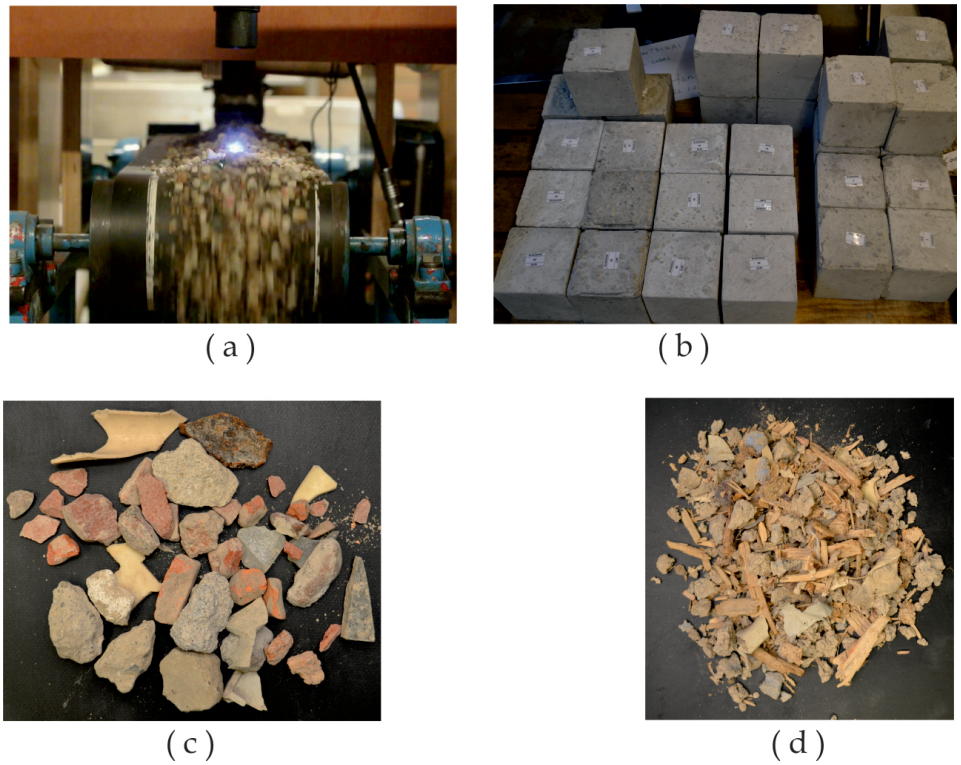


Figure 6.21: (a): LIBS measurement on coarse demolition concrete aggregate on a conveyor belt, (b): the concrete cubes casted using coarse demolition concrete aggregate, (c): sink contaminants (brick, glass, PVC, gypsum, rebar) and (d): float contaminants (wood, foam)

We first determine the contamination level (composition and contents) of the coarse fraction of demolition concrete (4-16 mm). Then we investigate the influence of contamination level on the quality of concrete samples produced from these materials. Selected quality parameters are: 2- and 28 day mechanical strengths, resistivity measured using a two-electrode method (TEM), and workability of the mortar (slump and flow tests).

Samples were prepared as follows: 300 kg demolition concrete (0-44 mm) was sieved manually between 4 to 16 mm to obtain 160 kg material. It was then equal-partitioned into 4 fractions (40 kg for each) according to the Dutch standard EN 932-2, from which each 10 kg was processed by handpicking to determine the inherent material composition complying the Dutch standard EN933-11. The major components for the inherent sink contents ($0.63 \pm 0.23 wt\%$) are brick, glass, PVC, rebar and gypsum (cf. Fig. 6.21c). The major materials of the floating contents with total volume $1.29 \pm 0.24 cm^3/kg$ are wood and foam (cf. Fig. 6.21d). The rest of the four 30 kg fractions were modified as shown in Tab. 6.6.

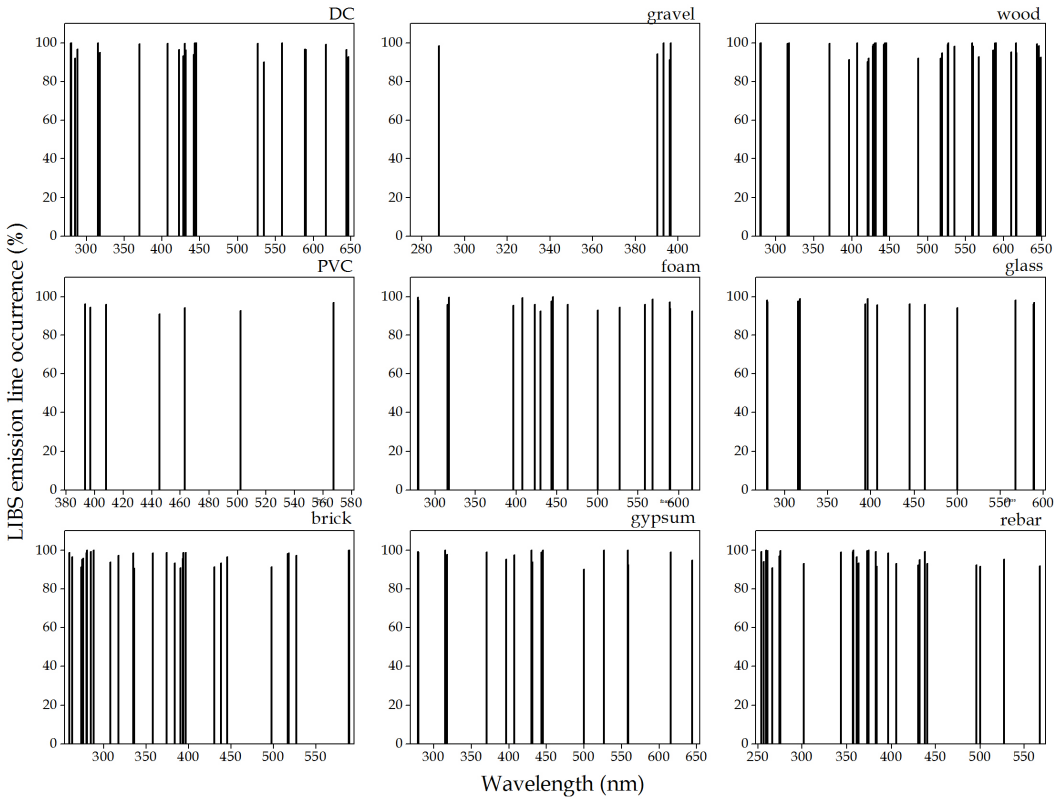


Figure 6.22: LIBS emission line occurrence [%] of DC, gravel (as reference), and real contaminants handpicked from the DC: wood, PVC, foam, glass, brick, gypsum, rebar.

LIBS measurements were performed 3 times per batch material, each time 6000 single-shot LIBS spectra were acquired at 30 kg/min throughput on a conveyer belt as shown in Fig. 6.21a. Using the procedure described in subsection 4.2.2, 77 robust emission lines were first determined based on the training dataset (cf. Fig. 6.22), which were then employed as inputs to build up the PLS-DA multi-classification model (cf. 6.3.2). During the training, we introduced a sample surface height fluctuation of $> \pm 20mm$ manually to emulate the real-inline condition for conveyer belt feeding. Note that gravel spectra are not included in the training dataset, but only used as a reference for demolition concrete (DC). It is noted that DC has even more persistent Ca and Fe lines (e.g. Ca 315.7, 429.9, 431.6, 443.3, 558.8, 616.1, 643.7 nm and Fe 370.5, 526.8 nm) compared with natural gravel. The CN 388.1 nm is absent from both the wood and PVC and Si 288 nm from glass spectra (compared with a better controlled training in subsection 4.2.2) because of their short ODs (cf. Chap. 4) and the relatively large surface height fluctuation. The LIBS results in identified shot

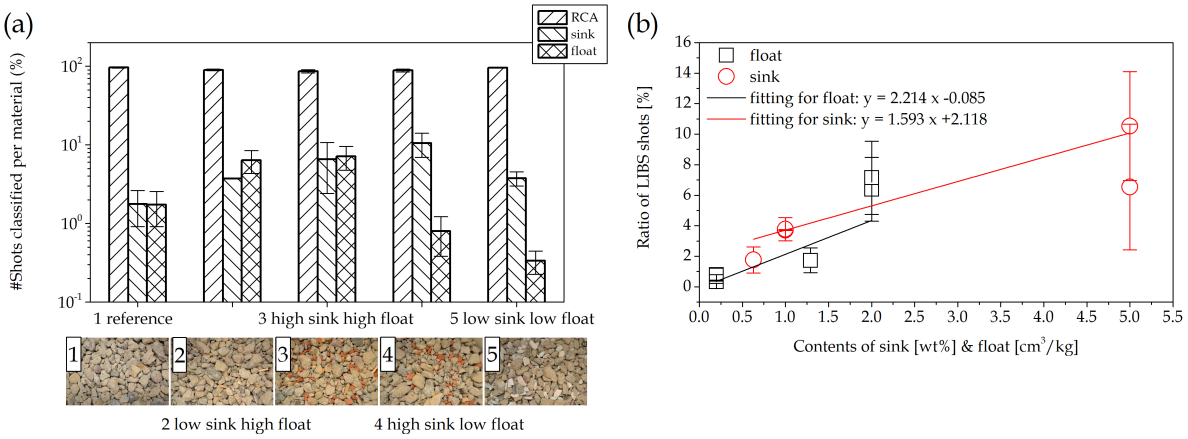


Figure 6.23: (a): PLS-DA LIBS results of DC, sink (PVC, brick, glass, gypsum, rebar) and float (wood, foam) contaminants on the five coarse concrete aggregate batches (cf. Tab. 6.6). Error bar represents 1STD of 3 duplicate measurements. (b): Fittings of ratio of classified LIBS shots [%] as function of sink $[wt\%]$ and float $[cm^3/kg]$ contents.

percentages of target materials using the trained PLS-DA model[3] for each material batch are shown in Fig. 6.23a. In general, these results agree reasonably well with the material compositions (cf. Tab. 6.6). The last 2 batches were cleaned using the sink-float approach before adding in extra contaminants. Therefore, the float contents are lower than the inherent float content of the reference batch. The linear fittings to translate the ratio of classified LIBS shots to corresponding sink and float contents (cf. Tab. 6.6) are shown in

[3]PLS-DA model: 5-fold cross-validation, MSE=0.22, 52 PCs

Fig. 6.23b. The ratio of classified sink LIBS shots [%] = 1.593 x sink contents [wt%] +2.118 and ratio of classified float LIBS shots [%] = 2.214 x float content [cm^3/kg]-0.085. These fittings will be used in Sec. 6.7.3 to translate the LIBS measurements into contamination contents for inline LIBS application on RCA at industrial scale. The mass of 30 kg per batch

Table 6.6: Five sets of self-made coarse recycled aggregate (4-16 mm, 30 kg) with varying contamination levels.

#Sample	Sink [$wt\%$]	Float [cm^3kg^{-1}]	Comments
1 Reference	0.63 ± 0.23	1.29 ± 0.24	Recycled aggregate
2 Low sink, high float	<1	2	Add extra 30 cm^3 float
3 High sink, high float	5	2	Add extra 30 cm^3 float and 1.5 kg sink
4 High sink, low float	5	<0.2	Clean the float, add 1.5 kg extra sink
5 Low sink, low float	1	<0.2	Clean the sink and float, add 0.3 kg gypsum

was used to produce 6 test cubes (150 mm) per batch for workability and mechanical strength tests after 2 days and 28 days of curing (cf. Fig. 6.24a). The recipe used to produce C30/37 XC3 F4 class strength concrete was as follows: mixture of cement using CEM I 52.5 N (80 kg/m^3) and CEM III/B 42.5 N LH HS/SR (240 kg/m^3); 5 batches of coarse aggregate 4-16 mm (915 kg/m^3); river sand 0-2 mm (805 kg/m^3); water-to-cement ratio of 0.54 and added is a small amount of super-plasticizer (1.92 kg/m^3).

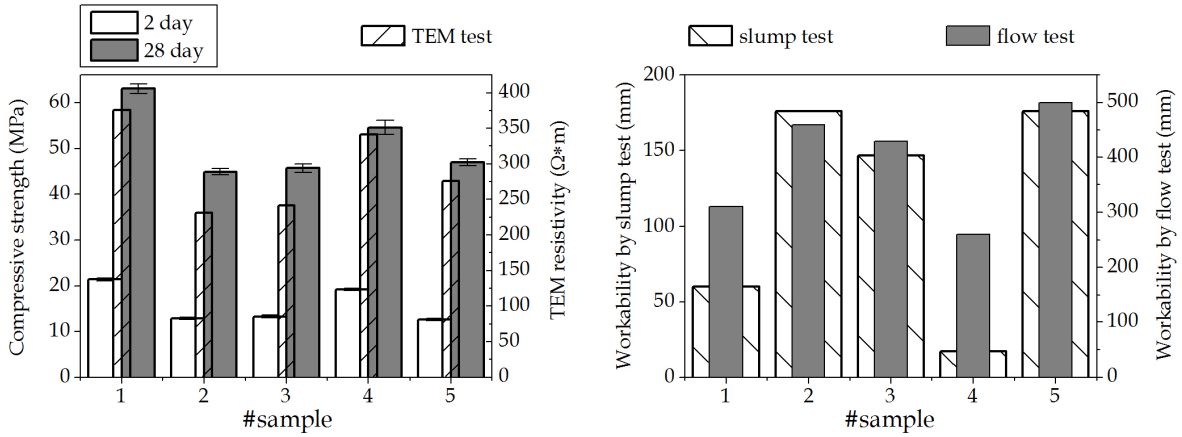


Figure 6.24: Quality tests on concrete cubes using five material batches in Tab. 6.6. STD are obtained from three concrete cubes per day test. Left: White bar: 2 day compressive strength test, dark grey bar: 28 day compressive strength test, dashed bar: resistivity test using TEM; right: dashed bar: slump workability test, light grey bar: flow workability test.

Fig. 6.24a shows a clear correspondence in the trends of 2- and 28-day mechanical strength and TEM tests. The reference sample shows the highest strength and largest resistivity. The high sink, low float batch shows the second best performance, where brick is the major sink contaminant. This implies that brick degrades the strength and resistivity to a small

degree. The low sink, low float batch consisting of 1wt% gypsum indicates that gypsum affects the concrete strength and resistivity more than brick, even with this lower content. Compared with brick and aggregate, gypsum is more brittle and broken gypsum as a consequence of mixing may influence the cement paste. According to its high workability the gypsum batch may require less water. The 2nd and 3rd batches show similar strength and resistivity indicating that the float contaminants are the major components that degrade the concrete performance.

It is demonstrated that different contaminants in the raw recycled materials used in new concrete can affect the main engineering properties in different ways. Most important is that the variations in properties can be correlated to the quality of the recycled raw materials and that this quality can be determined using LIBS spectra and a statistical method such as PLS-DA.

6.6. QUANTITATIVE ELEMENT ANALYSIS USING PLS

Table 6.7: Element contents (Cr and Zn in [10^{-2} wt%], and rests in [wt%]) of reference cement samples.

	#100	#101	#103	#105	#106	#107	#108	#109	#110
Al	4.58	7.67	6.61	3.53	4.72	3.50	3.86	3.50	3.88
Ca	72.0	56.7	63.2	72.7	73.7	75.0	72.8	73.8	76.0
Cr	0.96	1.13	0.77	0.85	0.86	0.64	0.75	0.85	0.43
Fe	2.87	4.05	2.01	2.73	2.17	1.41	3.25	2.52	0.20
K	1.06	2.86	1.03	1.60	1.11	0.91	0.96	1.36	1.22
Mg	1.39	1.69	4.31	1.48	0.90	0.66	2.03	1.49	0.61
Na	0.27	0.83	0.39	0.24	0.14	0.21	0.10	0.21	0.06
S	1.86	2.08	1.76	2.10	1.88	1.96	2.07	1.93	1.80
Si	15.2	23.3	20.3	15.2	14.8	15.9	14.6	14.8	16.0
Sr	0.38	0.34	0.10	0.19	0.27	0.20	0.11	0.19	0.05
Ti	0.27	0.46	0.36	0.17	0.25	0.18	0.17	0.19	0.16
Zn	6.40	5.81	1.81	6.77	1.51	1.63	4.52	5.24	0.38

Model-based LIBS for quantitative measurements (cf. Chap. 5) requires good quality and well resolved LIBS spectra, seeing that MLIBS cannot make effective use of overlapping or weak emission lines, or continuous bands. In this section a PLS-based quantitative model is introduced which relaxes this issue at the expense of utilizing more redundant data. Whereas MLIBS is model based, the PLS methods performs a linear calibration using a training session on samples with well quantified contents. This means that, within the calibration range of the training set, the PLS method compensates for possible self-absorbed

spectra, is not very particular to the time window of integration, and is more robust towards the minor elements. As an additional advantage, the spectra do not have to be corrected for the spectrometer sensitivity since this is implicitly accounted for in the calibration stage.

First, 100 single shot spectra are collected per sample from the CRM cement reference

Table 6.8: XRF based element contents (wt%) of four demolition concrete samples.

	A100S4		B100S4		C50S4		D15S4	
	mean	rstd%	mean	rstd%	mean	rstd%	mean	rstd%
Al	6.44	19.5	6.23	22.5	6.93	20.3	6.17	22.5
Ca	33.9	17.2	21.9	20.3	30.1	17.9	22.8	20.1
Cr	0.08	24.4	0.04	26.5	0.05	25.8	0.10	26.5
Fe	3.53	6.66	2.81	9.29	3.75	7.51	3.17	9.35
K	1.37	10.3	1.57	6.75	1.43	9.22	1.60	6.88
Mg	2.06	21.4	2.00	23.9	2.43	21.9	2.02	23.8
Na	0.00	0.00	0.65	25.7	0.00	0.00	0.10	25.2
S	1.41	50.3	0.92	52.6	1.30	51.3	0.97	52.6
Si	50.4	12.1	63.5	8.06	53.5	10.9	62.6	8.27
Sr	0.08	27.7	0.06	28.9	0.06	26.7	0.06	28.1
Ti	0.40	24.7	0.32	26.8	0.42	25.5	0.34	26.9
Zn	0.36	26.2	0.06	27.7	0.04	25.5	0.03	30.2

sample set, which contents are listed in Tab. 6.7. Second, the model is trained by applying 5 fold CV (cf. Fig. 6.25). Third, the trained model is tested on blind cement samples and then on four sample of demolition concrete, which XRF reference contents are listed in Tab. 6.8. The first blind tests demonstrate the capabilities of quantitative PLS, while the concrete reveals that PLS is still a calibration approach and, as such, sensitive to the training content range and material matrix. The relative mean square error (R%) and number of loadings (#L) obtained from training using the cement set are shown in Tab. 6.9.

Table 6.9: Results of PLS2-based quantitative characterization in combination with one of the seven pre-processing methods. Shown are the relative mean square error (RMSE%) and number of loadings (L) for the training data obtained from the reference cement samples.

Pre-processing methods													
1: R		2: N		3: AS		4: BG		5: BG+N		6: BG+AS		7: WS	
RMSE	#L	RMSE	#L	RMSE	#L	RMSE	#L	RMSE	#L	RMSE	#L	RMSE	#L
4.48	33	3.83	42	4.93	10	4.23	42	3.94	37	3.63	23	4.49	26

The blind tests on the demolition concrete samples using the cement-trained model are shown in Fig. 6.26 for five different pre-processing methods. The AS and BG+AS methods lead to very poor results and are ignored. Note that the error bars are derived from the variance (one STD) and indicate the class width for each element. The comparison of PLS with the XRF reference measurements for the different pre-processing methods depends on the element under investigation.

Although PLS2 is able to model contents of more elements of cement reference samples besides beyond Ca and Si, its overall performance on testing DC samples is not as good as MLIBS. This indicates that a PLS2 model should only be applied for testing samples with same matrix as its training samples.

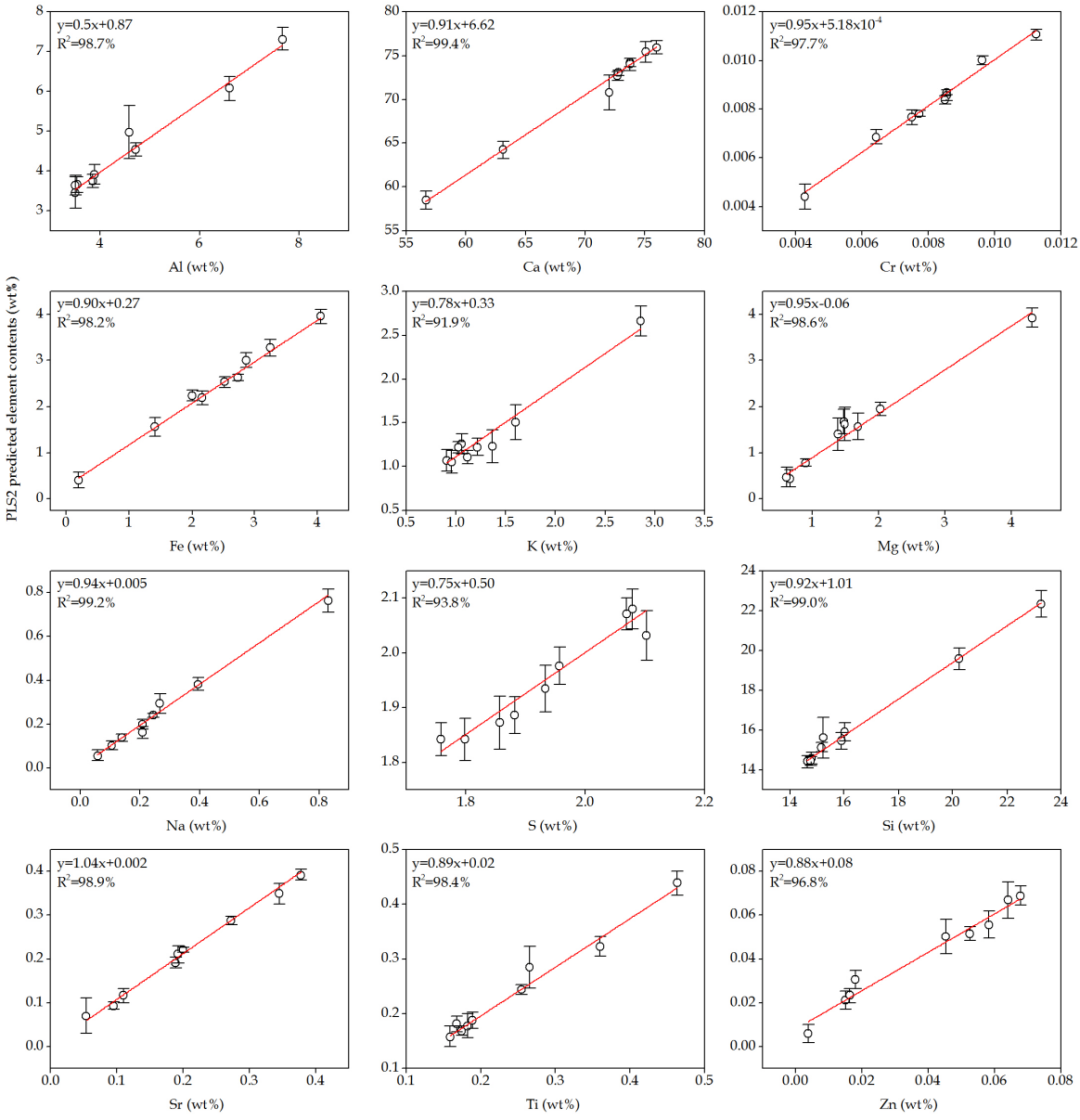


Figure 6.25: PLS2 model predictions for cement samples (10 blind shots) with 90 single-shots for training, using pre-processing method 1 R.

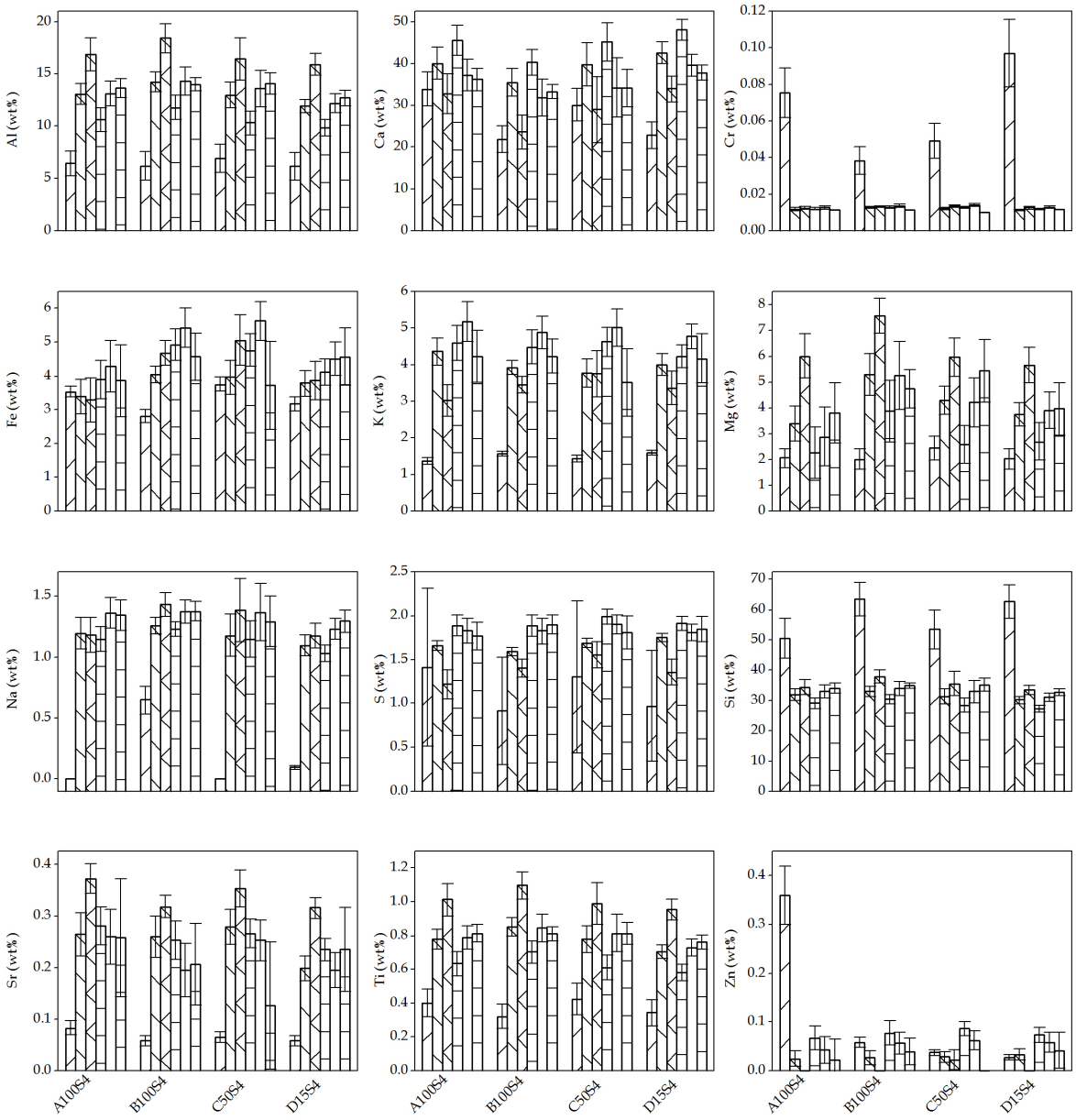


Figure 6.26: PLS results of element contents (wt%) and RSTD over 100 shots of four DC samples. Per sample the bars indicate the XRF reference (left bar) and followed by 5 different pre-processing methods from left to right: 1 R, 2 N, 4 BG, 5 BG+N, 7 WS.

6.7. DEMONSTRATION OF INLINE LIBS IN AN INDUSTRIAL SETTING

6.7.1. INLINE LIBS CLASSIFICATION RESULTS ON RCA

We outline the prototype LIBS unit, describe the industrial settings and corresponding conditions under which it was tested, and present the main inspection results for the coarse recycled concrete aggregates (RCA).



Figure 6.27: Inline LIBS quality inspection on ADR 4-12 mm coarse output in Hoorn, the Netherlands on 10th June, 2016.

6.7.2. LIBS UNIT, SETTING, AND MATERIALS

A wooden structure served as mobile frame for a LIBS prototype inline unit, as shown in Fig. 6.27. The unit contained all necessary hard- and software needed to perform LIBS measurements on individual particles lying on top of a layer of coarse recycled concrete aggregates (RCA) that was moved at 0.5 m/s by a conveyor belt. The belt is part of the product output system of an ADR that sieves moist concrete waste 0-12 mm into a coarse product (2-12 mm) and a fines residue (0-2 mm). The fines are sold as sieve sand for applications such as filler for road beds and landscaping. The coarse product is sold as a replacement for virgin gravel in the production of new concrete and must be inspected for quality, as laid down in EU norms for recycled aggregates. The ADR and LIBS unit were setup at a concrete waste recycling plant in Hoorn, next to the Ijsselmeer, the largest water lake in the Netherlands. The advantage of the site was that right next door was a concrete production facility, which eliminated the need for further transport of the ADR coarse concrete product. The disadvantage was that the site offered no protection from rain, wind and dust. Though the LIBS unit was shielded to protect the sensitive electronics, if it rained too hard

it still had to shut down. The LIBS unit simulated real-time processing as it had enough RAM memory to store some 30 seconds of data, acquired at 100 full spectra per second. When the RAM buffer was full the results were statistically processed to plot the number and type of identified materials. For this purpose we used the normalised LIBS spectra as input to a PLS-DA multi-classification model. This model was trained and validated in section 6.5 using manually prepared coarse RCA batches with different types and levels of contaminants. Because this "batch process" can be repeated as many times as required, the results are representative for uninterrupted real-time acquisition. An assumption is that each shot is associated with a different particle. This is reasonable as there is some 5 mm distance between two shots and the coarse particles shapes and their 3D packing in the belt layer makes a sequential hit of the same particle less likely. Assuming the layer on the belt was homogeneous for each type of contaminant, the laser sampled the concrete layer and build statistics of each contaminant. The sampling theorem predicts that the relative spread (uncertainty) for a particular contaminant decreases with the square root of the number of detected particles. The overall shot success rate of the unit was 95%, meaning that only 5% of the laser shots resulted in an unusable spectrum. This was mainly due to the used long depth of field (200 mm focusing lens), which depth corresponded to the maximum surface height variations ($\pm 4\ mm$) of the concrete layer on the conveyor belt.

6.7.3. RESULTS FOR INLINE LIBS QUALIFICATION OF RCA

During the demonstration in the Hoorn site a total of 60 tonnes of ADR coarse concrete aggregates product was inspected by the LIBS unit. Fig. 6.28a shows the percentage of LIBS spectra classified in real-time over 82 cumulative tracks of full RAM buffer data acquisition. Thus, a total of 195235 LIBS single-shot spectra were collected of which 184920 shots could be classified, amounting to a 95% success rate in LIBS sampling. The absolute numbers are shown in Fig. 6.28b. A total of 125064 shots were classified as concrete aggregates, 2334 as brick, 6468 as gypsum, 4122 as steel rebar, 398 as foam, 318 as wood and 153 as PVC plastic. Next these particle numbers must be converted to the proper units used in the European-EN standards [10, 11] so we can interpret them in terms of quality. Foam and wood amount to 0.3872 % of total qualified LIBS shots for the float fraction and brick, gypsum, steel rebar and PVC plastic amount to 7.0717 % of total qualified LIBS shots for

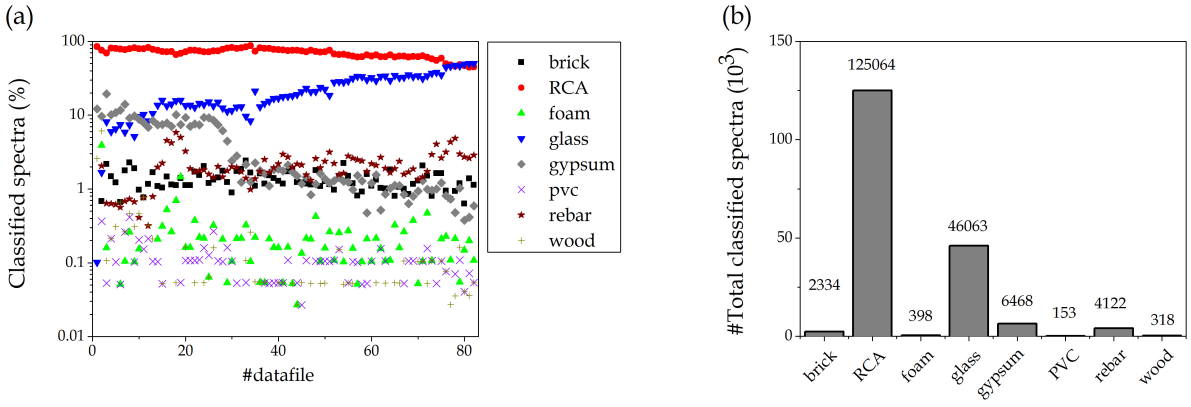


Figure 6.28: (a): Percentages of classified contaminants of each sampling burst in RCA over time. (b): Total number of classified contaminants in RCA.

the sink fraction. Using the linear fitting functions shown in Fig. 6.23b, the float and sink contents are determined to be 0.2133 cm^3/kg and 3.1097 wt%, respectively.

Using another approach we simply assume the average floating particle is a cube with 7 mm edges=0.34 cm^3 (average of 2-12 mm product size). For 716 particles this comprises a total volume of 245.6 cm^3. Using the same cube size and the mass density of concrete, and ignoring contaminant mass, we calculate a total concrete mass of 103 kg in the total LIBS sample, giving a total float content of 2.4 cm^3/kg-product. More specifically, for just wood the float content is 1.3 cm^3/kg-product. However, a manual test on a 10 kg sample of same product revealed a wood content smaller than 0.2 cm^3/kg-product. This complies with the highest category FL0.2 for floating pollutants, as shown in Tab. 1.4 (Sec. 1.7). The cause of the deviation with LIBS is most likely that our assumption of average particle size is way off. Soft wood particles, as are brittle particles like glass and brick, are grinded down in concrete waste. Moreover, wood particles tend to be elongated in shape due to the wood fibres. Therefore, an average wood particle size of $3 \times 3 \times 6$ mm brings the LIBS results much closer to the manual test. Also, the 103 kg samples taken for handpicking might not be 100% representative for the whole material stream measured by LIBS. A similar exercise may be carried out for quality related to the sinking contaminants. Either which, this shows that taking at least one representative sample is an important complement to LIBS inspection in order to find more accurately the average particle volume or average mass of contaminants.

REFERENCES

[1] H. Xia and M. Bakker, *Reliable classification of moving waste materials with libs in concrete recycling,* Talanta **120**, 239 (2014).

[2] H. Hotelling, *Analysis of a complex of statistical variables into principal components.* Journal of educational psychology **24**, 417 (1933).

[3] H. Wold, *Path models with latent variables: The NIPALS approach* (Acad. Press, 1975).

[4] S. Wold, A. Ruhe, H. Wold, and W. Dunn, III, *The collinearity problem in linear regression. the partial least squares (pls) approach to generalized inverses,* SIAM Journal on Scientific and Statistical Computing **5**, 735 (1984).

[5] S. De Jong, *Simpls: an alternative approach to partial least squares regression,* Chemometrics and intelligent laboratory systems **18**, 251 (1993).

[6] S. Wold, M. Sjöström, and L. Eriksson, *Pls-regression: a basic tool of chemometrics,* Chemometrics and intelligent laboratory systems **58**, 109 (2001).

[7] J. P. Singh and S. N. Thakur, *Laser-induced breakdown spectroscopy* (Elsevier, 2007).

[8] M. Gaft, L. Nagli, I. Fasaki, M. Kompitsas, and G. Wilsch, *Laser-induced breakdown spectroscopy for on-line sulfur analyses of minerals in ambient conditions,* Spectrochimica Acta Part B: Atomic Spectroscopy **64**, 1098 (2009).

[9] A. P. Michel, *Review: Applications of single-shot laser-induced breakdown spectroscopy,* Spectrochimica Acta Part B: Atomic Spectroscopy **65**, 185 (2010).

[10] *European Committee for Standardization, EN 12620+A1: Aggregates for Concrete,* (2008).

[11] *European Committee for Standardization, EN 933-11: Tests for Geometrical Properties of Aggregates - Part 11: Classification Test for the Constituents of Coarse Recycled Aggregate,* (2009).

7

CONCLUSIONS

This research is dedicated to adopting Laser Induced Breakdown Spectroscopy (LIBS) for quality inspection in concrete waste recycling. The state of the state-of-the-art physics and technology are established and investigated with the aim to optimize and adapt methods and techniques to the harsh processing conditions of the recycling industry.

7.1. PRINCIPLES AND PROCESSES

In Chapter 2, the literature study revealed different possible principles and processes underlying laser-matter interaction and ablation. These prove to depend mainly on the levels of laser fluence and laser average power density in relation to the physical properties (e.g. metal or dielectric, grain size, crystalline or amorph) and chemical properties (e.g. types of elements and molecules) of the sample material. It also proves that the difference in laser ablation between metals and dielectrics mainly occurs in the first fraction of a nanosecond of laser irradiation. In that small fraction of time, the sparse free electrons in a dielectric are multiplied through avalanche processes until they are as abundant as in metals. Metals therefore tend to break down at lower laser fluences but otherwise the ensuing ablation processes are similar to dielectrics. The various transient processes are connected and discernible: from the first moment of laser irradiation to the onset of material breakdown and plasma formation and ending with the photonic emissions from the cooling plasma plume. The existence of local thermal equilibrium (LTE) in different stages of plasma plume development could be established. Of these, only the LTE in the last stages are of importance for LIBS. On this basis, plasma models could be built that simulate the

various processes as separate events and allow identification and measurement of the key parameters.

The breakdown threshold is the fluence at which solid material is effectively ablated and evaporated. The damage fluence (onset of melting) and sublimation fluence (onset of sublimation) correlate strongly with the experimental breakdown threshold. We made several pragmatic assumptions and modelled the transient ablation processes as a sequence of heat transfer states, and correlated the absorbed laser energy with material-dependent thermal parameters. The breakdown threshold predicted by the model may be measured in a more convenient way using an experimental parameter that we call "observation depth". This is based on experimental or theoretical knowledge of the shape of the laser beam near the ablation zone. The observation depth is measured as the distance between the two points where plasma photonic emissions can still be observed experimentally as a function of the distance between the sample surface and the focus of the laser lens. The breakdown threshold then follows by using the known laser beam shape as absolute fluence reference. The observation depth may be regarded as a bridge between what can be observed experimentally and the thermal parameters occurring in the ablation model. This theory was tested and validated using pure samples in Chapter 3. The theory was also applied in a correction procedure for surface sampling bias where LIBS was tested on a variety of waste materials.

After the end of the laser pulse it takes a certain time before the laser plasma plume becomes optically transparent so the detectable emitted wavelengths can be uniquely related to specific species. It is noted that a high degree of self-absorption in the plume reduces transparency. This undesired effect tends to increase with the concentration of the emitting species and causes a nonlinear relation between the species content and the corresponding detectable emissions. Optical transparency is the basis for identification of the sample material and its contents. The time to optical transparency for a targeted wavelength depends on the contents of the plume as a whole. This dependence is called the (sample material-) matrix effect. On the other hand, this means that the time before the plasma plume becomes optically transparent for a targeted wavelength (species) also

depends on the matrix. It is noted that using multiple spectrometers, one for each species to accommodate specific time delays, can quickly become excessively expensive. Moreover, linear models linking species concentration and emissions are not reliable for the large practical ranges of element concentrations found in waste materials. The nonlinear effects hamper the development of a calibration-free LIBS method and can therefore at present only be approached by a LIBS method incorporating some form of calibration, as investigated also in Chapter 5. The pragmatic solution to deal with the described nonlinear effects in multi-element analysis is to employ statistical methods and to determine a single delay time and fixed duration of photon collection (integration time) in a compromise. This is the subject of Chapter 6.

An optical investigation into the ablated surface geometry of flat and homogeneous materials was performed using white light interferometry. We correlated the observed geometrical parameters with the LIBS data. This confirmed the findings of Chapter 2 that the ns-LIBS experiment is governed by a number of transient, coupled physical processes. This implies that it is not possible to find a perfect correspondence between a process and associated light emissions for time-integrated spectra. And time integration is vital to establish a sufficient signal-to-noise ratio for both strong and weak emissions in the spectral range of the acquired data. Using time integration we did find that the amount of ablated material strongly correlates with certain continuum bands. This correlation is successfully utilized for quantitative measurements in a spectral normalization scheme in Chapter 4. It reduced the laser shot-to-shot relative uncertainty from over 10% to below 3%. The continuous bands were also quite successfully included in the MLIBS fingerprinting scheme in Chapter 6.

7.2. TECHNIQUES AND INLINE ADAPTATION

With the aim to minimize the probability of anomalous shots on samples without surface preparation measures, optical configurations were studied in open air at different laser pulse rates (1 - 100 Hz) and fluence. The possible influences of operational parameters and ambient conditions were determined. A higher laser fluence leads to more abundant LIBS spectra with little interference from air molecules or dust. In general, increasing the

laser energy improves the reproducibility of the LIBS signal (cf. Chapter 3). However, care must be taken not to exceed the fluence to a level where the ablation mechanism changes (thermodynamic pathways, cf. Chapter 2). Increased moisture levels in the air or on the sample surface decrease to some degree the laser energy that is absorbed by the sample, but under normal operational conditions this is a negligible side effect with $-5\%/mm$ dissipation rate.

For a targeted element (wavelength) in the sample an optimum delay time can be applied, and for multiple targeted elements an average delay time has to be applied based on an experimentally determined statistical compromise. For an increasing working distance, inferring a longer focal depth of the laser lens, the size of the focus increases and the power density decreases. As a result, fewer emissions lines are detected, which mainly are associated with low excited energy levels and a high transition probability of the species in the plasma plume. For material fingerprinting these emissions are the best reproducible. However, different waste materials can be quite similar in certain elements, so these high-probability emission lines may not yield sufficient information for reliable fingerprinting. At shorter working distances more different emission lines can be detected since the power density is higher, but this comes at the cost of decreased observation depth and thus reduced reproducibility of the spectrum. Having more emission lines available improves the performance of quantitative methods aiming at sample contents analysis. Experiments show that the higher energy emission lines live shorter and therefore produce weaker signals than other emissions, but they tend to correlate better with the element contents of the sample. The observation depth is maximum when using the configuration of an anti-parallel laser and collection optics as examined in Chapter 3. It is also shown that the influence of the laser incident angle (LIA) may be ignored up to 40 degrees from normal incidence on the sample surface. As a result, the percentage of laser shots producing unusable spectra is decreased to 5%.

A model-based, quantitative analysis method named model-based LIBS (MLIBS) was developed in Chapter 5 to determine the element contents of different products arising in the processing of concrete waste. The method was validated using a cement reference

sample set and successfully applied to different samples from a demolition concrete recycling line. In particular we mention the ADR fines ($0-2\ mm$, sand fraction), concrete drill cores (100 mm diameter solid concrete), and coarse aggregates ($4-16\ mm$, granulate). This constituted a challenge as it concerned a variety of waste materials that were sampled by LIBS either in the form of a powder, a granulate, press-pellets, or as a solid sample, and all without the use of any matrix-matched calibrations.

Finally, pre-processing and classification algorithms were developed, implemented and tested for the purpose of inline materials characterization. For example PCA-Adaboost and PLS-DA. In particular, the hardware-efficient single-shot scenario was applied, thereby utilizing the full acquired LIBS spectrum. Indirectly this shows that different stages of ablation and plasma plume development may contribute detectable emissions that can help discriminate one material from another. In a more profound application, MLIBS may even be used to track and trace the country or manufacturer of a cementitious waste material. Indeed, it may do so for any waste material which composition varies slightly according to the natural resources used or according to the manufacturer's specific material receipt. The only condition is that those waste materials are included in a LIBS spectral reference database. The misclassification rate is defined as the percentage of samples that is not correctly identified or, equivalently, the sum of the false negatives and false positives. Under well-controlled feeding conditions the achieved misclassification rate for various cementitious samples was 0.28 % for single-shot data and 0 % when averaging just ten spectra. Single-shot LIBS constitutes the most efficient real-time detection method but its success depends strongly on the quality of the training set. A prototype MLIBS platform (hardware, software and weather protective casing) was developed for 100 Hz real-time data acquisition rate and detection of concrete materials and pollutants commonly found in concrete waste. After Integration with a product conveyor belt in an outdoors concrete recycling plant it was successfully tested for inline quality inspection capabilities. The plant was operated with 30 $tonnes/hour$ input of $0-12\ mm$ concrete waste. The LIBS system sampled and analysed the composition of the $4-12\ mm$ concrete aggregates product, which was output at a rate of about 18 $tonnes/hour$. This prototype demonstration complied with technology readiness level 6.

7.3. QUESTIONS FOR FUTURE RESEARCH

Following the results of the research in this thesis, some fundamentally aimed questions have arisen that may be of importance for future research and indeed the success of LIBS as a valuable tool for quality inspection of waste materials.

- Can research into the dynamics of the laser ablation processes reveal new information that can be utilized to improve LIBS performance? Specifically knowledge about the plasma plume development and composition as relating to nonlinearities for LIBS such as self-absorption, material-matrix effects and non-stoichiometric sampling.
- Can the optimum delay time and duration of photon collection for a targeted element or species in a given sample be determined?
- Can the existence and duration of LTE in a laser plasma plume be confirmed experimentally for a given sample and for selected emissions?
- Can the laser fluence and its profile at the ablation zone be determined for a given sample?
- Can the laser energy partitioning during ablation be determined for a given sample?

APPENDICES

.1. APPENDIX A: MOST ABUNDANT LIBS EMISSION LINES OF CEMENTITIOUS MATERIALS

Tab. 1 shows the analytical emission lines from cement and concrete literature. The reported LOD lies between 1 and 50 ppm.

Table 1: Emissions lines observed from cementitious materials and ambient atmosphere. Assignments *I* and *II* refer to emission lines from neutral atoms and singly charged ions complying with NIST database, respectively.

Elemer	Wavelength (nm)	Delay time (μm)	Int. time (μm)	LOD (ppm)
$Al\,(I)$	257.58[1]			
	308.21[2]			
	308.30[1]			
	309.27[2],[3]	9[3]	20[3]	40.6[3]
	309.36[1]			
	396.15[4]			
	394.40[2, 5, 6]	4.5[6]	$1\cdot10^3$[6]	8.0[6]
	396.10[5]			
	396.15[2]			
$Al\,(II)$	281.70[1]			
$Ar\,(I)$	912.30[7],[8]			
	922.50[7],[8]			
$Ba\,(II)$	455.40[4]	2[4]	1[4]	
	493.40[6]	5.0[6]	$1\cdot10^3$[6]	5.0[6]
$C\,(I)$	193.00[9]			
	247.85[1][1]			
	247.90[9],[4]	0.5[4]	1[4]	
	833.51[10],[11]			
$C\,(II)$	426.72[2]			
$Ca\,(I)$	247.90[9]			
	299.73[1]			
	300.68[1]			

See next page

See next page

Elemer	Wavelength (nm)	Delay time (μm)	Int. time (μm)	LOD (ppm)
	315.88[1]			
	317.93[1]			
	362.40[5]			
	363.10[5]			
	364.40[5]			
	422.60[12]			
	422.67[2]			
	430.25[2]			
	442.54[2]			
	443.56[2]			
	445.58[2]			
	558.20[13]			
	560.13[13]			
	560.29[13]			
	610.27[2]			
	612.21[2]			
	649.37[2]			
	657.27[2]			
	671.76[2]			
$Ca\,(II)$	315.88[2]			
	317.93[2]			
	318.13[13]			
	370.60[2]			
	373.69[13],[2]			
	393.30[12]			
	393.36[2]			
	396.85[12],[2],[6]	5.0[6]	$1 \cdot 10^3$[6]	6.0[6]

See next page

See next page

Elemer	Wavelength (nm)	Delay time (μm)	Int. time (μm)	LOD (ppm)
	396.90[4]			
	824.88[10],[14],[11]			
	825.47[11]			
	849.80[2]			
	849.80[10],[15],[14]			
	852.57[10],[14]			
	854.20[2]			
	866.21[2]			
	866.32[14],[10]			
	891.22[8, 14–16]			
	892.74[14],[16],[8]			
$Cl\ (I)$	133.57[17]			
	134.72[18],[19]			
	585.70[6]	5.0[6]	$1 \cdot 10^3$[6]	12.0[6]
	594.80[20]			
	594.85[2]			
	837.59[2, 10, 11, 14, 15, 19, 21]			
$Cr\ (I)$	427.30[6]	5.5[6]	$1 \cdot 10^3$[6]	4.0[6]
$Cu\ (I)$	261.91[1]			
	282.50[1]			
	296.20[1]			
	310.95[1]			
	324.85[1]			
	327.50[1]			
	329.15[1]			
	330.89[1]			

See next page

See next page

Elemer	Wavelength (nm)	Delay time (μm)	Int. time (μm)	LOD (ppm)
$Fe\,(I)$	274.31[1]			
	293.69[22]			
	358.21[2]			
	367.99[13]			
	368.75[13]			
	370.92[13]			
	372.76[13]			
	374.34[13]			
	376.55[13]			
	382.44[13]			
	387.25[13]			
	389.97[13]			
	526.95[6]	3.5[6]	$1 \cdot 10^3$[6]	7.0[6]
	832.71[11]			
	838.78[11]			
$Fe\,(II)$	259.94[1]			
	274.04[1]			
	274.73[1]			
	275.09[1]			
	275.60[4]	0.9[4]	1[4]	
	275.65[1]			
	298.48[13]			
	298.55[13]			
H_α	565.6[23, 24]			
$K\,(I)$	404.40[4]			
	766.49[3]	9[3]	20[3]	40.5[3]
$Mg\,(I)$	285.21[22],[4]	1.5[4]	1[4]	

See next page

See next page

Elemer	Wavelength (nm)	Delay time (μm)	Int. time (μm)	LOD (ppm)
	285.29[1]			
	333.21[13]			
	333.67[13]			
	382.94[13]			
	518.36[6]	4.5[6]	$1 \cdot 10^3$[6]	2.0[6]
$Mg\,(II)$	279.55[3]	1[3]	20[3]	24[3]
	279.63[1]			
	280.35[1]			
	292.87[1]			
	293.74[1]			
$Mn\,(I)$	403.40[6]	4.5[6]	$1 \cdot 10^3$[6]	4.0[6]
$Mn\,(II)$	257.61[3]	3[3]		7.9[3]
$N\,(I)$	821.63[11]			
	822.31[11]			
	824.24[11]			
$Na\,(I)$	588.90[6]	3.5[6]	$1 \cdot 10^3$[6]	3.0[6]
	588.99[3]	1[3]	20[3]	3.7[3]
	589.59[3, 4]			
	818.32[2, 10, 14]			
	819.50[2, 10, 10, 14]			
$Na\,(II)$	284.17[2]			
	328.56[2]			
	363.12[2]			
$O\,(I)$	777.20[24, 25]			
	822.20[10, 14]			
	823.30[10, 14]			
	844.54[18]			

See next page

See next page

Elemer	Wavelength (nm)	Delay time (μm)	Int. time (μm)	LOD (ppm)
	844.64[10, 14, 15]			
	844.67[2]			
	926.10[8, 16]			
	926.30[8, 16]			
	926.60[8, 14–16]			
$P\,(II)$	438.54[6]	4.5[6]	$1 \cdot 10^3$[6]	7.0[6]
$Pb\,(I)$	405.78[26]	0.1 & 5[26]	0.05	10.0[26]
$S\,(I)$	180.70[19]			
	288.15[2]			
	921.29[16],[8]			
	921.30[8, 14, 15, 19, 27]			
	922.81[8, 14, 16]			
	923.75[8, 14, 16]			
$S\,(II)$	373.81[6]	4.0[6]	$1 \cdot 10^3$[6]	10.0[6]
$Si\,(I)$	250.76[1]			
	251.60[9]			
	251.68[1]			
	252.48[1]			
	252.93[1]			
	263.20[1]			
	288.16[22],[3],[1]	7[3]	20[3]	14.8[3]
	288.20[4]	0.3 & 0.5[4]	1[4]	
	390.50[6]	4.5[6]	$1 \cdot 10^3$[6]	11.0[6]
$Sr\,(I)$	460.70[4]			
$Sr\,(II)$	407.77[3]	7[3]	20[3]	20.3[3]
$Ti\,(II)$	323.54[1]			

See next page

See next page

Elemer	Wavelength (nm)	Delay time (μm)	Int. time (μm)	LOD (ppm)
	334.94[3]	9[3]	20[3]	34[3]
	334.90[4]	1.5[4]		
	335.03[1]			

REFERENCES

[1] F. J. Fortes, J. Cunat, L. M. Cabalin, and J. J. Laserna, *In situ analytical assessment and chemical imaging of historical buildings using a man-portable laser system,* Applied Spectroscopy **61**, 558 (2007).

[2] M. A. Gondal, M. A. Dastageer, M. Maslehuddin, A. J. Alnehmi, and O. S. B. Al-Amoudi, *Detection of chloride in reinforced concrete using a dual pulsedlaser-inducedbreakdownspectrometersystem: Comparative study of the atomic transition lines of cl (i) at 594.85 and 837.59 nm,* Applied Optics **50**, 3488 (2011).

[3] A. Mansoori, B. Roshanzadeh, M. Khalaji, and S. H. Tavassoli, *Quantitative analysis of cement powder by laser induced breakdown spectroscopy,* Optics and Lasers in Engineering **49**, 318 (2011).

[4] T. Ctvrtnickova, M.-P. Mateo, A. Yanez, and G. Nicolas, *Characterization of coal fly ash components by laser-induced breakdown spectroscopy,* Spectrochimica Acta Part B: Atomic Spectroscopy **64**, 1093 (2009).

[5] X. Shen, H. Ling, and Y. Lu, *Laser-induced breakdown spectroscopy with high detection sensitivity,* in *Laser-based Micro-and Nanopackaging and Assembly III*, Vol. 7202 (International Society for Optics and Photonics, 2009) p. 72020D.

[6] M. A. Gondal, Z. H. Yamani, T. Hussain, and O. S. B. Al-Amoudi, *Determination of chloride content in different types of cement using laser-induced breakdown spectroscopy,* Spectroscopy Letters **42**, 171 (2009).

[7] R. Weast, *Handbook of Chemistry and Physics*, 64th ed. (CRC Press Inc., 1983-1984).

[8] F. Weritz, S. Ryahi, D. Schaurich, A. Taffe, and G. Wilsch, *Quantitative determination of sulfur content in concrete with laser-induced breakdown spectroscopy,* Spectrochimica Acta Part B: Atomic Spectroscopy **60**, 1121 (2005).

[9] K. Kagawa, N. Idris, M. Wada, H. Kurniawan, K. Tsuyuki, and S. Miura, *Carbon analysis for inspecting carbonation of concrete using a tea co(2) laser-induced plasma,* Applied Spectroscopy **58**, 887 (2004).

[10] G. Wilsch, F. Weritz, D. Schaurich, and H. Wiggenhauser, *Determination of chloride content in concrete structures with laser-induced breakdown spectroscopy,* Construction and Building Materials **19**, 724 (2005).

[11] K. Sugiyama, T. Fujii, T. Matsumura, Y. Shiogama, M. Yamaguchi, and K. Nemoto, *Detection of chlorine with concentration of 0.18 kg/m3 in concrete by laser-induced breakdown spectroscopy,* Applied Optics **49**, C181 (2010).

[12] K. Tsuyuki, S. Miura, N. Idris, K. H. Kurniawan, T. J. Lie, and K. Kagawa, *Measurement of concrete strength using the emission intensity ratio between $Ca(II)$ 396.8 nm and $Ca(I)$ 422.6 nm in a Nd : YAG laser-induced plasma,* Applied Spectroscopy **60**, 61 (2006), tsuyuki, K Miura, S Idris, N Kurniawan, KH Lie, TJ Kagawa, K.

[13] B. Praher, V. Palleschi, R. Viskup, J. Heitz, and J. D. Pedarnig, *Calibration free laser-induced breakdown spectroscopy of oxide materials,* Spectrochimica Acta - Part B Atomic Spectroscopy **65**, 671 (2010).

[14] M. Bruns, M. Raupach, C. D. Gehlen, R. Noll, G. Wilsch, and A. Taffe, *High speed chemical analysis of concrete surfaces using the LIBS method within the ILCOM project,* (2009) pp. 225–226, bruns, M. Raupach, M. Gehlen, C. D. Noll, R. Wilsch, G. Taffe, A. 2nd International Conference on Concrete Repair, Rehabilitation and Retrofitting Nov 24-26, 2008 Cape Town, SOUTH AFRICA.

[15] F. Weritz, D. Schaurich, A. Taffe, and G. Wilsch, *Effect of heterogeneity on the quantitative determination of trace elements in concrete,* Analytical and Bioanalytical Chemistry **385**, 248 (2006), weritz, F Schaurich, D Taffe, A Wilsch, G 3rd Euro-Mediterranean Symposium on Laser Induced Breakdown Spectroscopy Sep 06-09, 2005 Aachen, GERMANY.

[16] R. Kurucz and B. Bell, *Atomic Line Data* (Smithsonian Astrophysical Observatory, 1995) cD-ROM No. 23.

[17] L. J. Radziemski, D. A. Cremers, K. Benelli, C. Khoo, and R. D. Harris, *LIBS-based detection of As, Br, C, Cl, P and S in the VUV spectral region in a Mars atmosphere,* Lunar Planet. Sci. **XXXVI**, 1747 (2005).

[18] C. D. Gehlen, E. Wiens, R. Noll, G. Wilsch, and K. Reichling, *Chlorine detection in cement with laser-induced breakdown spectroscopy in the infrared and ultraviolet spectral range,* Spectrochimica Acta Part B-Atomic Spectroscopy **64**, 1135 (2009).

[19] F. Weritz, D. Schaurich, and G. Wilsch, *Detector comparison for sulfur and chlorine detection with laser induced breakdown spectroscopy in the near-infrared-region,* Spectrochimica Acta Part B: Atomic Spectroscopy **62**, 1504 (2007).

[20] M. Gondal, A. Dastageer, M. Maslehuddin, A. Alnehmi, and O. Al-Amoudi, *Sensitivity enhancement at 594.8 nm atomic transition of Cl I for chloride detection in the reinforced concrete using libs,* Journal of Environmental Science and Health, Part A **46**, 198 (2011).

[21] V. Burakov, V. Kiris, and S. Raikov, *Optimization of conditions for spectral determination of chlorine content in cement-based materials,* Journal of Applied Spectroscopy **74**, 321 (2007), cited By (since 1996) 3.

[22] L. Caneve, F. Colao, F. Fabbri, R. Fantoni, V. Spizzichino, and J. Striber, *Laser-induced breakdown spectroscopy analysis of asbestos,* Spectrochimica Acta - Part B Atomic Spectroscopy **60**, 1115 (2005).

[23] A. M. E. Sherbini and C. G. Parigger, *Wavelength dependency and threshold measurements for nanoparticle-enhanced laser-induced breakdown spectroscopy,* Spectrochimica Acta Part B: Atomic Spectroscopy **116**, 8 (2016).

[24] P. Lucena, A. Dona, L. Tobaria, and J. J. Laserna, *New challenges and insights in the detection and spectral identification of organic explosives by laser induced breakdown spectroscopy,* Spectrochimica Acta Part B: Atomic Spectroscopy **66**, 12 (2011).

[25] A. M. El Sherbini, A. A. S. Al Amer, A. T. Hassan, T. M. El Sherbini, *et al.*, *Spectrometric measurement of plasma parameters utilizing the target ambient gas oi & ni atomic lines in libs experiment,* Optics and Photonics Journal **2**, 286 (2012).

[26] A. V. Pakhomov, W. Nichols, and J. Borysow, *Laser-induced breakdown spectroscopy for detection of lead in concrete,* Applied Spectroscopy **50**, 880 (1996).

[27] F. Weritz, A. Taffe, S. Dieter, and G. Wilsch, *Detailed depth profiles of sulfate ingress into concrete measured with laser induced breakdown spectroscopy,* Construction and Building Materials **23**, 275 (2009).

.2. APPENDIX B: LASER ABLATION PARAMETERS ON SIX MATERIALS USING WHITE LIGHT INTERFEROMETRY IMAGE ANALYSIS-METHOD 1 WITH VARYING WORKING DISTANCE

Tab. 2 shows the extracted WLI geometric parameters from experiment type 1 defined in sec. 3.6, chap. 3. The S_{std} [10^{-1} μm], A_1 [10^3 μm^2], Avg_h [10^{-1} μm], V_1 10^3 μm^3, Max_h [μm], A_2 [10^3 μm^2], Avg_d [μm], V_2 [10^3 μm^3] and Max_d [μm].

Table 2: Single-shot LIBS-WLI geometric parameters on six materials (each sample is moved using away-in-away focus style).

shots	S_{std}	A_1	Avg_h	V_1	Max_h	A_2	Avg_d	V_2	Max_d
Cu1	2.28	5.93	4.02	2.38	1.80	15.31	0.32	4.85	1.02
Cu2	3.08	2.40	4.69	1.13	1.52	3.52	0.37	1.31	0.95
Cu3	2.35	2.07	3.79	0.79	1.30	11.27	0.30	3.39	0.97
Cu4	2.11	2.24	3.91	0.88	1.58	10.77	0.28	3.01	0.82
Cu5	2.16	1.68	3.55	0.60	1.28	7.42	0.29	2.13	0.70
Cu6	2.66	0.60	4.77	0.29	2.47	2.50	0.50	1.26	2.05
Cu7	2.72	0.95	5.33	0.51	2.22	2.78	0.61	1.69	2.64
Cu8	2.55	0.99	5.85	0.58	2.53	2.53	0.40	1.01	1.74
Cu9	2.29	1.90	4.80	0.91	2.64	3.16	0.31	0.99	0.84
Cu10	2.24	1.61	4.44	0.72	1.98	3.57	0.31	1.10	0.88
Cu11	2.69	1.55	5.22	0.81	3.34	3.85	0.91	3.51	3.34
Cu12	2.06	2.00	3.42	0.68	1.43	8.63	0.28	2.41	0.98
Cu13	2.33	1.83	3.76	0.69	1.24	13.42	0.33	4.42	0.92
Cu14	3.03	1.32	4.75	0.63	1.70	9.88	0.37	3.63	0.74
Cu15	2.54	2.63	4.25	1.12	1.46	12.58	0.34	4.23	0.80
Cu16	2.20	2.73	4.12	1.13	1.61	14.01	0.29	4.03	1.00
Cu17	2.89	1.16	4.82	0.56	1.45	4.80	0.37	1.80	0.89
Mo1	4.26	11.39	8.71	9.92	2.89	105.02	2.22	233.44	7.36
Mo2	4.23	38.93	11.33	44.10	5.06	23.86	1.95	46.51	5.11
Mo3	3.38	35.57	9.05	32.18	4.78	22.29	1.27	28.31	5.21
Mo4	4.36	19.03	9.78	18.60	5.58	41.86	1.75	73.08	5.57
Mo5	3.24	20.63	7.97	16.44	3.14	38.40	1.67	64.22	5.31

See next page

See next page

$shots$	S_{std}	A_1	Avg_h	V_1	Max_h	A_2	Avg_d	V_2	Max_d
Mo6	3.16	6.92	7.27	5.03	2.67	25.01	1.34	33.61	4.16
Mo7	3.67	9.58	9.22	8.84	4.19	2.49	2.04	5.10	7.00
Mo8	2.43	8.34	8.35	6.96	5.78	10.43	1.50	15.59	7.61
Mo9	2.13	14.44	8.01	11.56	5.17	3.55	0.95	3.38	3.31
Mo10	4.01	5.71	8.40	4.79	6.81	38.54	1.64	63.37	7.69
Mo11	5.43	7.70	11.09	8.54	6.06	46.30	1.58	73.33	5.67
Mo12	5.64	14.48	11.31	16.38	4.72	39.29	1.50	59.09	5.58
Mo13	6.32	9.34	11.24	10.50	3.23	48.88	1.99	97.29	6.49
Mo14	6.11	10.22	10.80	11.04	4.02	61.31	2.17	132.83	6.45
Mo15	5.04	17.85	9.00	16.05	2.71	72.13	2.09	150.51	6.16
Ni1	4.28	51.84	8.79	45.59	3.54	3.37	0.59	1.98	1.15
Ni2	4.32	35.41	8.85	31.34	3.46	2.31	0.59	1.37	1.43
Ni3	5.14	20.77	9.53	19.79	3.22	1.14	0.65	0.74	1.79
Ni4	7.91	7.52	12.18	9.16	3.14	0.08	0.89	0.07	1.38
Ni5	15.62	0.99	21.28	2.10	3.82	0.19	1.88	0.35	2.10
Ni6	4.28	5.17	16.55	8.55	7.51	3.61	2.58	9.32	5.87
Ni7	6.24	3.77	29.42	11.10	11.10	5.02	1.87	9.40	4.09
Ni8	5.72	2.66	21.02	5.59	8.73	3.33	2.28	7.59	6.07
Ni9	4.36	3.22	16.68	5.37	6.54	3.27	1.31	4.29	3.29
Ni10	4.63	3.30	14.30	4.72	5.87	3.03	1.06	3.21	2.34
Ni11	6.02	5.11	15.16	7.75	6.93	2.78	2.04	5.66	3.24
Ni12	4.79	16.04	9.51	15.26	3.98	3.42	0.69	2.34	1.57
Ni13	5.68	18.52	9.58	17.74	3.69	2.23	0.70	1.56	1.38
Ni14	5.02	28.14	8.32	23.41	3.69	1.34	0.64	0.85	1.45
Sb1	11.27	20.42	18.30	37.37	6.22	0.36	1.23	0.45	1.79
Sb2	8.16	18.01	14.33	25.80	6.35	4.10	1.05	4.29	1.81
Sb3	8.82	23.76	22.38	53.17	10.26	0.17	0.99	0.17	1.64
Sb4	8.28	17.35	17.08	29.64	7.45	0.57	1.03	0.58	1.95

See next page

See next page

$shots$	S_{std}	A_1	Avg_h	V_1	Max_h	A_2	Avg_d	V_2	Max_d
Sb5	7.31	11.48	15.00	17.22	6.36	2.98	1.46	4.36	3.00
Sb6	7.03	7.97	13.64	10.87	5.24	3.27	1.42	4.66	3.00
Sb7	8.04	9.50	15.83	15.05	6.67	4.77	2.11	10.06	7.50
Sb8	5.34	9.24	11.41	10.54	5.83	5.19	1.02	5.28	3.33
Sb9	28.76	4.07	36.56	14.88	8.39	0.02	2.93	0.06	3.11
Sb10	10.18	15.95	16.95	27.03	6.68	0.85	1.14	0.97	2.07
Sb11	7.31	65.84	34.42	226.64	11.83	2.26	2.40	5.41	3.11
Ti1	2.76	29.11	9.88	28.77	10.70	47.06	0.57	26.92	3.18
Ti2	2.43	16.06	10.20	16.39	8.64	25.64	0.70	17.99	4.20
Ti3	2.45	15.59	11.22	17.48	7.66	18.37	1.08	19.90	5.95
Ti4	2.90	16.54	10.16	16.80	7.40	21.82	0.92	20.07	5.88
Ti5	2.80	20.29	11.28	22.89	10.38	33.42	0.82	27.32	2.78
Ti6	2.40	25.72	10.97	28.22	8.50	41.74	0.75	31.17	3.91
Ti7	2.50	27.37	11.39	31.18	12.93	50.96	0.62	31.84	2.12
Ti8	2.62	26.26	11.60	30.48	13.78	58.42	0.56	32.59	1.93
Si1	3.33	24.26	9.47	22.98	5.71	24.99	0.56	14.04	1.94
Si2	3.51	19.89	9.28	18.47	4.94	19.98	0.58	11.63	7.34
Si3	3.80	18.27	9.57	17.48	4.28	18.01	0.65	11.76	2.00
Si4	4.03	13.65	10.10	13.79	5.36	11.98	0.77	9.22	2.96
Si5	3.26	6.35	15.16	9.63	44.66	9.60	1.04	10.00	6.49
Si6	3.38	10.22	8.54	8.73	5.38	12.37	1.08	13.39	3.95
Si7	4.03	7.07	10.41	7.36	24.98	7.94	1.22	9.65	5.58
Si8	3.68	9.62	9.24	8.89	5.65	10.10	0.96	9.71	33.94
Si9	3.87	11.68	11.05	12.91	38.46	13.74	0.87	12.00	2.96
Si10	3.92	14.61	11.61	16.96	14.92	16.56	0.86	14.22	4.15
Si11	3.45	18.04	10.51	18.97	46.24	16.68	0.74	12.41	4.34
Si12	4.70	16.06	11.25	18.06	33.14	12.48	0.74	9.25	38.40
Si13	3.56	22.94	8.83	20.25	5.20	20.58	0.58	11.94	21.28

.3. APPENDIX C: LASER ABLATION PARAMETERS ON FOUR MATERIALS USING WHITE LIGHT INTERFEROMETRY IMAGE ANALYSIS-METHOD 2 WITH VARYING LASER FLUENCE

Tab. 3 shows the extracted WLI geometric parameters from experiment type 2 defined in sec. 3.6, chap. 3. The S_{std} [10^{-1} μm], A_1 [10^3 μm^2], Avg_h [10^{-1} μm], V_1 10^3 μm^3, Max_h [μm], A_2 [10^3 μm^2], Avg_d [μm], V_2 [10^3 μm^3] and Max_d [μm].

Table 3: Five single-shot LIBS-WLI geometric parameters on four materials. Each shot energy varied using a different Q-switch delay.

shots	S_{std}	A_1	Avg_h	V_1	Max_h	A_2	Avg_d	V_2	Max_d
Cu1	2.23	1.73	3.65	0.63	1.26	17.99	0.26	4.72	0.70
Cu2	2.05	2.48	3.56	0.88	1.53	17.02	0.25	4.26	0.72
Cu3	2.34	2.09	3.88	0.81	1.38	10.35	0.27	2.77	0.69
Cu4	1.98	2.08	3.75	0.78	1.89	16.80	0.27	4.53	0.75
Cu5	2.78	1.33	4.97	0.66	1.43	6.25	0.32	1.97	0.70
Mo1	5.29	55.69	21.64	120.52	12.71	2.02	1.50	3.03	3.02
Mo2	2.92	69.28	16.14	111.80	10.15	5.68	0.43	2.46	2.05
Mo3	5.20	47.30	20.40	96.48	21.23	2.73	0.94	2.55	2.31
Mo4	2.49	54.70	18.11	99.05	16.66	7.73	0.46	3.57	4.62
Mo5	3.07	52.08	15.74	81.96	16.85	8.21	0.59	4.82	1.80
Ni1	5.43	37.64	9.15	34.44	2.95	2.87	0.67	1.92	1.45
Ni2	7.75	18.76	11.06	20.75	3.03	0.62	0.86	0.54	1.50
Ni3	5.32	34.07	9.04	30.81	2.98	2.67	0.67	1.78	1.60
Ni4	6.83	21.83	10.39	22.68	3.04	1.01	0.79	0.79	1.41
Ni5	5.87	25.27	10.19	25.75	3.54	1.92	0.70	1.34	2.07
Si1	2.23	25.79	8.03	20.72	6.00	34.98	0.50	17.33	2.32
Si2	3.08	21.75	9.31	20.24	5.41	26.50	0.59	15.58	2.53
Si3	2.90	22.53	9.73	21.92	5.46	27.36	0.64	17.44	1.99
Si4	2.01	21.44	9.42	20.20	6.24	29.28	0.66	19.24	1.99
Si5	2.11	16.42	10.33	16.95	8.35	26.68	0.70	18.60	1.70

ACKNOWLEDGEMENTS

My curiosity for physics started when my grandfather showed me how to burn a piece of paper by a focused spot of sun light using a magnifier. Doing a PhD goes definitely beyond curiosity. Only after one "pumps" a significant amount of effort continuously to keep oneself at the "excited levels", pulses of ideas might "burst" at some given moments. Ultimately, the interaction of such "high power pulses" with the unknown targets to explore might lead one to new discoveries. Ultimately, achieving a PhD is about my dream coming true. At this particular moment, I have so many people to thank during the course of my PhD.

To my promoter Prof. Peter Rem, I would like to express my deepest gratitude for creating this research project that allows me to combine applied physics with recycling. I appreciate your extensive advises, patient guidance, and proofreading my papers and thesis. Particularly, you demonstrated (as a theoretical physicist) how to instantiate industrial scale applications using innovative technologies, which is what I am trying to achieve for the rest of my career.

I am greatly indebted to my daily suppressor Dr. Maarten Bakker to whom I can never express my appreciation adequately, not only for initiating and coordinating this project, but also for supporting and guiding me through tough research challenges, for proofreading papers and thesis, for giving me the great freedom to try out my ideas, and for always keeping the door open for discussions. Following your heritage, I will be humble, and keep learning and absorbing new insights on daily basis, and not give up the root-cause finding easily.

I would like to thank my doctoral committee members, Prof.ir. Peter Luscuere, Prof.dr.ir. Arno Smets, Prof.dr. Andrei Metrikine, Prof.dr.ing. Mircea Tierean, Dr. Yongxiang Yang, and

Dr.ir. Marijn Sandtke. It is a great honor to have you all in my committee and I appreciate very much all your contributions.

My appreciation is due to Dr. Francesco Di Maio, for initiating and coordinating this research project, and for giving me many precious advises to keep our project deliverables on the right track. I also enjoyed the time very much when we gathered together in our off hours.

I am so grateful to Bin and Yuguang for providing their considerate helps for and outside work. Just to name one of those that I will never forget: during the night when Tessie was born, you picked up my parents-in-law from the airport and brought them home right in time. I just have the regret that I could not provide my help for you like you did for us, and I wish we can make our friendship last lifetime.

I acknowledge all the helps and contributions from Kees, Marten, Steve, Ruben for helping build up multiple variations of LIBS setups, incl. the laser lab, the mobile LIBS chamber for in-situ demonstration and etc. Thanks to Peter for arranging the demonstration and helping adopt our mobile LIBS chamber onto ADR in a real industrial production line. I would also like to thank Guus for those memorable lunch times and beautiful Orchid, Ron for helping with XRF measurements and your advices for becoming a better father. Thanks to Somi for a very good collaboration during the C2CA project and for offering your helps together with Mohi outside work. Thank Walter, Anna, Abdur, Francesco, Mohamed, and Claudia for all your helps and supports towards the finish of my PhD.

Words cannot express how grateful I am to my family. Particularly, I would like to express my deepest gratitude to my parents and parents-in-law. This work would not have been possible without your warm love, everlasting patience, sacrifices on behalf of us, and endless supports. A special thanks to my lovely daughters Tessie, Eva and Lucy, for making our life thus colourful and enjoyable, and for giving me the chance to grow as a father.

At last but most importantly, my appreciation to my beloved wife Min can never be

overstated for being the best confidant, wife and mother at the same time. Thinking of all the ways we have paved, I have no doubt that we will create a brighter future together.

About the author

Han Xia was born on 4^{th} April, 1985 in Suichang, Zhejiang province, China. He received his bachelor degree in Applied Physics at Huazhong University of Science and Technologies in Wuhan, China, in June 2008. He continued his master study at Clausthal University of Technology in Germany, where he obtained his master degree in Physical Technologies in June 2011. From July 2011 to October 2017, he was appointed as a PhD researcher in the Faculty of Civil Engineering and Geosciences at Delft University of Technology in the Netherlands under the supervision of Prof. Dr. Peter Rem and Dr. Maarten C.M. Bakker, of which work results in this present thesis. From November 2017 on, he joins the Development and Engineering department for EUV Source at ASML in Veldhoven, the Netherlands. As a design engineer he is engaged in the insertion of next generation EUV lithography technology into high volume production for semi-conductor manufacturing industry.

PUBLICATIONS RELATED TO THIS WORK

JOURNAL PAPERS

3. **H. Xia**, **MCM. Bakker** *Reliable classification of moving waste materials with LIBS in concrete recycling,* Talanta, Elsevier **Vol. 120**, p.239-247 (2014).

2. **H. Xia**, **MCM. Bakker** *Single-shot LIBS spectral quality for waste particles in open air,* tm - Technisches Messen **Vol. 82, Issue 12**, p.606-615 (2015).

1. **MCM. Bakker**, **H. Xia** *Sensing & Measurement Laser-induced breakdown spectroscopy for identification of solid recycled materials,* SPIE-Newsroom (2015).

CONFERENCE PROCEEDINGS

8. **H. Xia**, **MCM. Bakker** *Quality inspection on recycled coarse aggregates using laser-induced breakdown spectroscopy,* 2017 Optical Characterization of Materials conference, Karlsruhe, Germany, KIT Scientific Publishing, p.53-63 (2017).

7. **MCM. Bakker**, **H. Xia** *On the homogeneity of a thick layer of mixed granules in optical quality inspection,* Conference Proceedings, The Third Symposium on Urban Mining and Circular Economy, CISA Publisher, (2016).

6. **MCM. Bakker**, **H. Xia** *Recycling of End of Life Concrete to New Concrete,* Proceedings SUM2016, 3rd Symposium on Urban Mining and Circular Economy, Bergamo, Italy, CISA Publisher, (2015).

5. **H. Xia**, **MCM. Bakker** *Quality of open air, single-shot LIBS spectra from waste particles,* 2015 Optical Characterization of Materials conference, Karlsruhe, Germany, KIT Scientific Publishing, p.169-178 (2015).

4. **H. Xia**, **S. Lotfi**, **MCM. Bakker** *Laser-induced breakdown spectroscopy for quality inspection of a fine fraction of demolition concrete,* Abstract proceedings of the 8th Euro-Mediterranean Symposium on Laser-Induced Breakdown Spectroscopy, EMSLIBS 2015, Johannes Kepler University in Linz, Austria, p.66 (2015).

3. **S. Lotfi**, **F. Di Maio**, **H. Xia**, **S. Serranti**, **R. Palmieri**, **G. Bonifazi** *Assessment of the contaminants level in recycled aggregates and alternative new technologies for contaminants recognition and removal,* Proceedings of the 15th Euroseminar on microscopy applied to building materials, Delft, The Netherlands, p.319-331 (2015).

2. **H. Xia**, **MCM. Bakker** *LIBS inspection and particle segregation in the transport of recycled concrete waste,* Abstract proceedings of the 8th International Conference on Laser Induced Breakdown Spectroscopy, LIBS2014. TsingHua University in Beijing, China (2014).

1. **H. Xia**, **MCM. Bakker** *Online Sensor System Based on Laser-induced Breakdown Spectroscopy in Quality Inspection of Demolition Concrete,* The 27th International Conference on Solid Waste Technology and Management, Philadelphia, PA U.S.A., p.832-840 (2012).

HONORS AND AWARDS

2. **BouwRecycling 2nd Pitch Award,** the 5th Recycling symposium, Evenementenhal Gorinchem (Oct. 2016)

1. **Student Paper Award,** the 27th international conference on Solid Waste Technologies and Management, Philadelphia, PA, USA, (Mar. 2012)